AMBIENT ENERGY HARVESTING–AN ELECTROSTATIC APPROACH

A DISSERTATION SUBMITTED TO THE GRADUATE DIVISION OF THE
UNIVERSITY OF HAWAI‘I AT MĀNOA IN PARTIAL FULFILLMENT
OF THE REQUIREMENTS FOR THE DEGREE OF

DOCTOR OF PHILOSOPHY

IN

CIVIL AND ENVIRONMENTAL ENGINEERING

JUNE, 2018

By

Jian Yu

Dissertation Committee:

David T. Ma, Chairperson

Olga Boric-Lubecke

Aaron Ohta

Ian Robertson

Lin Shen

Keywords: Electrostatic Energy harvesting, variable capacitor, exponential growth, positive feedback, contact electrification, electrostatic induction, water drop, hydrophobic surface

ACKNOWLEDGMENTS

A great number of people help me during my journey to pursue Ph.D. degree. I would like to thank my advisor, Dr. David Ma, for his continued support. His suggestions, encouragement and belief gave me strength to overcome difficulties in research. I also thank my committee members (Dr. Olga Boric-Lubecke, Dr. Aaron Ohta, Dr. Ian Roberston, and Dr. Shen) for their comments. My gratitude also goes to Dr. Joseph Brown who helping me for the dissertation editing.

I would also like to thank all these colleagues for their advice and help with experiments. I won't attempt to name them all because of fear of leaving one out. I appreciate all the help and hard work of undergraduate helpers, Enze Ma and Blake Kadomoto.

Last, but not least, I would like to thank my parents for their eternal love and support through my life. I'm indebted to my wife Chengcheng for her unwavering love, consistent support, and endless patience. I also thank my two-year-old son, Matthew, for always cheering me up.

ABSTRACT

With the rapid advancement of very-large-scale integration and miniaturization, wireless micro-sensors, wearable devices and biomedical implants have been implemented all over the world. Nowadays, batteries are considered as primary power sources for the majority of electronics. They need to be periodically charged or replaced due to their limited lifetime, which is inconvenient and may lead to increased costs. One promising solution is to harvest unused energy sources surrounding those electronic devices into electric energy, which can be considered as alternative or auxiliary power sources. There is a variety of ambient energy sources, such as solar, mechanical, thermal and chemical. Among the existing energy harvesting mechanisms, electrostatic energy harvesting draws our attention because of its various advantages, such as low-cost fabrication, high achievable energy harvesting efficiency and capability for large-scale integration and miniaturization. Furthermore, the electrostatic approach can be used to harvest a variety of ambient energy sources, such as mechanical, thermal and chemical. However, some challenges also exist, such as relatively small initial charge and capacitance, requirement for an external power supply, and complex power management control circuits to extract generated energy at the appropriate time.

Two novel methods have been proposed in this dissertation to solve the current challenges for electrostatic energy harvesting. The first method utilizes an appropriate, repetitive reconfiguration process to create a positive feedback mechanism, thus, restoring the generated energy back to the system. Even a small disturbance on a system could significantly amplify electric outputs. Because of the exponentially growth rate of energy extraction, this method is particularly effective for distributed devices to scavenge energy from low-level ambient sources,

thus enabling self-powered operation. As proof of concept, two rotary variable capacitors in addition with a fixed ceramic capacitor are used to establish a positive-feedback system. To achieve relatively high capacitance, liquid-contact variable capacitors are developed for the system. Because of contact electrification and electrostatic induction, the contact variable capacitors can provide relatively high extra charge in each cycle. In our experiments, the prototype using three mercury droplets can generate 10.2 μJ per cycle, corresponding to a harvesting efficiency of 12.2% and the values for the prototype with three water droplets will be 1.2 μJ per cycle and 7.9%. The efficiencies of the devices far exceed those of the existing droplet generators. Since the concept of exponential energy harvesting is not domain specific, it may lead to new research in directional energy transfer systems in various energy domains, such as salinity gradients and temperature differences.

An additional proposed method utilizes water droplets that alternate contacts between CYTOP and PTFE thin films to provide high initial charge for vibration energy harvesting. Because CYTOP and PTFE develop significantly different surface charge densities during contact with water, they can be utilized to generate electricity effectively. More importantly, the proposed method utilizes the strong electrostatic induction in the water droplets due to the electrical double layer formed at the interface. A harvesting efficiency of 2.5% has been achieved in this study. It is more effective than existing methods that are based on the much weaker electrostatic induction in the substrate. Also, unlike existing methods, in which the charge of the drop is not delivered to external circuits, in our method, the water droplets possesses a dual function as both an electrode and a passive switch, leading to the direct harvesting of the peak electric potential energy. This method not only results in simple device architecture but also allows schemes based on variable capacitors to improve the performance. Using prototype devices, we demonstrate the effectiveness of this approach in scavenging energy from low-level and low-frequency ambient vibrations.

TABLE OF CONTENTS

LIST OF TABLES

LIST OF FIGURES

1 INTRODUCTION

1.1 Background and motivation

In a broad sense, energy harvesting is a process of one-way energy transfer from an ambient energy source to a targeted system. While the idea dates back hundreds of years as seen in windmills that harness wind energy to rotate the wheels for pumping water and milling grains, scientific research of energy harvesting did not start until the last century. In a modern world that relies heavily on electricity to support the majority of human activity, energy harvesting usually refers to electricity generation, i.e. the conversion of energy from an energy source to electricity. The dominant primary energy sources on earth are fossil fuels, such as oil, coal and natural gas. However, uses of fossil fuels cause large emissions of greenhouse gases. Moreover, reserves of fossil energy sources are finite and unsustainable because the process of formation takes millions of years, which causes fossil fuels to deplete rapidly. Increasing electricity demand around the world [1] makes the situation even worse. Energy harvesting is considered a promising alternative to fossil energy sources for providing on-grid or off-grid energy services [2, 3]. There are a variety of preferable clean ambient energy sources, such as solar energy, mechanical energy, thermal energy and chemical energy. Tremendous efforts have been devoted to developing efficient technologies to generate electricity from ambient energy sources. It is estimated that the total availability of ambient energy is equal to 3000 times the current global energy consumption [4, 5]. Such huge potential encourages intensive research to develop more efficient methods for energy harvesting.

There are also high demands to develop low-level energy harvesting technologies for electronics. With the rapid technological advancement, wireless micro-sensors, wearable devices and biomedical implants have gained use across the world. For example, wireless sensors have been developed to monitor continuously infrastructure, industry, and for use in many other applications. Various implantable devices are deployed to monitor health conditions. Meanwhile, the power consumptions of the sensors have been reduced enormously due to technological advancement. Nowadays, batteries are considered primary power sources for a majority of electronics. They need to be periodically charged or replaced due to their limited lifetime, which is inconvenient and may lead to increased costs, especially for those that are inaccessible after deployment, such as biomedical implants and sensors on unreachable locations. Even with some advanced technologies, batteries still need frequent recharge or replacement because of their limited growth of energy capacity. Therefore, powering electronics with batteries is still considered a critical bottleneck [6]. One promising solution is to harvest the unused ambient energy into electric energy, which can be considered to be alternative or auxiliary power sources for batteries. Using this method, the powered devices can be self-sustained in long term without any human intervention. Corresponding energy transduction technologies have been developed in recent decades to harness a variety of ambient energy sources. Among them, electrostatic energy harvesting draws our attention because this method can be used to harvest a variety of energy sources, i.e. mechanical, thermal and chemical.

1.2 Literature review

Fundamentally, electrostatic energy harvesting relies on the work done by the ambient energy source against the electrostatic force between charges in an equivalent capacitor. Therefore, a variable capacitor is one key component to extract ambient energy. In early studies, the electrostatic method was mainly used to harvest mechanical energy. After encountering the promising potential of the method, such as in low-cost fabrication, high output voltage, high

reachable energy harvesting efficiency and the capability of large-scale integration and miniaturization, many researchers regained their interest and attempted to improve the method to harvest other energy domains. In the literature review, after introducing basic principles and main categories of electrostatic energy harvesting, a variety of electrostatic devices for mechanical energy harvesting are discussed. They can be divided into two types based on the initial charge sources, i.e. external power supply and electret. Some other electrostatic devices are then discussed for other types of ambient energy sources, such as thermal energy and concentration gradient.

1.2.1 Power consumption of wireless nodes and wearable devices

With the rapid technological advancement, wireless micro-sensors, portable, and implantable devices are used enormously in many applications. Sensing systems have been exploited to measure a wide variety of signals, such as heat, light radiation, vibration, magnetic field, chemical and electrical signals. In automotive and aerospace industries, sensors can be used to monitor distance, acceleration, force, pressure, temperature, etc. In civil structures, sensors can be used to check the performance of buildings, bridges, and roads. In the chemical industry, sensors can be used to monitor humidity, pH level, pollutants, etc. In the biomedical industry, sensors can be used to monitor blood pressure, organ function, prosthetic attachment, drug delivery and assimilation, etc. In recent studies, wearable devices [7, 8] and biomedical implants [9], such as smart watches and pacemakers, have garnered increased interest. Because of the technological advancement, the power consumption of the sensors has been enormously reduced.
State-of-the-art digital acceleration, temperature, humidity, and light sensors only require power on the order of micro-watt (μW) for full functional operations. Taking an accelerometer for example, ADXL362, a 3-axis MEMS accelerometer from Analog Devices®, consumes less than 4 μW at a 100 Hz output data rate and the standby power consumption is about 20 nW [10]. For wearable devices, an analog quartz watch, for example, consumes as low as 1 μW [11]. For implantable medical devices, such as retinal implants, cardiac pacemakers, and deep brain

stimulators, their power consumption typically ranges from hundreds of nW to hundreds of μW [12] [13, 14]. For remote data transmission, a compliant radio transceiver with IEEE 802.15.4 protocol requires 0.5–1 mW under continuous mode [15], which is higher than the generated power of most proposed small-scale electrostatic energy harvesters. If intermittent mode is used, i.e. the energy can be temporarily accumulated until it can power remote data transmission for a certain time, the power consumption can be heavily reduced to the order of μW. Because of such ultra-low power consumption, it is possible to make the sensors self-sustained without maintenance by using ambient energy harvesters.

1.2.2 Basic principle of electrostatic energy harvesting

The basic principle of state-of-the-art electrostatic energy harvesting is to change capacitance cyclically using the ambient energy source. The generated energy in each cycle is equal to the work done against the electrostatic force between the initial charges in a device. A variable capacitor is one of the key components for electrostatic energy harvesting. In most cases, the equivalent capacitor can be usually modeled as a parallel-plate capacitor, i.e. $C = \epsilon A/d$. Therefore, the capacitance can be changed by three ways: permittivity of the dielectric material ϵ, overlap area A, and the separation between two electrode plates d. If the ambient energy source can be used to change any of the above parameters, electrical energy can be generated via this electrostatic approach. In addition to a variable capacitor, an initial charge needs to be provided for the method. In many studies, a charged capacitor or battery in addition with an appropriate circuit was used to provide the necessary initial charge. In order to reduce the complexity introduced by using external sources of power supply, a variety of alternative approaches have been developed, such as electrets and contact electrification.

1.2.3 Categories of electrostatic energy harvesting

Numerous electrostatic devices have been developed in recent decades, which can be divided into three categories based on the variety of the energy harvesting cycle: fixed charge, variable charge & voltage, and fixed voltage.

Figure 1.1 illustrates the schematic diagram of electrostatic energy harvesting using a charge-constrained cycle. A capacitor or battery can be used to provide an initial charge for the variable capacitor. In order to demonstrate the energy generation system, one capacitor is chosen in the schematic diagram, which is denoted the source capacitor. Here, the charge of C_0 in the i^{th} cycle as $q_0(i)$. At the beginning state of the $(i+1)^{th}$ charge-constrained cycle, there is no charge in the variable capacitor and its capacitance is at its maximum state C. Switch S_1 is closed and switch S_2 is opened. C_0 starts to provide charge for the variable capacitor. After the equilibrium, the charge is distributed as

$$\begin{aligned} q_0(i+1) &= \frac{C_0}{C_0+C} q_0(i) \\ q(i+1) &= \frac{C}{C_0+C} q_0(i) \end{aligned} \tag{1.1}$$

where $q_0(i+1)$ and $q(i+1)$ are the charge during $(i+1)^{th}$ cycle in the source capacitor and variable capacitor, respectively. In the second step, S_1 is opened and S_2 remains open. Meanwhile, the capacitance of the variable capacitor changes from C to C' by the ambient energy source. During this state, the charge is constant. According to $E = \frac{Q^2}{2C}$, the electrical energy of the variable capacitor increases due to the decreasing capacitance. In the third step, S_2 is closed while S_1 remains open. An electric load R is connected to the variable capacitor until the capacitor is fully discharged. In the fourth step, the capacitance of the variable capacitor returns to C and both switches remain open for the next cycle. In the whole cycle, the theoretical generated energy can be expressed as

$$\begin{aligned} E(i+1) &= \frac{C^2 q_0^2(i)}{2C'(C_0+C)^2} + \frac{C_0 q_0^2(i)}{2(C_0+C)^2} - \frac{q_0^2(i)}{2C_0} \\ &= \frac{\kappa(C_0\kappa - C - 2C_0) q_0^2(i)}{2C_0 C'(C_0+C)^2} \end{aligned} \tag{1.2}$$

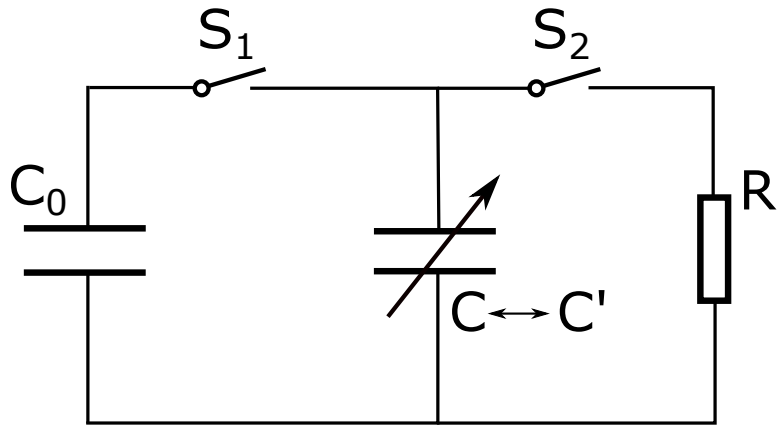

Figure 1.1: Schematic diagram of electrostatic energy harvesting using charge-constrained cycle.

where $\kappa = C/C'$. In order to make the net energy positive, i.e. $E(i+1) > 0$, κ needs to satisfies the following condition,

$$\kappa > 2 + C/C_0 \tag{1.3}$$

The above requirement is caused by the energy loss of the charging process in the first step of the charge-constrained cycle, which is unfortunately ignored in many studies [16, 17].

Figure 1.2 shows the schematic diagram for the variable charge & voltage cycle. In this diagram, both the charge and voltage of the variable capacitor are changing while the total charge of the circuit, which can be denoted as Q, is constant during the cycle. There are two states for the variable charge & voltage cycle. In the first state, the variable capacitor is at its maximum capacitance C. The charge is distributed as

$$\begin{aligned} q_0^{(1)}(i+1) &= \frac{C_0}{C_0 + C} Q \\ q^{(1)}(i+1) &= \frac{C}{C_0 + C} Q \end{aligned} \tag{1.4}$$

where $q_0^{(1)}(i+1)$ and $q^{(1)}(i+1)$ is the charge during first state of the $(i+1)^{th}$ cycle in the source capacitor and variable capacitor, respectively. In the second state, the variable capacitor is at its

minimum capacitance C'. The corresponding charge is distributed as

$$\begin{aligned} q_0^{(2)}(i+1) &= \frac{C_0}{C_0 + C'} Q \\ q^{(2)}(i+1) &= \frac{C'}{C_0 + C'} Q \end{aligned} \tag{1.5}$$

The electric load R is constantly connected in the circuit and the current is alternating. The capacitance of the variable capacitor is decreased from C to C', reduced capacitance leads to increasing voltage. Therefore, the charge of variable capacitor moves towards the source capacitor. During this process, the consumed energy by electric load is shown as

$$\begin{aligned} E^{(1)}(i+1) &= \frac{Q^2}{2(C_0 + C')} - \frac{Q^2}{2(C_0 + C)} \\ &= \frac{(C - C')Q^2}{2(C_0 + C')(C_0 + C)} \end{aligned} \tag{1.6}$$

When the capacitance of the variable capacitor returns to C, the voltage of variable capacitor decreases due to the increasing capacitance. Therefore, the produced current flows towards the variable capacitor, which is opposite to the previous process. After equilibrium, the consumed energy by R during this process is equal to that of the previous process, i.e. $E^{(2)}(i+1) = E^{(1)}(i+1)$. Therefore, the total generated energy from the ambient energy source in each cycle is given as

$$E_t(i+1) = \frac{(C - C')Q^2}{(C_0 + C')(C_0 + C)} \tag{1.7}$$

According to equation 1.4 and 1.5, the voltage of the variable capacitor can be expressed as

$$\begin{aligned} V^{(1)}(i+1) &= \frac{Q}{C_0 + C} \\ V^{(2)}(i+1) &= \frac{Q}{C_0 + C'} \end{aligned} \tag{1.8}$$

If C_0 is much higher than C, the change in the voltage of the variable capacitor is negligible during the entire cycle, this is called a constrained voltage cycle by some studies [18, 17]. In this

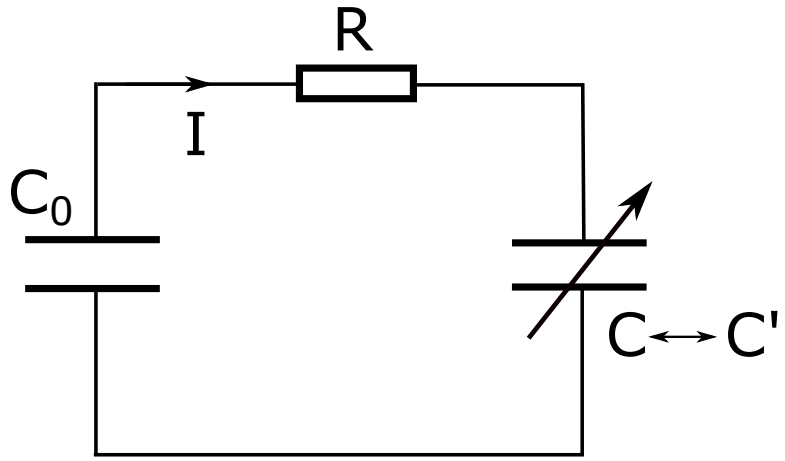

Figure 1.2: Schematic diagram of electrostatic energy harvesting using a variable charge & voltage cycle.

dissertation, the constrained voltage cycle is considered one specific example of the variable charge & voltage cycle.

In the variable charge & voltage cycle, the charge of the source capacitor is not consumed during energy harvesting. A rectifying circuit may be needed because the current alternates. According to equation 1.6, the condition for the system harvesting ambient energy is $C > C'$. Compared to the charge-constrained cycle, direct current (DC) is produced and thus the rectifying circuit is no longer needed. However, the charge of the source capacitor is continuously consumed during energy harvesting, resulting in the need for repeated charging. Also, the variable capacitor must meet the condition of equation 1.3 so that the system can harvest energy from an ambient energy source. Furthermore, switches are also needed to achieve different steps in the charge-constrained cycle. Here the extracted energy is consumed by a resistor R. If the energy needs to be stored, a power management control circuit is needed to extract the electricity at the appropriate time for both types of cycles.

1.2.4 Using electrostatic approach to harvest mechanical energy

Vibration sources exist ubiquitously in most environments, such as in structures, moving vehicles, ocean or lake waves, rainfall, and even human motion. Advancements in modern technologies

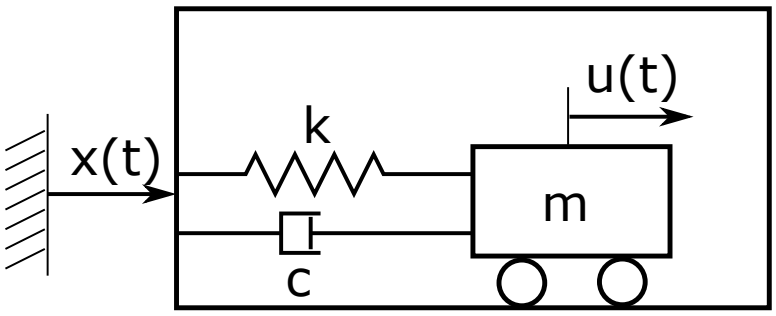

Figure 1.3: Schematic diagram of generic vibration transducer.

reduce the power requirements for remote sensors with low duty cycles down to the order of μW [19, 20, 21]. Such advancements make self-powered sensors possible by scavenging ambient energy. Existing methods of small-scale mechanical-to-electrical energy conversion are divided into three major types: electromagnetic, piezoelectric, and electrostatic, each of which has numerous examples reported in literature. Figure 1.3 illustrates a generic model for mechanical-to-electrical energy conversion [22]. This mass-spring model consists of mass m, linear spring k, and damping c. Motion of the mass takes place when there is external vibration $x(t)$. The equation of mass motion can be described as

$$m\ddot{u} + c\dot{u} + ku = -m\ddot{x} \tag{1.9}$$

where $c = c_e + c_m$, c_e and c_m are the electric coupling damping coefficient and the mechanical damping coefficient, respectively. The effectiveness of the system converting ambient energy into electrical energy can be represented by the electric coupling damping coefficient.

Among the mechanisms noted earlier, electrostatic energy harvesting has attracted increasing interest due to its convenience for electrostatic energy storage, high output voltage, high achievable coupling efficiency, and the capability of harvesting various types of ambient energy sources. In 2001, Meninger and his colleagues fabricated an air variable MEMS capacitor [18]. The proposed electrostatic energy generator utilizes the plates of a variable capacitor moving against the electrostatic force between two plates to convert mechanical energy into

electrical energy. Since then, a great deal of electrostatic energy generators in literature have been developed[16, 23, 24, 17]. Based on the methods of providing initial charge, they can be divided into three major types: external power supply, electret, and contact electrification.

External charge bias for initial charge

In early studies, the initial charge of the capacitor was usually provided by external power sources, such as commercial batteries or capacitors. In 2001, the first MEMS electrostatic energy harvester was fabricated to convert mechanical vibration into electrical energy [18]. Although the report claimed that a voltage-constrained method provided higher power output, use of a charge-constrained circuit allowed for easier power management. By using the charge-constrained cycle, a 2.25-cm^2 energy harvester can generate up to 8.6 μW with a 1.5V external voltage source under 2.5 kHz vibration. Using a complex circuit which includes an inductor, the proposed system was able to generate 5.6 μW of usable power. However, the resonant frequency of the proposed MEMS energy harvester was higher than that of most ambient energy sources. Since then, numerous studies have been developed to improve the performances of electrostatic energy harvesters, such as lowering the resonant frequency of electrostatic energy harvesters [25, 26], and increasing the power density [27, 28, 29] .

One of main advantages for electrostatic energy harvesters is the capability of large-scale integration by using micro-fabrication. Currently, capacitive transducers are routinely manufactured through standard micro-fabrication techniques. This reduces the cost associated not only with manufacturing the generator but also with its integration of power control and wireless communication circuitry. Moreover, this particular technique has a high potential for miniaturization because ultra-small features can be routinely fabricated in silicon technologies. These advantages constitute a powerful motivation to improve the state-of-the-art design in electrostatic power generators. However, The cantilever structure is used in most silicon-based MEMS devices. The resonant frequencies of these devices are much higher than the typical frequencies of ambient energy sources heavily reduce harvesting efficiencies. According to

equation 1.9, the frequency mismatch results in the prototypes with lower amplitudes, leading to a reduced harvesting efficiency. Relatively macroscopic devices were proposed in some studies to lower their resonant frequencies. In Tashiro's study [25], a 15 cm^3 electrostatic generator was developed to convert the motion of the ventricular wall into electrical energy for a cardiac pacemaker. In order to match the low frequency of motion of the ventricular wall, the device consists of multiple layers of aluminum-evaporated polyester film sheets to achieve lower structural stiffness. Diodes were used in the charge-constrained circuits to function as passive switches. A mean power of about 36 μW was generated under 6 Hz vibration with a 45 V external voltage bias. Such generated power was enough to drive a working cardiac pacemaker. In Despesse's study [26], a 18 cm^3 electrostatic device with bulk tungsten as the mass was developed to achieve high electrical damping coefficient c_e. In the study, high density of tungsten leads to higher mass in a limited space, thus reducing the resonant frequency of devices to 50 Hz. The proposed prototype can generate 1 mW with a 3 V external voltage bias under 50 Hz sinusoidal vibration.

Other than silicon-based variable capacitors, two other types of capacitors were proposed in the electrostatic energy harvesting. Krupenkin *et al.* [29] proposed a high-power energy harvesting generator by applying the reverse electrowetting phenomenon. The generator utilized the interaction of microscopic liquid droplets with multilayer thin films to convert a broad range of mechanical vibrations into electricity. The capacitance of the fabricated device is changed due to the overlap area between stationary electrode and movable microscopic liquid droplets. Using voltage-constrained cycle, the proposed prototype can generate up to 3 $\mu J/cm^2$ per cycle with a 70 V external voltage bias under 50 Hz vibration. The other type of capacitor, a dielectric elastomer generator, was proposed by numerous studies for electrostatic energy harvesting. Dielectric elastomers are relatively soft materials and can be stretched to high strain, and these allow them to be used as actuators. Pelrine *et al.* [30] first utilized dielectric elastomers as dielectric materials of variable capacitors for electrostatic energy harvesting. Because of the relatively low elastic modulus, the natural frequencies of elastomer-based generators are much

lower than majority of silicon-based variable capacitors. The range of energy density for the elastomer-based generators is from 2.15 to 400 mJ/g [30, 31, 32, 33].

According to equations 1.2 and 1.7, the generated energy per cycle has a quadratic relationship with the initial charge of the variable capacitor. In the previous section, commercial batteries or capacitors were usually deployed as external voltage biases in addition with voltage boost converters, which complicate the system. Second, the generated energy is not usually restored to the external voltage bias in the current method. As discussed earlier, the external voltage bias is depleted eventually for the charge-constrained cycle, which stops energy harvesting. For the voltage-constrained cycle and the variable charge & voltage cycle, theoretically, the electricity of the external power supply is not consumed during the energy harvesting cycle. In practice, spontaneous current leakage drains the external power supply gradually.

Electret and Contact electrification for providing initial charge

In order to make the electrostatic approach more practical, numerous studies have been done to develop other alternatives of external power supply. There are two up-to-date alternative methods to provide initial charge: electret and contact electrification. An electret is a quasi-permanent charged dielectric material that is caused by injected electric charge or dipole polarization due to a strong electric field. Well-known electrets, such as Teflon [34, 35, 36], CYTOP [37, 38], and SiO_2 [39, 40, 41], are coated on one of electrode. Because of electrostatic induction, induced charge is developed in the counter electrode when there is relative displacement between the electret and counter electrode. Contacts between electrets and electrodes are avoided as they lead to discharge of electrets. In early studies, dipole-polarized electrets were usually used in electrostatic energy harvesting [42]. The basic fabrication process is to apply a strong electric field when electrets are heated to their melting temperatures. Charge-injected electrets were commonly utilized later due to their easy fabrication process, in which a metal tip with high voltage is used to launch ions into the selected dielectrics [39, 34]. The injected charge density can achieve up to 0.1-10 mC/m^2

[43, 44, 45, 46], depending on the properties of selected dielectric materials. The electrets have proven to be effective alternatives to external voltage bias by numerous studies [17, 46]. However, electret stability is a critical limitation for this method. The excess charge in electrets decay gradually [17]. The decaying speed depends on the surrounding environments, such as humidity and temperature. Moisture and high temperature deteriorate electrets [47, 48].

Another solution is proposed by Wang *et al.* [49, 50, 51, 52]. They utilized contact electrification and electrostatic induction to provide initial charge for a variable capacitor. When two different materials contact each other, net charge is transferred between them due to contact electrification. Such established surface charge is quasi-permanent, making the surfaces behave as electrets. Unlike electrets, the surface charge can be maintained at a certain value due to repeated contacts even under harsh environmental conditions. Other than the properties of materials, the surface charge density also depends on specific contact area, which can be improved by rough surface [51]. In solid-to-solid contact applications, a high applied pressure on two different materials can also get higher contact area, which leads to higher induced charge. In one paper [50], a 6 in^2 triboelectric generator can convert 0.74 mJ when applied force is 500 N. Its energy density is up to 19 $\mu J/cm^2$. Frequent tight contacts between two solid materials may decrease the surface roughness, which results in less energy output. One solution is to replace one of the solid material by liquid droplets. Wang *et al.* [52] obtained 40 nJ when a 30 μL water droplet traveled a height of 90 cm across the PTFE thin film. Some other papers reported similar results. Moon *et al.* [53] modulated a 40 μL water droplet to obtain about 40 nW at 30 Hz vibration. From the above studies, although liquid-solid contact does not need external high force such as solid-solid contact, the low surface charge density due to contact electrification reduces the energy conversion efficiency.

1.2.5 Using the electrostatic approach to harvest other energy sources

Other than harvesting mechanical energy, the electrostatic approach can be used to harvest other types of ambient energy sources, such as salinity gradients and temperature differences.

Supercapacitors, or ultracapacitors, achieve large capacitance several orders of magnitude above conventional capacitors by utilizing electrode materials with high specific surface area and new energy storage principles [54]. In recent years, much research focused on supercapacitors because of their high power density and cycling stability [55]. In 1957, H. Becker accidentally found that porous carbon electrodes cause significantly high capacity of energy storage [56]. The mechanism of the electric double layers could be applied to store massive electrostatic energy [57] at the interface between the electrolyte and porous carbon materials. Since then, the corresponding devices, electric double layer capacitors (EDLCs), were also developed. These high-capacitance capacitors can offer much higher power density, longer cycle life and shorter charging time than conventional batteries. EDLCs utilize the double layer mechanism to store electric potential energy [58, 59]. Because the distance between the electron layer on porous electrodes and the ion layer in electrolyte is only a few of molecules thick [60], the theoretical capacitance of EDLCs per area is 5-20 $\mu F/cm^2$ depending on the electrolyte used [61, 55]. Theoretically, the higher the specific surface areas (SSAs) of carbon electrodes are, the higher the capacitance of the EDLC. Various forms of porous carbon materials have been developed to improve the performance and capacitance in the recent decades, such as activated carbon [62, 63, 64, 65], carbon aerogel [66, 67, 64, 68], carbon nanotube [69, 70, 71], and graphene [72, 73, 74]. Those carbon materials all have good electronic conductivity and extremely high specific surface areas in the order of 1000 m^2/g, which leads to high capacitance of many tens of farads per gram [71, 65, 74]. EDLCs have high cycling stabilities in the order of 10^6 cycles due to non-faradaic processes while conventional batteries are limited to $\sim 10^3$ cycles.

In Brogioli's research [75], a variable EDLC was developed to extract renewable energy from the solutions of different salinity. The relationship between ion concentrations c and the electric potential of EDLCs $\Delta\varphi$ can be given by Gouy-Chapman equation [76]:

$$\Delta\varphi(\sigma, c) = \frac{2\kappa_B T}{e} sinh^{-1}(2\pi\lambda_B\lambda_D\frac{\sigma}{e}) \tag{1.10}$$

where σ is the charge per specific surface area on the porous electrode, κ_B is the Boltzmann constant, T is the temperature in kelvin, e is the charge of one electron, λ_B is the Bjerrum length, and λ_D is the Debye length. From the above equation, in the charge-constrained cycle, the electric potential of EDLCs $\Delta\varphi$ increases with decreasing ion concentration c, which can be used to extract energy by mixing salinity-gradient solutions. Activated carbon was chosen as the electrode material. The proposed prototype can achieve 5 μJ per cycle when it is dipped alternatively into 24 mM and 0.6 M NaCl solutions. The extracted energy was increased to 4 mJ/cm^3 per cycle after further improvement [77]. The electrostatic prototype proposed by Brogioli *et al.* still needs an external power supply to provide initial charge for the variable EDLCs. In order to solve this problem, Sales *et al.* [78] proposed that ion-exchanged membranes can be used as the alternatives of external power supply. The driving force for ions between anion-exchange membrane and cation-exchange membrane can be used to establish a polarity voltage for the EDLC. The fabricated prototype can generate a peak power of $\sim 60\ mW/m^2$.

The electrostatic approach can also be used to harvest thermal energy via constant-capacitance EDLC. According to equation 1.10, the electric potential of EDLCs is proportional to the ambient temperature under constant charge. $Härtel$ *et al.* [79] used a commercial EDLC to harvest energy from ambient temperature gradient. The electric potential of the 10-Farad supercapacitor was charged to 2.5 V under 0 ^oC. Using charge-constrained cycle, the generated energy per cycle can achieve up to 500 mJ under 65 ^oC.

1.2.6 Generic form of variable energy element

A variable capacitor is usually selected to convert ambient energy sources into electrical energy for electrostatic energy harvesting. In generic form, any energy element that enables change to its energy capacity can be used in the electrostatic approach. In this section, some other types of variable energy elements are discussed.

An entropy mixing battery was proposed by La Mantia *et al.* [80] to extract energy from salinity-gradient solutions by using a AgCl/$Na_2Mn_5O_{10}$ system. The equilibrium potential of the

constructed chemical interactions in this electrochemical cell depends on the ion concentration: the equilibrium potential is higher in salt water than in river water. The proposed prototype was charged in freshwater. The electric potential is increased in saltwater according to Nernst equation [81]. The generated energy per cycle can be achieved up to 29.6 mJ/cm^2 with a 0.25V voltage bias under 24 mM and 0.6 M NaCl solutions. Lee *et al.* [82] reported an electrochemical system using CuHCF as cathode and Cu/Cu^{2+} as anode to extract thermal energy between 10 ^oC and 60 ^oC. The generated energy per cycle is 5.2 J/g under a 0.613V power supply, in which the conversion efficiency can reach 3.7% and still has room to improve by using heat recuperation.

1.2.7 Challenges of electrostatic energy harvesting

Electrostatic energy harvesting has been applied in various areas and applications because of its advantages. However, this method also has some challenges. First, electrostatic energy harvesting relies on work done by the ambient energy source against the electrostatic force between the charges in a harvester. The variable capacitor is one of the key components for the electrostatic approach. According to equations 1.2 and 1.6, a high voltage bias is needed to increase the generated energy per cycle. A commercial battery or capacitor in addition to voltage boost converter is usually chosen to provide high voltage polarization, which complicates the system. Furthermore, the proposed harvesters do not restore the generated energy back to external power supply, which causes the external power supply to deplete continuously during the energy harvesting process. Many studies have been conducted to develop other alternatives of external voltage bias and make the electrostatic approach more practical. However, the proposed methods also have their limitations as discussed earlier. Second, the electric load is generally chosen to consume the generated energy instantaneously. In practice, the generated energy should be stored in an energy element. In the electrostatic approach, a complex power management control circuit is needed to extract electricity at the appropriate time. Otherwise the generated energy will be consumed by the parasitic resistance of the system. The required circuit also complicates the device architecture. Third, the energy conversion efficiency for many proposed harvesters is

limited by the low capacitance. For example, in vibration energy harvesting, in order to avoid contact and charge loss during the harvesting process, air is usually used as part or even whole dielectric materials. Its low dielectric permittivity and relatively high thickness lead to low capacitance, which limits the energy conversion efficiency. A higher capacitance will allow more charge involved, which will increase the generated energy.

1.3 Objectives and organization of dissertation

In this dissertation, two proposed methods are illustrated to solve the challenges of the electrostatic energy harvesting. The first method utilizes an appropriate, repetitive reconfiguration process to create a positive feedback mechanism, in which even a small disturbance on a system could significantly amplify the amplitude of electric outputs. Because of the exponentially increasing rate of energy extraction, this method is particularly effective for distributed devices to scavenge energy from low-level ambient sources, thus enabling self-powered operation. The proposed system does not need either an external power supply or a voltage boost converter. The voltage of the proposed system can be accumulated to a high level via positive-feedback mechanism. Because the new method can achieve exponentially increasing rate of energy extraction, an optimal energy coupling efficiency can be obtained. The system has a capability to store temporarily the electrical energy so that the power management control circuit does not need to extract the energy at the specific time. Several types of variable capacitors are illustrated to show that a positive feedback mechanism can be created through an appropriate, repetitive reconfiguration process of the system. Because the concept of exponential energy harvesting is not domain specific, it may lead to new research in directional energy transfer systems in various energy domains.

The other proposed method utilizes water droplets alternate contacts with CYTOP and PTFE thin films to provide high initial charge for vibration energy harvesting. Because CYTOP and PTFE acquire significantly different surface charge densities during contact with water, they

can be utilized to effectively generate electricity. The larger the difference in surface charge density is, the greater the harvested energy. More importantly, the proposed method utilizes the strong electrostatic induction in the water droplet due to the electrical double layer formed at the interface. Therefore, it is more effective than existing methods that are based on the much weaker electrostatic induction in the substrate. Also, unlike in existing methods, in which the charge of the drop is not delivered to external circuits, in our method, the water droplet possesses a dual function as both an electrode and a passive switch, leading to the direct harvesting of the peak electric potential energy. This method not only results in simple device architecture but also allows for the use of schemes based on variable capacitors to improve its performance. Using prototype devices, we demonstrate the effectiveness of this approach in scavenging energy from low-level and low-frequency ambient vibrations.

Chapter 2 presents the methodology of exponential energy harvesting. Through theoretical derivations, it is shown that a positive feedback mechanism can be created through an appropriate, repetitive reconfiguration process of the system. Conditions of positive mechanism and the influencing factors of the growth rate are also discussed in that chapter. Chapter 3 illustrates several types of prototypes to show the effectiveness of the exponential energy harvesting. The first application utilizes two rotary variable capacitors to prove the model. In the second application, liquid-contact variable capacitors are developed to achieve relatively high capacitance. Compared to air variable capacitors, contact variable capacitors use much less space to achieve high capacitance. Mercury and water are both used as the movable electrode. Chapter 4 proposes another method to provide initial charge for the variable capacitor. The electrostatic harvesting approach takes advantage of water moving across dielectric materials that possess significantly different surface charge densities. The differential surface charge densities can be used effectively to convert low-level, low-frequency vibration energy into electric energy.

2 EXPONENTIAL ENERGY HARVESTING

2.1 Introduction of concept

Because electricity has become the primary form of power supply in the modern world, energy harvesting often refers to electricity generation. More recently, the need for reliable, in situ power generation in distributed and autonomous systems has spawned tremendous research in harvesting energy from the ambient environment. In conventional energy harvesting systems, energy is extracted from a fixed-level source at a constant rate at best. The resulting growth of harvested energy is bound by a linear function. Consequently, in low-level ambient sources, the extraction rate usually becomes too low to be of practical use. In principle, electricity generation involves cross domain energy transfer. Except in photovoltaic-based technologies, energy that can be extracted and converted to electricity is determined by certain macroscopic variations of the states of an energy source, such as mechanical oscillations in electromechanical technologies, temperature differences in thermoelectric technologies, and concentration gradients in electrochemical technologies. To sustain a continuous conversion process, energy from an environmental source must be coupled continuously into a harvesting system, resulting in a cyclic response from the harvester, e.g. the vibrations of a cantilever beam in an electromechanical energy harvester or the rotations of turbine blades on a windmill. In these conventional technologies, the energy coupled into the harvester in a cycle is converted to electricity and then exits the harvesting system either delivered to storage or consumed by electric loads. Removal of the harvested energy from the system is necessary because the harvester needs to return to its original state to continue with the next harvesting cycle. Therefore, the harvested energy does not

assist with the harvesting process, i.e. no energy feedback is established. In low-level ambient sources, the extraction rates of conventional methods usually become too low to be of practical use because the generated electricity is not sufficient to satisfy the conditioning requirements for storage or consumption.

In this chapter, a novel method is proposed to achieve exponential growth of harvested energy [83]. The method is developed so that positive feedback, in which even a small disturbance on a system could significantly amplify the electric outputs, is utilized to extract energy from an external source at an exponentially increasing rate. It is shown that in a system of reconfigurable energy storage elements, a positive feedback mechanism can be created through an appropriate, repetitive reconfiguration of the system. The external energy source, which enables the reconfiguration, is both harvested exponentially and stored without rectification in the system. Because of the exponentially increasing rate of energy extraction, this method is particularly effective for distributed devices to scavenge energy from low-level ambient sources, i.e. the local environment, thus enabling self-powered operation. If applied to systems with elements of high energy and power densities, this method may become a viable path to large-scale power generation.

According to the previous chapter, it is known that the electrostatic energy harvesting has some challenges to limit its practical use. The proposed method is attempted to solve the current limitations. Because of the positive feedback mechanism, the voltage of the system can be self excited to a high level, which avoids high external voltage bias. Also, the system is enabled to temporarily store the electrical energy so that the power management control circuit doesn't need to extract the energy in a screened time. Furthermore, the new system can achieve exponentially increasing rate of energy extraction, which leads to an optimal energy coupling efficiency.

2.2 Methodology of exponential energy harvesting

In order to better understand the proposed concept, the classic chessboard and wheat problem is considered as a good metaphor. One grain of wheat is put on the first square of a chessboard, and then two grains are put on the second square of the chessboard, four on the third, and so on. Because of exponential growth, the amounts of wheat on the 64^{th} square are about $9 * 10^{18}$ grains, which is much higher than intuitively expected. The entire concept of the proposed method attempts to achieve the same objective: exponential growth.

Consider a reconfigurable system of interconnected energy storage elements, in which environmental energy is harvested through positive work done on the system and then stored in the system as potential energy. The stored energy in the system can be reconfigured via changing the internal connectivity or parameters of the elements, or both. Because of positive work done to the system, the environmental energy can be harvested and then stored in the system. Figure 2.1 schematically shows the process of the exponential growth of the harvested energy when the system is repetitively switched between two configurations with positive external work performed only in one of the configurations. Without loss of generality, we assume that there are two configurations for the system. In figure 2.1, an energy harvesting cycle starts from the equilibrium state of configuration 1. In configuration 2, according to the principle of minimum potential energy, some of the system energy is lost because of reconfiguration. The environmental energy is harvested, which leads to a much higher system energy. The last part of the cycle completes when the system is switched from configuration 2 back to the equilibrium state of configuration 1. Again, some of the system energy is lost due to reconfiguration. In this cycle, if the harvested energy is higher than the lost energy, the system energy will increase. The initial energy in the next cycle is higher, the total energy after the second cycle will increase even more. Therefore, the system energy achieves an exponential growth when the system is repetitively switched between two configurations and positive external work by ambient energy sources is performed in configuration 2.

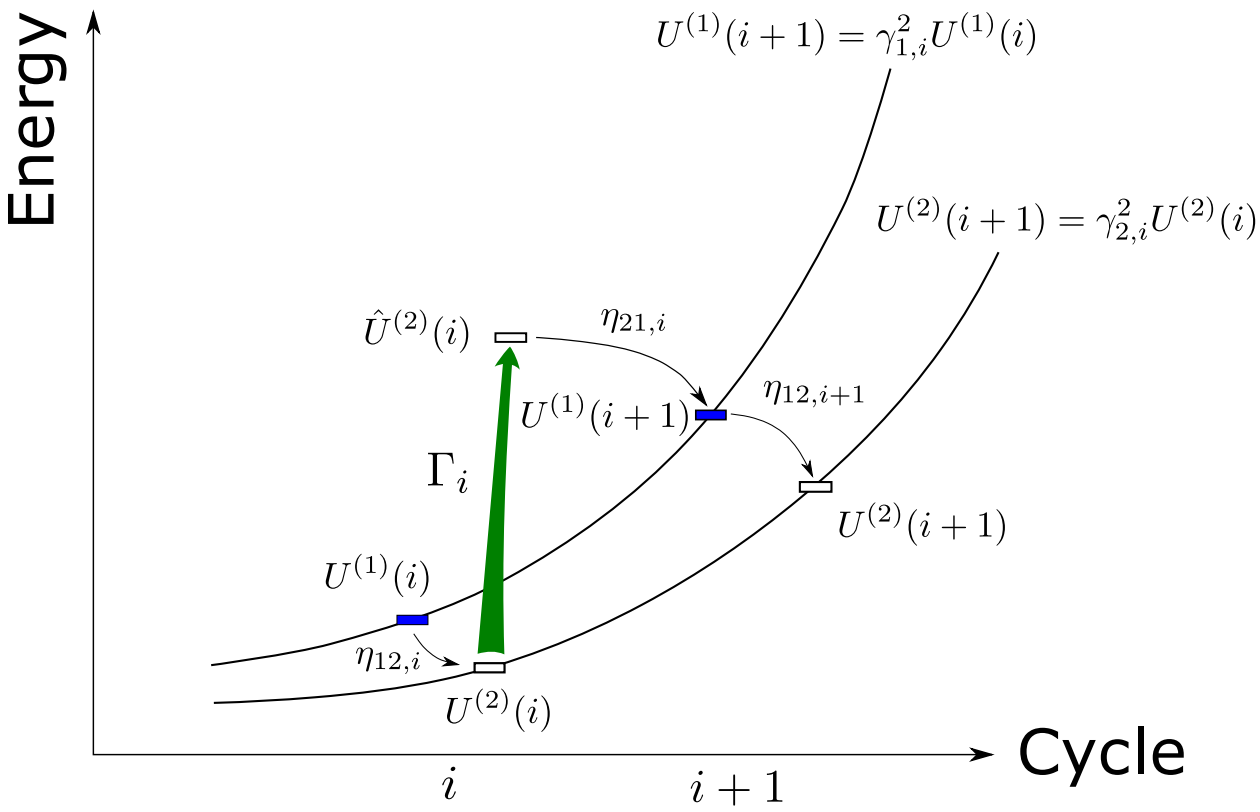

Figure 2.1: Schematic diagrams of the proposed concept.

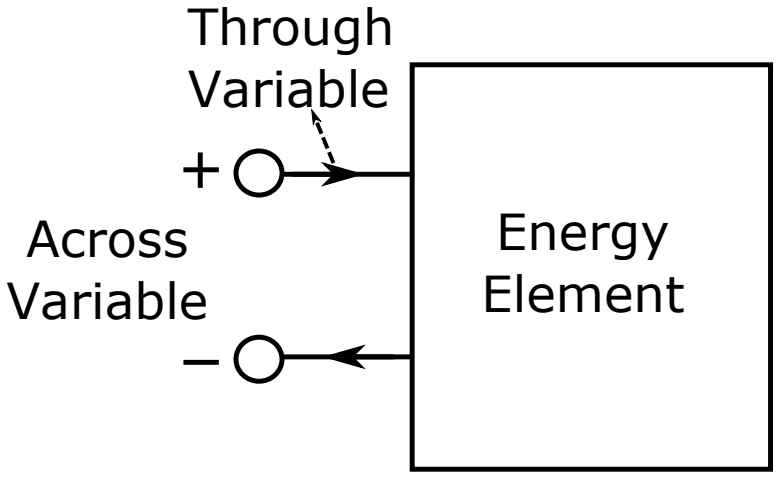

Figure 2.2: A one-port energy element

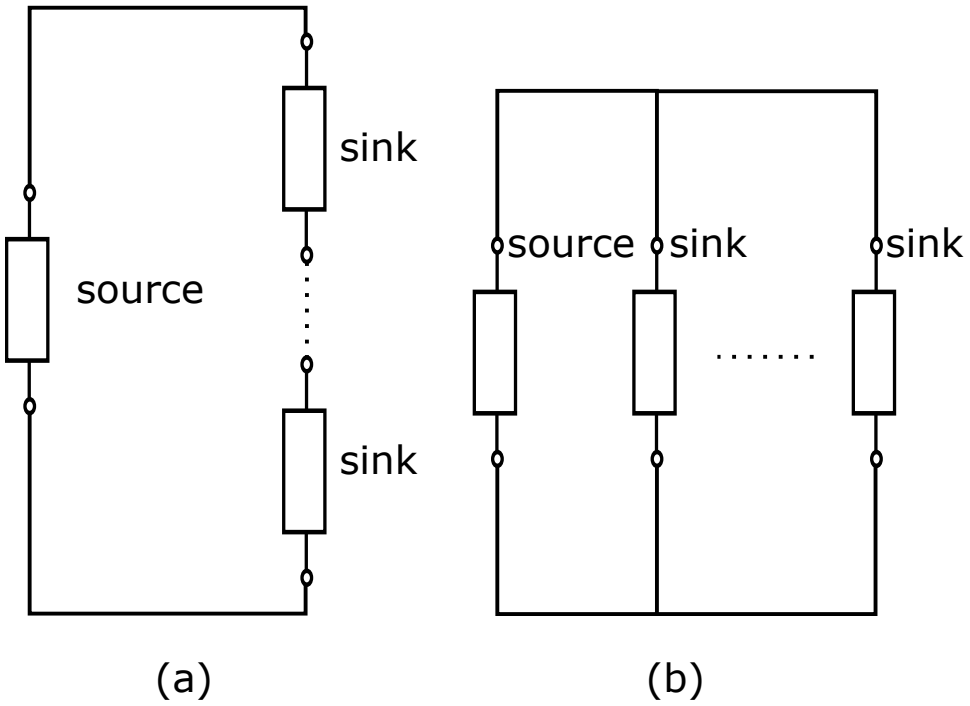

Figure 2.3: Two configurations of the system using one-port energy elements. **(a)** Duplicative configuration. **(b)** Distributive configuration.

Physical Domain	**Across Variable**	**Through Variable**
Electrical	Voltage	Current
Mechanical	Velocity	Force
Thermal	Temperature	Heat
Hydraulic	Pressure	Flow rate

Table 2.1: Examples of physical domains for the energy element.

The system energy can be represented as

$$U^{(w)}(i+1) = \gamma_{w,i}^2 U^{(w)}(i) \tag{2.1}$$

where $w = 1, 2$ indicating the configurations, $U^{(1)}(i)$ and $U^{(2)}(i)$ represents the system energy in configuration 1 and 2 during the $i^{th} cycle$ respectively, $\gamma_{1,i}^2$ is the growth rate of the system energy in configuration 1 during $i + 1^{th}$ cycle comparing to i^{th} cycle while $\gamma_{2,i}^2$ is the growth rate in

configuration 2. They can be expressed as below

$$\begin{aligned} \gamma_{1,i} &= \sqrt{\Gamma_i \eta_{12,i} \eta_{21,i}} \\ \gamma_{2,i} &= \sqrt{\Gamma_i \eta_{21,i} \eta_{12,i+1}} \end{aligned} \tag{2.2}$$

where $\eta_{12,i} = U^{(2)}(i)/U^{(1)}(i)$ and $\eta_{12,i+1} = U^{(2)}(i+1)/U^{(1)}(i+1)$, $\eta_{21,i} = U^{(1)}(i+1)/\hat{U}^{(2)}(i)$, $\Gamma_i = \hat{U}^{(2)}(i)/U^{(2)}(i)$. $\hat{U}^{(2)}(i)$ denotes the system energy in configuration 2 during the i^{th} cycle after external work is done. $\eta_{12,i}$, $\eta_{12,i+1}$, and $\eta_{21,i}$ all represent the energy loss due to reconfiguration. Because of the principle of minimum potential energy, $\eta_{12,i}, \eta_{12,i+1}, \eta_{21,i} \leq 1$. Without sufficient external work, the system energy cannot move to a higher level. If the positive external work by ambient energy sources is sufficient to compensate the loss, i.e. $\Gamma_i > \max\{(1/\eta_{12,i} \cdot 1/\eta_{21,i}), (1/\eta_{12,i+1} \cdot 1/\eta_{21,i})\}$, the growth rates will be larger than 1, i.e. $\gamma_{1,i}, \gamma_{2,i} > 1$. This leads to a system of exponential growth. In order to prove the above result quantitatively, assume a reconfigurable system is composed of one-port, two-terminal energy storage elements with generalized across and through variables. The basic energy element has one port with a single pair of input/output terminals as shown in figure 2.2. The element can refer to mechanical or electric equipments. In fact, the element can be located in many domains, such as electrical, mechanical,and thermal domains. Table 2.1 shows some examples of physical domains for the energy element. If the energy element is a capacitor or battery, it is known that the current or charge flowing into the energy element must be equal to the current or charge flowing away when a voltage is applied at the terminals. If the element is a mass, the inflow velocity is equal to the outflow velocity when a force is applied. Two defined variables, one through and one across, can be used to express energy flow. The across and through variables can be measured with a gauge connected in parallel and in series, respectively, to an element. The across variable of an element is a monotonic, single-valued function of the through variable. Multiple energy elements are deployed in the reconfigurable system. One of the them is taken as the source element and all others as sinks. Figure 2.3 illustrates two configurations of the proposed system. One of the configurations is defined as the duplicative configuration as shown

in Figure 2.3**(a)**. In this configuration, the difference of the through variable for every sink element is equal and in the same direction while the difference of through variable for the source element is equal but in the opposite direction to that of every sink element. Furthermore, the summation of cross variables for the sink elements at equilibrium is equal to the cross variable for the source element. Figure 2.3**(b)** shows the other configuration of the proposed system, which is defined as the distributive configuration. In this configuration, all the elements have same values of cross variables and the summation of difference of through variables for the sink elements is equal and opposite to that of the source element.

Assume that the system is repetitively switched between the two configurations. Without loss of generality, assume that the i^{th} cycle starts from the duplicative state after equilibrium is reached. $Q^{(1)}(i)$ and $Q^{(2)}(i)$ represent the total amount of the through variables in the duplicative configuration and the distributive configuration during the i^{th} cycle respectively. $\Delta Q^{(12)}(i)$ is denoted as the change of the total amount of through variables corresponding to the transition from the duplicative state to the distributive state whereas $\Delta Q^{(21)}(i)$ is the change from the distributive configuration to the duplicative configuration. The energy and the through variable for the k^{th} element are denoted as $U_k^{(1)}(i)$ and $q_k^{(1)}(i)$, respectively. The total system energy and the summation of all through variables are denoted as $U^{(1)}(i) = \sum_{l=0}^{n} U_l^{(1)}(i)$ and $Q^{(1)}(i) = \sum_{l=0}^{n} q_l^{(1)}(i)$, respectively. The cycle completes when equilibrium is established after the system is switched to the distributive state. The energy and the through variable of the k^{th} element for the distributive state are denoted as $U_k^{(2)}(i)$ and $q_k^{(2)}(i)$, respectively. The change of the total through variables in the transition from the duplicative state to the distributive state is denoted by

$$\Delta Q^{(12)}(i) = \zeta^{(12)}(i) Q^{(1)}(i) \tag{2.3}$$

The through variables can be determined using the Lagrangian defined as

$$\mathcal{L}(i) = U^{(2)}(i) + \lambda(i) \left(\sum_{k=0}^{n} q_k^{(2)}(i) - Q^{(2)}(i) \right) \tag{2.4}$$

where $\lambda(i)$ is the Lagrange multiplier, $k = 0$ denotes the source element. $U^{(2)}(i) = \sum_{l=0}^{n} U_l^{(2)}(i)$, and $Q^{(2)}(i) = \sum_{k=0}^{n} q_k^{(2)}(i)$. Each partial derivative of equation 2.4 is expressed as below

$$\begin{aligned} \frac{\partial \mathcal{L}(i)}{\partial q_k^{(2)}(i)} &= \frac{\partial U^{(2)}(i)}{\partial q_k^{(2)}(i)} + \lambda(i) = 0, \quad k = 0, 1, 2 \cdots n \\ \frac{\partial \mathcal{L}(i)}{\partial \lambda(i)} &= \sum_{l=0}^{n} q_l^{(2)}(i) - Q^{(2)}(i) = 0 \end{aligned} \tag{2.5}$$

The through variable of each element can be obtained as

$$q_k^{(2)}(i) = \eta_k(i) Q^{(2)}(i), \quad \sum_{k=0}^{n} \eta_k(i) = 1 \tag{2.6}$$

When the system is subsequently switched to the duplicative state, which is the start of the $i + 1^{th}$ cycle, based on the characteristics of the duplicative state, a new Lagrangian is defined as

$$\begin{aligned} \mathcal{L}(i+1) = U^{(1)}(i+1) + \sum_{l=1}^{n} \lambda_l(i+1) \left(q_l^{(1)}(i+1) - q_l^{(2)}(i) - \Delta Q^{(21)}(i) \right) \\ + \lambda_0(i+1) \left(q_0^{(1)}(i+1) - q_0^{(2)}(i) + \Delta Q^{(21)}(i) \right) \end{aligned} \tag{2.7}$$

where $\Delta Q^{(21)}(i)$ denotes the change of the total through variables required for equilibrium, which can be expressed as $\Delta Q^{(21)}(i) = \zeta^{(21)}(i) Q^{(2)}(i)$. Therefore, each partial derivative of equation 2.7 is given as

$$\begin{aligned} \frac{\partial \mathcal{L}(i+1)}{\partial q_k^{(1)}(i+1)} &= \frac{\partial U_k^{(1)}(i+1)}{\partial q_k^{(2)}(i)} + \lambda_k(i+1) = 0 \\ \frac{\partial \mathcal{L}(i+1)}{\partial \lambda_k(i+1)} &= q_k^{(1)}(i+1) - q_k^{(2)}(i) - \Delta Q^{(21)}(i) = 0 \\ \frac{\partial \mathcal{L}(i+1)}{\partial \lambda_0(i+1)} &= q_0^{(1)}(i+1) - q_0^{(2)}(i) + \Delta Q^{(21)}(i) = 0 \\ \frac{\partial \mathcal{L}(i+1)}{\partial \Delta Q(i)} &= -\sum_{l=1}^{n} \lambda_l(i+1) + \lambda_0(i+1) = 0 \\ k &= 1, 2 \cdots n \end{aligned} \tag{2.8}$$

Therefore, the total amount of the through variables for the duplicative and the distributive states in the $i+1^{th}$ cycle are obtained as

$$\begin{aligned} Q^{(1)}(i+1) &= \gamma_1(i)Q^{(1)}(i), \quad \gamma_1(i) = \left[1+\zeta^{(12)}(i)\right]\left[1+(n-1)\zeta^{(21)}(i)\right] \\ Q^{(2)}(i+1) &= \gamma_2(i)Q^{(2)}(i), \quad \gamma_2(i) = \left[1+\zeta^{(12)}(i)\right]\left[1+(n-1)\zeta^{(21)}(i+1)\right] \end{aligned} \tag{2.9}$$

When $n \geq 1$ and $\zeta^{(12)}(i), \zeta^{(21)}(i) > 0$ for all cycles, the growth rates $\gamma_1(i)$ and $\gamma_2(i)$ are both larger than one, i.e. $\gamma_w(i) > 1$. This leads to the exponential growth of the through variables and the across variables. and finally the harvested energy increases exponentially with the cycles.

2.3 Capacitor as energy element

Figure 2.4 shows an example of a reconfigurable system using $n+1$ capacitors. In duplicative configuration, the source capacitor C_0 is connected in parallel to the sink capacitors, i.e. $C_1, C_2, \cdots C_n$, which are connected in series. After the equilibrium, all the capacitors are disconnected and their capacitance is changed by the ambient energy source to $C_0', C_1', \cdots C_n'$, respectively. In the distributive configuration, all the capacitors are connected in parallel as shown in figure 2.4**(c)**. During the fourth step, the capacitance of each capacitor returns to original state by the ambient energy source. The system is switched repetitively between those two configurations and positive external work is performed by decreasing the capacitance from C_k to C_k' ($k = 0, 1, 2 \cdots n$) while the charge carried by individual capacitors is constant (figure 2.4**(b)**).

Assume the system starts from the equilibrium state when the system is in figure 2.4**(a)**. The summation of the charge of each capacitor in the i^{th} cycle is denoted as $Q(i)$. $q_0^{(1)}(i)$ represents the charge stored in the source capacitor for the i^{th} cycle while $q_k^{(1)}(i)$ represents the charge stored in the k^{th} sink capacitor. The superscript 1 indicates the duplicative configuration. Because the sink capacitors are connected in series, the flowing charge for each capacitor should be equal. Using $\bar{q}^{(1)}(i)$ as flowing charge, the charge of each sink capacitor is shown as $q_k^{(1)}(i) = \bar{q}^{(1)}(i), k = 1, 2 \cdots n$. According to the characteristics of the capacitors, the charge of

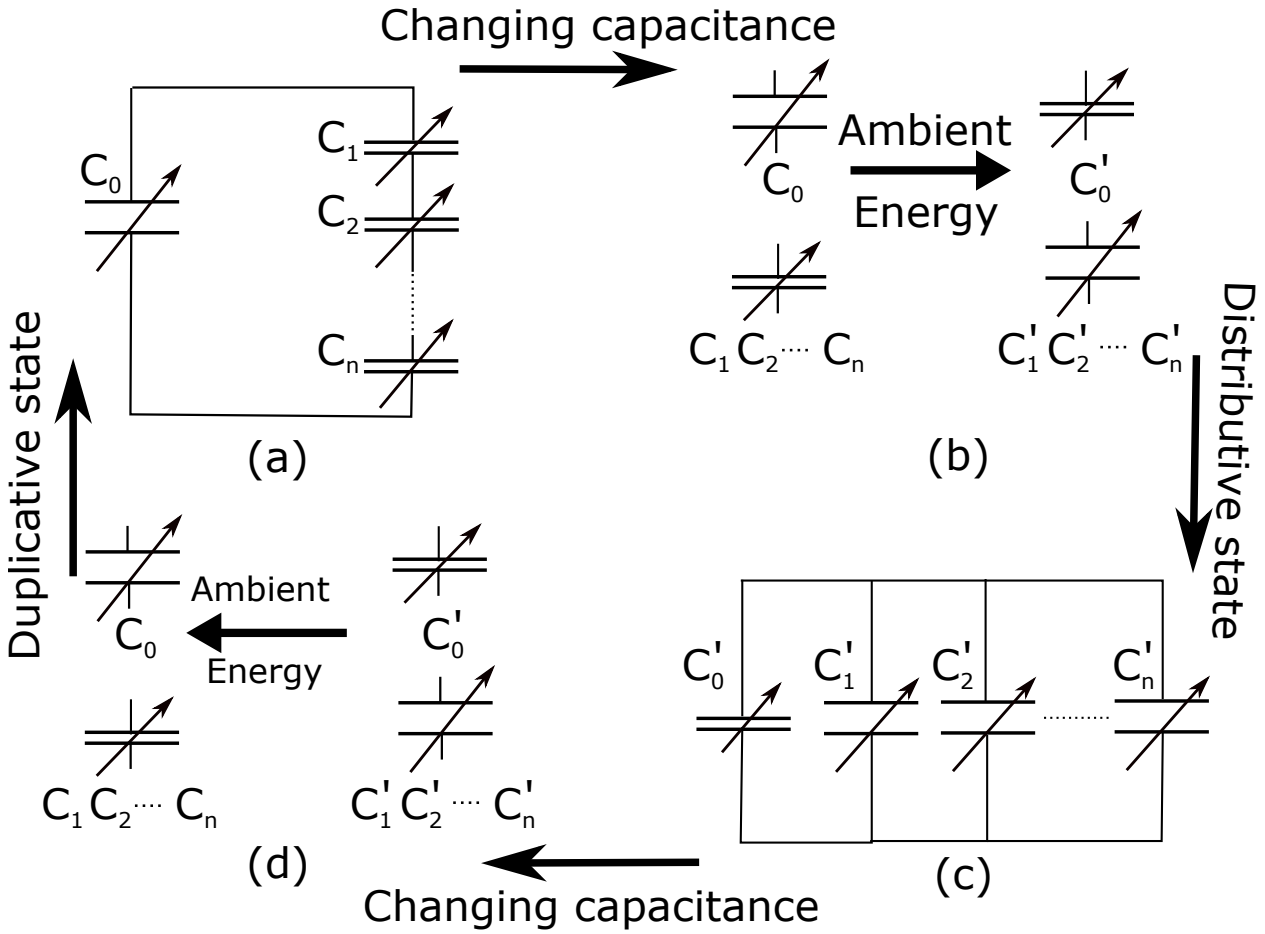

Figure 2.4: One example of a reconfigurable system using variable capacitors. **(a)** Duplicative state. **(b)** Capacitance changed by external energy. **(c)** Distributive state. **(d)** Capacitance changed back by external energy

the source capacitor can be expressed as

$$q_0^{(1)}(i) = C_0/C_{sr}^{(1)}\bar{q}^{(1)}(i), C_{sr}^{(1)} = 1/(\sum_{k=1}^{n} 1/C_k) \tag{2.10}$$

The total electrical potential energy of the system in the duplicative state is

$$U^{(1)}(i) = \frac{1}{2}\frac{Q^2(i)}{C_0}\frac{s(s+1)}{(s+n)^2} \tag{2.11}$$

where $Q(i) = q_0^{(1)}(i) + n\bar{q}^{(1)}(i)$ and $\bar{\eta}_0^{(1)} = s/(s+n)$ and $\bar{\eta}_k^{(1)}(i) = 1/(s+n)$, where $s = C_0/C_{sr}^{(1)}$. After the system is switched to distributive configuration and the equilibrium is

reached, the charge for each capacitor is given as

$$q_k^{(2)}(i) = \bar{\eta}_k^{(2)} Q(i) \quad k = 0, 1, 2 \cdots n \tag{2.12}$$

where $\bar{\eta}_k^{(2)} = C_k / C_{eqv}^{(2)}$ and $C_{eqv}^{(2)} = \sum_{l=0}^{n} C_l$. The capacitance is changed from C_k to C'_k because of the coupling of the external energy into the system. This leads to an increase of the system energy, which can be expressed as

$$\hat{U}^{(2)}(i) = \frac{1}{2} \frac{Q^2(i)}{C'_{eqv}} \tag{2.13}$$

where $C'_{eqv} = \sum_{l=0}^{n} C'_l$. The charge is redistributed as

$$\hat{q}_k^{(2)}(i) = \hat{\eta}_k^{(2)} Q(i) \tag{2.14}$$

where $\hat{\eta}_k^{(2)} = C'_k / C'_{eqv}$. Thus

$$\Gamma_i = \sum_{k=0}^{n} \frac{1}{C'_k} \hat{\eta}_k^2 / \sum_{k=0}^{n} \frac{1}{C_k} \left[\bar{\eta}_k^{(2)} \right]^2 \tag{2.15}$$

The capacitance was then driven to the original values by ambient energy (figure 2.4**(c)**) and the system is switched back to duplicative configuration (figure 2.4**(d)**). The summation of the charge after equilibrium is the summation of the charge for the start of the $(i+1)^{th}$ cycle. The initial charge of each capacitor for the $(i+1)^{th}$ cycle is distributed as

$$\begin{aligned} q_0^{(1)}(i+1) &= \hat{q}_0^{(2)}(i) - \Delta Q(i) \\ q_k^{(1)}(i+1) &= \hat{q}_k^{(2)}(i) + \Delta Q(i) \quad k = 1, 2 \cdots n \end{aligned} \tag{2.16}$$

In the duplicative state, the voltage of the source capacitor is equal to the summation of the voltages of individual sink capacitors, i.e.

$$q_0^{(1)}(i+1)/C_0 = \sum_{k=1}^{n} q_k^{(1)}(i+1)/C_k \tag{2.17}$$

Substituting equation 2.16 into equation 2.17,

$$(\hat{q}_0^{(2)}(i) - \Delta Q(i))/C_0 = \sum_{k=1}^{n} (\hat{q}_k^{(2)}(i) + \Delta Q(i))/C_k \tag{2.18}$$

After the rearrangement, equation 2.18 becomes

$$\hat{q}_0^{(2)}(i) - \sum_{k=1}^{n} \hat{q}_k^{(2)}(i) C_0/C_k = \Delta Q(i)(1+s) \tag{2.19}$$

Substituting equation 2.14 into the above equation,

$$C_0'/C_{eqv}' Q(i) - C_0 \sum_{k=1}^{n} C_k'/C_{eqv}' Q(i)/C_k = \Delta Q(i)(1+s) \tag{2.20}$$

After the rearrangement, $\Delta Q(i)$ is given as

$$\Delta Q(i) = \frac{C_0(r_0 - \sum_{k=1}^{n} r_k)}{C_{eqv}'(1+s)} Q(i) \tag{2.21}$$

where $r_l = C_l'/C_l, l = 0, 1, 2 \cdots n$. Therefore,

$$\begin{aligned} Q(i+1) &= Q(i) + (n-1)\Delta Q(i) = \gamma Q(i) \\ \gamma &= 1 + (n-1)\frac{C_0(r_0 - \sum_{k=1}^{n} r_k)}{C_{eqv}'(1+s)} \end{aligned} \tag{2.22}$$

The total summation of the charge in the system follows $Q(i+1) = \gamma Q(i)$, where

$$\gamma = 1 + (n-1)\frac{C_0(r_0 - \sum_{k=1}^{n} r_k)}{C_{eqv}' \cdot (1+s)} \tag{2.23}$$

where $r_l = C_l'/C_l, l = 0, 1, 2 \cdots n$, $C_{eqv}' = \sum_{k=0}^{n} C_k'$ and $s = C_0/C_{sr}$ in which $C_{sr} = 1/(\sum_{k=1}^{n} 1/C_k)$. When $n > 1$ and $r_0 > \sum_{k=1}^{n} r_k$, and thus, $\gamma > 1$, the total amount of

charge grows exponentially. According to equation 2.11, $U^{(1)}(i+1)$ can be expressed as

$$U^{(1)}(i+1) = \frac{1}{2}\frac{Q^2(i+1)}{C_0}\frac{s(s+1)}{(s+n)^2} \tag{2.24}$$

Substituting equation 2.11 into the above equation,

$$U^{(1)}(i+1) = \frac{Q^2(i+1)}{Q^2(i)}U^{(1)}(i) \tag{2.25}$$

Substituting equation 2.22 into the above equation,

$$U^{(1)}(i+1) = \gamma^2 U^{(1)}(i) \tag{2.26}$$

Therefore, the corresponding electrostatic energy stored in the system grows exponentially with a base of γ^2. Multiple variable capacitors are utilized to form the positive feedback mechanism, which leads to system instability. Here even a tiny charge disturbance would self-excite the system and allow the electric outputs to grow exponentially. For example, say there are only ten electrons perturbed in one 1-μF capacitor. The positive feedback system is developed and the growth rate of the voltage is 2. After 50 cycles, the generated voltage can reach up to 1.8 kV if there is no current leakage and a sufficiently high dielectric strength. In reality, an electric disturbance is inevitable due to many factors, such as dielectric relaxation, ubiquitous electromagnetic waves, and contact electrification. For instance, a charge difference exists between any two electric conductors during the contact due to work function [84]. Such various types of electric disturbance can be utilized to trigger the positive-feedback system. The proposed self-excited energy harvester generally includes two components: multiple sink capacitors and one source capacitor. According to equation 2.23, at least one of the two components needs to be a variable capacitor to form the positive feedback mechanism. In other words, there are three ways of combinations for a positive-feedback system: variable-capacitance source capacitor and constant-capacitance sink capacitors, constant-capacitance source capacitor and

variable-capacitance sink capacitors, and variable-capacitance source capacitor and sink capacitors.

2.4 Identical capacitors as sink capacitors

In the previous section, capacitors are used as energy elements for the new system concept. In order to further understand the system, each sink capacitor is considered identical for simplification, i.e. $C_1 = C_2 = \cdots C_n = C$ and $C_1' = C_2' = \cdots C_n' = C'$. This section will discuss the system from different aspects, such as what parameters affect the growth rate and the harvested energy, and how to achieve the condition for positive feedback.

2.4.1 Modeling

Figure 2.5 shows the system using identical capacitors as sink elements to form the positive feedback mechanism. As discussed earlier, the total charge stored in the system grows exponentially proportional with increasing cycles. Here the modeling of the proposed system using the basic knowledge of capacitors is shown.

Assume the i^{th} cycle of energy harvesting starts with the duplicative state as shown in Figure 2.5. $Q_t^{(1)}(i)$ represents the total charge of the system in the duplicative state during the i^{th} cycle. It's worth noting the definition of $Q_t^{(1)}(i)$ is different from $Q(i)$ in equation 2.11. According to the connection patterns of capacitors, the charge is distributed as below

$$\begin{aligned} q_0^{(1)}(i) &= \frac{nC_0}{nC_0 + C} Q_t^{(1)}(i) \\ q^{(1)}(i) &= \frac{C}{nC_0 + C} Q_t^{(1)}(i) \end{aligned} \tag{2.27}$$

where $q_0^{(1)}(i)$ and $q^{(1)}(i)$ are the charge stored in the source capacitor and each sink capacitor in the duplicative state during the i^{th} cycle. In the second step, the capacitance is decreased from C_0 and C to C_0' and C' respectively while the stored charge for each capacitor is constant. In the

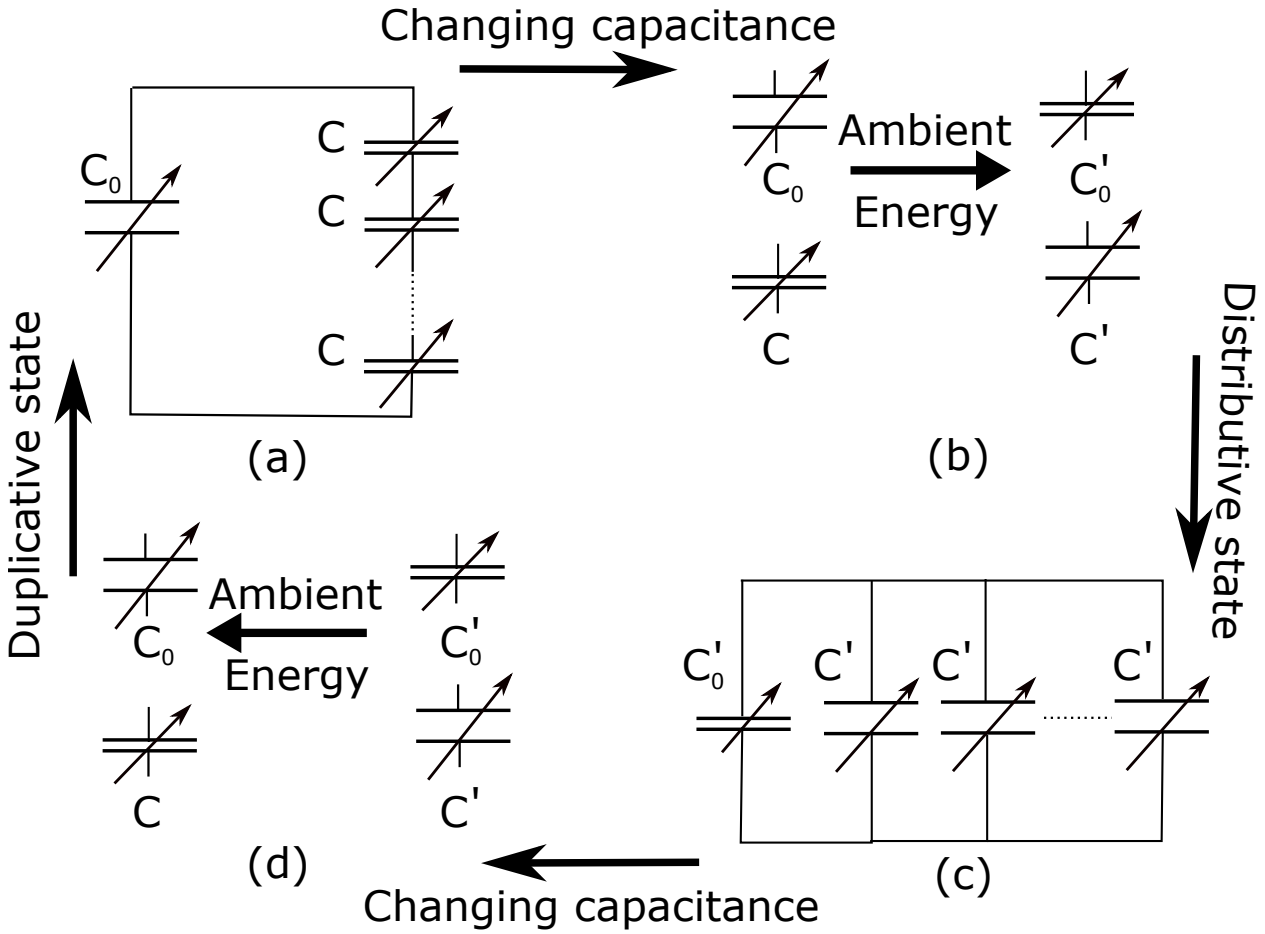

Figure 2.5: Using identical capacitors as sink elements. **(a)** Duplicative state. **(b)** Capacitance changed by external energy. **(c)** Distributive state. **(d)** Capacitance changed back by external energy

distributive state, each capacitor will be connected in parallel. The total charge in the state, $Q_t^{(2)}(i)$, is the summation of the charge in the source capacitor in the duplicative state $q_0^{(1)}(i)$ and the charge in each sink capacitor in the duplicative state $q^{(1)}(i)$. i.e.

$$Q_t^{(2)}(i) = q_0^{(1)}(i) + nq^{(1)}(i) \tag{2.28}$$

Since every capacitor is connected in parallel, the charge is distributed as below

$$\begin{aligned} q_0^{(2)}(i) &= \frac{C_0'}{C_0' + nC'} Q_t^{(2)}(i) \\ q^{(2)}(i) &= \frac{C'}{C_0' + nC'} Q_t^{(2)}(i) \end{aligned} \tag{2.29}$$

where $q_0^{(2)}(i)$ and $q^{(2)}(i)$ are the charge stored in the source capacitor and each sink capacitor in the distributive state during the i^{th} cycle respectively. In the fourth step, under constant charge, the capacitance is recovered from C_0' and C' to C_0 and C respectively . At the beginning of $i + 1^{th}$ cycle, $Q_t^{(1)}(i+1)$ can be expressed as

$$Q_t^{(1)}(i+1) = q_0^{(2)}(i) + q^{(2)}(i) \tag{2.30}$$

In the duplicative state, the charge is distributed as below

$$\begin{aligned} q_0^{(1)}(i+1) &= \frac{nC_0}{nC_0 + C} Q_t^{(1)}(i+1) \\ q^{(1)}(i+1) &= \frac{C}{nC_0 + C} Q_t^{(1)}(i+1) \end{aligned} \tag{2.31}$$

In the distributive state, the total charge can be expressed as

$$Q_t^{(2)}(i+1) = q_0^{(1)}(i+1) + nq^{(1)}(i+1) \tag{2.32}$$

Substituting equation 2.27 into 2.28,

$$Q_t^{(2)}(i) = \frac{n(C_0 + C)}{nC_0 + C} Q_t^{(1)}(i) \tag{2.33}$$

Substituting equation 2.29 into 2.30,

$$Q_t^{(1)}(i+1) = \frac{C_0' + C'}{C_0' + nC'} Q_t^{(2)}(i) \tag{2.34}$$

Substituting equation 2.31 into 2.32,

$$Q_t^{(2)}(i+1) = \frac{n(C_0+C)}{nC_0+C} Q_t^{(1)}(i+1) \tag{2.35}$$

Substituting equation 2.33 into 2.34,

$$Q_t^{(1)}(i+1) = \gamma Q_t^{(1)}(i), \quad \gamma = \frac{n(C_0+C)(C_0'+C')}{(nC_0+C)(C_0'+nC')} \tag{2.36}$$

Substituting equation 2.34 into 2.35,

$$Q_t^{(2)}(i+1) = \gamma Q_t^{(2)}(i), \quad \gamma = \frac{n(C_0+C)(C_0'+C')}{(nC_0+C)(C_0'+nC')} \tag{2.37}$$

Denote $\alpha = C_0'/C', \beta = C/C_0$, therefore, the growth rate γ is can be expressed as

$$\gamma = \frac{n(1+\alpha)(1+\beta)}{(n+\alpha)(n+\beta)} \tag{2.38}$$

The expression of γ can also be proved by equation 2.23,

$$\gamma = 1 + (n-1)\frac{\alpha\beta - n}{(\alpha+n)(\beta+n)} = \frac{n(1+\alpha)(1+\beta)}{(n+\alpha)(n+\beta)} \tag{2.39}$$

From the above equation, the value of the γ depends on three variables: α, β, and n. When $\gamma > 1$, the charge stored in the system grows exponentially. Substituting this condition into equation 2.38,

$$(n - \alpha\beta)(n-1) < 0 \tag{2.40}$$

Since $n > 1$, $\alpha\beta > n$. Therefore, the condition for a positive-feedback system is

$$\alpha\beta > n \geq 2 \tag{2.41}$$

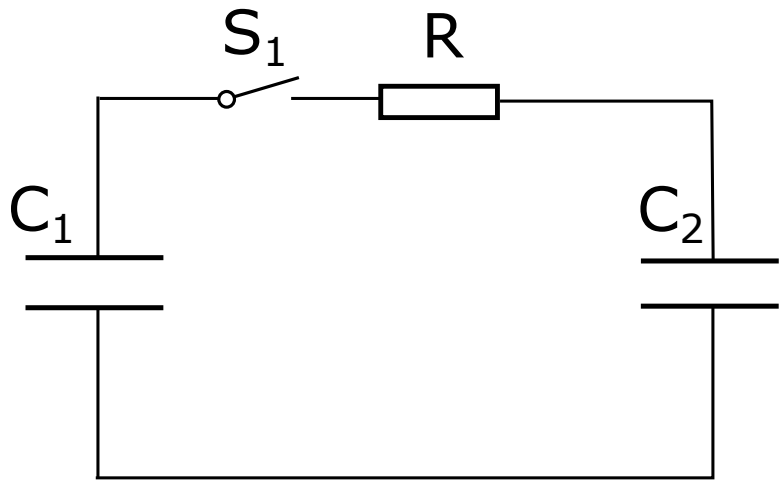

Figure 2.6: Energy transfer in two capacitors

If the condition is satisfied, the charge in the system can be self-excited. The positive feedback mechanism can push the energy conversion efficiency to the optimal level. To better understand the condition, assume two sink capacitors are used in the system, i.e. $n = 2$, and sink capacitors and the source capacitor is identical, i.e. $C_0 = C'$ and $C'_0 = C$. Therefore, $\alpha = \beta > 1.414$. This means the ratio between maximum and minimum capacitance needs to be higher than 1.414, so that the system can achieve the positive feedback mechanism. Otherwise, the total energy of the system will decrease to zero. Here is the key question: where was the energy transferred? Figure 2.6 can be used to illustrate the reason for the condition of equation 2.41. Two capacitors are connected in parallel. Assume only C_1 has initial charge Q_0 while there is no charge in C_2. The initial total energy is $E_0 = \dfrac{Q_0^2}{2C_1}$. After S_1 is closed, the charge is redistributed as follows

$$\begin{aligned} q_1 &= \frac{C_1}{C_1 + C_2} Q_0 \\ q_2 &= \frac{C_2}{C_1 + C_2} Q_0 \end{aligned} \tag{2.42}$$

The total energy after the equilibrium can be expressed as

$$E_1 = \frac{Q_0^2}{2(C_1 + C_2)} \tag{2.43}$$

Therefore, the energy difference is

$$\Delta E = E_0 - E_1 = \frac{C_2 Q_0^2}{2C_1(C_1 + C_2)} \tag{2.44}$$

R represents the parasitic resistance of the system. Therefore, the lost energy in the system was consumed by R. However, the value of R doesn't affect how much energy will be consumed. One solution to avoid the energy consumption is to utilize an inductor to transfer kinetic energy into potential energy. The inductor is a passive electric component that energy is stored via magnetic field during the current flow. In the ideal situation, all the energy from C_1 can be transferred into C_2 using an inductor. Therefore, using an inductor may avoid the requirement of equation 2.41.

2.4.2 Factors influencing the growth rate

Equation 2.38 shows that the growth rate of the system is determined by three variables: α, β, and n. In this section, the discussion is focused on how those three variables impact the growth rate. The partial derivatives of the growth rate γ with respect to three variables are shown below,

$$\frac{\partial r}{\partial \alpha} = \frac{n(n-1)(1+\beta)}{(n+\alpha)^2(n+\beta)} \tag{2.45}$$

$$\frac{\partial r}{\partial \beta} = \frac{n(n-1)(1+\alpha)}{(n+\beta)^2(n+\alpha)} \tag{2.46}$$

$$\frac{\partial r}{\partial n} = \frac{(1+\alpha)(1+\beta)(\alpha\beta - n^2)}{(n+\alpha)^2(n+\beta)^2} \tag{2.47}$$

From the definitions, it is known that $\alpha > 0$, $\beta > 0$, and $n \geq 2$. Substituting the above inequalities into equation 2.46 and 2.47, we know the partial derivatives of γ with respect α and β are permanently greater than zero. i.e.,

$$\begin{aligned} \frac{\partial r}{\partial \alpha} &> 0 \\ \frac{\partial r}{\partial \beta} &> 0 \end{aligned} \tag{2.48}$$

Consequently, γ monotonically increases with the increasing α and β, respectively. Since $\beta = C/C_0$, it is known that β represents the ratio between sink capacitor and source capacitor in

the duplicative state. Higher β means more charge is transferred to sink capacitors from the source capacitor in the duplicative step. α represents the ratio between source capacitor and sink capacitor in the distributive state. A higher α allows more charge to be transferred into the source capacitor from the sink capacitors in the distributive state. More involved charge will lead to higher γ. Compared to equation 2.46 and 2.47, the partial derivative of γ with respect to n is not Monotonic function. Set $\partial r/\partial n = 0$, equation 2.47 becomes

$$n = \sqrt{\alpha\beta} \tag{2.49}$$

This means γ has a maximum value when n satisfies the condition of equation 2.49. It is also known that if $n < \sqrt{\alpha\beta}$, then γ monotonically increases with increasing n, i.e. $\partial r/\partial n > 0$. If $n > \sqrt{\alpha\beta}$, γ monotonically decreases with increasing n, i.e. $\partial r/\partial n < 0$. Therefore, γ has the maximum value when $n = \sqrt{\alpha\beta}$. Note that for a constant source capacitor, $\alpha\beta = C/C'$. Therefore, if the maximum and minimum capacitance is determined, γ has a maximum value when $n = \alpha = \beta$. Also, since n represents the number of sink capacitors, n must be a positive integer while $\sqrt{\alpha\beta}$ is a positive real number. Therefore, the accurate description of equation 2.49 is expressed as

$$n = \begin{cases} \lfloor\sqrt{\alpha\beta}\rfloor, & if \quad \left|\frac{\partial r}{\partial n}|_{n=\lfloor\sqrt{\alpha\beta}\rfloor}\right| < \left|\frac{\partial r}{\partial n}|_{n=\lceil\sqrt{\alpha\beta}\rceil}\right| \\ \lceil\sqrt{\alpha\beta}\rceil, & if \quad \left|\frac{\partial r}{\partial n}|_{n=\lfloor\sqrt{\alpha\beta}\rfloor}\right| \geq \left|\frac{\partial r}{\partial n}|_{n=\lceil\sqrt{\alpha\beta}\rceil}\right| \end{cases} \tag{2.50}$$

where $\lfloor\rfloor$ is the floor symbol to give the greatest integer that is less than or equal to the input number, $\lceil\rceil$ is the ceiling symbol to give the least integer that is greater than or equal to the input. For example, $\lfloor 3.5\rfloor = 3$, and $\lceil 3.5\rceil = 4$. In summary, higher α and β lead to higher γ; when n satisfies the condition of equation 2.50, γ has the maximum value. γ increase with the increasing n when $n < \sqrt{\alpha\beta}$. Meanwhile, γ decreases with the increasing n when $n > \sqrt{\alpha\beta}$.

2.4.3 Electric outputs

According to equation 2.36 and 2.37, it is known that the charge of the system grows exponentially with cycles. In this section, other electric parameters are discussed, such as voltage and electric potential energy.

Substituting equation 2.27 and 2.31 into 2.36,

$$\begin{aligned} q_0^{(1)}(i+1) &= \gamma q_0^{(1)}(i) \\ q^{(1)}(i+1) &= \gamma q^{(1)}(i) \end{aligned} \tag{2.51}$$

It is known that the charge in each capacitor also grows exponentially with cycles. In the duplicative state of the i^{th} cycle, denote $v_0^{(1)}(i)$ and $v^{(1)}(i)$ as the potential difference of source and sink capacitor respectively. Denote $u_0^{(1)}(i)$ and $u^{(1)}(i)$ as the electric potential energy of source and sink capacitor respectively. Denote $U_t^{(1)}(i)$ as the electric potential energy of the system. According to $C = Q/V$, the above equation becomes

$$\begin{aligned} v_0^{(1)}(i+1) &= \gamma v_0^{(1)}(i) \\ v^{(1)}(i+1) &= \gamma v^{(1)}(i) \end{aligned} \tag{2.52}$$

Therefore, the potential difference of source and sink capacitor grows exponentially with cycles where the growth rate is γ. According to $U = CV^2/2$, the above equation becomes

$$\begin{aligned} u_0^{(1)}(i+1) &= \gamma^2 u_0^{(1)}(i) \\ u^{(1)}(i+1) &= \gamma^2 u^{(1)}(i) \end{aligned} \tag{2.53}$$

Similarly, equation 2.36 becomes

$$U_t^{(1)}(i+1) = \gamma^2 U_t^{(1)}(i) \tag{2.54}$$

The total energy in the distributive state also has same results, i.e. $U_t^{(2)}(i+1) = \gamma^2 U_t^{(2)}(i)$. Therefore, the total energy of the system grows exponentially with cycles with the corresponding growth rate of γ^2.

In the duplicative state, assume the initial charge of the system is Q_0. After i^{th} cycle, the charge of the system is given as

$$Q_{t1}(i) = \gamma^i Q_0 \tag{2.55}$$

Therefore, the stored energy of the system with cycles is given as

$$U_t^{(1)}(i) = \frac{Q_0^2 \gamma^{2i}}{2C_t^{(1)}} \tag{2.56}$$

where $C_t^{(1)}$ represents the total capacitance in the duplicative step, which can be expressed as $C_t^{(1)} = C_0 + C/n$. From the above equation, the key parameter of coupling energy is γ. Higher γ will lead to more harvested energy. The harvested energy in each cycle is given as

$$\begin{aligned} \Delta U_t^{(1)}(i) &= U_t^{(1)}(i) - U_t^{(1)}(i-1) \\ &= \frac{Q_0^2(\gamma^2 - 1)\gamma^{2i}}{2\gamma^2 C_t^{(1)}} \end{aligned} \tag{2.57}$$

$\Delta U_t^{(1)}(i)$ increases exponentially with the corresponding growth rate of γ^2.

In reality, a capacitor has a maximum working voltage and would break down once the voltage exceeds it. Therefore, the total energy of system cannot grow indefinitely. One of the practical solutions is to control the voltage of the system below the maximum working voltage. A electric load with power management ciruit can be introduced to the current system to keep the voltage back to the certain value. A voltage-controlled switch, such as Zener diode, can be used to close the electric load circuit. Figure 2.7 shows one circuit diagram using a Zener diode to control the voltage. Zener diode, like a switch, is deployed to keep the electric load disconnected until the voltage of system reaches to the certain voltage. The Zener diode allows current to flow through when the voltage is higher than Zener breakdown voltage, V_z. Otherwise the circuit keep

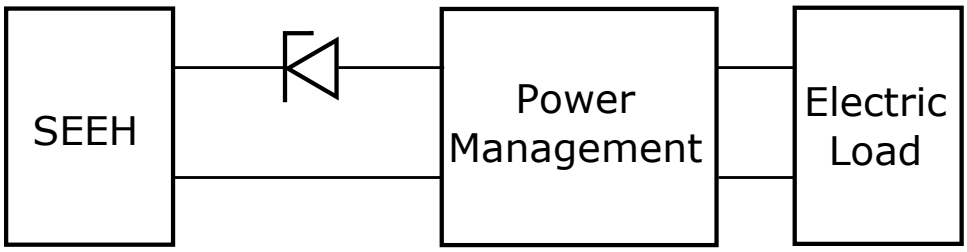

Figure 2.7: One possible way to control the maximum voltage of the system and extract harvested energy from the system.

disconnected. When the voltage of source capacitor is higher than V_z, the circuit is closed and the energy is transferred to energy storage device via power management control circuits. At that time, the voltage is constantly dropping until it is lower than V_z, which triggers Zener diode disconnecting the circuit. Therefore, the Zener diode maintains the voltage of the source capacitor slightly lower than Zener breakdown voltage.

3 APPLICATIONS OF EXPONENTIAL ENERGY HARVESTING

The previous chapter discussed a new concept of exponential energy harvesting through repetitive reconfigurations of a system. In this chapter, several applications are illustrated to show promising potential of this approach [83]. Two types of variable capacitors are fabricated to harvest mechanical energy via positive-feedback mechanism. The first application utilizes two rotary variable capacitors as energy elements to prove the concept of the model by showing that the harvested energy increases exponentially as expected. In the second application, liquid-contact variable capacitors are developed to achieve relatively high capacitance. Because of contact electrification and electrostatic induction, the contact variable capacitors can provide relatively high extra charge in each cycle. Compared to air variable capacitors, contact variable capacitors require less space to achieve high capacitance. Mercury and water are used as the movable electrode in the experiments. In our experiments, it is known that mercury-contact variable capacitor can reach higher maximum working voltage than water-contact variable capacitor under the same condition. A device with three mercury drops can reach up to 168 V while the same device with water droplets can reach 56 V. In our experiments, three 150 μL mercury drops were used for sink capacitors with a fixed source capacitor of 0.94 nF, the generated energy can achieve 10.2 μJ per cycle, corresponding to a harvested efficiency of 12.2%.

3.1 Measurements

Prior to the discussion of applications, this section first addresses the measurement methods for the key parameters in the system: capacitance and voltage & charge. Because the capacitance is relatively low ($\sim pF$ to $\sim nF$), using generic multimeter will disturb the measurement due to low internal resistance of a normal multimeter (10 $M\Omega$). Consequently a normal multimeter will consume electrical energy from the capacitors during the measurement. Here we use electrometer to measure the electric outputs of capacitors, such as voltage and charge. A Keithley 6517B is selected here as shown in Figure 3.1**(a)**. The Keithley 6517B has a 10 pF parasitic capacitance. Because of a 10-ft low noise triax cable provided by Keithley Inc (Figure 3.2**(a)**), the total capacitance of the electrometer is $\sim 300\ pF$. During the process of voltage and charge measurements, very low current leakage takes place to the electrometer, as low as 1 femtoampere (fA). Such low magnitude of current leakage is negligible even for $\sim pF$ capacitor. Therefore, a capacitor can be used to model the behavior of the electrometer as shown in Figure 3.1**(b)**. When the electrometer is connected to one charged capacitor C, the charge is redistributed due to circuit model of electrometer. If the measured voltage of the capacitor is V_m, then the actual voltage is

$$V_c = \frac{C + C_p}{C} V_m \tag{3.1}$$

Therefore, the triax cable can be used for the voltage or charge measurement if the capacitance is known. The measured values need to be adjusted by the equation 3.1. In order to avoid the parasitic capacitance of the triax cable, handmade cables are fabricated to directly obtain the direct measurements as shown in figure 3.2**(b)**. The electrometer has an internal capacitance of 10 pF, which is negligible if the measured capacitance is much higher. The communication between a computer and the electrometer is established with a KUSB-488B cable in order to obtain the measurement continuously.

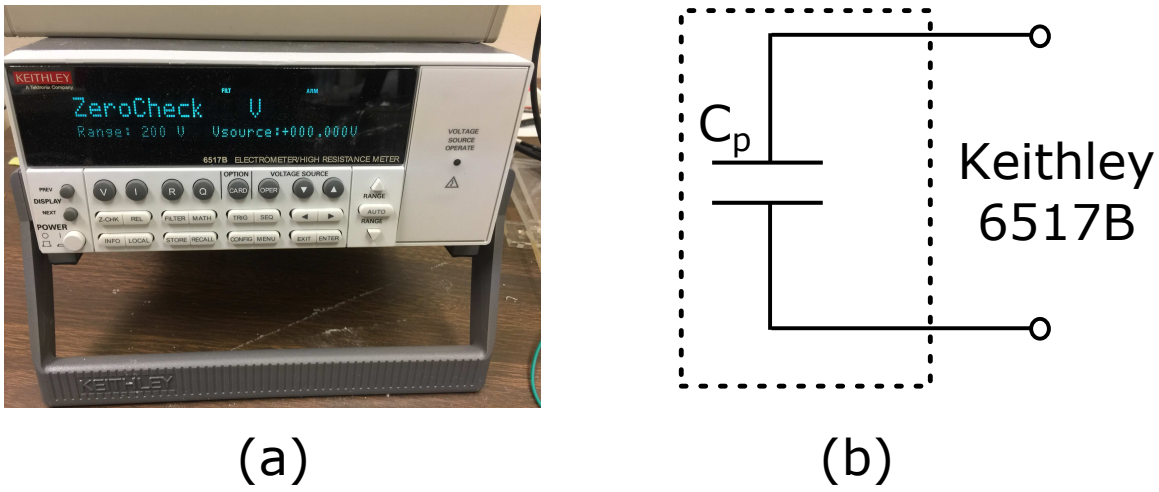

Figure 3.1: Electrometer: Keithley 6517B **(a)** Front panel of the electrometer. **(b)** circuit model

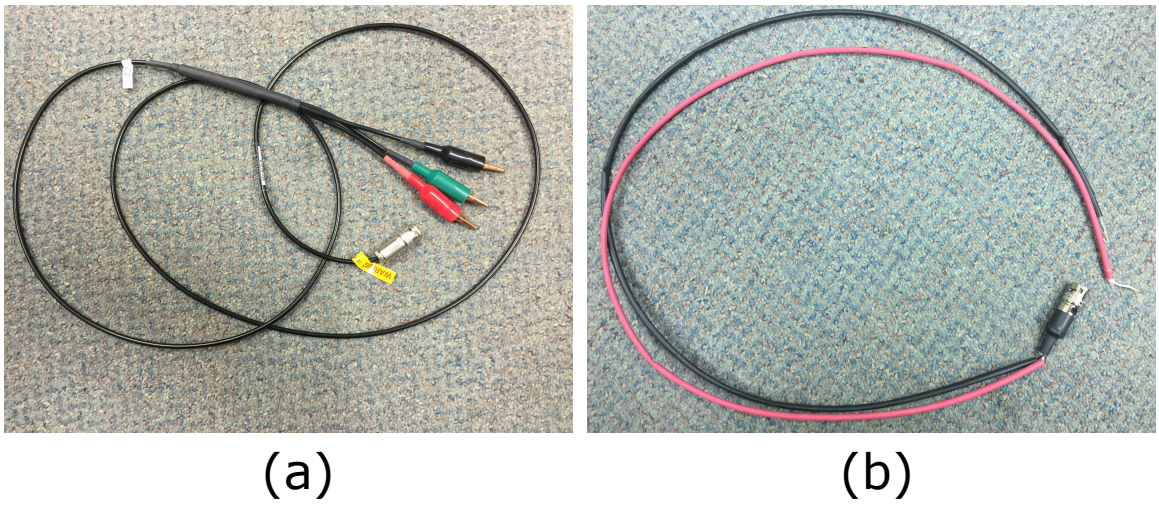

Figure 3.2: Terminator cables for Keithley 6517B **(a)** Triax cables. **(b)** hand-made cables with physically separate wires

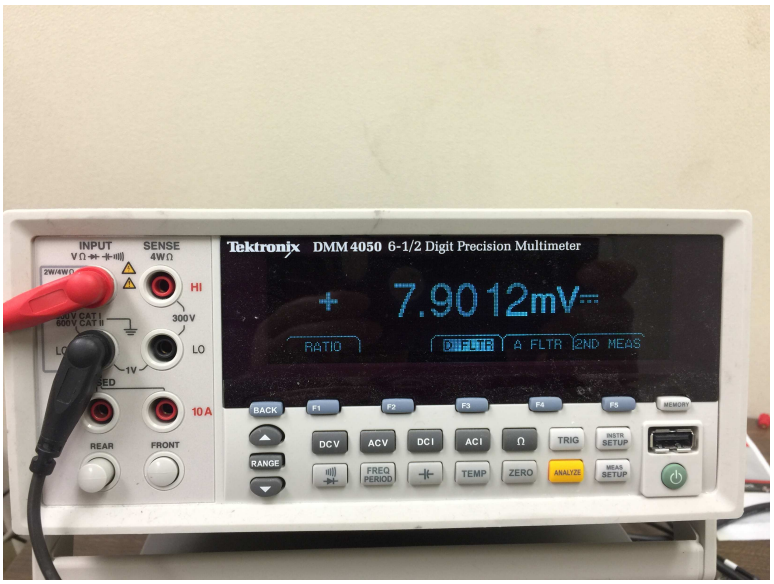

Figure 3.3: Tektronix DMM 4050

The capacitance is measured using a Tektronix DMM 4050 (figure 3.3). Other than Tektronix DMM 4050, Keithley 6517B can also be used to measure the capacitance. If the applied voltage and measured voltage are both known, according to equation 3.1, the capacitance can be calculated based on $C = \frac{V_m C_p}{V_c - V_m}$.

3.2 Rotary variable capacitors as sink capacitors

In this section, two commercial rotary variable capacitors are chosen to form the positive feedback mechanism. In the rotary variable capacitor, air is used as the dielectric material. A rotating shaft is used to change the capacitance. Passive switches are fabricated so that two configurations of the system can be achieved by rotating the shafts of the capacitors. The maximum capacitance is 314 pF while the minimum capacitance is 57 pF. In our experiments, a small amount of charge transfer is observed when two metal needles are manually brought into contact, which increases extra charge in each cycle. For the source capacitor, one commercial ceramic capacitor with constant capacitance is chosen for the system.

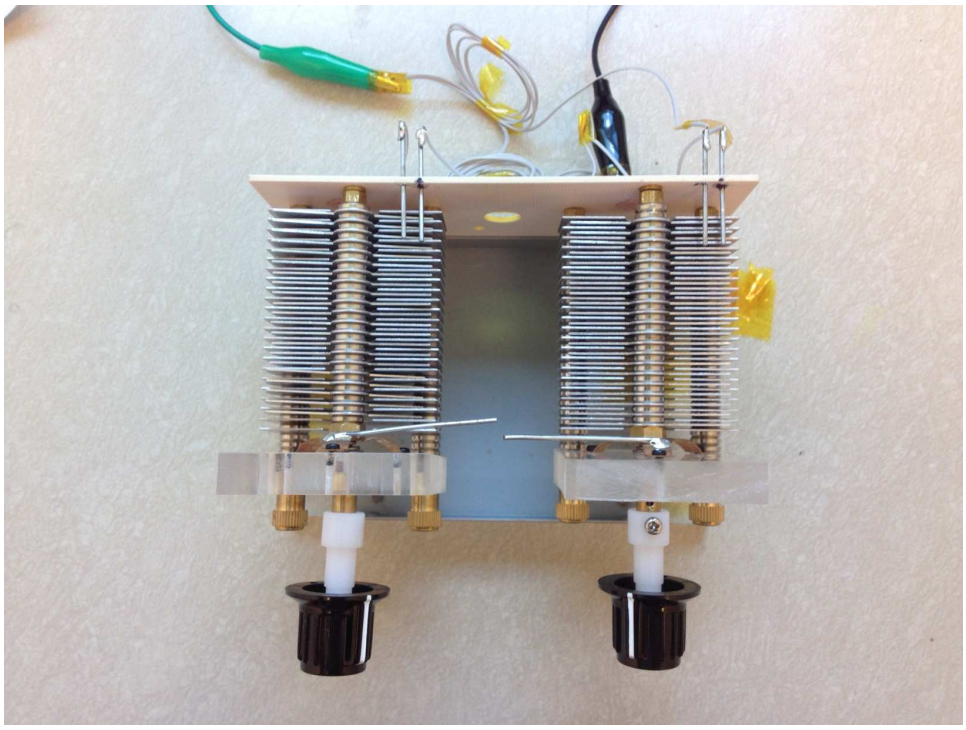

Figure 3.4: Two commercial rotary variable capacitors

3.2.1 Design of rotary variable capacitors

In the self-excited system, two commercial rotary variable capacitors are used as the sink capacitors as shown in figure 3.4. One ceramic capacitor with constant capacitance is chosen as the source capacitor. A set of semicircular metal plates, called stationary plates, are fixed in the shelf. The other set of semicircular metal plates, called rotary plates, are located in the gaps between the fixed metal plates, and they can be rotated by the shaft. The overlap area between the stationary plates and the rotary plates can be changed by rotating the shaft. According to $C = \epsilon A/d$, the capacitance is changed correspondingly. The capacitance range of each rotary variable capacitor ranges from 57 pF to 314 pF.

Figure 3.5 shows the circuit diagram of the positive-feedback system by using two rotary variable capacitors. Three switches are used to achieve four steps of energy conversion as shown in Figure 2.5. In the duplicative state, SW1 is closed while SW2 and SW3 are opened. Two sink capacitors are connected in series. Since these two capacitors are at their maximum capacitance,

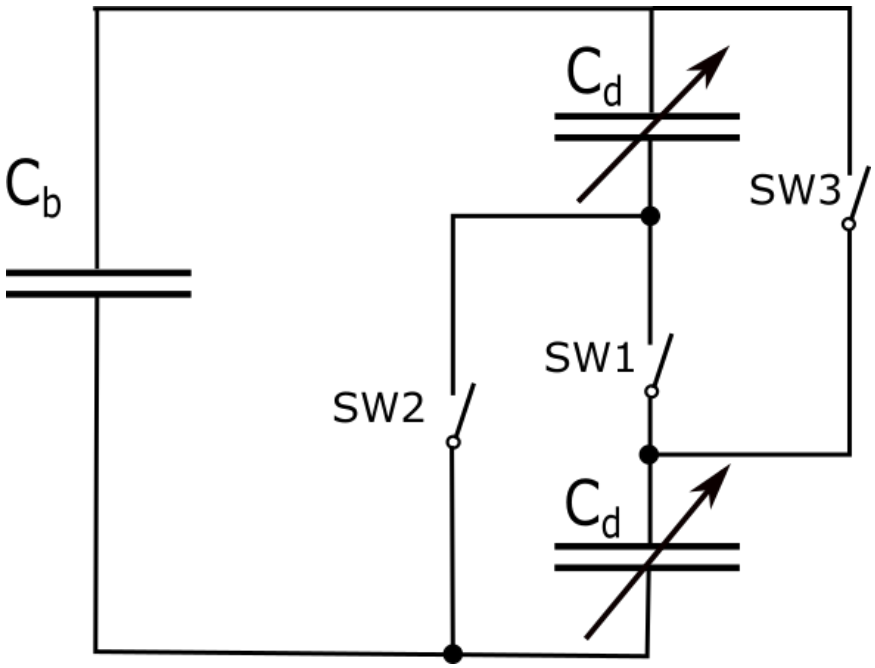

Figure 3.5: One circuit diagram of a self-excited energy harvesting system using two variable and one constant capacitors

majority of charge in the source capacitor is transferred to the sink capacitors. In the second step, all three switches are opened. The capacitance of sink capacitors is driven by external mechanical energy into the minimum value. In the distributive state, SW2 and SW3 are closed while SW1 is opened. Two sink capacitors are connected in parallel. Since these two capacitors are at their minimum capacitance, majority of charge in the sink capacitors are brought back to the source capacitor. In the final step, three switches are all opened. The capacitance of sink capacitors is driven back to the maximum value for the next energy harvesting cycle.

Figure 3.6 and 3.7 show how sink capacitors achieve two configurations. Two needle contacts are deployed on the top side of stationary plates for each rotary capacitor. In Figure 3.6, $\#2$ and $\#4$ needle contacts are connected by electric wires. When rotary plates contact with $\#2$ and $\#4$ needles, two capacitors are connected in series. At the same time, the capacitance of each rotary capacitor is reached to the maximum value due to the maximum overlapping area. Therefore, two capacitors are connected in series when rotary electrode plates contacts with $\#2$ and $\#4$ needles. In Figure 3.7, two other needles, $\#1$ and $\#3$, are deployed above $\#2$ and $\#4$

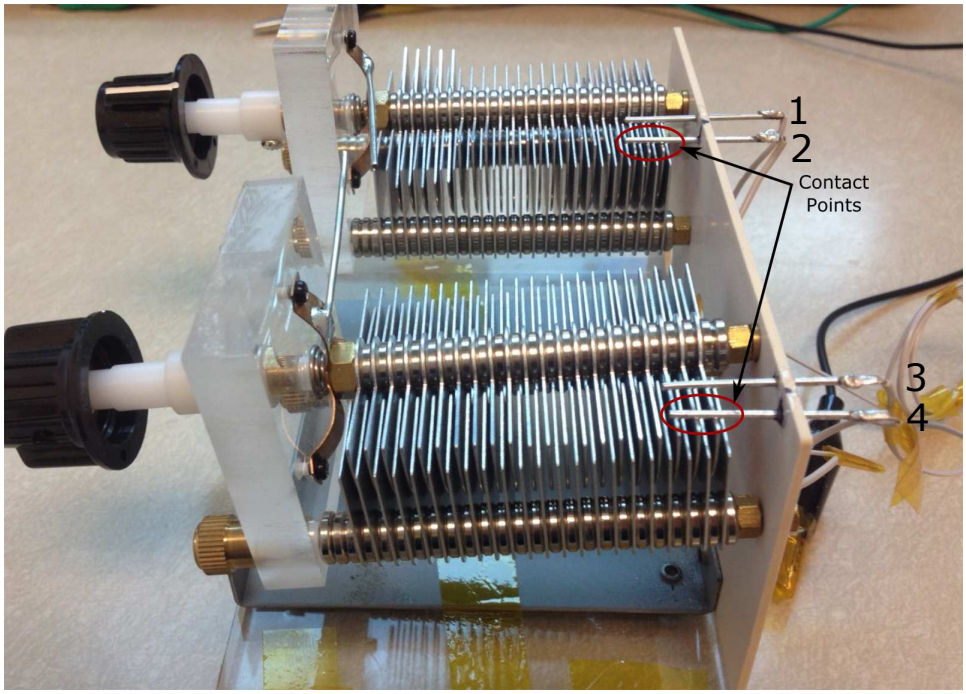

Figure 3.6: Two rotary variable capacitors connected in series

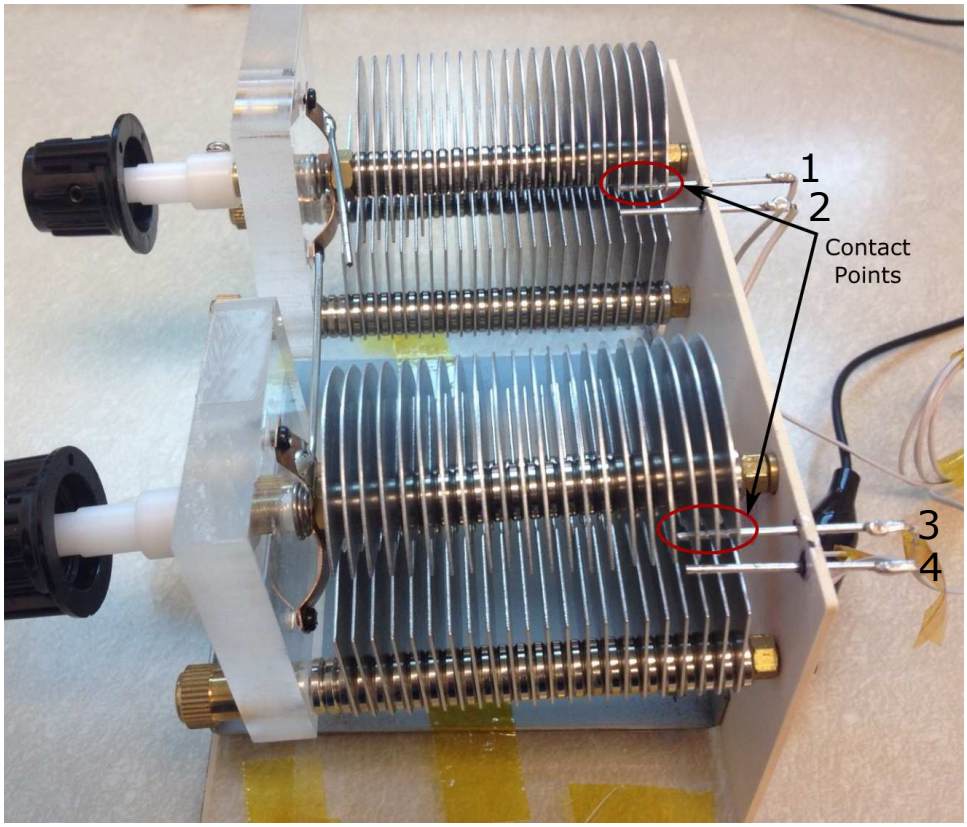

Figure 3.7: Two rotary variable capacitors connected in parallel

respectively. One ceramic capacitor, which is considered as the source capacitor, is connected between $\#1$ and $\#3$, When rotary electrode plates contact with $\#1$ and $\#3$, all three capacitors are connected in parallel. Meanwhile, the capacitance of each rotary capacitor is achieved to the minimum value. According to the above descriptions, the four steps in each cycle as shown in Figure 2.5 can be achieved by using four needle contacts.

3.2.2 Adjusted modeling

In the experiment, a small amount of charge transfer was observed when two metals were manually brought into contact, which increases the extra charge in each energy harvesting cycle, a phenomenon that may be explained by the different work functions, which is the minimum work required to remove an electron from one material. When two materials with different work functions are brought contact, different Fermi levels cause electron transfer. Therefore, such charge transfer leads to a potential difference between these two materials.

Because of extra charge in each cycle, equation 2.37 becomes

$$Q_t^{(2)}(i+1) = \gamma Q_t^{(2)}(i) + q_w, \quad \gamma = \frac{n(C_0+C)(C_0'+C')}{(nC_0+C)(C_0'+nC')} \tag{3.2}$$

where q_w is the extra charge in each cycle due to work functions. The above equation can be transformed as below

$$Q_t^{(2)}(i+1) + q_{eq} = \gamma(Q_t^{(2)}(i) + q_{eq}), \quad \gamma = \frac{n(C_0+C)(C_0'+C')}{(nC_0+C)(C_0'+nC')} \tag{3.3}$$

where $q_{eq} = q_w/(\gamma - 1)$. Assume the initial charge is zero, i.e. $Q_t^{(2)}(0) = 0$. According to the above equation, $Q_t^{(2)}(i)$ can be expressed as

$$Q_t^{(2)}(i) = (\gamma^i - 1)q_{eq} \tag{3.4}$$

Divided by $C_t^{(2)}$, the above equation can be changed

$$V_t^{(2)}(i) = (\gamma^i - 1)V_{eq} \tag{3.5}$$

where $V_t^{(2)}(i)$ is the voltage of the total equivalent capacitor of the system, $V_{eq} = q_{eq}/C_t^{(2)}$, and $C_t^{(2)} = C_0' + nC'$. The logarithm form of the above equation can written as

$$LogV_t^{(2)}(i) = Log(\gamma^i - 1) + LogV_{eq} \tag{3.6}$$

Based on equation 3.4, the total energy of the system can be given as

$$U_t^{(2)}(i) = \frac{(\gamma^i - 1)^2 q_{eq}^2}{2C_t^{(2)}} \tag{3.7}$$

The energy difference in each cycle is defined as

$$\begin{aligned} \Delta U_t^{(2)}(i) &= U_t^{(2)}(i) - U_t^{(2)}(i-1) \\ &= \frac{(\gamma - 1)(\gamma^i + \gamma^{i-1} - 2)\gamma^{i-1} q_{eq}^2}{2C_t^{(2)}} \end{aligned} \tag{3.8}$$

3.2.3 Experimental data

According to equation 3.3, the condition of positive feedback is $\gamma > 1$. Based on equation 2.41, the condition becomes $\alpha\beta > 2$. It is known that the maximum capacitance and minimum capacitance for the sink capacitors is 314 pF and 57 pF respectively. Therefore, $\alpha\beta = C/C' = 5.51 > 2$, and thus, a system using two rotary variable capacitors as sink capacitors and one commercial ceramic capacitor as the source capacitor can display a positive feedback mechanism. This mechanism allows the total charge and other electric outputs in the system growing exponentially.

In the experiments, a Keithley 6517B is chosen to measure the voltages of the capacitor. Each measurement is taken when the self-excited energy harvesting system is in the distributive

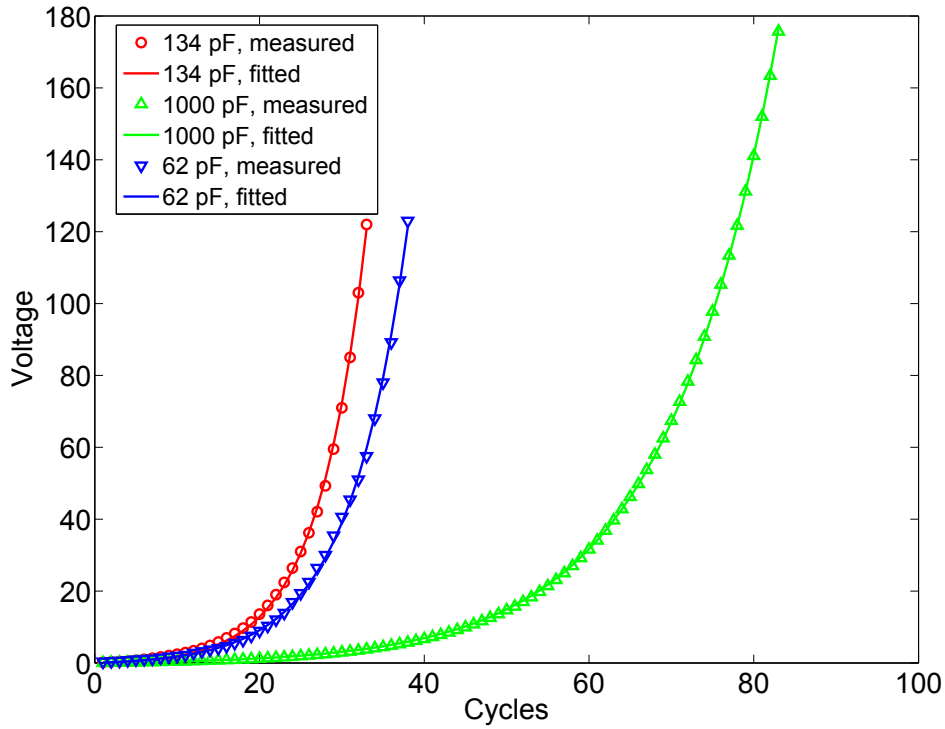

Figure 3.8: The voltage of the source capacitor versus cycles using two rotary variable capacitors

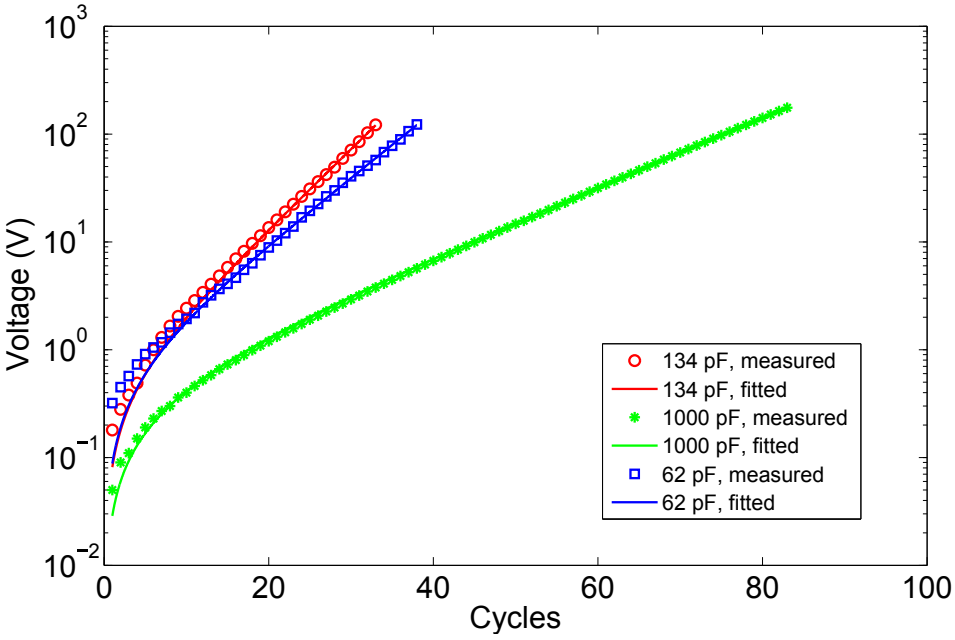

Figure 3.9: Logarithm form of the voltage of source capacitor versus cycles using two rotary variable capacitors

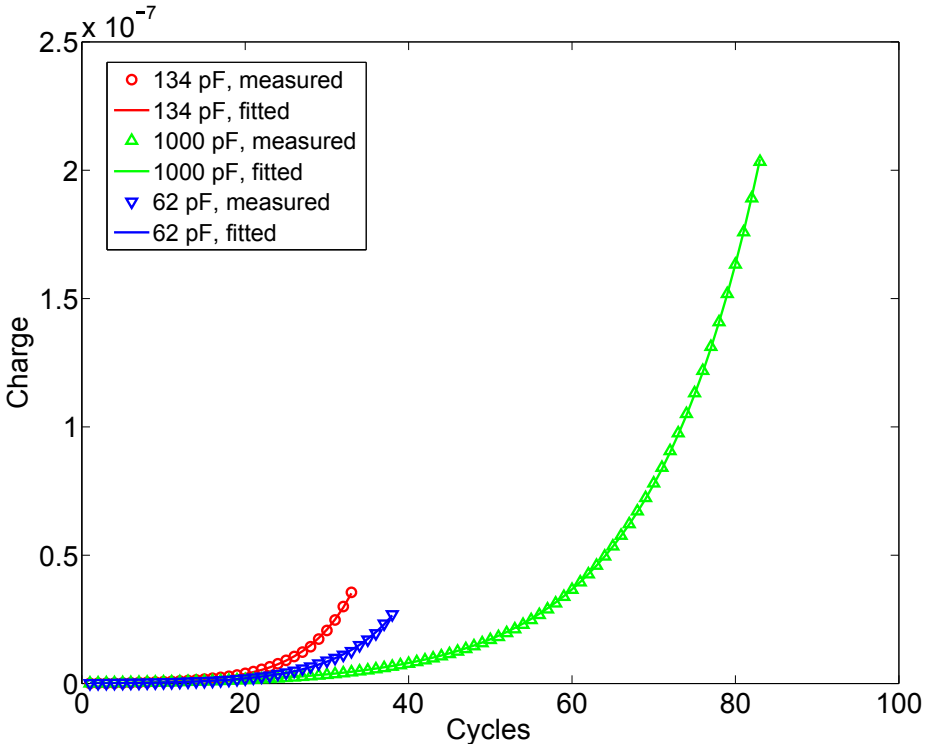

Figure 3.10: The total charge of the system versus cycles using two rotary variable capacitors

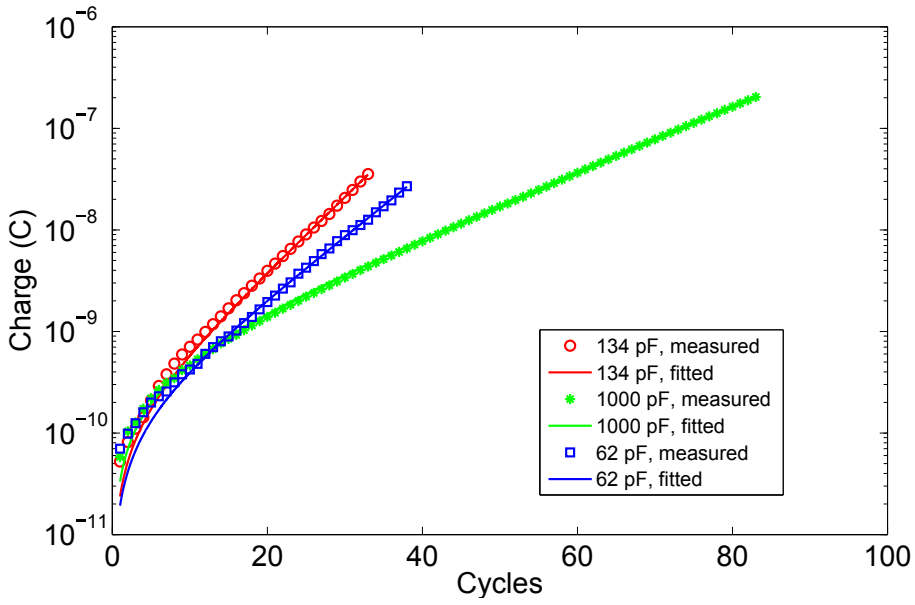

Figure 3.11: Logarithm form of total charge of the system versus cycles using two rotary variable capacitors

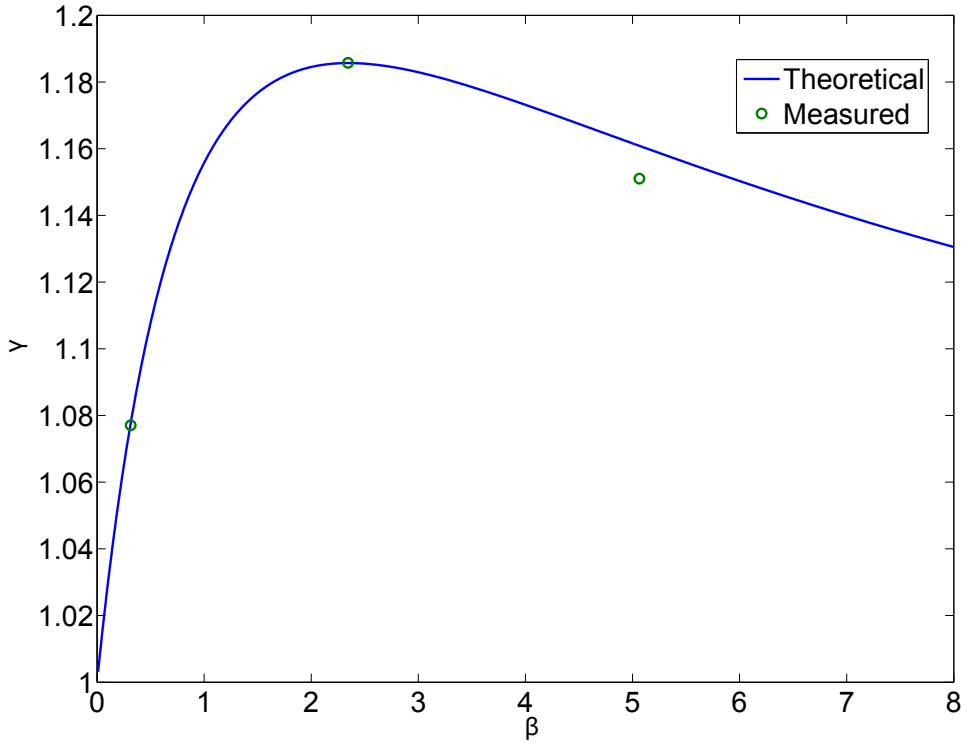

Figure 3.12: The growth rate γ versus β using two rotary variable capacitors

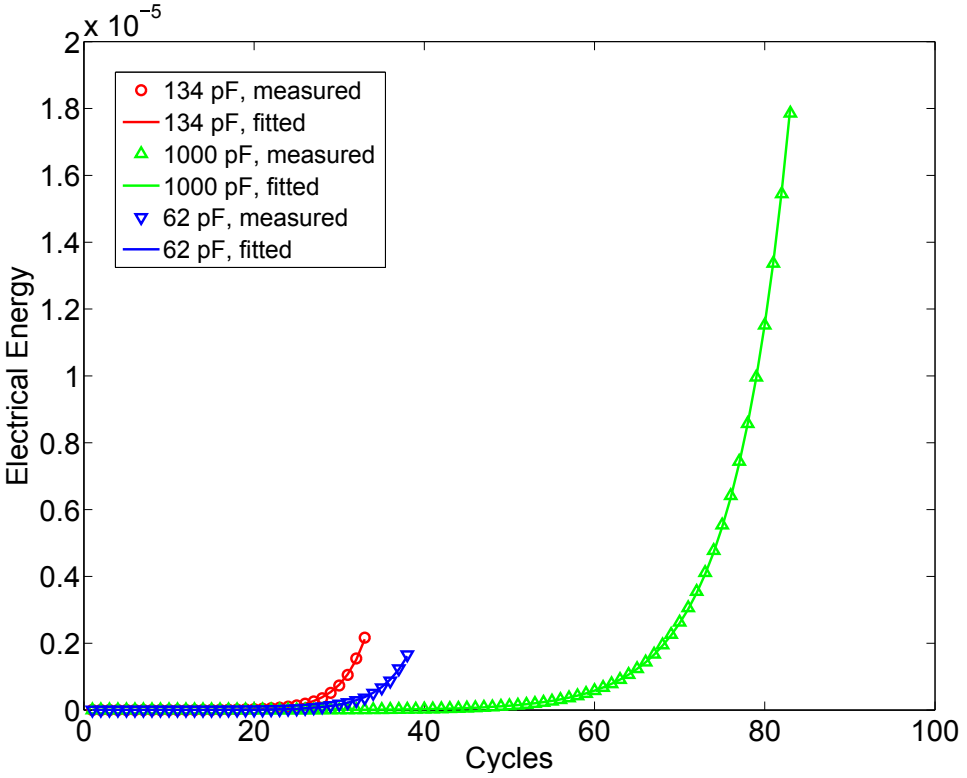

Figure 3.13: The total energy of the system versus cycles using two rotary variable capacitors

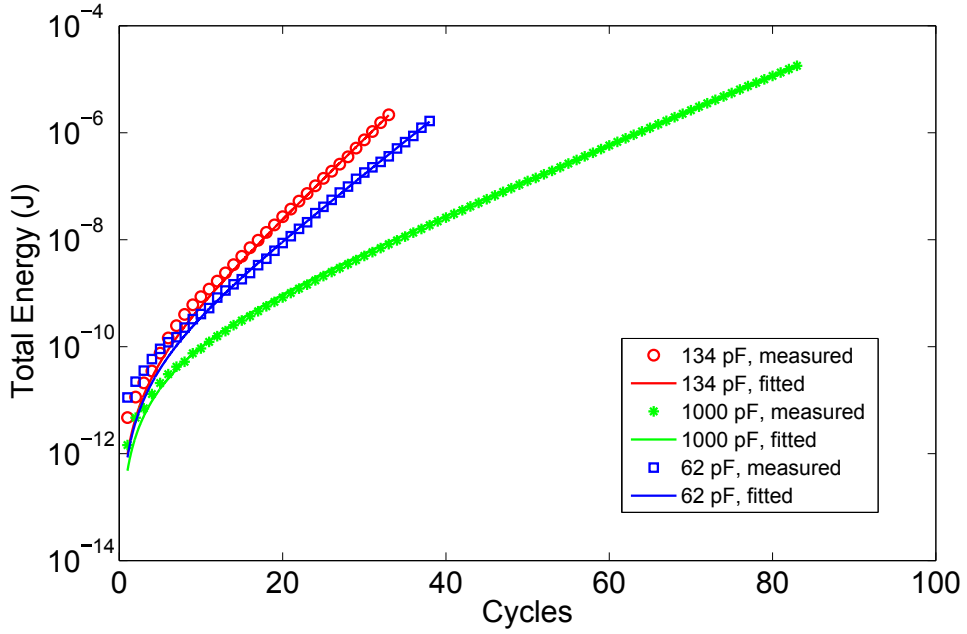

Figure 3.14: Logarithm form of total energy of the system versus cycles using two rotary variable capacitors

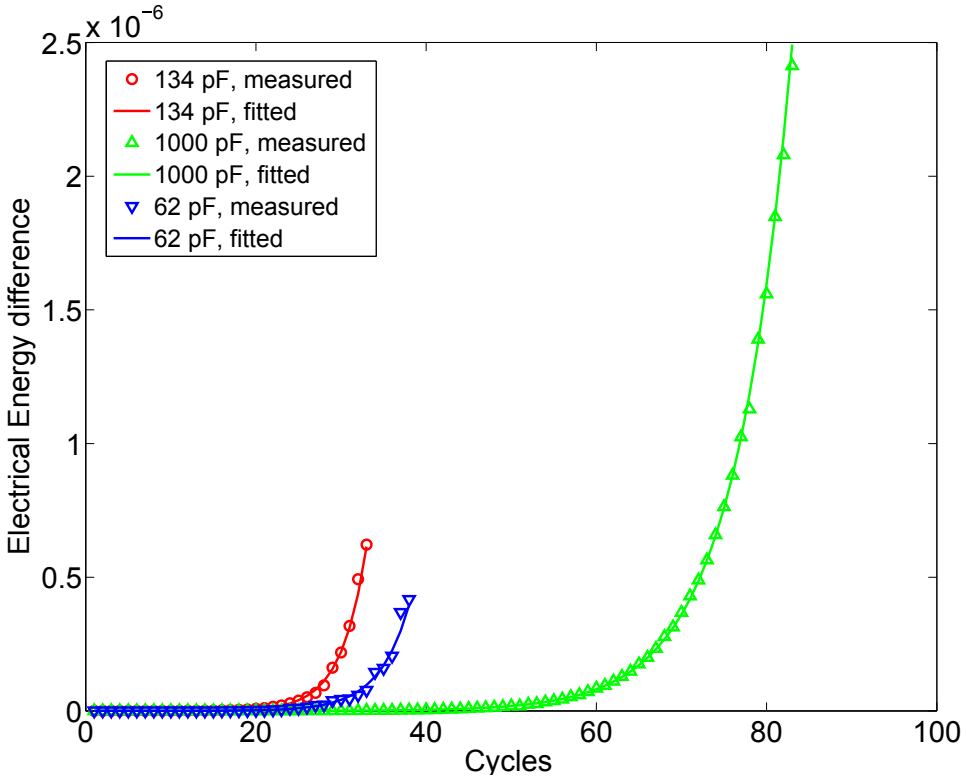

Figure 3.15: The energy difference in each cycle using two rotary variable capacitors

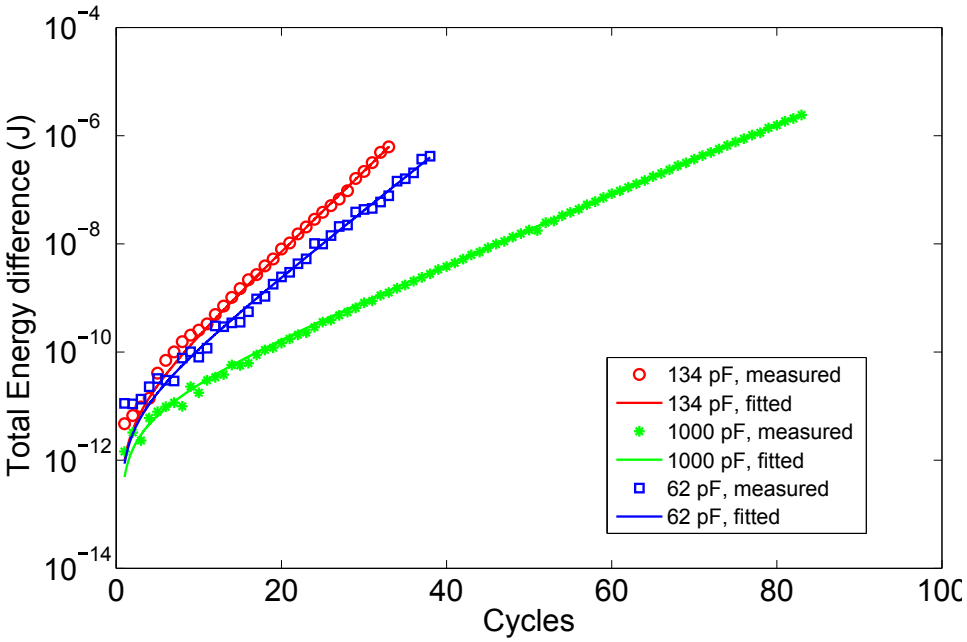

Figure 3.16: Logarithm form of the energy difference in each cycle using two rotary variable capacitors

state. All experiments started after the source capacitor had been discharged in order to minimize charge leakage. One ceramic capacitor with constant capacitance is chosen as the source capacitor. Therefore, $C_0 = C_0'$ in equation 3.3. Three different values of source capacitance are used in the experiments: 62 pF, 134 pF, and 1000 pF, which led to different growth rates γ according to equation 3.3. Figure 3.8 shows the voltage of the source capacitor in the distributive state with three different values of the source capacitance. In all three sets of experiments, the initial voltage was low, in the order of tenths of a volt. The positive feedback mechanism of the system led to exponential growth of the voltages, which can achieve hundreds of volts in just tens of cycles as shown in Figure 3.8. Taking the system with 134-pF source capacitor for example, the voltage is measured at 0.18 V in the first cycle with an increase of only 0.1 V in the second cycle. After tens of cycles of accumulation, the voltage is increased up to 122 volts in the 33rd cycle, in which the voltage increase is as high as 19 volts. From the figure, it is shown that the voltage of the system with 134-pF source capacitor increases at the fastest rate, whereas the growth rate in other two sets of experiment is lower. This means the systems with 1000-pF and

62-pF source capacitors require more cycles to achieve the same voltage as the system with 134-pF source capacitor even though all three systems have the same sink capacitors. This implies an optimal value of the source capacitance that achieves the greatest voltage. In order to demonstrate the increasing rate more clearly, Figure 3.9 shows the logarithm scale of the voltage versus the linear scale of cycles. In this figure, the slope of each line can be considered as the increasing rate, which is the ratio between logarithm voltages and cycles. The increasing rates of all three experiments are higher at the first cycles and then reduced to certain values where they remained constant. Higher increasing rates in the first cycles are caused by the extra charge from the metal contact. After the voltage accumulated to a sufficiently high value, the effect of the positive-feedback mechanism is dominant and the increasing rate becomes constant when the voltage remains high. During this state, the increasing rate is approximately equal to the logarithm of growth rate, which can be proved by equation 3.6. In this equation, if $\gamma^i >> 1$, then $Log(\gamma^i - 1) = ilog\gamma$. The equation 3.6 can be written as $LogV_t^{(2)}(i) = iLog\gamma + LogV_{eq}$. Therefore, the current increasing rate is equal to $Log\gamma$. In Figure 3.9, equation 3.5 is used to fit the experimental data. It is known from the figure that the measured data agree with the theory very well. The fitted growth rates γ and equal voltage V_{eq} for 134 pF, 1000 pF, and 62 pF source capacitors are 1.186 and 0.439 volts, 1.077 and 0.373 volts, and 1.15 and 0.582 volts, respectively. Based on equations 3.4 and 3.5, the total charge of the system is illustrated in Figure 3.10. From this figure, it is known that the charge also increases exponentially with each cycle. The total charge with the 134-pF source capacitor increases at the fastest rate compared to the two other sets of systems. In other words, to obtain the same charge, the system with the 134-pF source capacitor requires the least number of cycles. Figure 3.11 illustrates the logarithm scale of the total charge versus linear scale of cycles. It is known from the figure that the increasing rate in the first cycles is higher than that of the subsequent cycles. The extra charge is due to the metal contact causing a greater increasing rate in the first cycles.

Figure 3.12 shows the growth rates γ corresponding to different values of β, i.e C/C_0. Equation 2.39 is used to estimate the theoretical values. The capacitance in the equation can be

measured via a Tektronix DMM4050 or by the charge distribution method via a Keithley 6517B. In the charge distribution method, the capacitor to be measured is powered by a certain voltage V_0 and then connected to an empty capacitor with known capacitance C_k. After the equilibrium of charge distribution, Keithley 6517B is used to measure the balanced voltage V_1. Because the charge is constant during the process, the measured capacitance can be expressed as $C_m = C_k V_1/(V_0 - V_1)$. The fitted growth rates can be found from Figure 3.9. It is shown that the fitted growth rates agree well with the theory. In the figure, there is an optimal β to make the γ highest, which can be found according to equation 2.39. If the source capacitance is constant and the maximum and minimum capacitance of the sink capacitor is known, γ reaches the highest when $\alpha = \beta = \sqrt{C/C'}$. Substituting the numbers into the above equation, γ can reach 1.186 when $\alpha = \beta = 2.35$. The corresponding value of the source capacitor is 133.8 pF. A 134-pF source capacitor is chosen in the experiments and the fitted growth rate agrees well with the theory. The total energy of the system with cycles and its logarithm form are shown in Figure 3.13 and 3.14 respectively. According to equation 3.7, the total energy increases exponentially and the growth rate is γ^2. The energy difference in each cycle and its logarithm form are shown in Figure 3.15 and 3.16. According to equation 3.8, the energy difference also increases exponentially with the growth rate of γ^2. In reality, a capacitor has a maximum working voltage and would break down once the voltage exceeds the working voltage. Figure 2.7 shows one way to control the voltage and extract the harvested energy. Taking the system with 1000-pF source capacitor as an example, the threshold can be set slightly higher than the voltage in the second-to-last cycle (163.9 volts). Let's say the threshold is 164 volts. Therefore, the electric load circuit is open until the last cycle. After the control process, the voltage returns to 164 volts. This process repeats continuously to extract the harvested energy. The harvested energy in each cycle is estimated to be about 2.41 μJ as shown in Figure 3.15.

In the experiments, two rotary variable capacitors are used as sink capacitors and one commercial ceramic capacitor is used as the source capacitor to establish a self-excited energy harvesting system. It is proven that the electric outputs of the system can grow exponentially if a

certain condition is satisfied. The measured data agree well with the theoretical modeling. The built system is only proof of concept. The capacitance of the system is several hundred picofarads, which leads to high voltage while only a few microjoules is stored. In reality, a insulating material has finite dielectric strength, which will limit the maximum working voltage for a capacitor. Therefore, a small capacitance limits the maximum stored energy, and thus limits the coupling efficiency. Also, the size of the capacitors is relatively large. Therefore, a more compact variable capacitor with higher capacitance is needed for the proposed method.

3.3 Mercury contact variable capacitors as sink capacitors

The basic components of a capacitor include two conductive plates separated by a dielectric material. Polar dielectric materials, such as SiO_2, and Ta_2O_5, would disturb the charge on the conductive plates during the contact, which is caused by surface chemistry. Therefore, in order to avoid the contact, air is used by many papers [18, 27, 17, 25, 28] as the whole or part of dielectric material for a variable capacitor. However, the low relative permittivity and relatively high thickness of the air as dielectric may lead to small capacitance and low coupling efficiency. In order to obtain high capacitance in limited space, a compacted droplet-based contact variable capacitor is designed and fabricated in this section. In this capacitor, the droplet is movable and considered to be one of the conductors for the capacitor. Two types of conductive liquid, mercury and water, are used as the movable electrodes. The design is slightly modified due to their different properties. Mercury-based variable capacitors are discussed in this section and water-based variable capacitors will be discussed in the next section. Non-polar material CYTOP is used as one of the dielectric materials. Compared to air variable capacitors, droplet-based contact variable capacitors use less space while achieving high capacitance. Also, when liquid is brought into contact with solid, it can minimize the gaps between them since liquid is shapeless and contacts the solid very tightly, and thus lead to high contact area and capacitance. Such high contact area can cause high surplus charge pumping into the system in each cycle because of

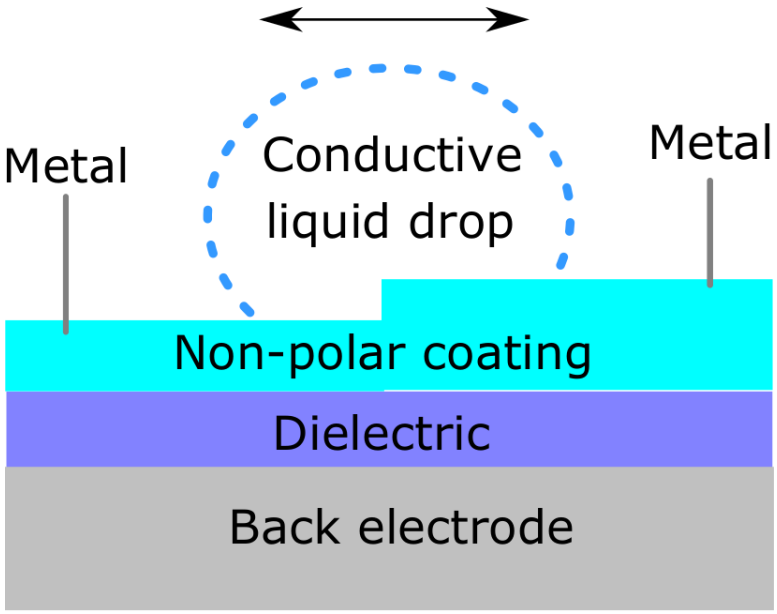

Figure 3.17: A schematic diagram of the cross-section for the liquid-based contact variable capacitor.

contact electrification and electrostatic induction effects. Surface charge trapping still happens during the contact but only an acceptable portion of the charge on the plates remains on the surface of CYTOP coating. An adjusted model is discussed here corresponding to contact electrification and electrostatic induction. According to the equation of capacitance for a parallel capacitor, i.e. $C = \varepsilon A/d$, variable dielectric constant, plate overlap, and separation between two plates can be used to achieve a variable capacitance. In this section, varying distance between two conductors is used as an example to establish a contact variable capacitor. The results illustrate a high energy harvesting efficiency for low-frequency and low-level vibration.

3.3.1 Design of mercury-droplet contact variable capacitors

As discussed before, as long as there is a small charge imbalance, the system can be self excited to a high level by means of a positive feedback mechanism. In reality, an electrical charge difference always exists between dissimilar and even identical materials. According to equation 2.55, it is known that higher initial charge leads to less number of cycles to achieve the certain charge in the system.

Figure 3.17 shows a cross-section schematic diagram for the liquid-based contact variable capacitors. One capacitor usually consists of three components, two conductive plates sandwiching one dielectric material. In this figure, one of the electrodes is stationary, which is also the support and substrate for the other two components. A movable drop of conductive liquid is considered the counter electrode. The dielectric materials include two layers: one layer of non-polar coating and the other insulating layer with a high dielectric constant. Non-polar material is hydrophobic, which has no attraction to water molecules and thus causes a high contact angle. Because of this, most of charge remains on the liquid drop when it is separated from non-polar surface. Because of the variation in thickness, the capacitance will change if the drop moves from one side to the other. The higher thickness of the coating on the right side causes lower capacitance (C) between the liquid drop and back electrode while the less thickness on the left side causes comparatively high capacitance (C'). The thickness of the coating is usually a few micrometers at most. In order to avoid charge leakage for the thin non-polar coating, an extra insulating layer with a relatively high dielectric constant is used. It can be seen from the figure that the drop can slide back and forth on the surface of the non-polar coating while two metal contacts that do not chemically interact with the drop are deployed on each side to facilitate the connectivity required for the two configurations. Compared to solid material, a liquid drop is chosen because it has no fixed shape. It can fully contact the solid surface more effectively to increase the capacitance. It also reduces the damage due to friction of the dielectric material in the long term. Another role for the liquid drop is that the contact electrification occurs when liquid drop is on the non-polar coating due to the charge exchange on their interface as shown in Figure 3.18. Such extra charge will also improve the increasing scale at the first cycles and thus reduce the number of cycles to achieve the optimal electric outputs of the system. Figure 3.18 shows the contact variable capacitor is fabricated on a doped silicon wafer with silicon dioxide on its surface. CYTOP is chosen as the non-polar material in the proposed device. If a liquid drop is brought into contact with an initially uncharged CYTOP surface and then separated for the first time, the surface will be electrified from contact electrification. Subsequent

oscillatory motion of the drop on the surface will cause the surface charge to increase to a saturation value, which will be different for the two sides because of the molecular-scale fluctuations of surface properties [85, 86, 87, 88, 52, 89]. The two sides will behave as electrets subsequently. Electrostatic induction will then become the dominating mechanism that determines the charge distribution on the liquid drop [85, 52, 89]. We have confirmed experimentally that the effect of electrostatic induction can be modeled by a fixed amount of charge, Q_c, which is transferred to or removed from the drop when it moves from one side to the other. The thin CYTOP side is created with a spin coater while the thick CYTOP side is manually brushed. Different coating methods will cause different surface properties, and thus leads to different surface charge density. Because of molecular scale differences in surface properties, the amount of charge resulting from contact electrification is different for the thinner and the thicker sides, which induces different amount of charge on the drop. Because the saturated charge in the CYTOP layer due to contact electrification is fixed, a constant charge, Q_c, is induced when the drop moves from one side to the other and the same amount of charge with an opposite sign, $-Q_c$, is induced when it returns to the original position. In our experiments, the observed surface charge on the thick layer is usually less than that on the thin layer. Because the surface property for each fabricated capacitor is different, net charge from thin surface to thick one, Q_c, is various correspondingly. The charge can be modeled as

$$Q_c(j) = sgn(q(j))[\sigma_{tk}(j) - \sigma_{tn}(j)])A(j) \tag{3.9}$$

where $q(j)$ represents the charge carried by the j^{th} drop, $\theta_{tk}(j)$ and $\theta_{tn}(j)$ are the surface charge densities of the thicker and the thinner CYTOP side for the j^{th} capacitor, respectively, and $A(i)$ represents the contact area. $sgn(x)$ is equal to 1 if $q(j) > 0$ and -1 if $q(j) < 0$. Such net charge can be further improved by using other non-polar materials with more distinguished surface properties, which will be discussed in the next chapter.

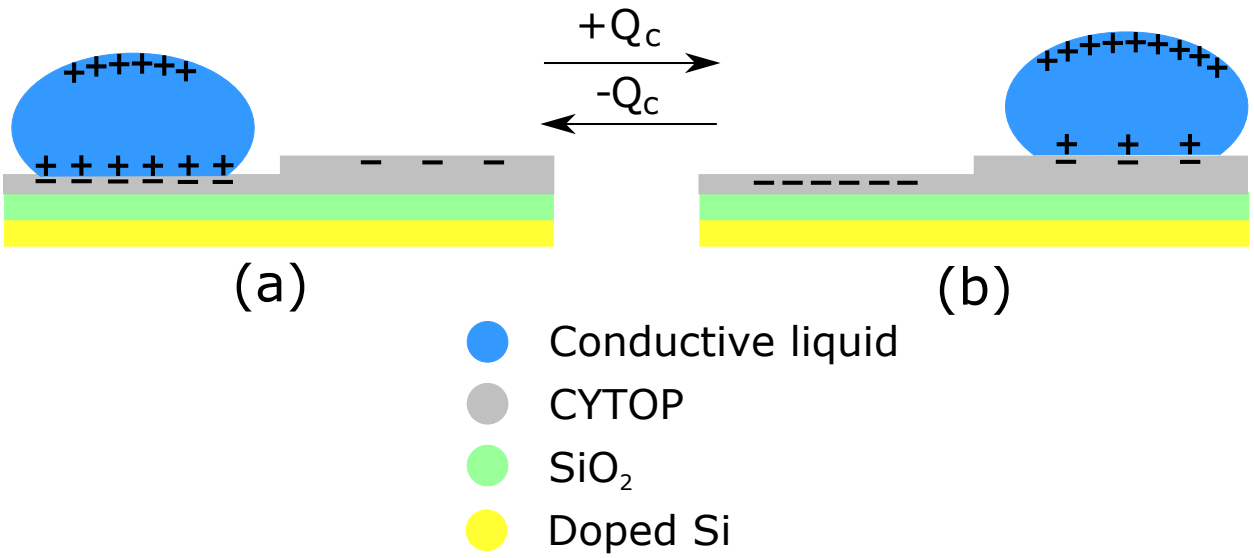

Figure 3.18: Structure design of contact variable capacitor. **(a)** A charged drop on the thinner side. **(b)** The drop on the thicker side.

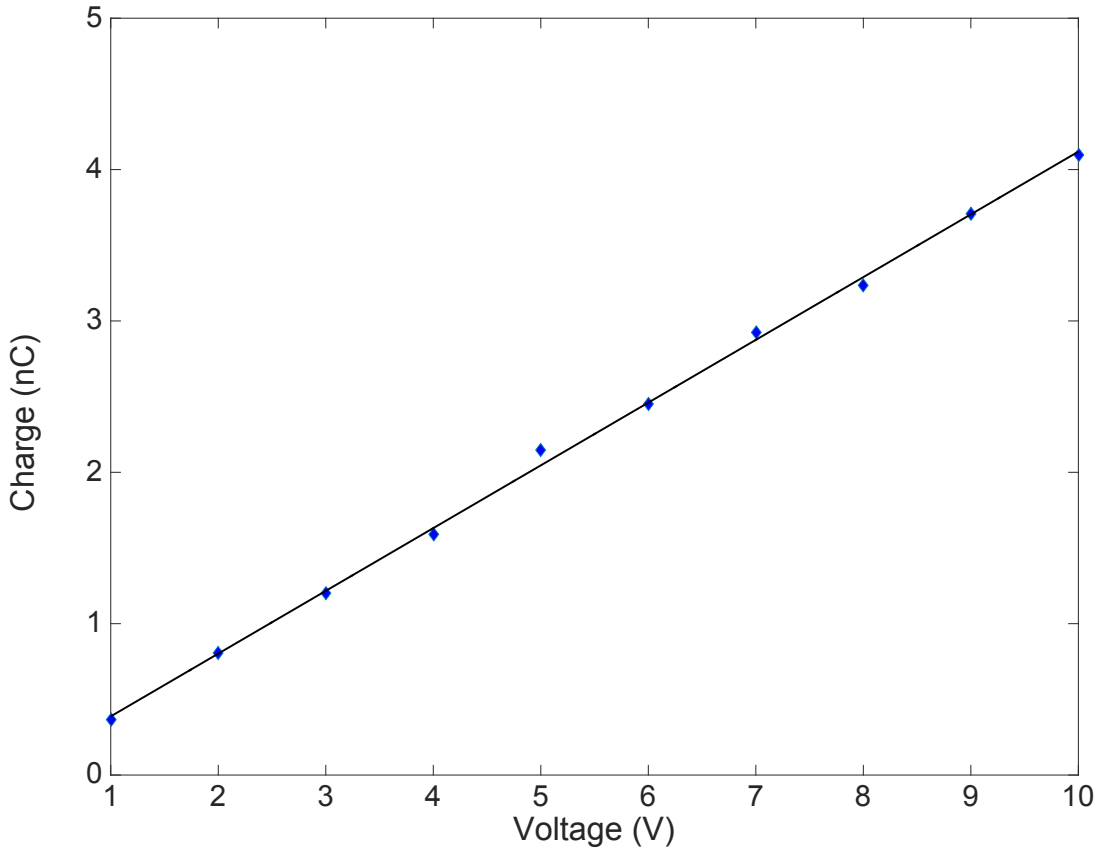

Figure 3.19: Thinner surface charge trapping effect using 300 μL mercury drop.

The contacts between a charged liquid drop and the CYTOP surface will also induce charge trapping at the surface, which limits the amount of charge that can move with the drop. However, the trapped charge can be removed by grounding the drop, which suggests that trapping occurs on the surface rather than in the insulator [29, 90, 91]. The trapped charge can be tested by the following procedures. A voltage source (V_C) was first used to charge the capacitor when the drop was on the thinner side (C). Then the voltage ($V_{C'}$) was measured after the drop was driven to the thicker side (C'). The charge, including that which was moving with the drop and that due to induction (Q_c), was determined by using the measured capacitance of the thicker side. The usual form by linear regression between V_C and $V_{C'}$ is $V_{C'} = aV_C + b$. Therefore, the extra charge Q_c can be expressed as $Q_c = bV_{C'}$. The trapped charge on the thinner side (Q_t) can be expressed as $Q_t = CV_C + Q_c - C'V_{C'}$. Figure 3.19 shows the results of the trapped charge on the thinner CYTOP surface with different initial voltages when a 300 μL mercury drop slides from thinner side to thicker side. The linear relationships in the figure indicate the behavior of the trapped charge can be described as a constant capacitor. The trapping on the thinner side can be accurately modeled with a parasitic capacitor C_p, connected in parallel to the effective capacitor ($\tilde{C}$) associated with the thinner side. The total capacitance of an individual capacitor in the duplicative state becomes

$$C = \tilde{C} + C_p \tag{3.10}$$

Charge trapping also happens on the thicker side. Because of the internal connectivity of the system, the drop is charged when it is on the thinner side and almost completely discharged when moving to the thicker side. Therefore, charge trapping is negligible for the thicker side.

3.3.2 Adjusted modeling

As discussed earlier, one of practical issues for the designed contact variable capacitor is the effect of surface charge trapping. The total capacitance of each individual capacitor in the duplicative state becomes $C = \tilde{C} + C_p$. Figure 3.20 illustrates the adjusted modeling and

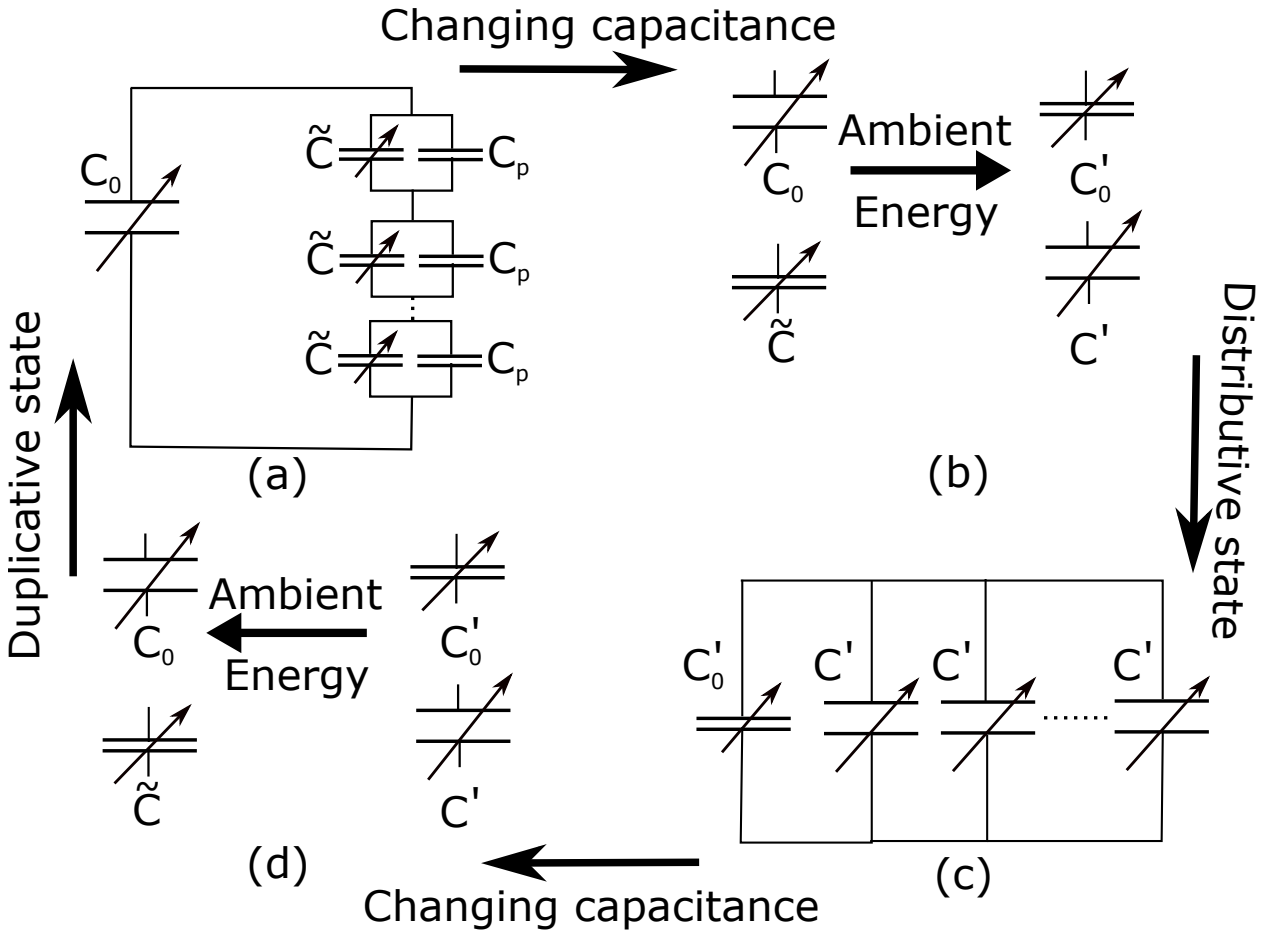

Figure 3.20: Adjusted model and corresponding steps of the system using contact variable capacitors.

corresponding steps of the system using contact variable capacitors. In the duplicative state, not all the charge can move with the liquid drops. C_p is a parasitic capacitor representing the trapped charge when the liquid droplet moves away from the thin layer of the dielectric material. $\tilde{C}$ is the real capacitor that can carry the charge with the liquid drop. Compared to the modeling discussed in chapter two, the excess charge due to contact electrification and electrostatic induction effects and the trapping charge due to the bonding force on their interface should both be considered into the adjusted model.

In the duplicative step, all the liquid drops are located on the thinner side and all the sink capacitors are connected in series. $Q_t^{(1)}(i)$ is the total charge during the i^{th} cycle. Such charge is

distributed as below

$$\begin{aligned} q_0^{(1)}(i) &= \frac{nC_0}{nC_0 + C} Q_t^{(1)}(i) \\ \tilde{q}_0^{(1)}(i) &= \frac{\tilde{C}}{nC_0 + C} Q_t^{(1)}(i) \\ q_p^{(1)}(i) &= \frac{C_p}{nC_0 + C} Q_t^{(1)}(i) \end{aligned} \tag{3.11}$$

where $q_0^{(1)}(i)$, $\tilde{q}_0^{(1)}(i)$, and $q_p^{(1)}(i)$ are the charge stored in the source capacitor, effective sink capacitor, and parasitic sink capacitor in the duplicative step of i^{th} cycle, respectively. In the second step, all the capacitors are disconnected and then all the liquid drops are driven to the thick CYTOP surfaces. The excess charge $Q_c(j)$ due to contact electrification and electrostatic induction is introduced in the system. In the distributive state, the effective parts of sink capacitors and the source capacitor are connected in parallel. The total charge of the system in this state, $Q_t^{(2)}(j)$, becomes

$$Q_t^{(2)}(i) = q_0^{(1)}(i) + n\tilde{q}_0^{(1)}(i) + n\bar{Q}_c \tag{3.12}$$

where $\bar{Q}_c = \dfrac{1}{n} \sum_{j=1}^{n} Q_c(j)$. Substituting equation 3.11 into 3.12, the equation becomes

$$Q_t^{(2)}(i) = \frac{n(C_0 + \tilde{C})}{nC_0 + C} Q_t^{(1)}(i) + n\bar{Q}_c \tag{3.13}$$

After the duplicative state reaches equilibrium, the charge is distributed as

$$\begin{aligned} q_0^{(2)}(i) &= \frac{C_0'}{C_0' + nC'} Q_t^{(2)}(i) \\ \tilde{q}^{(2)}(i) &= \frac{C'}{C_0' + nC'} Q_t^{(2)}(i) \end{aligned} \tag{3.14}$$

where $q_0^{(2)}(i)$ and $\tilde{q}_0^{(2)}(i)$ are the charge of the source capacitor and the effective sink capacitor in distributive state of i^{th} cycle, respectively. After the capacitance of the source capacitor and the effective sink capacitor returns to C_0 and $\tilde{C}$ respectively, the extra charge $Q_c(j)$ will be locked by the thicker CYTOP surface. Therefore, the total charge in the duplicative state of the $(i+1)^{th}$

cycle becomes,

$$Q_t^{(1)}(i+1) = q_0^{(2)}(i) + \tilde{q}^{(2)}(i) + q_p^{(1)}(i) - \bar{Q}_c \tag{3.15}$$

In order to get the relationship between $Q_t^{(1)}(i+1)$ and $Q_t^{(1)}(i)$, substitute equation 3.14 and 3.11 into equation 3.15,

$$Q_t^{(1)}(i+1) = \frac{C_0' + C'}{C_0' + nC'} Q_t^{(2)}(i) + \frac{C_p}{nC_0 + C} Q_t^{(1)}(i) - \bar{Q}_c \tag{3.16}$$

And then, substitute equation 3.13 into equation 3.16, the relationship between $Q_t^{(1)}(i+1)$ and $Q_t^{(1)}(i)$ is expressed as

$$Q_t^{(1)}(i+1) = \frac{n(C_0' + C')(C_0 + C)}{(C_0' + nC')(nC_0 + C)} Q_t^{(1)}(i) - \frac{(n-1)C_0' C_p}{(C_0' + nC')(nC_0 + C)} Q_t^{(1)}(i) + \frac{(n-1)C_0'}{C_0' + nC'} \bar{Q}_c \tag{3.17}$$

Denote $\alpha = C_0'/C'$, $\beta = C/C_0$, and $\delta = C_p/C$, the above equation becomes

$$Q_t^{(1)}(i+1) = \frac{n(1+\alpha)(1+\beta)}{(n+\alpha)(n+\beta)} Q_t^{(1)}(i) - \frac{(n-1)\delta\alpha\beta}{(n+\alpha)(n+\beta)} Q_t^{(1)}(i) + \frac{(n-1)\alpha}{n+\alpha} \bar{Q}_c \tag{3.18}$$

The above equation has three components. The first component represents the theoretical modeling, the second one is caused by surface charge trapping, and the third one is caused by contact electrification and electrostatic induction. Three symbols, γ, γ_p, and $\zeta^{(1)}$, are used to denote those three components, respectively.

$$\begin{aligned} \gamma &= \frac{n(1+\alpha)(1+\beta)}{(n+\alpha)(n+\beta)} \\ \gamma_p &= \frac{(n-1)\delta\alpha\beta}{(n+\alpha)(n+\beta)} \\ \zeta^{(1)} &= \frac{(n-1)\alpha}{n+\alpha} \end{aligned} \tag{3.19}$$

Therefore, equation 3.18 becomes

$$Q_t^{(1)}(i+1) = (\gamma - \gamma_p) Q_t^{(1)}(i) + \zeta^{(1)} \bar{Q}_c \tag{3.20}$$

The adjusted growth rate is $\gamma_r = \gamma - \gamma_p$. From equation 3.19, it is known that $\gamma_p > 0$. Therefore, The adjusted growth rate in the system is decreased by the surface charge trapping effect. γ_r needs to be higher than one to make the system grow exponentially. i.e. $\gamma_r > 1$. Substituting equation 3.19 into the above equation, the positive-feedback condition becomes

$$(n-1)(\alpha\beta - n - \delta\alpha\beta) > 0 \tag{3.21}$$

Since $n > 1$, the positive-feedback condition for the adjusted system is

$$\alpha\beta > n/(1-\delta) \tag{3.22}$$

According to equation 3.20, $\zeta^{(1)}\bar{Q}_c$ introduces extra charge in each cycle, which will make the growth higher at the first cycles. Equation 3.20 can be changed into the iterated function as follows

$$Q_t^{(1)}(i+1) + \bar{Q}_{eq1} = \gamma_r(Q_t^{(1)}(i+1) + \bar{Q}_{eq1}) \tag{3.23}$$

where $\bar{Q}_{eq1} = \dfrac{\zeta^{(1)}}{\gamma_r - 1}\bar{Q}_c$. Therefore, the total charge in the i^{th} cycle can be expressed as

$$Q_t^{(1)}(i) = (\gamma_r^i - 1)\bar{Q}_{eq1} \tag{3.24}$$

From equation 3.24, it is known that the total charge in the system grows exponentially with the cycles as long as $\gamma_r > 1$. Divided by $C_t^{(1)}$, the above equation can be changed

$$V_t^{(1)}(i) = (\gamma_r^i - 1)\bar{V}_{eq1} \tag{3.25}$$

where $V_t^{(1)}(i)$ is the voltage of the total equivalent capacitor of the system in the duplicative state of i^{th} cycle, $\bar{V}_{eq1} = \bar{Q}_{eq1}/C_t^{(1)}$, and $C_t^{(1)} = C_0 + C/n$. The logarithm form of the above equation becomes

$$LogV_t^{(1)}(i) = Log(\gamma_r^i - 1) + Log\bar{V}_{eq1} \tag{3.26}$$

Based on equation 3.24, the total energy of the system can be given as

$$U_t^{(1)}(i) = \frac{(\gamma_r^i - 1)^2 \bar{Q}_{eq1}^2}{2C_t^{(1)}} \tag{3.27}$$

The energy difference in each cycle is defined as

$$\begin{aligned} \Delta U_t^{(1)}(i) &= U_t^{(1)}(i) - U_t^{(1)}(i-1) \\ &= \frac{(\gamma_r - 1)(\gamma_r^i + \gamma_r^{i-1} - 2)\gamma_r^{i-1} \bar{Q}_{eq1}^2}{2C_t^{(1)}} \end{aligned} \tag{3.28}$$

The electric outputs of the system in the distributive state of i^{th} cycle can be derived by similar procedures. By rearranging equation 3.13, $Q_t^{(1)}(i)$ can be expressed in terms of $Q_t^{(2)}(i)$

$$Q_t^{(1)}(i) = \frac{nC_0 + C}{n(C_0 + \tilde{C})} Q_t^{(2)}(i) - \frac{n(nC_0 + C)}{n(C_0 + \tilde{C})} \bar{Q}_c \tag{3.29}$$

Substituting the above equation into 3.18,

$$Q_t^{(2)}(i+1) = (\gamma - \gamma_p) Q_t^{(2)}(i) + \zeta^{(2)} \bar{Q}_c \tag{3.30}$$

where $\zeta^{(2)} = \frac{n(n-1)}{n+\beta}$. The equation can also be transformed into an iterated function as

$$Q_t^{(2)}(i+1) + \bar{Q}_{eq2} = \gamma_r (Q_t^{(2)}(i+1) + \bar{Q}_{eq2}) \tag{3.31}$$

where $\bar{Q}_{eq2} = \frac{\zeta^{(2)}}{\gamma_r - 1} \bar{Q}_c$. Therefore, the total charge in the i^{th} cycle can be expressed as

$$Q_t^{(2)}(i) = (\gamma_r^i - 1) \bar{Q}_{eq2} \tag{3.32}$$

From equation 3.24, it is known that the total charge in the system grows exponentially with the cycles as long as $\gamma_r > 1$. Divided by $C_t^{(2)}$, the above equation can be changed

$$V_t^{(2)}(i) = (\gamma_r^i - 1)\bar{V}_{eq2} \tag{3.33}$$

where $V_t^{(2)}(i)$ is the voltage of the total equivalent capacitor of the system in the distributive state of i^{th} cycle, $\bar{V}_{eq2} = \bar{Q}_{eq2}/C_t^{(2)}$, and $C_t^{(2)} = C_0' + nC'$. The logarithm form of the above equation becomes

$$LogV_t^{(2)}(i) = Log(\gamma_r^i - 1) + Log\bar{V}_{eq2} \tag{3.34}$$

Based on equation 3.32, the total energy of the system can be given as

$$U_t^{(2)}(i) = \frac{(\gamma_r^i - 1)^2\bar{Q}_{eq2}^2}{2C_t^{(2)}} \tag{3.35}$$

The energy difference in each cycle is defined as

$$\begin{aligned} \Delta U_t^{(2)}(i) &= U_t^{(2)}(i) - U_t^{(2)}(i-1) \\ &= \frac{(\gamma_r - 1)(\gamma_r^i + \gamma_r^{i-1} - 2)\gamma_r^{i-1}\bar{Q}_{eq2}^2}{2C_t^{(2)}} \end{aligned} \tag{3.36}$$

3.3.3 Influencing factors of the adjusted growth rate

According to equation 3.18, the growth rate of the system is expressed as

$$\gamma_r = \frac{n(1+\alpha)(1+\beta)}{(n+\alpha)(n+\beta)} - \frac{(n-1)\delta\alpha\beta}{(n+\alpha)(n+\beta)} \tag{3.37}$$

In the above equation, δ is considered as a constant number and the function has three variables: α, β, and n. Each partial derivative of the loop gain γ_r with respect to three variables is shown

below,

$$\begin{aligned}
\frac{\partial \gamma_r}{\partial \alpha} &= \frac{n(n-1)(1+\beta-\delta\beta)}{(n+\alpha)^2(n+\beta)} \\
\frac{\partial \gamma_r}{\partial \beta} &= \frac{n(n-1)(1+\alpha-\delta\alpha)}{(n+\beta)^2(n+\alpha)} \\
\frac{\partial \gamma_r}{\partial n} &= \frac{(1+\alpha)(1+\beta)(\alpha\beta-\delta\alpha\beta-n^2)+\delta\alpha\beta(n-1)^2}{(n+\alpha)^2(n+\beta)^2}
\end{aligned} \tag{3.38}$$

Based on the definitions of the symbols, it is know that $\alpha > 0$, $\beta > 0$, $0 < \delta < 1$, and $n \geq 2$. Therefore, the partial derivatives of γ_r with respect to α and β are permanently greater than zero. i.e.,

$$\begin{aligned}
\frac{\partial r}{\partial \alpha} &> 0 \\
\frac{\partial r}{\partial \beta} &> 0
\end{aligned} \tag{3.39}$$

Therefore, γ_r monotonically increases with α and β respectively. Set $\frac{\partial \gamma_r}{\partial n} = 0$ and substitute this into equation 3.38, then

$$n = \frac{\sqrt{\alpha\beta(1+\alpha)(1+\beta)(\delta\beta-\beta-1)(\delta\alpha-\alpha-1)}-\delta\alpha\beta}{(1+\alpha)(1+\beta)-\delta\alpha\beta} \tag{3.40}$$

Therefore, γ has the extrema with respect to n. Also, n needs to be an integer. Here, $||x||$ is denoted as the symbol of the nearest integer to x. Equation 3.40 becomes

$$n = ||\frac{\sqrt{\alpha\beta(1+\alpha)(1+\beta)(\delta\beta-\beta-1)(\delta\alpha-\alpha-1)}-\delta\alpha\beta}{(1+\alpha)(1+\beta)-\delta\alpha\beta}|| \tag{3.41}$$

One of the specific cases is that the maximum and minimum capacitance of each sink capacitor have been determined. Denote $\alpha\beta = \lambda$. β can be presented by α, i.e. $\beta = \lambda/\alpha$. Substituting this equation into 3.37,

$$\gamma_r = \frac{n(1+\alpha)(\alpha+\lambda)}{(n+\alpha)(n\alpha+\lambda)} - \frac{(n-1)\delta\lambda\alpha}{(n+\alpha)(n\alpha+\lambda)} \tag{3.42}$$

There are two variables in the above equation. The partial derivative with respect to α is given below,

$$\frac{\partial \gamma_r}{\partial \alpha} = \frac{n(n-1)(\lambda-\alpha^2)(\lambda-n-\delta\lambda)}{(n+\alpha)^2(n\alpha+\lambda)^2} \tag{3.43}$$

According to equation 3.22, the positive-feedback condition leads to $\lambda - n - \delta\lambda > 0$. Therefore, Set equation 3.43 as zero,

$$\alpha = \sqrt{\lambda} \tag{3.44}$$

Therefore, $\frac{\partial \gamma_r}{\partial n}$ has the maximum value when α satisfies equation 3.44. Similarly, $\frac{\partial \gamma_r}{\partial \beta}$ also has the maximum value. The partial derivative with respect to β is given as

$$\frac{\partial \gamma_r}{\partial \beta} = \frac{n(n-1)(\lambda - \beta^2)(\lambda - n - \delta\lambda)}{(n+\beta)^2(n\beta + \lambda)^2} \tag{3.45}$$

Set the above equation as zero,

$$\beta = \sqrt{\lambda} \tag{3.46}$$

Therefore, $\frac{\partial \gamma_r}{\partial \beta}$ has the maximum value when α satisfies equation 3.46. Since α and β are known, n can be determined by substituting equation 3.44 and 3.46 into 3.41,

$$n = ||\frac{\sqrt{\lambda}(1+\sqrt{\lambda})(1+\sqrt{\lambda}-\delta\sqrt{\lambda}) - \delta\lambda}{(1+\sqrt{\lambda})^2 - \delta\lambda}|| \tag{3.47}$$

Therefore, if the maximum and minimum capacitance of each sink capacitor are determined, γ_r has the maximum value when $\alpha = \beta = \lambda$ and $n = ||\frac{\sqrt{\lambda}(1+\sqrt{\lambda})(\delta\sqrt{\lambda}-\sqrt{\lambda}-1) - \delta\lambda}{(1+\sqrt{\lambda})^2 - \delta\lambda}||$.

3.3.4 Materials and fabrication

The capacitors were fabricated on 2-in doped silicon wafers (with resistivity of 1-10 Ω·cm), one capacitor per wafer. The doped silicon was used as the back electrode. A layer of 200-nm silicon dioxide was grown on one side of the wafer. The bonding force between liquid drops and the dielectric material is significantly high if the surface molecules of dielectric material have massive polar groups, which lead to heavy surface charge trapping. Therefore, non-polar material is a better option here. In order to reduce surface charge trapping, an amorphous fluoropolymer, CYTOP, is chosen because of its low water contact angle hysteresis. The thinner CYTOP surface

Figure 3.21: Spin coating CYTOP on a silicon wafer.

is spin coated by using Spincoater model P6700 as shown in Figure 3.21. CYTOP was spin-coated on silicon dioxide to create a hydrophobic layer. The wafer with the coating was then oven dried at 200 ^oC for one hour. Additional CYTOP was manually brushed on one side of the spin-coated layer to create an area of a thicker CYTOP layer. After that, the wafer was cured at 250 ^oC for 24 hours.

Because the length scale of the contact area is much larger than that of the thicknesses of the dielectric materials, the droplet-based capacitor can be reasonably modeled as a parallel-plate capacitor. The effect of the thickness difference of the CYTOP layers on the electric output is shown in Figure 3.22. The results correspond to the devices with fixed source capacitors. Both the silicon dioxide layer and the thinner layer of CYTOP have been assumed to be 200 nm thick. It is seen that the effective growth rate γ_r increases monotonically and converges as the thickness ratio increases. A smaller capacitance of the source capacitor (i.e. larger β) leads to a larger limit value of γ_r with a lower converging rate. Therefore, it may not be practical to achieve the limit values corresponding to very low source capacitance. For example, if the capacitance of the source

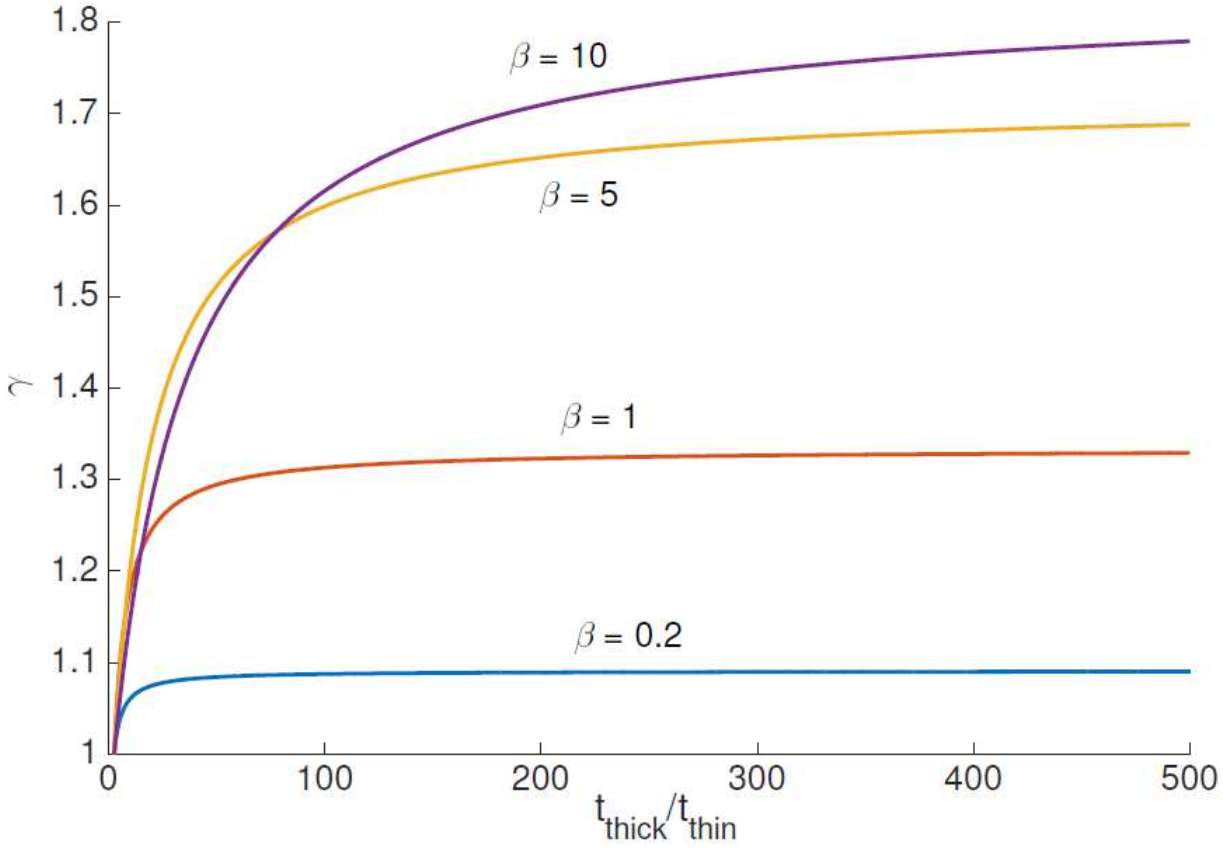

Figure 3.22: Effect of thickness difference of CYTOP layers. t_{tk} and t_{tn} represent the thicknesses of the thicker and the thinner CYTOP layers, respectively.

capacitor is one-tenth that of the droplet capacitor when the drop is on the thinner side, i.e. $\beta = 10$, it will require a thickness difference larger than 5000 times to achieve the limit $\gamma_r = 1.833$. In this experiments, the thicknesses of thinner and thicker CYTOP coatings are about 200 nm and $3\mu m$, respectively.

As a movable electrode, liquid metal is currently the best option so far. Its high surface tension leads to less charge trapping. In room temperature, Hg and Galinstan alloy are the only common metal that remain liquid state. However, they both present problems. Hg is toxic and Galinstan is easy to oxidize in the presence of oxygen. Other than electrons as charge carriers, electrolytes are considered as the other option, which will be discussed in the next section. The size of the liquid drops also affects the amount of electrical energy harvested. A larger liquid drop creates a larger contact area that leads to a higher capacitance. However, there will be no size

effect on the base of the exponential growth of the charge in the system or the voltages across the capacitors if the maximum and minimum capacitance of each sink capacitor are fixed. While it may be favorable to use larger drops because more charge will be collected due to higher capacitance, the largest size of the drops is limited by the physical constraints of the device and ultimately by the surface energy of the liquid. For capacitors in which a mercury drop of 150 μL was used, the maximum and the minimum capacitance was 2.74 nF and 0.27 nF, respectively. The parasitic capacitance was approximately 0.40 nF to represent surface charge trapping. Measurements were obtained using a Tektronix© electrometer 6517B or Tektronix© DMM 4050.

3.3.5 Experimental data and results

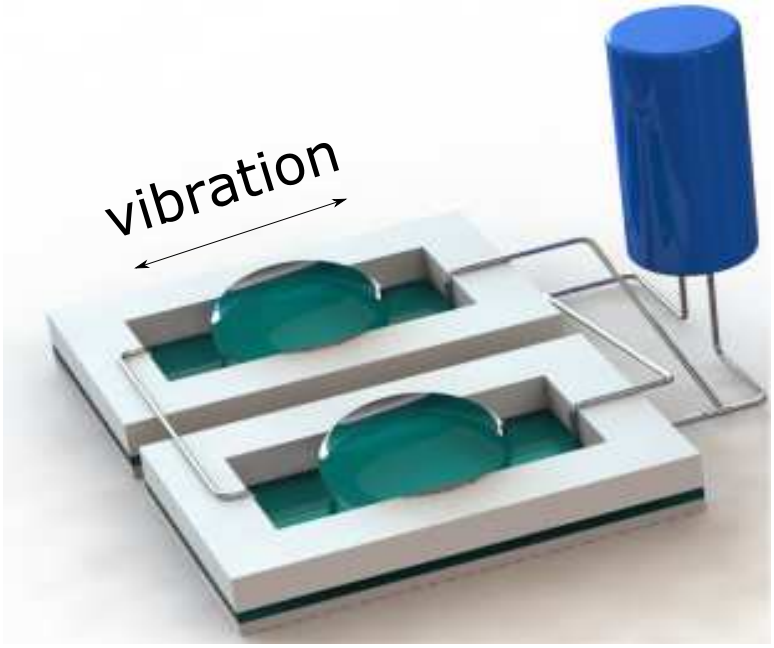

Figure 3.23: A three-dimensional rendered model of the device.

One of the simplest self-excited systems is to utilize two contact variable capacitors as sink capacitors and one commercial ceramic capacitor as source capacitor. Figure 3.23 shows a 3D rendered model of the device according to the circuit diagram as shown in Figure 3.5. Metal contacts are used to achieve the functions of switches in Figure 3.5. When there is vibration, liquid drops are driven back and forth to generate electricity, which will be transferred into the

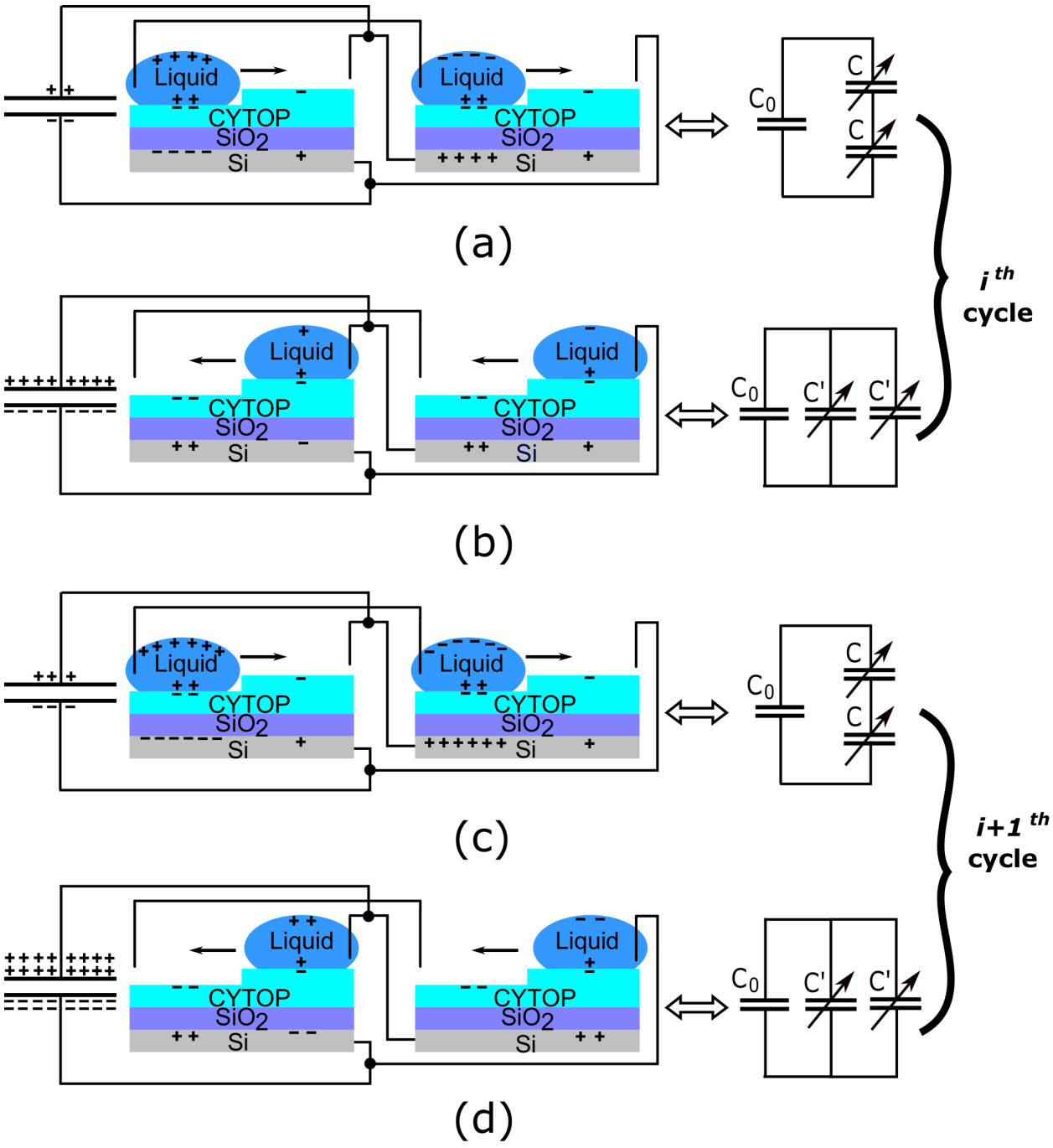

Figure 3.24: Working principle of the device with two contact variable capacitors and one commercial capacitor. **(a)** Liquid drops on the thinner side of the amorphous fluoropolymer (CYTOP) coating with the maximum sink capacitance. Sink capacitors are connected in series. **(b)** Drops on thicker side with the minimum sink capacitance. Sink capacitors connected in parallel. **(c)** Drops back to the thinner side again ($i + 1^{th}$ cycle) with increased charge. **(d)** Drops to thicker side again ($i + 1^{th}$ cycle) with more charge flowing to the source capacitor.

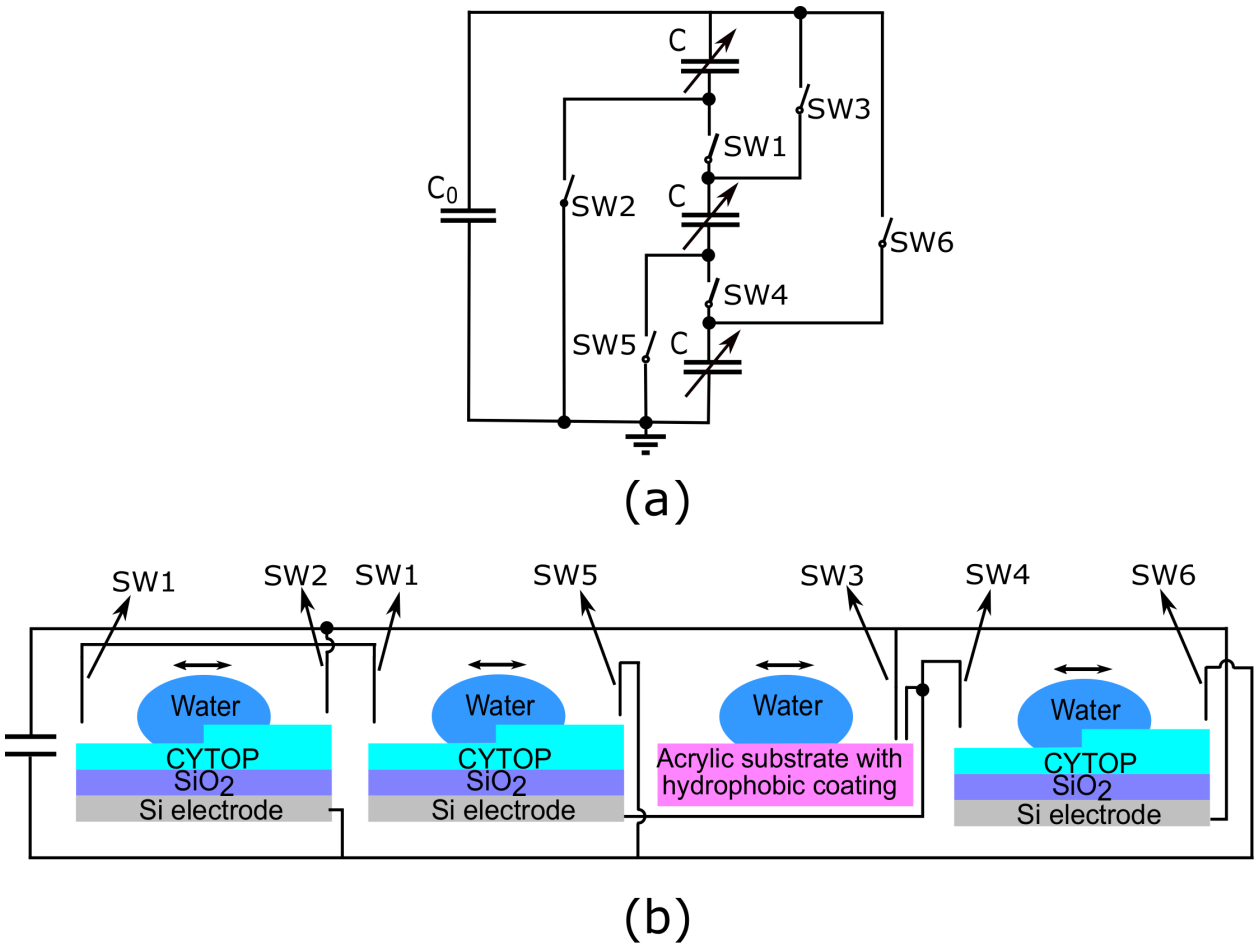

Figure 3.25: Schematic diagrams of a device with three sink capacitors. **(a)** The equivalent circuit diagram. **(b)** A device with three sink capacitors.

source capacitor. A commercial ceramic capacitor is used here as the source capacitor for simplicity. The working principle of the system is illustrated in Figure 3.24. When a free-standing conductive liquid drop is placed on the surface, a variable capacitor is formed. The drop and the doped silicon substrate function as the electrodes of the capacitor. The capacitance will change if the drop moves across the junction because of the thickness variation. Metal contacts that do not chemically interact with the drops are used at both sides as passive switches to facilitate the connectivity required for the reconfigurations. When both drops touch the metal contacts on the thinner side of the CYTOP coating, the device enters the duplicative state as shown in Figure 3.24**(a)**, which corresponds to closing SW1 while keeping SW2 and SW3 open in the equivalent circuit as shown in Figure 3.5. Charge begins to flow from the source capacitor to the sink

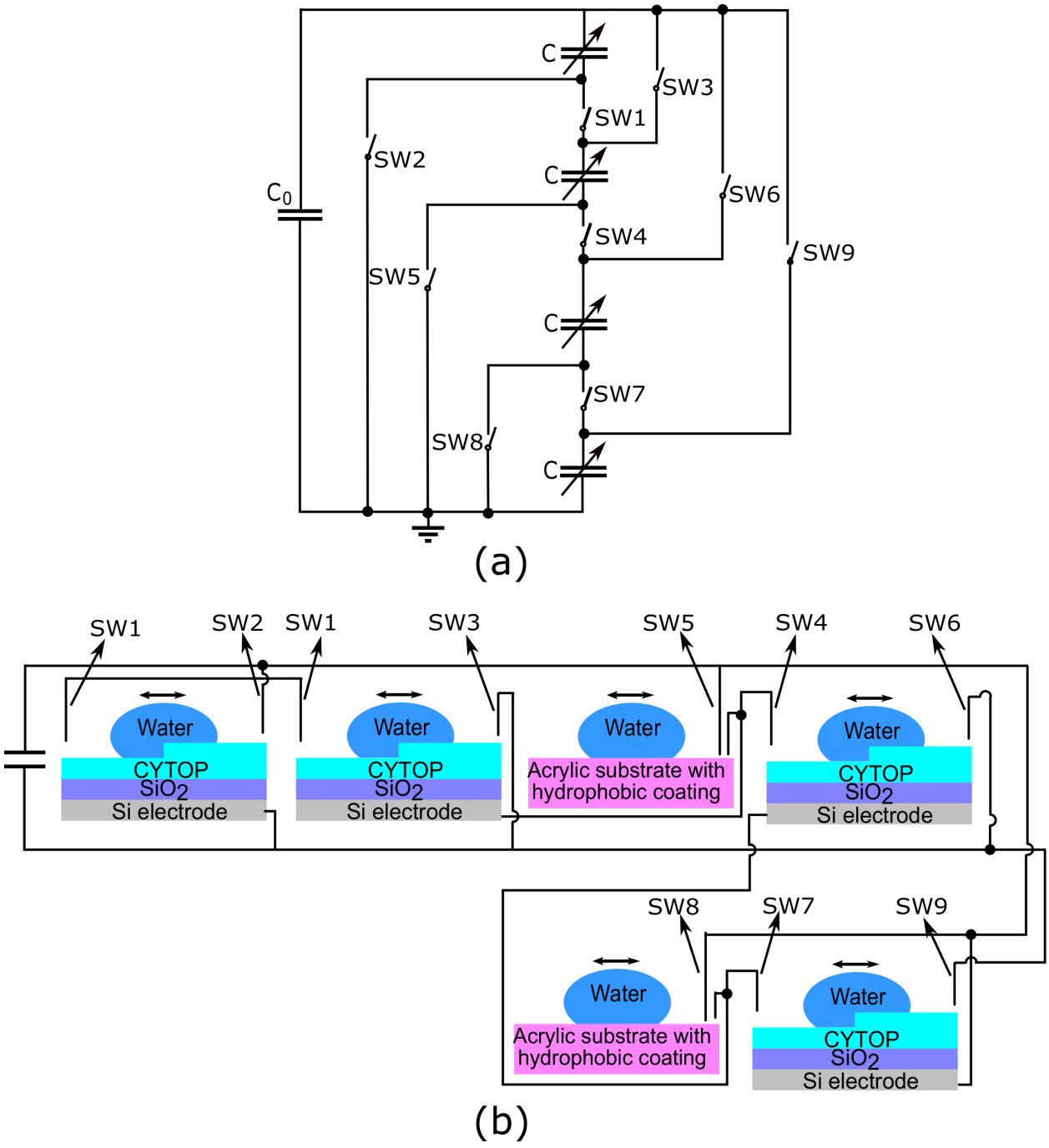

Figure 3.26: Schematic diagrams of a device with four sink capacitors. **(a)** The equivalent circuit diagram. **(b)** A device with four sink capacitors.

capacitors. The drops then move to the thicker side so that the device enters the distributive state as shown in Figure 3.24**(b)**, which corresponds to opening SW1 while closing SW2 and SW3 in Figure 3.5. Charge then flows back to the source capacitor due to the reduction of sink

capacitance. If the capacitance variation satisfies the positive feedback condition described in equation 3.22, the subsequent motion of the drops between the thinner side (Figure 3.24**(c)**) and the thicker side (Figure 3.24**(d)**) will create geometric growth of total charge in the system. If the surface charge densities for each capacitor are identical as shown in Figure 3.24, then no extra charge is given for each cycle since the net charge due to electrostatic induction cancels each other. In reality, there is variation of surface charge densities for each fabricated capacitor even though the process is exactly same. The net charge for each capacitor can be expressed by equation 3.9. For a given number of capacitors, the average extra charge for each cycle is expressed as $\bar{Q}_c = \frac{1}{n}\sum_{j=1}^{n} Q_c(j)$. There is an optimal number of sink capacitors to make the base of the exponential growth greatest if n follows equation 3.40. Additional liquid drops have been used in this study as passive switches to facilitate the connectivity required by three or more sink capacitors. In the experiments, two, three and four sink capacitors are used respectively to find the optimal number of sink capacitors. Figure 3.25 illustrates the schematic diagrams of a system with three sink capacitors. The equivalent circuit diagram is shown in Figure 3.25**(a)**. Six passive switches are needed for the connectivity of the reconfigurations. In order to achieve those switches, metal contacts on each side of the device are deployed as well as one additional switching device. The motion of the additional conductive liquid drop is synchronized with those of the sink capacitors so that six passive switches can be realized. Figure 3.26 shows the schematic diagrams of a system with four sink capacitors. Nine passive switches are needed to achieve the connectivity of reconfigurations using four sink capacitors. The corresponding metal contacts are deployed on Figure 3.26**(b)**. It is also noted that the equivalent circuits shown in Figures 3.5, 3.25, and 3.26 are only capacitors. In reality, the parasitic resistance should also be considered. However, the effect of resistance can be ignored when the frequency of switching is low compared to the time constants of the RC circuits so that the equilibrium state of each configuration is established before subsequent switching. Therefore, the conductivity of the liquid drops does not affect the base of the exponential growth of the electric output in low-frequency

applications, which implies that mechanism depends only on the position of the drops, and thus, the speed of the drops does not affect the electric output.

In the experiments, various numbers of mercury-drop contact variable capacitors are used as the sink capacitors while one commercial ceramic capacitor with constant capacitance is used as the source capacitor. Each sink capacitor uses 150 μL mercury droplet. The maximum and minimum capacitance of each sink capacitor is determined, which is 2.74 nF and 0.27 nF, respectively. The parasitic capacitance due to surface charge trapping was approximately 0.40 nF. According to equation 3.17, the source capacitance and the number of sink capacitors are still unknown. In the experiments, a variety of numbers of sink capacitors and different values of source capacitance have been used to find out the maximum effective growth rate γ_r. The equation 3.22 can be used to check whether the system satisfies the positive-feedback condition. The maximum number of sink capacitors used in the experiments is four. Substituting $n = 4$ into the equation 3.22, $\alpha\beta = 10.15 > n/(1-\delta) = 4.68$. Therefore, the system using four mercury-drop contact variable capacitors satisfies the positive-feedback condition. According to equations 3.44, 3.46, and 3.47, the effective growth rate γ_r has the maximum value when $\alpha = \beta = \sqrt{C/C'} = 3.186$ and $n = ||3.001|| = 3$. Substituting the above numbers into equation 3.42, the maximum growth rate is given as $\gamma_r = 1.296$. Therefore, according to equations 3.44, 3.46, and 3.47, the growth rate γ_r has the theoretical maximum value 1.296 when $\alpha = \beta = 3.186$ and $n = 3$. At this state, the optimal source capacitance is $C_0 = 0.86\ nF$. Under the same source capacitance, the system with two mercury contact variable capacitors has the maximum effective growth rate of 1.248 while the system with four mercury contact variable capacitors has the maximum effective growth rate of 1.271.

In order to prove the aforementioned theory, a variety of experiments has been done with different numbers of sink capacitors and various values of source capacitance. Four different values of source capacitance were used in the experiments: 0.32 nF, 0.94 nF, 5.32 nF, and 10.12 nF. The devices were manually rocked at a frequency of approximately 0.25 Hz and the tilting angle was within $\pm 5^o$ so that the mercury drops were synchronously driven to touch the

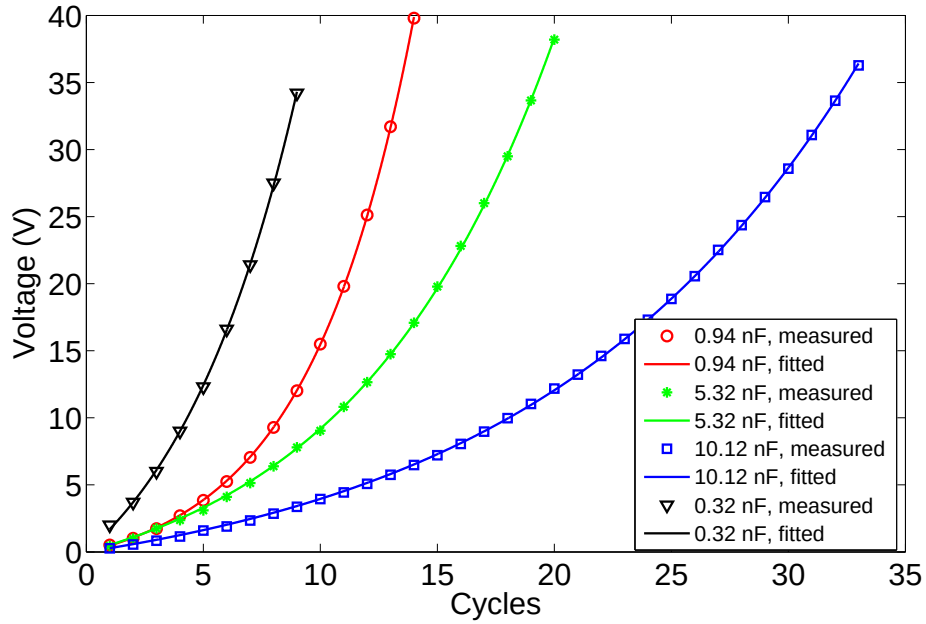

Figure 3.27: The voltages of different source capacitance versus cycles by using two 150 μL mercury-drop variable capacitors.

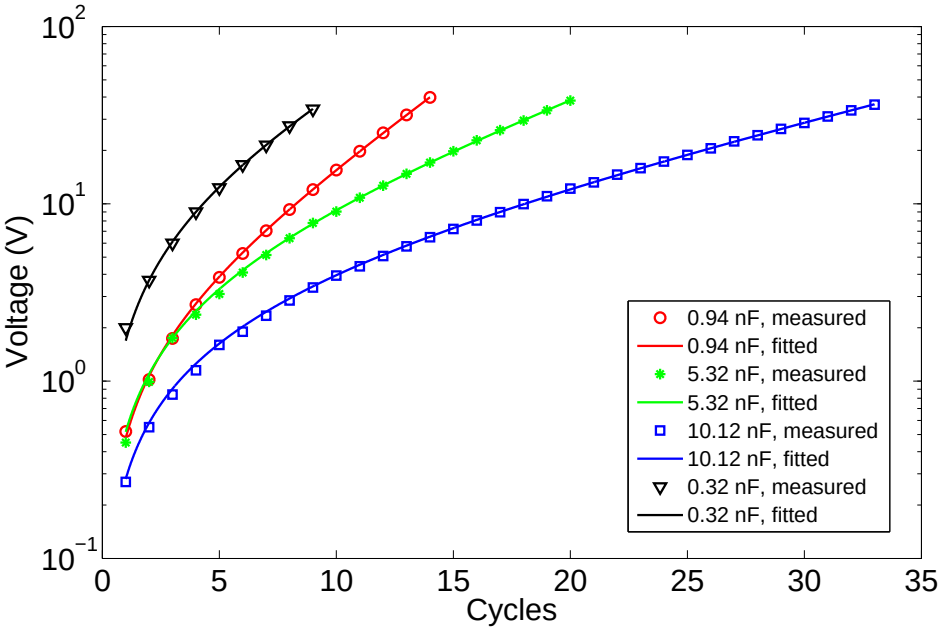

Figure 3.28: Logarithmic scale of the voltages of different source capacitance versus cycles by using two 150 μL mercury-drop variable capacitors.

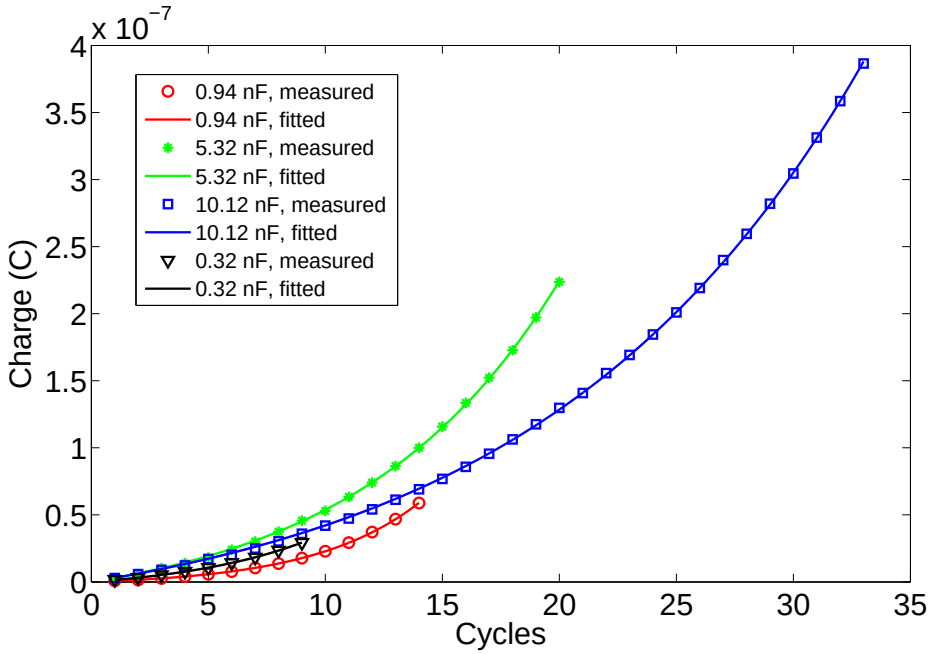

Figure 3.29: The charges of different source capacitance versus cycles by using two 150 μL mercury-drop variable capacitors.

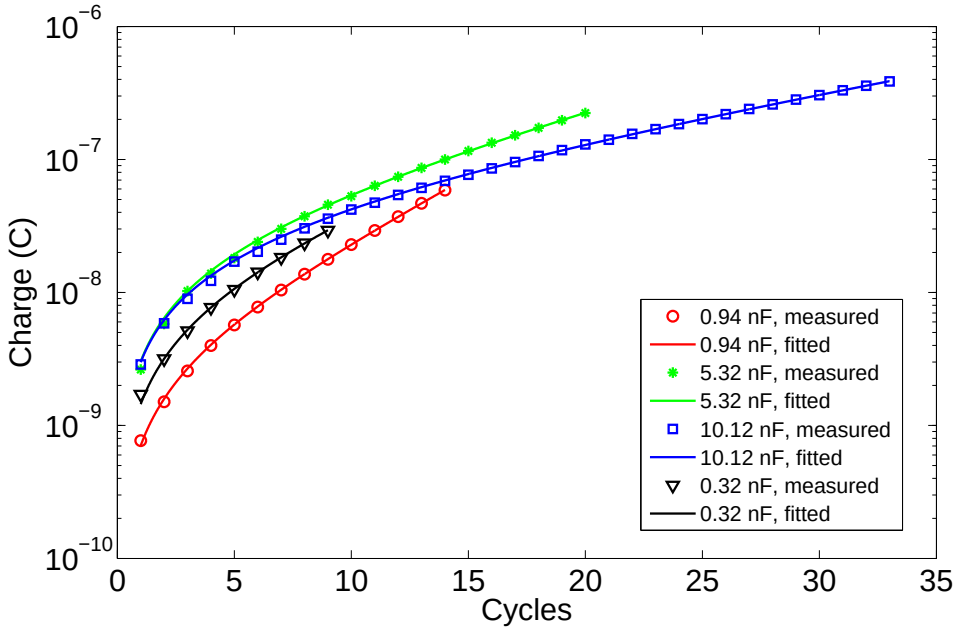

Figure 3.30: Logarithmic scale of the charges of different source capacitance versus cycles by using two 150 μL mercury-drop variable capacitors.

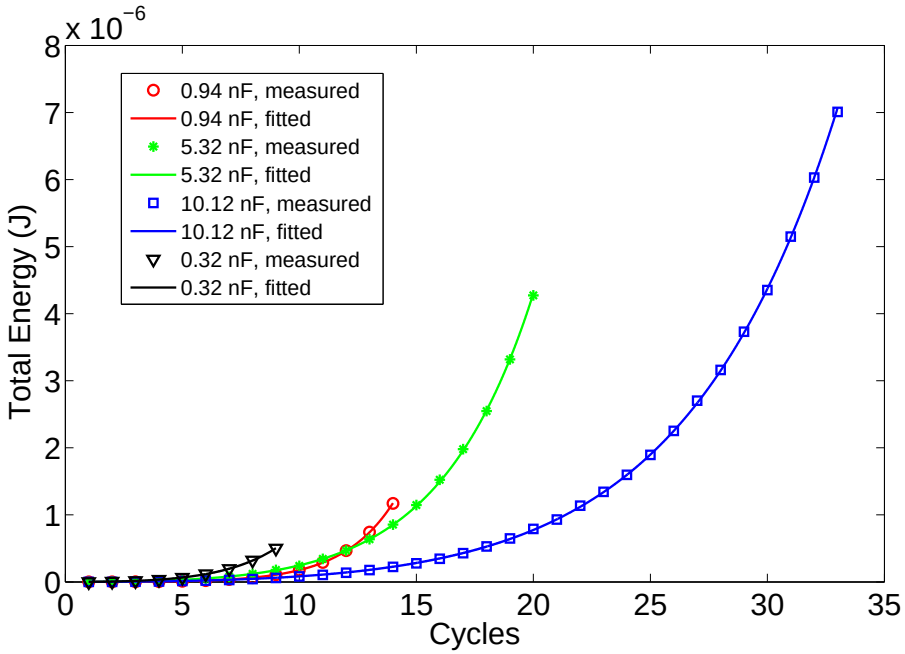

Figure 3.31: The total energy of the system with different source capacitance versus cycles by using two 150 μL mercury-drop variable capacitors.

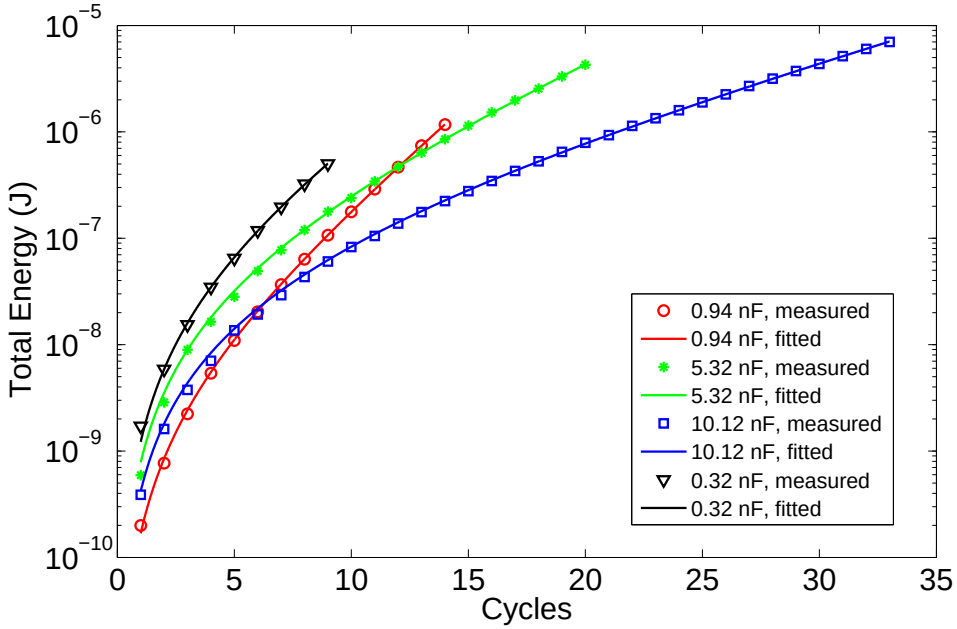

Figure 3.32: Logarithmic scale of the total energy of the system with different source capacitance versus cycles by using two 150 μL mercury-drop variable capacitors.

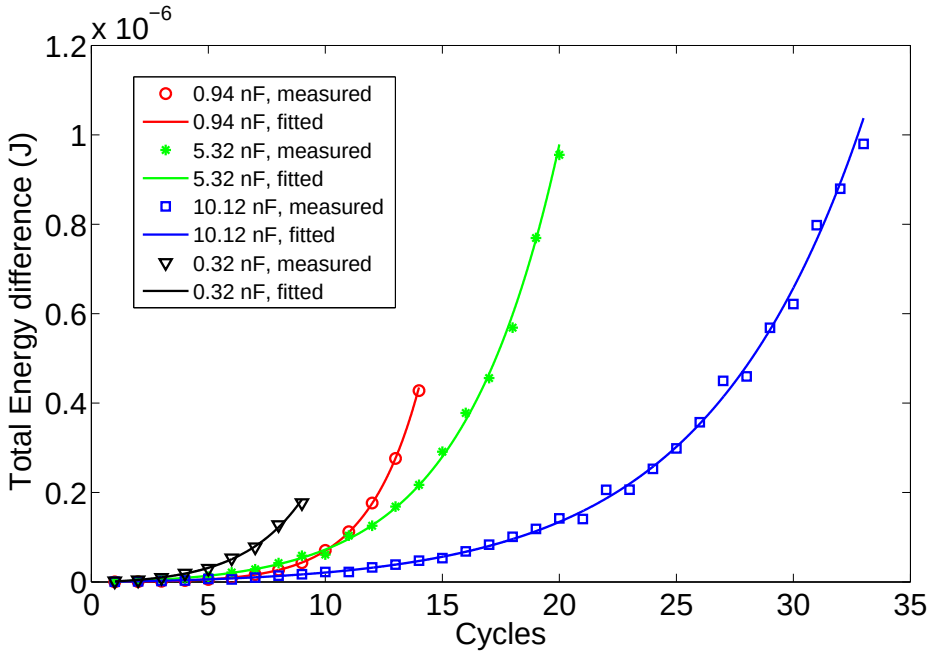

Figure 3.33: The total energy difference of the system with different source capacitance versus cycles by using two 150 μL mercury-drop variable capacitors.

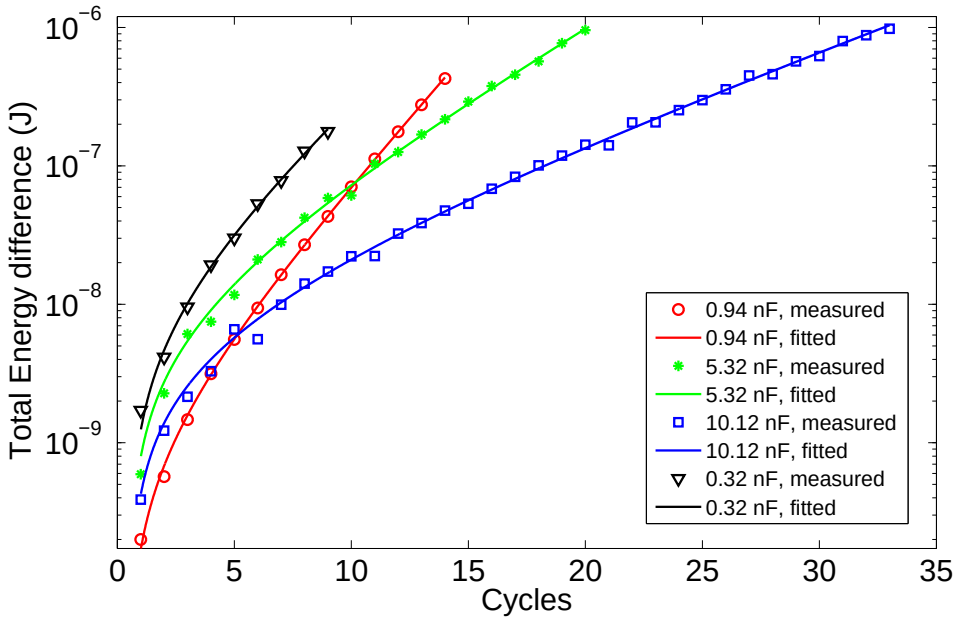

Figure 3.34: Logarithmic scale of the total energy of the system with different source capacitance versus cycles by using two 150 μL mercury-drop variable capacitors.

metal contacts. Keithley electrometer 6517B is used to measure the voltages of the source capacitor. Because the devices generate sufficiently high charge, the charge leakage can be negligible. Unlike the system using two rotary variable capacitors, the measurements can be read continuously in each distributive state. Figures 3.27-3.34 illustrate the electric outputs of the positive-feedback system using two 150 μL mercury-drop variable capacitors as sink capacitors and one constant-capacitance capacitor as the source capacitor. Figure 3.27 shows the relationships between the voltage of the source capacitor and cycles. In this figure, the voltages of all four systems grow exponentially. Among them, it is clear that the voltages for 10.12 nF and 5.32nF source capacitance grow slowest and secondly slowest, respectively. Meanwhile, the voltages for 0.94 nF and 0.32 nF source capacitance do not show significant differences. In order to show the growth rate more clearly, Figure 3.28 shows the logarithmic scale of the voltage for the source capacitor versus linear scale of cycles. The slope of each line represents the total increasing rate, which is the ratio between logarithm voltages and cycles. The increasing rate includes both the factor from extra charge effect due to contact electrification and electrostatic induction and the factor from positive-feedback mechanism. It is noted that the effective growth rate γ_r only represents the factor from the positive-feedback mechanism. According to equation 3.34, from Figure 3.28, it is seen that the slope for the device with 0.94 nF source capacitance is slightly higher than that with 0.32 nF, which will be also proved by the fitted parameters. Equation 3.33 is used to fit the effective growth rate γ_{rf} and the equivalent voltage due to extra charge V_{eq2}. Based on the capacitance measurements, equation 3.37 can be used to estimate the theoretical effective growth rates γ_{rt} as shown in Table 3.2. The results show the fitted effective growth rates are in the small difference with the theoretical effective growth rates. It also shows the device with 0.94 nF has the maximum effective growth rate. According to equation 3.34, the increasing rate at the first cycles is usually higher than that at the later cycles because of extra charge effect from contact electrification and electrostatic induction. At the first cycles, the voltage is relatively small, which limits the effects of positive-feedback mechanism. Therefore. the extra charge effect dominates the increasing rate. At the latter cycles, the charge accumulates

and remains high. The effect of the positive-feedback mechanism takes charge compared to extra charge effect, which can be proven by equation 3.34. At the first cycles, $Log\bar{V}_{eq2}$ is much higher than $Log(\gamma_r^i - 1)$. When the voltage accumulates to a high level, $Log(\gamma_r^i - 1)$ becomes high and $Log\bar{V}_{eq2}$ can be negligible.

C_0 (nF)	**Fitted** V_{eq2} (V)	**Fitted** γ_{rf}	**Theoretical** γ_{rt}	**Difference between** γ_{rf} **and** γ_{rt}
0.32	8.683	1.195	1.198	-0.25%
0.94	1.951	1.245	1.247	-0.16%
5.32	4.226	1.122	1.122	0%
10.12	3.778	1.074	1.074	0%

Table 3.1: The fitted equivalent voltage V_{eq2}, effective growth rates γ_{rf} and theoretical effective growth rates γ_{rt} using two 150 μL mercury-drop variable capacitors.

Figure 3.29 shows the charges of the system versus cycles while Figure 3.30 shows the logarithmic scale of the charges versus the linear scale of cycles. Figure 3.29 shows that the charge for all four devices grows exponentially. In Figure 3.30, the increasing rate with 0.94 nF source capacitance is the highest. It is noted that a higher initial charge leads to a higher increasing rate in the first cycles. According to equation 3.35, Figures 3.31 and 3.32 show the total energy of the system with different value of source capacitance versus cycles and its logarithmic scale, respectively. The total energy of all the four devices grows exponentially, and the total energy with 0.94 nF source capacitance increases fastest. After 14 cycles, the stored energy with 0.94 nF source capacitance can reach 1.17 μJ from zero. When the voltage control circuit is used as shown in Figure 2.7, the increased stored energy in the system can be extracted while part of the stored energy can be remained in the system to provide initial charge. According to equation 3.36, Figures 3.33 and 3.34 show the total energy difference of the system with different values of source capacitance versus cycles and its logarithmic scale, respectively. Similarly, the total energy difference of each device grows exponentially and the device with 0.94 nF has the maximum increasing rate. Among this state, 0.43 μJ can be released in the 14^{th} cycle. If Figure 2.7 is used to maintain the voltage to that of 14^{th} cycle, 0.43 μJ can be extracted in each cycle. The corresponding power is 2.2 μW if the 5 Hz vibration is applied, which is sufficient to

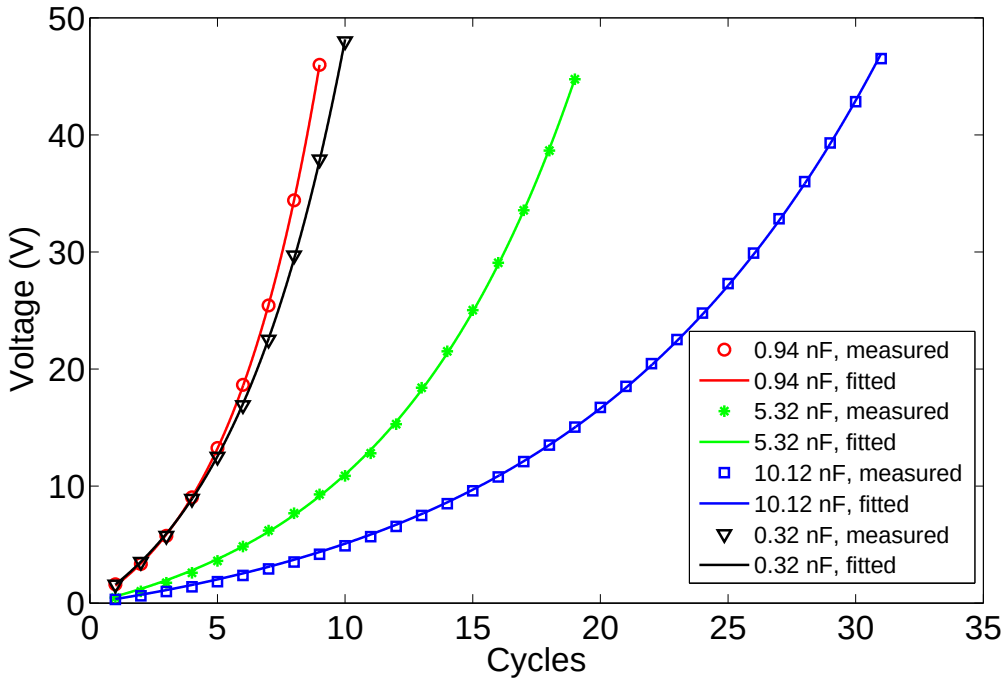

Figure 3.35: The voltages of different values of source capacitance versus cycles by using three 150 μL mercury-drop variable capacitors.

power many MEMS sensors. In summary, two 150 μL mercury-contact variable capacitors as sink capacitors and one constant-capacitance ceramic capacitor as source capacitor are utilized in the system to establish the positive-feedback mechanism. In the experiments, the voltages of the source capacitor are measured by electrometer with four different values of source capacitance to find out the effective maximum growth rate. Among them, the electric outputs with 0.94 nF source capacitance has the maximum effective growth rate. Furthermore, the measured experimental data all agree with the theory very well.

Figures 3.35-3.42 illustrate the electric outputs of the system using three 150 μL mercury-drop variable capacitors as sink capacitors and one constant-capacitance ceramic capacitor as the source capacitor. Figure 3.35 and 3.36 show the voltages of the source capacitor versus cycles and its logarithm scale, respectively. Four different values of source capacitor were also used in the experiment. In Figure 3.35, the voltages of all four devices increase exponentially. Among them, it is clear that the voltages of the system with 0.94 nF source

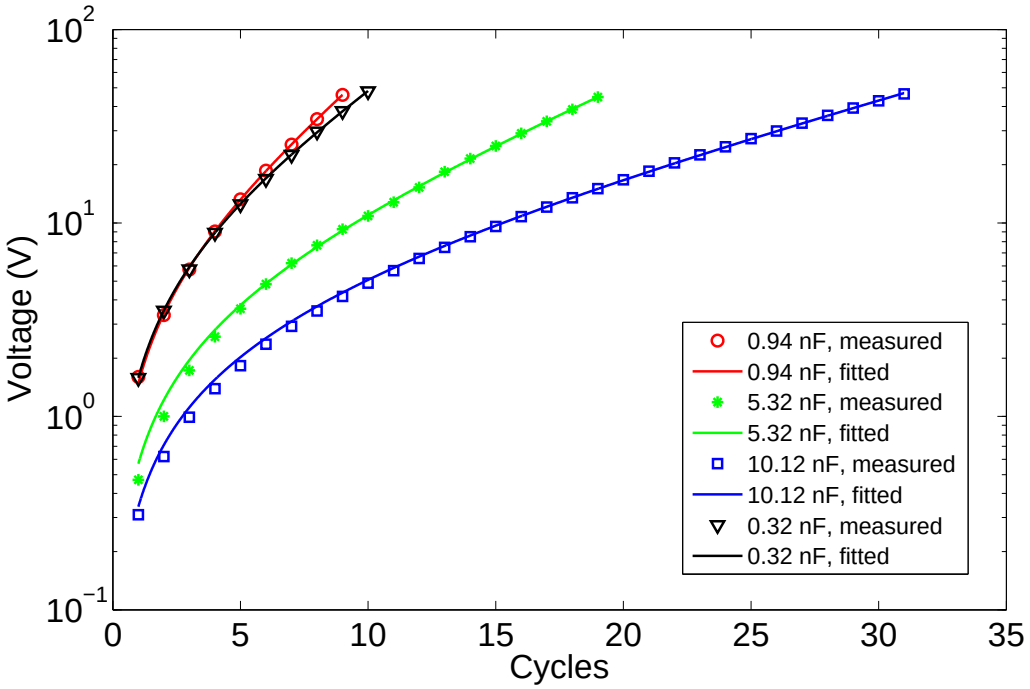

Figure 3.36: Logarithmic scale of the voltages of different values of source capacitance versus cycles by using three 150 μL mercury-drop variable capacitors.

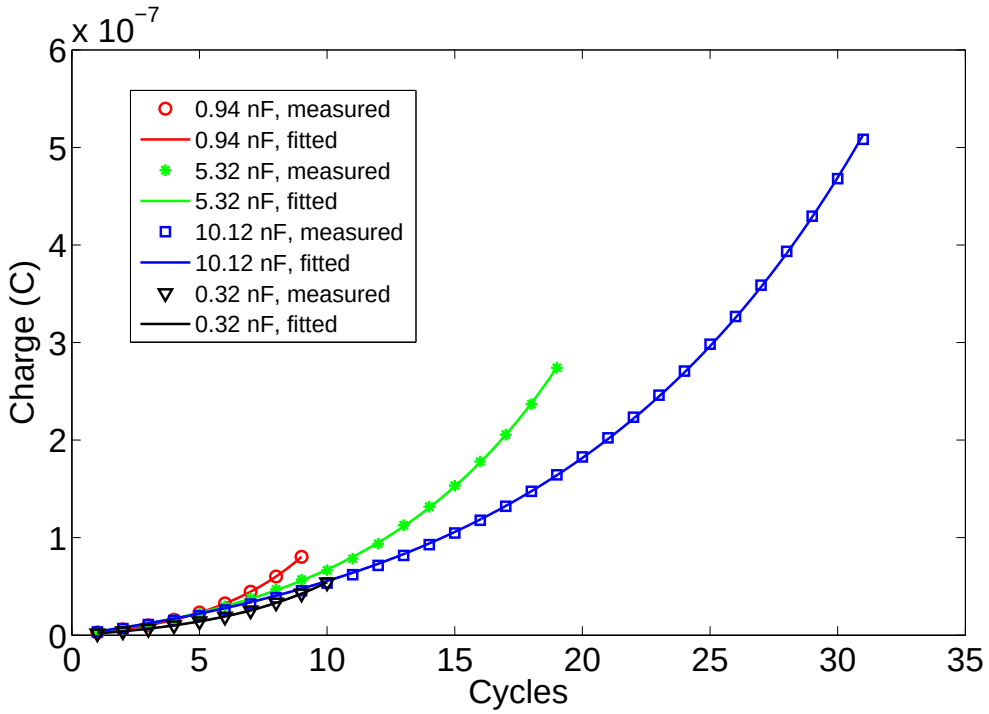

Figure 3.37: The charges of different values of source capacitance versus cycles by using three 150 μL mercury-drop variable capacitors.

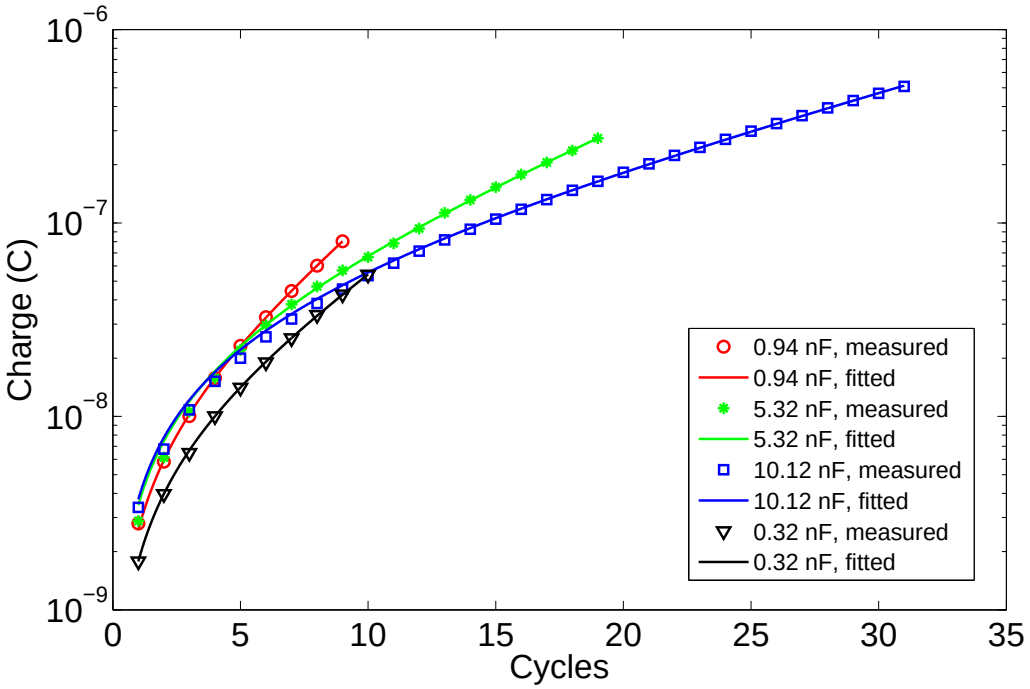

Figure 3.38: Logarithmic scale of the charges of different values of source capacitance versus cycles by using three 150 μL mercury-drop variable capacitors.

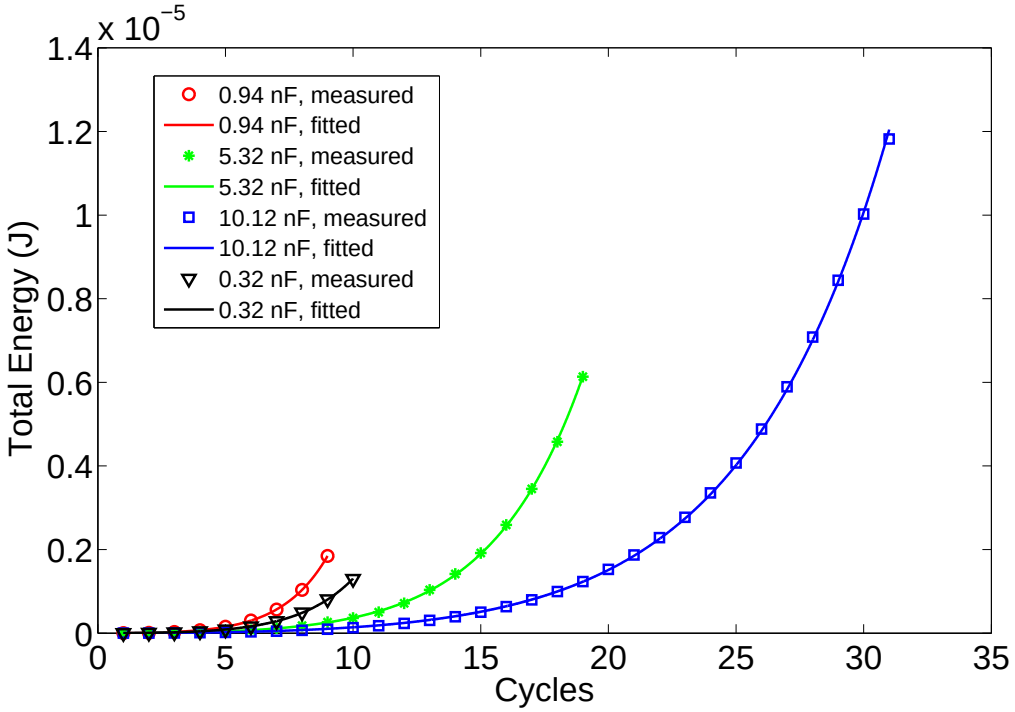

Figure 3.39: The total energy of the system with different values of source capacitance versus cycles by using three 150 μL mercury-drop variable capacitors.

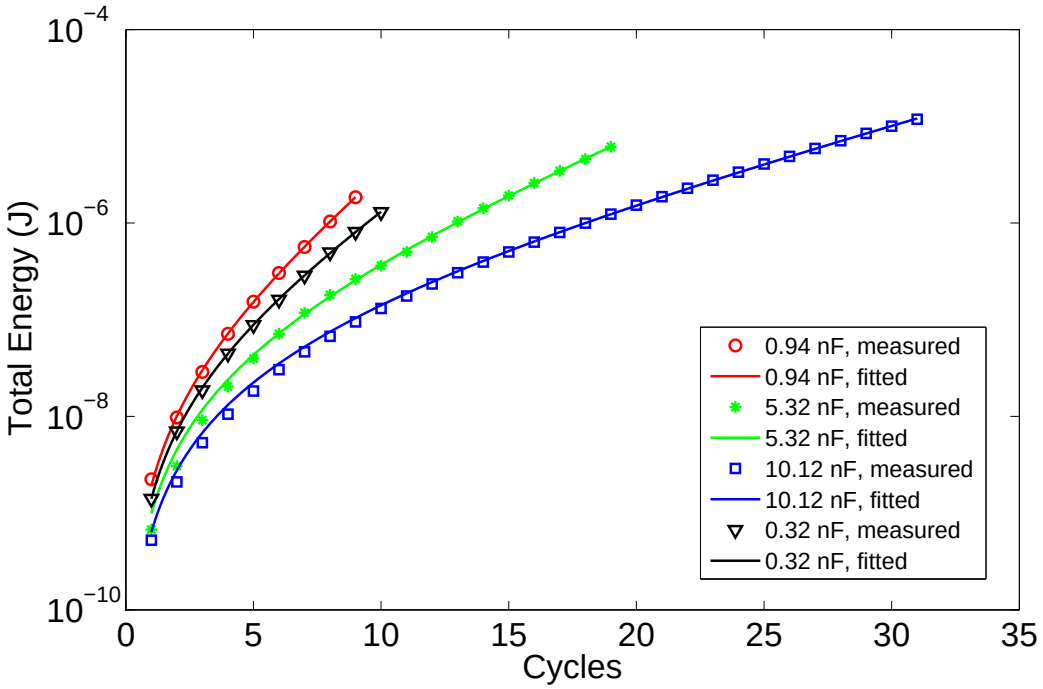

Figure 3.40: Logarithmic scale of the total energy of the system with different values of source capacitance versus cycles by using three 150 μL mercury-drop variable capacitors.

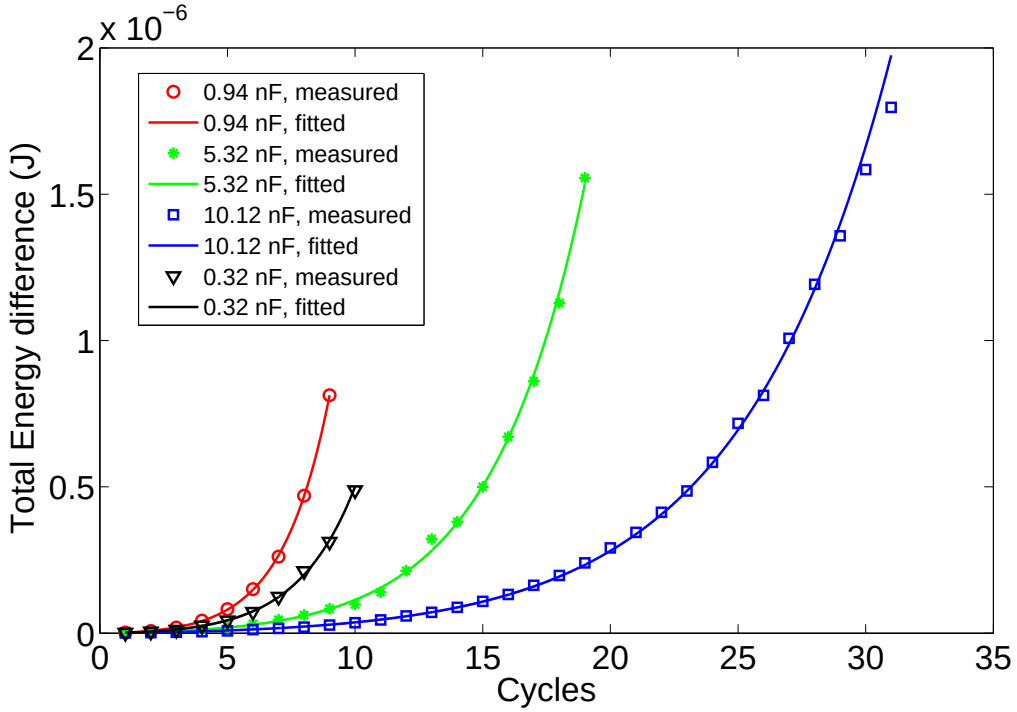

Figure 3.41: The total energy difference of the system with different values of source capacitance versus cycles by using three 150 μL mercury-drop variable capacitors.

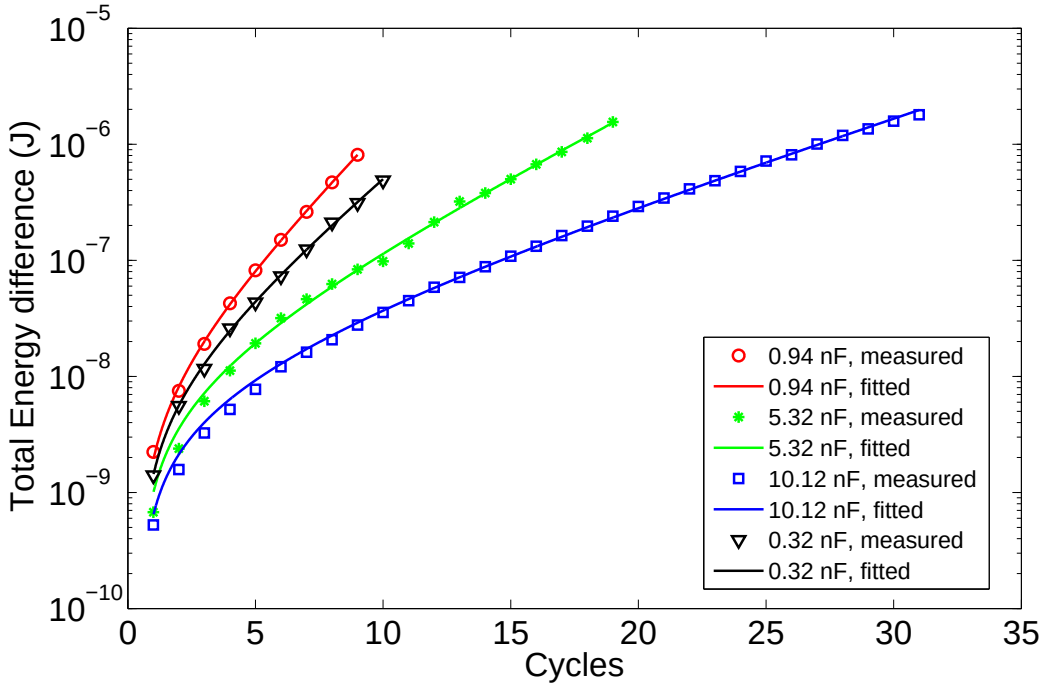

Figure 3.42: Logarithmic scale of the total energy difference of the system with different values of source capacitance versus cycles by using three 150 μL mercury-drop variable capacitors.

capacitance increases fastest. Three other systems have lower increasing rate despite the change of the source capacitance, which indicates the source capacitance has an optimal value to make the growth rate highest. According to equation 3.34, From Figure 3.28, it is seen that the slope of 0.94 nF source capacitance, is the highest one. Equation 3.33 can be used to fit the effective growth rate γ_{rf} and the equivalent voltage V_{eq2} while equation 3.37 can be used to estimate the theoretical effective growth rates γ_{rt}. The fitted and theoretical parameters are shown in Table 3.2. The results show the fitted effective growth rates have perfect match with the theoretical effective growth rates. Compared to the results in Table 3.2, it is known that each effective growth rate using three mercury drops is higher than that using two mercury drops, which indicates the system using three sink capacitors can grow faster than that using two sink capacitors.

According to equation 3.33, Figures 3.37 and 3.38 show the charges of different values of source capacitance versus cycles and its logarithmic scale, respectively. The charges of all four source capacitors grow exponentially. Figure 3.38 shows the effective growth rate with 0.94 nF

C_0 (nF)	**Fitted** V_{eq2} (V)	**Fitted** γ_{rf}	**Theoretical** γ_{rt}	**Difference between** γ_{rf} **and** γ_{rt}
0.32	6.810	1.232	1.234	-0.16%
0.94	5.047	1.293	1.296	-0.23%
5.32	4.068	1.140	1.142	-0.18%
10.12	3.980	1.086	1.086	0%

Table 3.2: The fitted equivalent voltage V_{eq2}, effective growth rates γ_{rf} and theoretical effective growth rates γ_{rt} using three 150 μL mercury-drop variable capacitors.

source capacitance is the highest among four devices. According to equation 3.35, Figures 3.39 and 3.40 show the total energy of the system with differentvalues of source capacitance versus cycles and its logarithmic scale, respectively. The total energy of all the four devices grows exponentially, and the total energy with 0.94 nF source capacitance increases fastest. Figure 3.41 and 3.42 show the total energy difference of the system with different values of source capacitance versus cycles and their logarithmic scales, respectively. Similarly, each total energy difference of each device grows exponentially and the device with 0.94 nF has the maximum growth rate. Similar to the system with two mercury drops, the electric outputs with 0.94 nF source capacitance has the maximum effective growth rate. However, the effective growth rate is higher under each same source capacitance. The electric outputs of the system using three mercury droplets grow faster than that using two mercury droplets. The measured experimental data all agree with the theory very well.

C_0 (nF)	**Fitted** V_{eq2} (V)	**Fitted** γ_{rf}	**Theoretical** γ_{rt}	**Difference between** γ_{rf} **and** γ_{rt}
0.32	26.221	1.210	1.215	-0.41%
0.94	23.200	1.267	1.270	-0.24%
5.32	25.222	1.120	1.131	-0.97%
10.12	23.505	1.072	1.079	-0.65%

Table 3.3: The fitted equivalent voltage V_{eq2}, effective growth rates γ_{rf} and theoretical effective growth rates γ_{rt} using four 150 μL mercury-drop variable capacitors.

Figures 3.43-3.50 illustrate the electric outputs of the system using four 150 μL mercury-drop variable capacitors as sink capacitors. It is known that the voltages of all four devices increase exponentially. Among them, the voltages of the system with 0.94 nF source

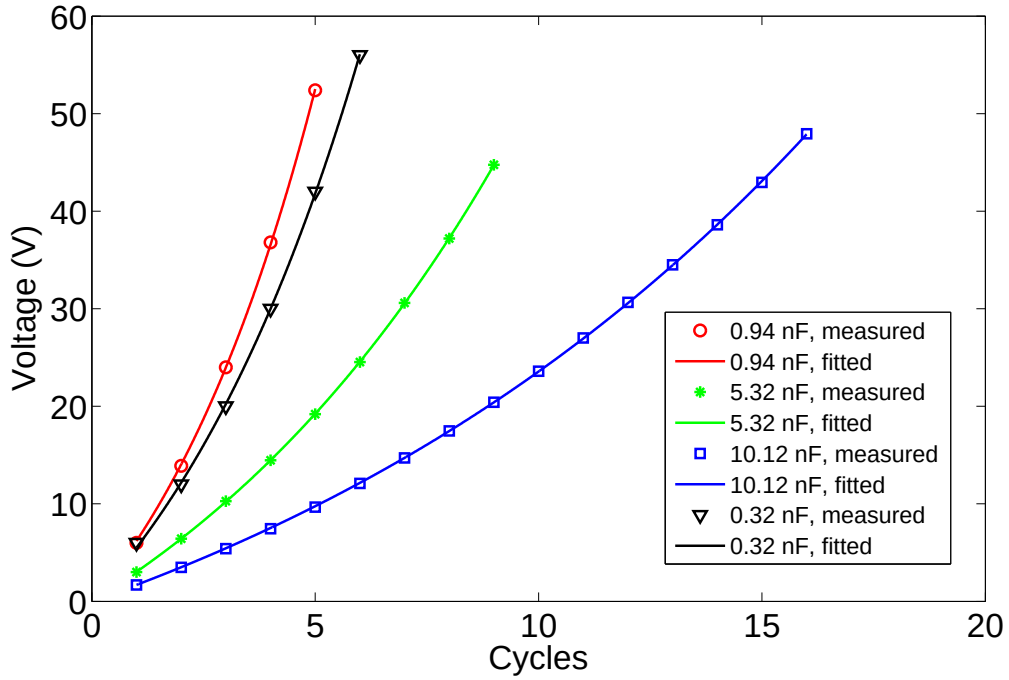

Figure 3.43: The voltages of different values of source capacitance versus cycles by using four 150 μL mercury-drop variable capacitors.

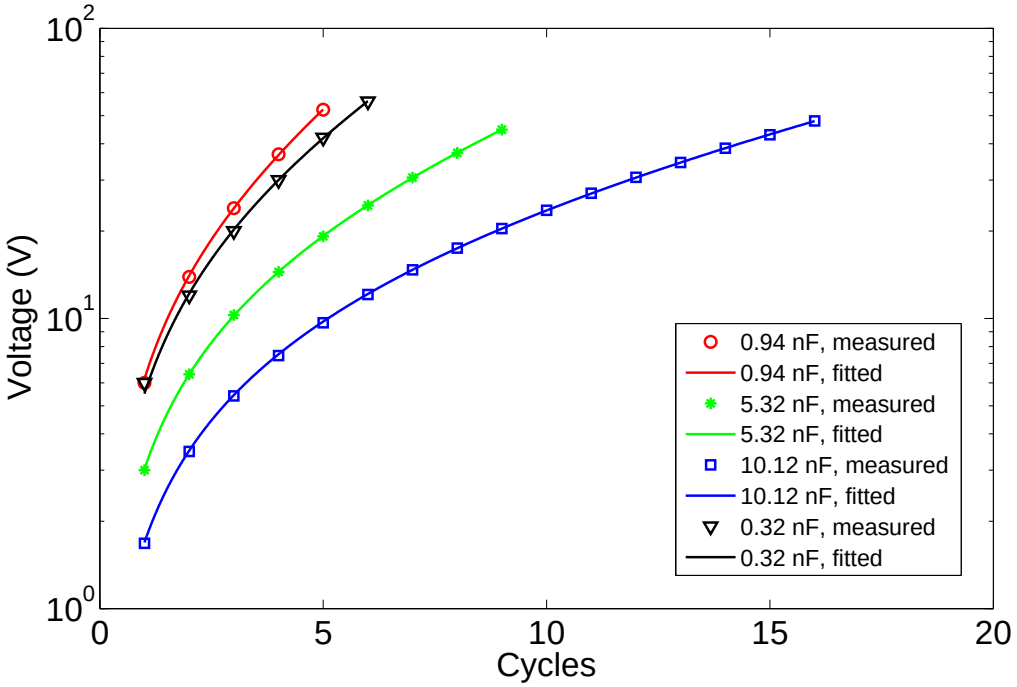

Figure 3.44: Logarithmic scale of the voltages of different values of source capacitance versus cycles by using four 150 μL mercury-drop variable capacitors.

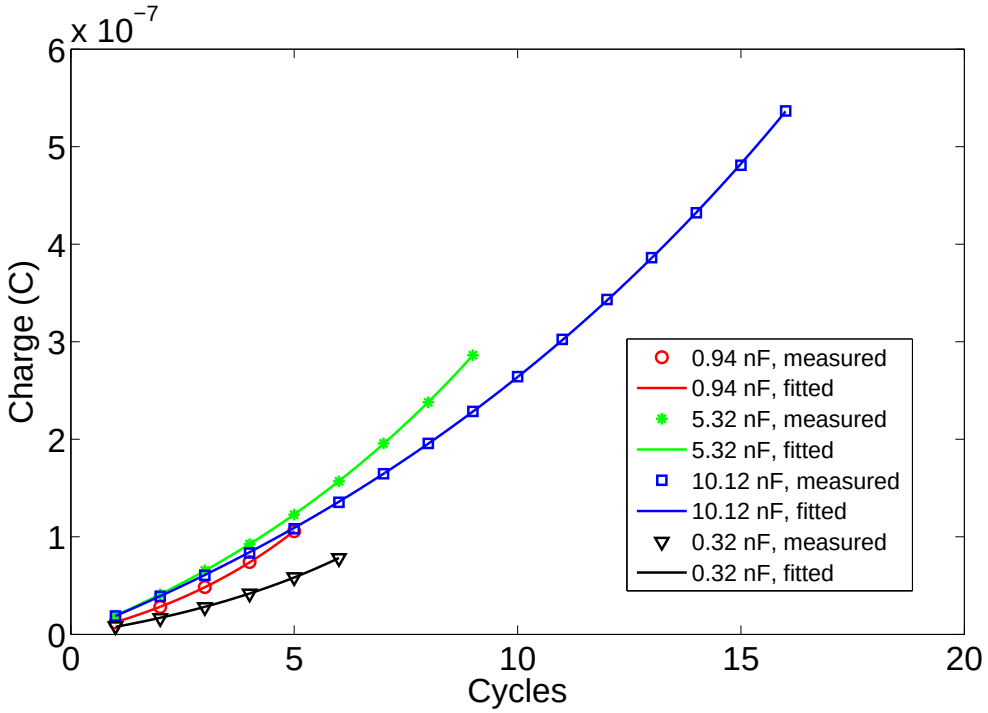

Figure 3.45: The charges of different values of source capacitance versus cycles by using four 150 μL mercury-drop variable capacitors.

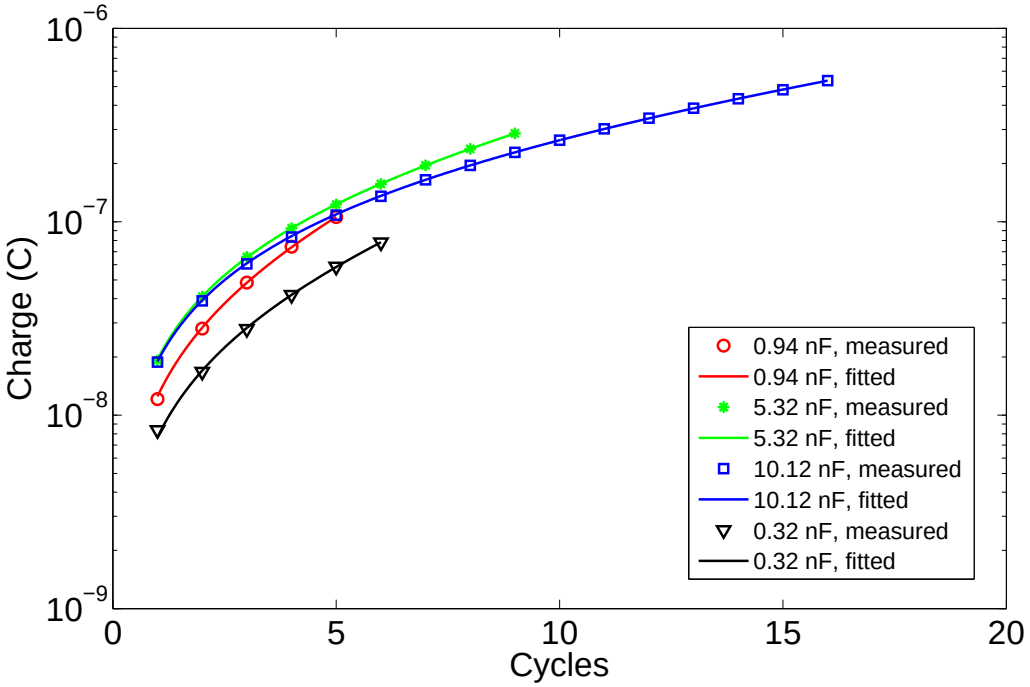

Figure 3.46: Logarithmic scale of the charges of different values of source capacitance versus cycles by using four 150 μL mercury-drop variable capacitors.

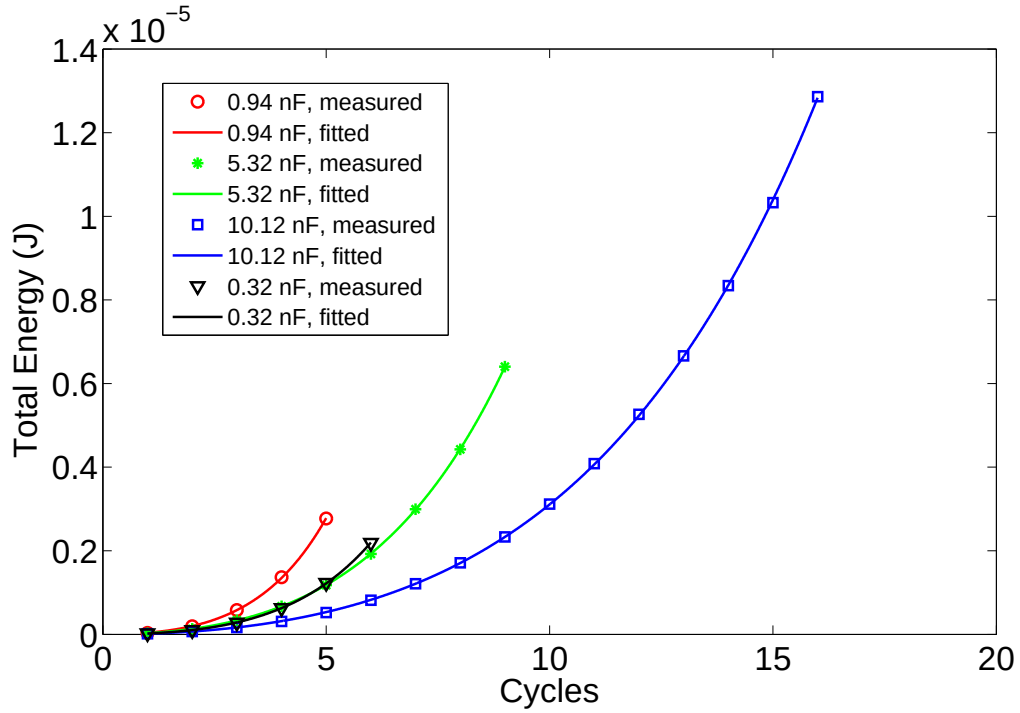

Figure 3.47: The total energy of the system with different values of source capacitance versus cycles by using four 150 μL mercury-drop variable capacitors.

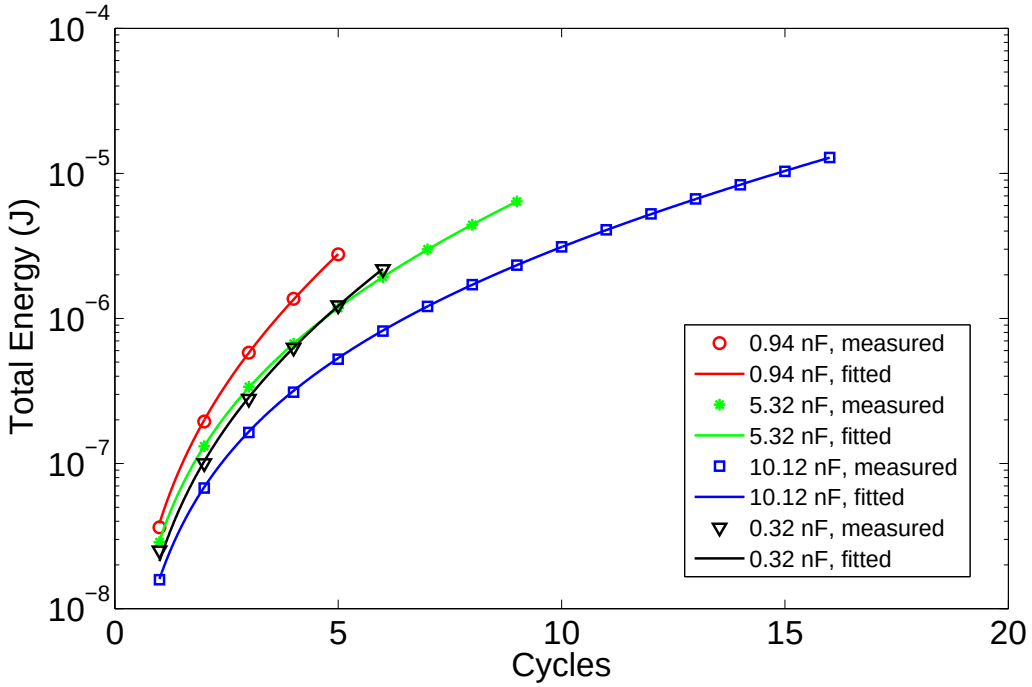

Figure 3.48: Logarithmic scale of the total energy of the system with different values of source capacitance versus cycles by using four 150 μL mercury-drop variable capacitors.

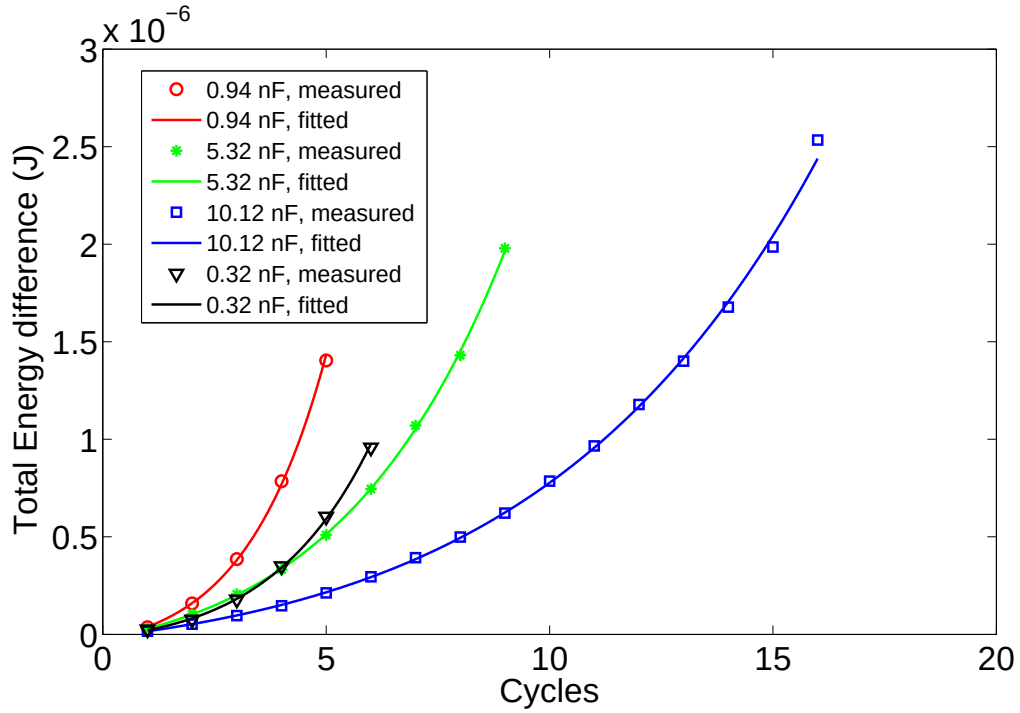

Figure 3.49: The total energy difference of the system with different values of source capacitance versus cycles by using four 150 μL mercury-drop variable capacitors.

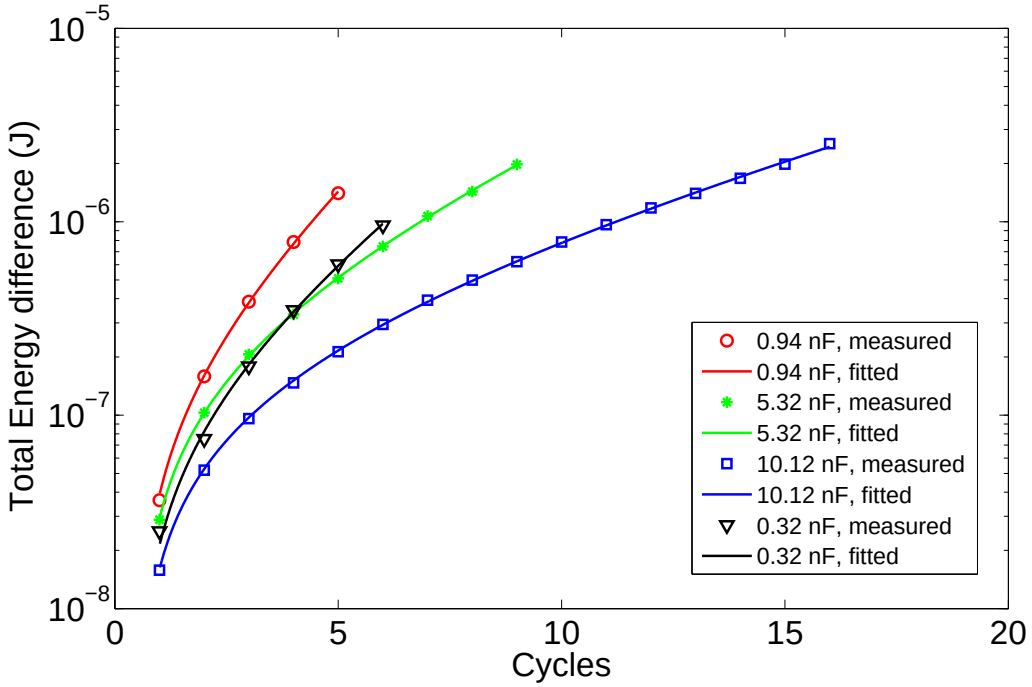

Figure 3.50: Logarithmic scale of the total energy difference of the system with different values of source capacitance versus cycles by using four 150 μL mercury-drop variable capacitors.

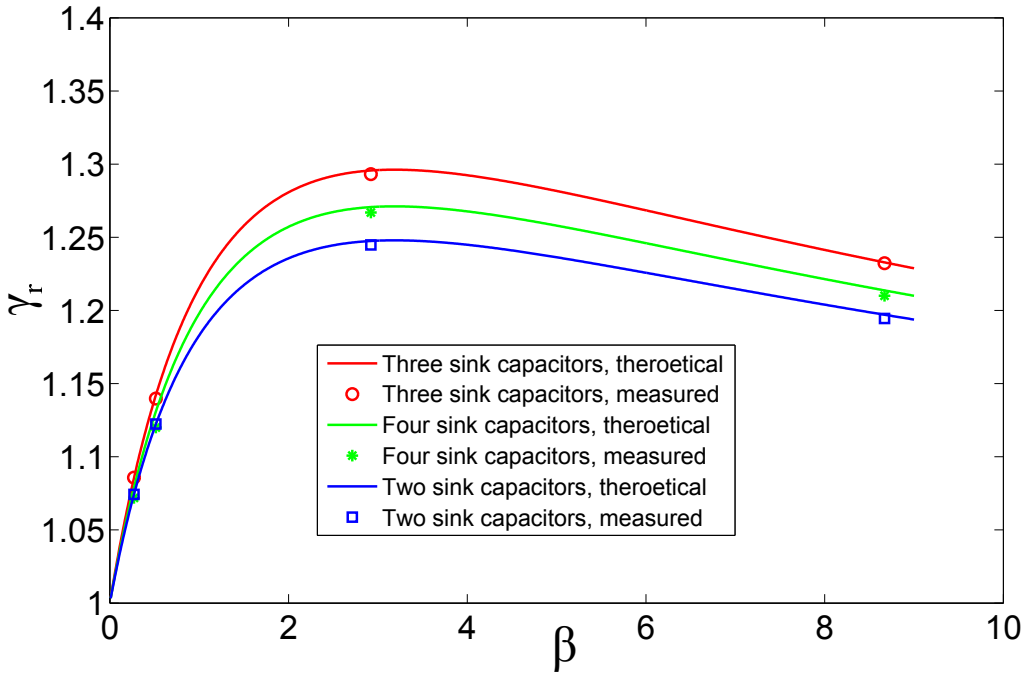

Figure 3.51: γ_r versus β using mercury-drop variable capacitors as sink capacitors.

capacitance increases fastest. The effective growth rate γ_{rf}, the equivalent voltage V_{eq2} and the theoretical effective growth rates γ_{rt} are shown in Table 3.3. The results show the fitted effective growth rates agree well with the theoretical effective growth rates. Compared to the results in Tables 3.1 and 3.2, under the same source capacitance, the effective growth rate of the systems using three mercury drops is the highest while this using four mercury drops is second highest. Figure 3.51 shows all the effective growth rates versus β. Equation 3.37 is used to calculate the theoretical data in the figure. According to equations 3.44, 3.46, and 3.47, based on the measured capacitance of C, C', and C_p, the maximum theoretical effective growth rate is 1.296 when $\alpha = \beta = 3.186$, $C_0 = 0.86\ nF$ and $n = 3$. Other than three mercury drops, the effective growth rates with two and four mercury drops are also shown in the figure. Three systems have the maximum effective growth rates at the same source capacitance $C_0 = 0.86\ nF$. Furthermore, the effective growth rates with four mercury drops are higher than these with two mercury drops under same β.

3.4 Water contact variable capacitors as sink capacitors

In the previous section, mercury droplets were used as movable conductors in the contact variable capacitors. Even though the surface charge trapping effect reduces the growth rate to some extent, high extra charge due to contact accelerates the increasing rates of the electric outputs especially at the first cycles. The experiment data also agree well with the theory. The systems generate relatively high power density to sufficiently power many MEMS sensors, and shows promising potentials for practical use. However, mercury is toxic and not environment friendly. Other alternatives need to be found to solve these issues. In this section, water droplets are used to explore the possibility of replacing liquid metals. The electric outputs of the system using water-droplet contact variable capacitors are illustrated in this section. Afterwards, two identical devices with identical size mercury and water droplets are then illustrated under 2.5 Hz vibration to compare their performance.

3.4.1 Design of water contact variable capacitors

In the experiments, it is found that the same type of dielectric material breaks down easier when contacted with water than mercury. Therefore, the thickness of CYTOP coating for water droplets is increased to 400 nm from the previous 200 nm. Figure 3.52 shows the photograph of a water-droplet contact variable capacitor. The volume of each water droplet is around $300\mu L$. For the water-droplet contact variable capacitor, the maximum capacitance is 3.52 nF and the minimum capacitance is 0.45 nF. The thicknesses of the thinner and thicker CYTOP layers for water droplets are 400 nm and 4 μm, respectively. Its parasitic capacitance is 0.76 nF to represent surface charge trapping. Figure 3.53 compares the surface trapping effects using 300 μL water and mercury drops. It is realized from the figure that more charge is trapped on the interface between water droplets and CYTOP coating than mercury drops, which can also be proved by the designated parameter, i.e. $\delta_{water} = 0.216 > \delta_{mercury} = 0.164$. For the variable capacitor with a 150 μL mercury drop described in the previous section, the maximum capacitance is 2.74 nF,

while the parasitic capacitance is 0.4 nF due to surface charge trapping. In other words, 14.6 percent of contact area is charge trapped during the energy harvesting process. The maximum capacitance for the water contact capacitor is 3.52 nF, while its parasitic capacitance is 0.76 nF. This means 21.6 percent of charge will be trapped, which is 50 % larger than mercury-drop variable capacitors. one possible reason is that the cohesive force between water molecules is significantly less than mercury. Because of that, water molecules are easier to trap on the interface. Figure 3.54 shows the cross section of one water-droplet contact variable capacitor. Because of its low cohesive force, water droplets usually stick to most surfaces. Acrylic sheets coated with a commercial super-hydrophobic material (RUST-OLEUM NeverWet®) are used as side walls to keep the water droplet within the desired area. In order to avoid chemical reaction with water, tungsten wires are deployed as metal contacts.

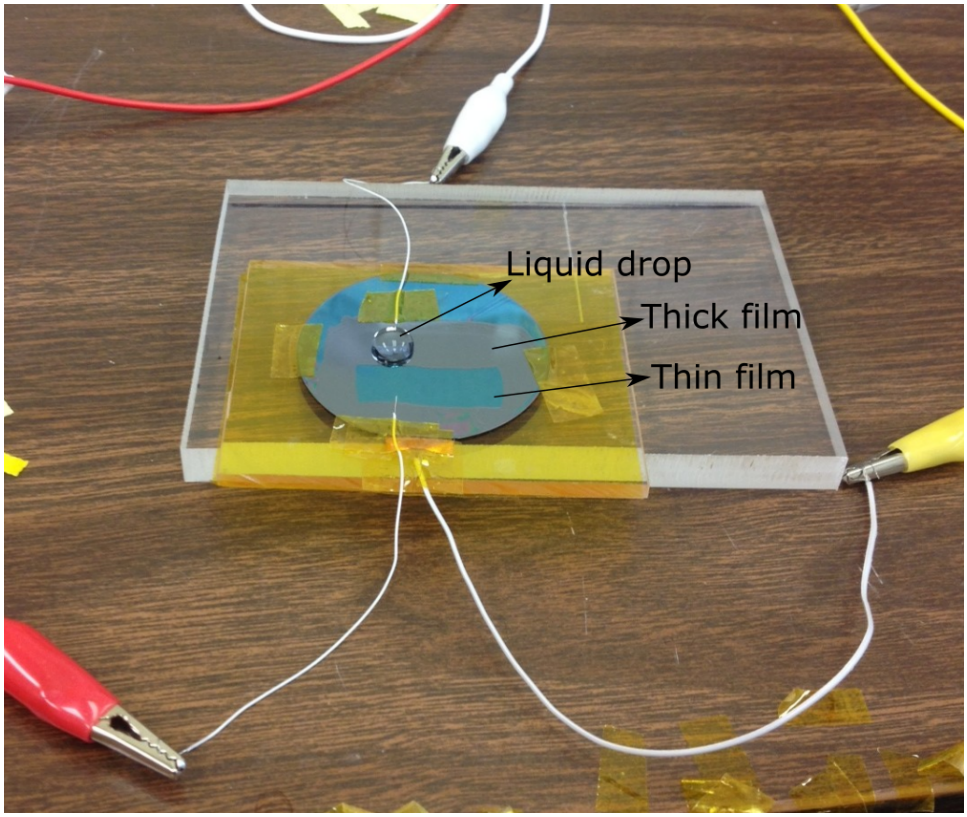

Figure 3.52: Photograph of a water-droplet contact variable capacitor.

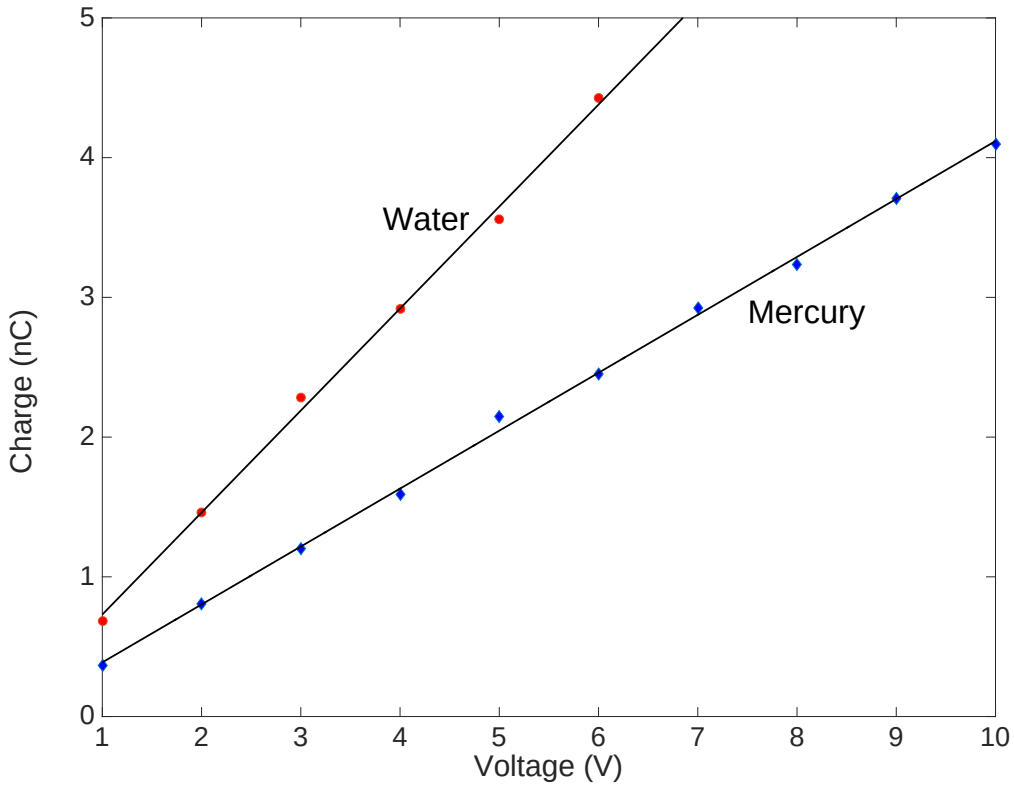

Figure 3.53: Thinner surface charge trapping effect using 300 μL water and mercury drop, respectively.

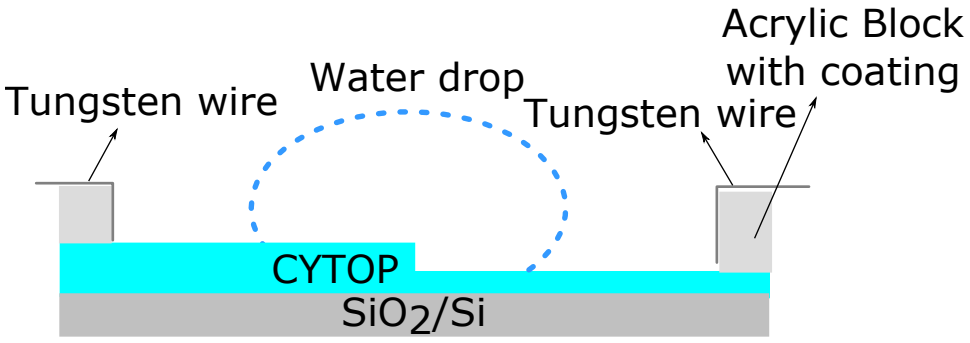

Figure 3.54: Cross section of one water-droplet contact variable capacitor.

3.4.2 Experiment data and results

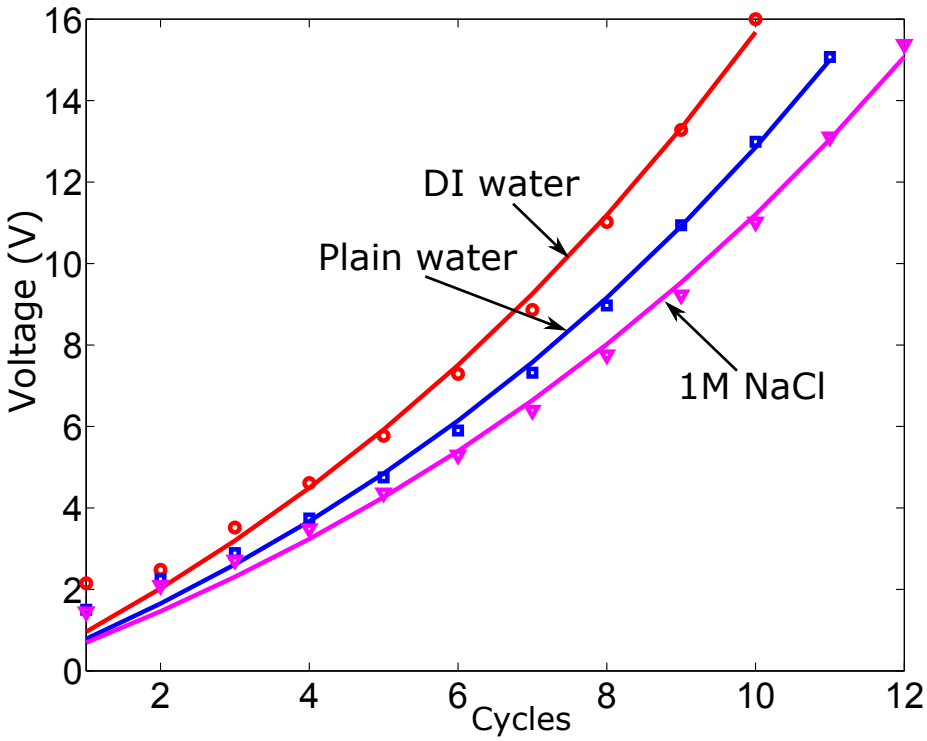

Figure 3.55: Electric output of devices (1 source, 2 sinks) using deionized water, plain water, and 1 mol/L sodium chloride solution.

In the experiments, two, three, and four 300 μL water contact variable capacitors are used as the sink capacitors, respectively. One commercial ceramic capacitor with constant capacitance is used as the source capacitor. The maximum and minimum capacitance of each water contact variable capacitor is 3.52 nF and 0.45 nF, respectively. The parasitic capacitance due to surface charge trapping was approximately 0.76 nF. Different values of source capacitance and various numbers of sink capacitors are used in the experiments to find out the maximum effective growth rate γ_r. The maximum number of sink capacitors used in the experiments is four. $\alpha\beta = 7.82 > n/(1-\delta) = 5.10$. Therefore, the system using four water contact variable capacitors satisfies the positive-feedback condition. According to equations 3.44, 3.46, and 3.47, the effective growth rate of the system using water contact variable capacitors has the maximum

value when $\alpha = \beta = \sqrt{C/C'} = 2.797$ and $n = ||2.532|| = 3$. Using equation 3.42, the maximum growth rate is given as $\gamma_r = 1.187$. Therefore, the growth rate γ_r has the theoretical maximum value 1.187 when $\alpha = \beta = 2.797$,$C_0 = \alpha C' = 1.259\ nF$, and $n = 3$. Under the same source capacitance, the effective growth rates of the system using two and four water contact variable capacitors have the maximum values of 1.180 and 1.139, respectively. Among them, the system using three water drops grows fastest while the system using four water drops grows slowest.

In addition to plain water, the deionized water with the conductivity of 0.055 $\mu S/cm$ and 1 mol/l sodium chloride solution was also used in the experiments. Figure 3.55 shows the difference of electric output results using two water-droplet contact variable capacitors as sink capacitors. Lines in the figure represent the theoretical models shown in equation 3.37 while markers represent the experimental results. The capacitance was measured to be 3.01 nF for the thinner side and 0.42 nF for the thicker side, respectively. The used source capacitance is 0.51 nF. The fitted growth rates are identified as $\hat{\gamma}_{DI}$ = 1.105; $\hat{\gamma}_{plain}$ = 1.106, and $\hat{\gamma}_{NaCl}$= 1.102 for three cases, respectively. Therefore, very close values of γ_r were obtained for three cases. There is a negligible effect of the ion concentration towards the effective growth rates. The ion concentration, however, has been shown to influence the charge due to electrostatic induction. The charge due to electrostatic induction $\bar{Q}_c$ was identified to be 3.44 nC, 2.80 nC, and 2.49 nC for the cases of deionized water, plain water, and 1 mol/l NaCl solution, respectively. The time histories of the output voltages were thus different for the three cases due to different charge $\bar{Q}_c$ resulting from electrostatic induction. Here in the experiments, plain water from the faucet is used. Three different values of source capacitance are used: 0.32 nF, 1.26 nF, and 7.60 nF.

Figure 3.56-3.63 illustrate the electric outputs of the system using two 300 μL water-droplet variable capacitors as sink capacitors and one commercial ceramic capacitor. It is known from Figure 3.56 that the voltages of all three devices grow exponentially. Among them, the voltage of the system with 1.26 nF source capacitance grows fastest while the voltage of the system with 7.60 nF source capacitance grows slowest. The effective growth rate γ_{rf}, the equivalent voltage V_{eq2} and the theoretical effective growth rates γ_{rt} are shown in Table 3.4. The results show the

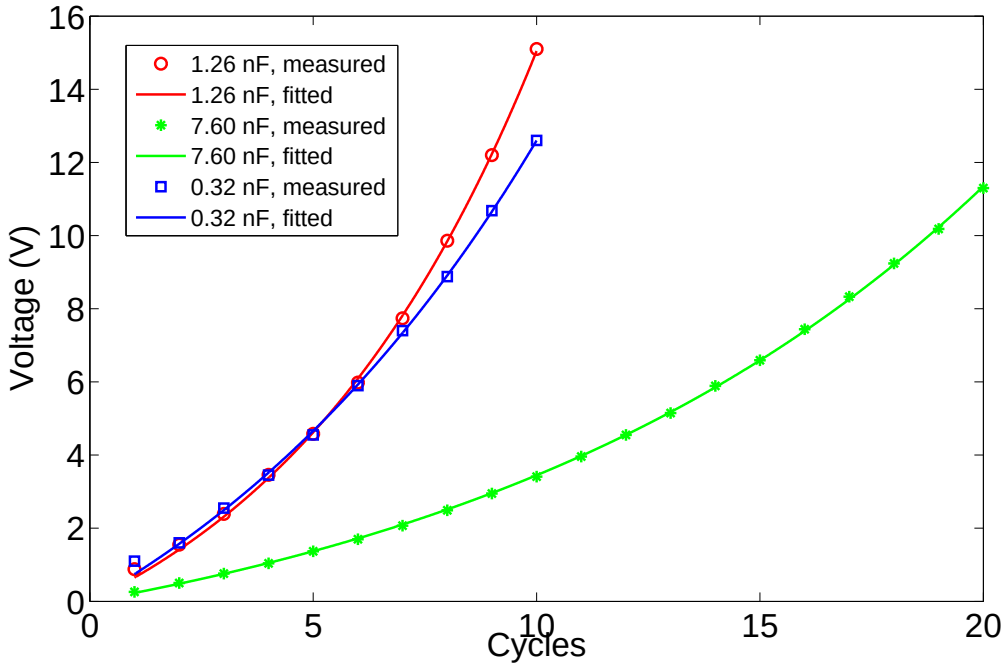

Figure 3.56: The voltages of different values of source capacitance versus cycles by using two 300 μL water-droplet variable capacitors.

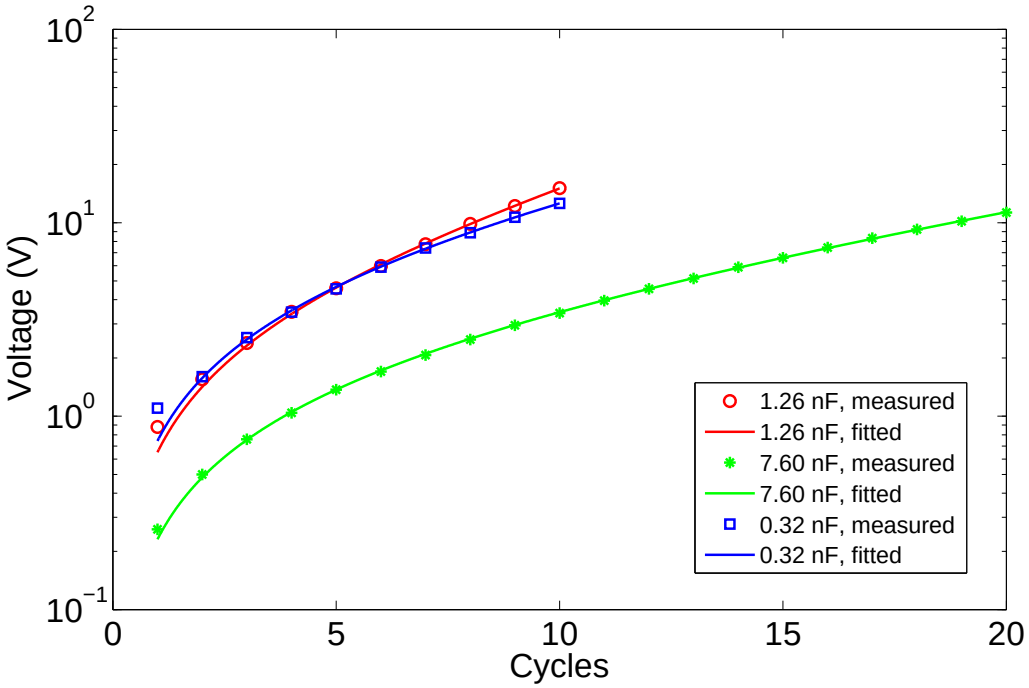

Figure 3.57: Logarithmic scale of the voltages of different values of source capacitance versus cycles by using two 300 μL water-droplet variable capacitors.

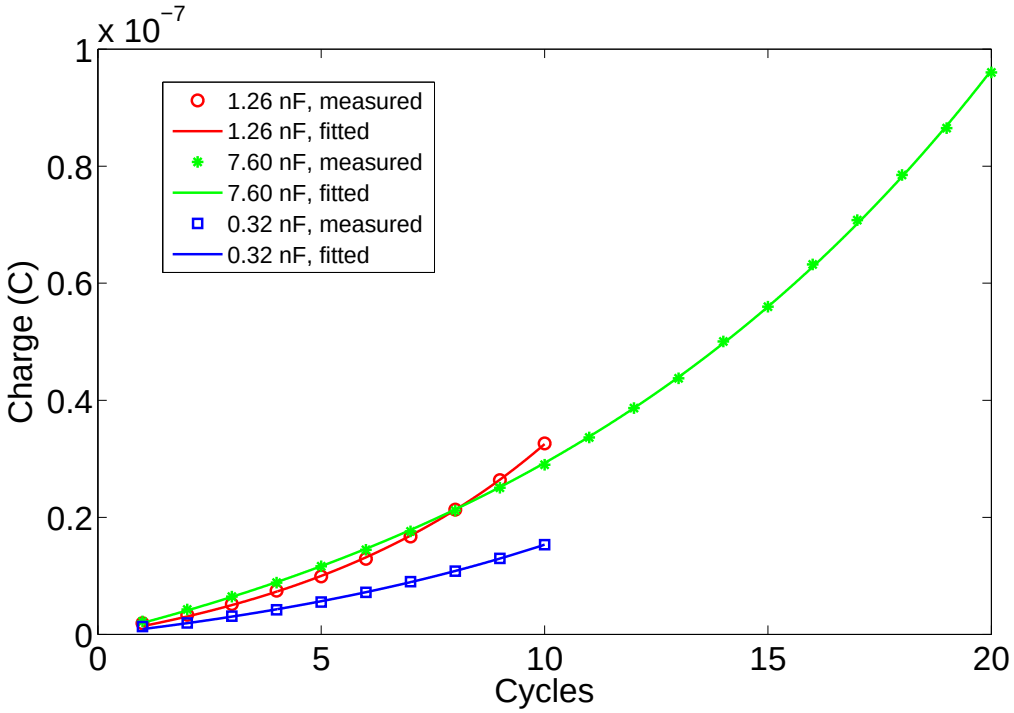

Figure 3.58: The charges of different values of source capacitance versus cycles by using two 300 μL water-droplet variable capacitors.

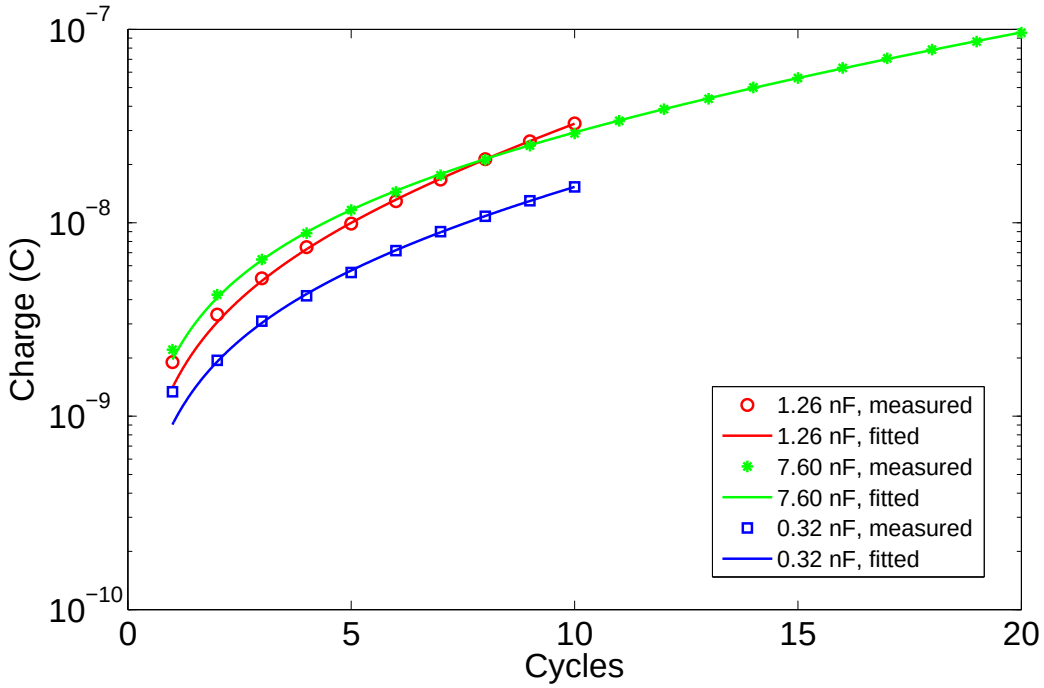

Figure 3.59: Logarithmic scale of the charges of different values of source capacitance versus cycles by using two 300 μL water-droplet variable capacitors.

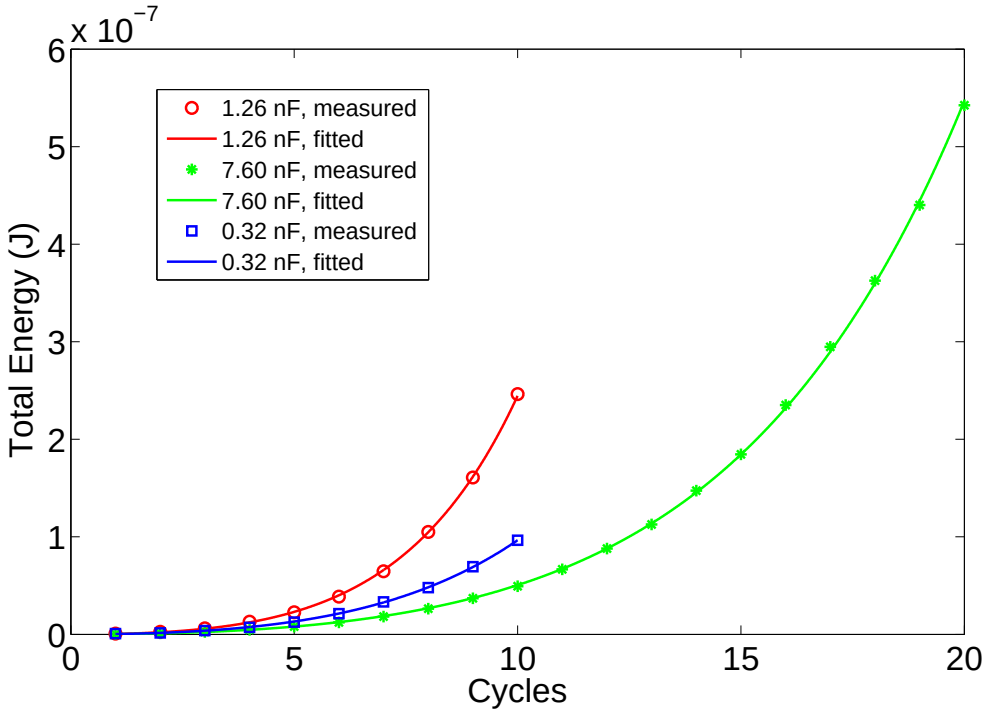

Figure 3.60: The total energy of the system with different values of source capacitance versus cycles by using two 300 μL water-droplet variable capacitors.

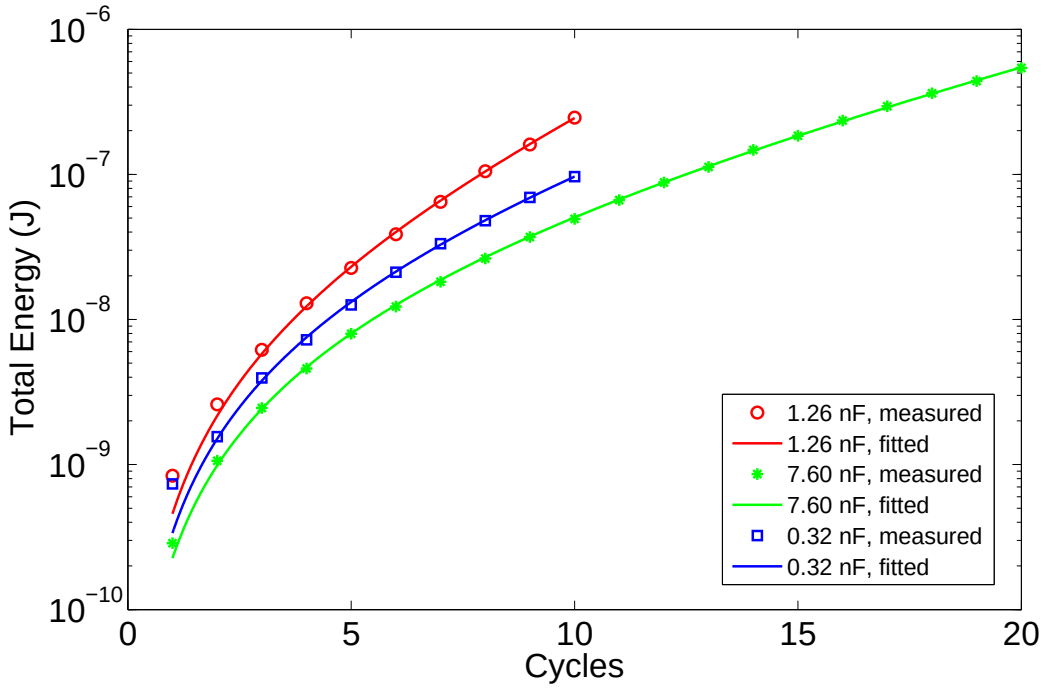

Figure 3.61: Logarithmic scale of the total energy of the system with different values of source capacitance versus cycles by using two 300 μL water-droplet variable capacitors.

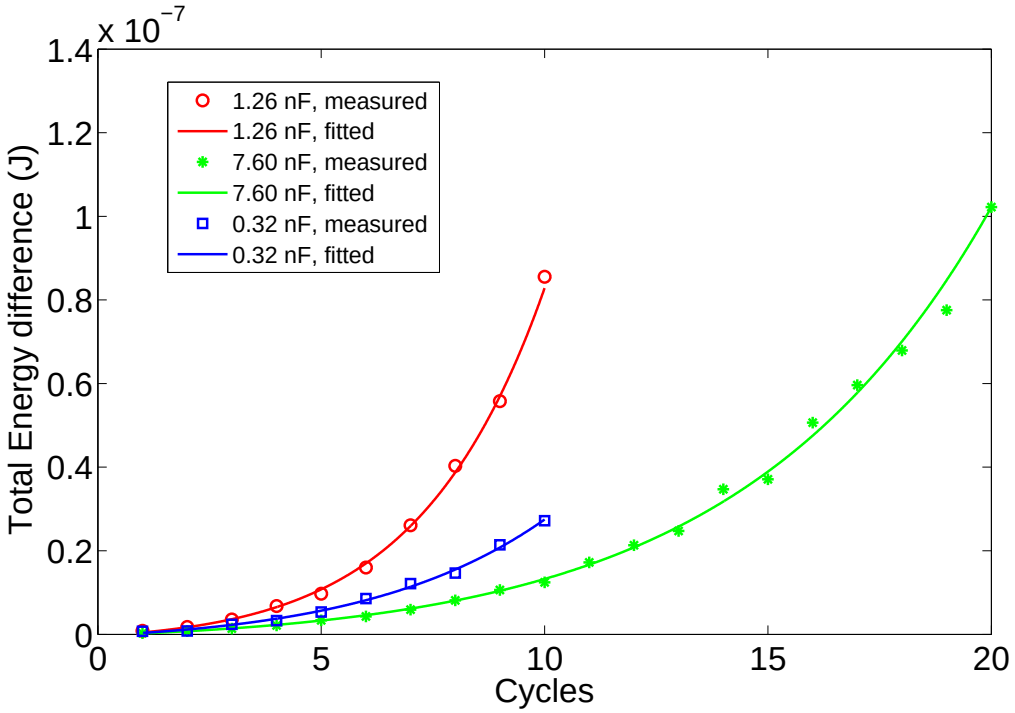

Figure 3.62: The total energy difference of the system with different values of source capacitance versus cycles by using two 300 μL water-droplet variable capacitors.

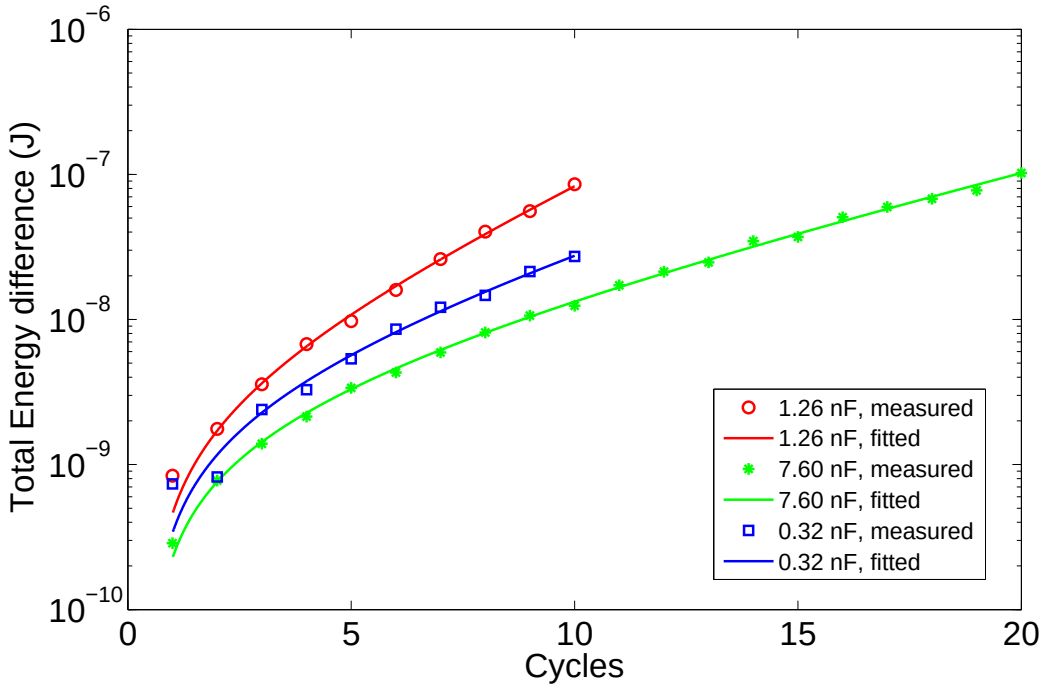

Figure 3.63: Logarithmic scale of the total energy of the system with different values of source capacitance versus cycles by using two 300 μL water-droplet variable capacitors.

fitted effective growth rates agree well with the theoretical effective growth rates. Compared to the results in Table 3.1, the extra charge from water droplets is generally lower than that from mercury drops, which is caused by the relatively low surface tension of water. Figure 3.58 and 3.59 show the charges of different values of source capacitance versus cycles and its logarithmic scale, respectively. The charges of all four source capacitors grow exponentially. In Figure 3.59, the growth rate with 1.26 nF is the highest. Figures 3.60 and 3.61 show the total energy of the system with different values of source capacitance versus cycles and its logarithmic scale, respectively. The total energy of all the four devices grows exponentially, and the total energy with 1.26 nF source capacitance increases fastest. Figures 3.62 and 3.63 show the total energy difference of the system with different values of source capacitance versus cycles and its logarithmic scale, respectively. Similarly, each total energy difference of each device grows exponentially and the device with 1.26 nF has the maximum growth rate.

C_0 (nF)	**Fitted** V_{eq2} (V)	**Fitted** γ_{rf}	**Theoretical** γ_{rt}	**Difference between** γ_{rf} **and** γ_{rt}
0.32	6.619	1.113	1.117	-0.36%
1.26	3.684	1.177	1.180	-0.25%
7.60	2.671	1.086	1.089	-0.28%

Table 3.4: The fitted equivalent voltage V_{eq2}, effective growth rates γ_{rf} and theoretical effective growth rates γ_{rt} using two 300 μL water-droplet variable capacitors.

C_0 (nF)	**Fitted** V_{eq2} (V)	**Fitted** γ_{rf}	**Theoretical** γ_{rt}	**Difference between** γ_{rf} **and** γ_{rt}
0.32	6.396	1.118	1.121	-0.27%
1.26	1.402	1.187	1.186	0.08%
7.60	2.223	1.088	1.091	-0.27%

Table 3.5: The fitted equivalent voltage V_{eq2}, effective growth rates γ_{rf} and theoretical effective growth rates γ_{rt} using three 300 μL water-droplet variable capacitors.

Figures 3.64-3.71 illustrate the electric outputs of the system using three 300 μL water-droplet variable capacitors as sink capacitors. In those figures, the electric outputs of each system, i.e. voltage, charge, energy, and energy difference, all grow exponentially. Among three values of source capacitance, the electric outputs of the systems with 1.26 nF source capacitance

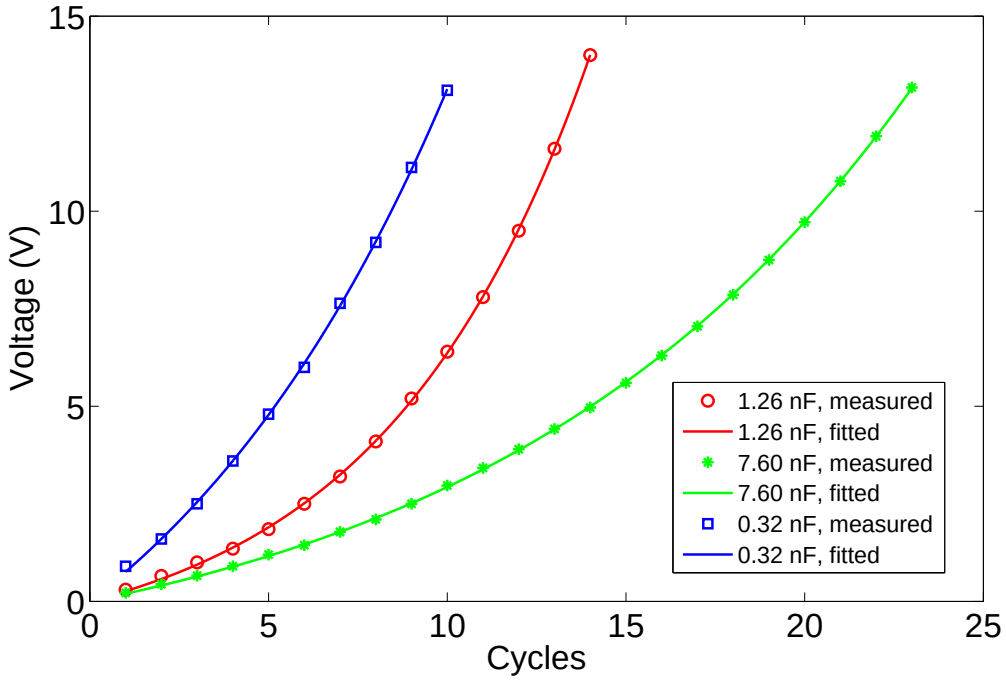

Figure 3.64: The voltages of different values of source capacitance versus cycles by using three 300 μL water-droplet variable capacitors.

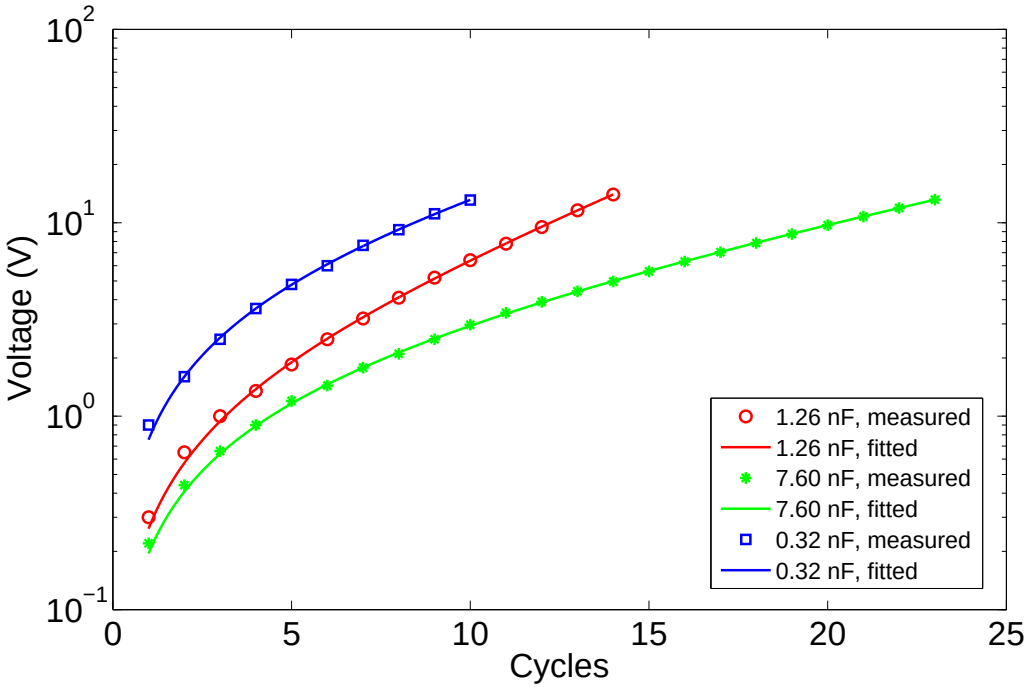

Figure 3.65: Logarithmic scale of the voltages of different values of source capacitance versus cycles by using three 300 μL water-droplet variable capacitors.

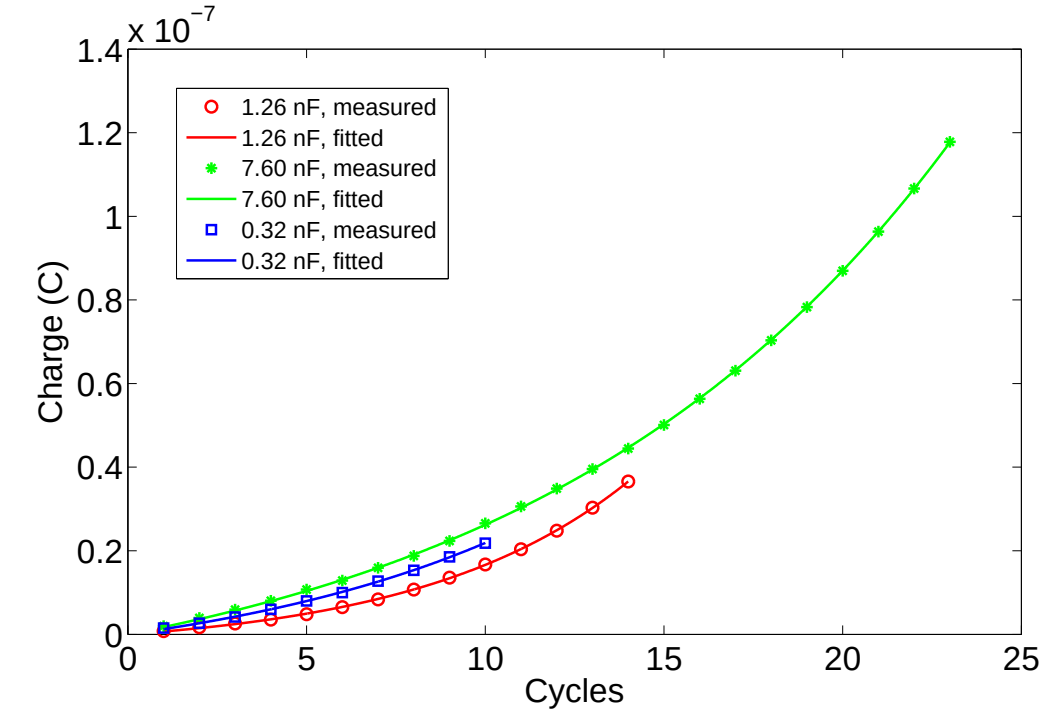

Figure 3.66: The charges of different values of source capacitance versus cycles by using three 300 μL water-droplet variable capacitors.

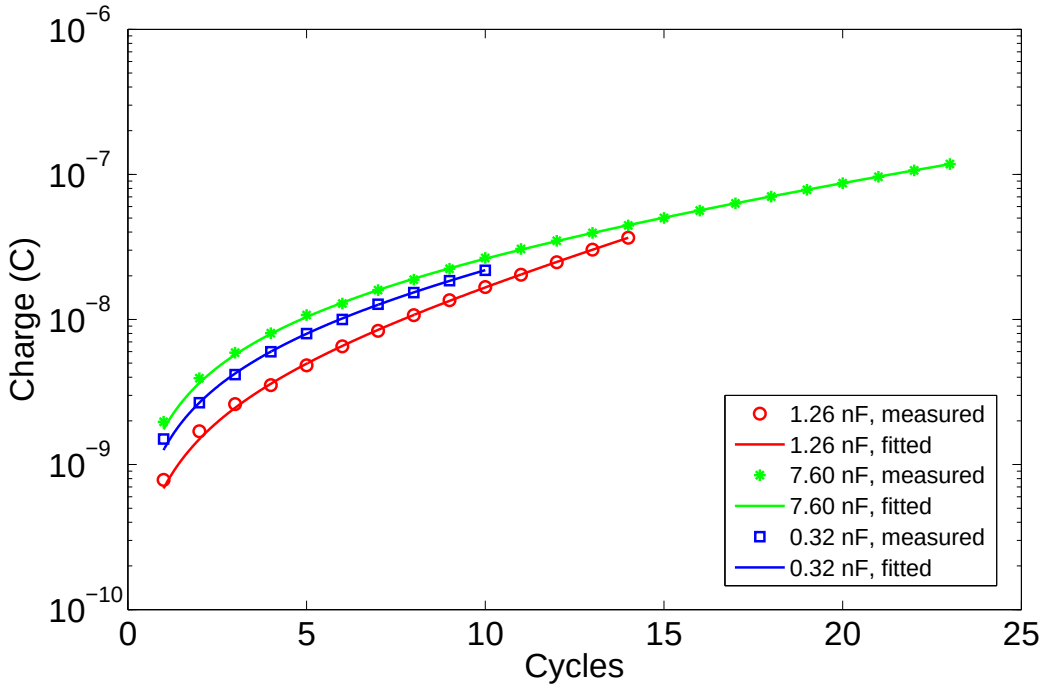

Figure 3.67: Logarithmic scale of the charges of different values of source capacitance versus cycles by using three 300 μL water-droplet variable capacitors.

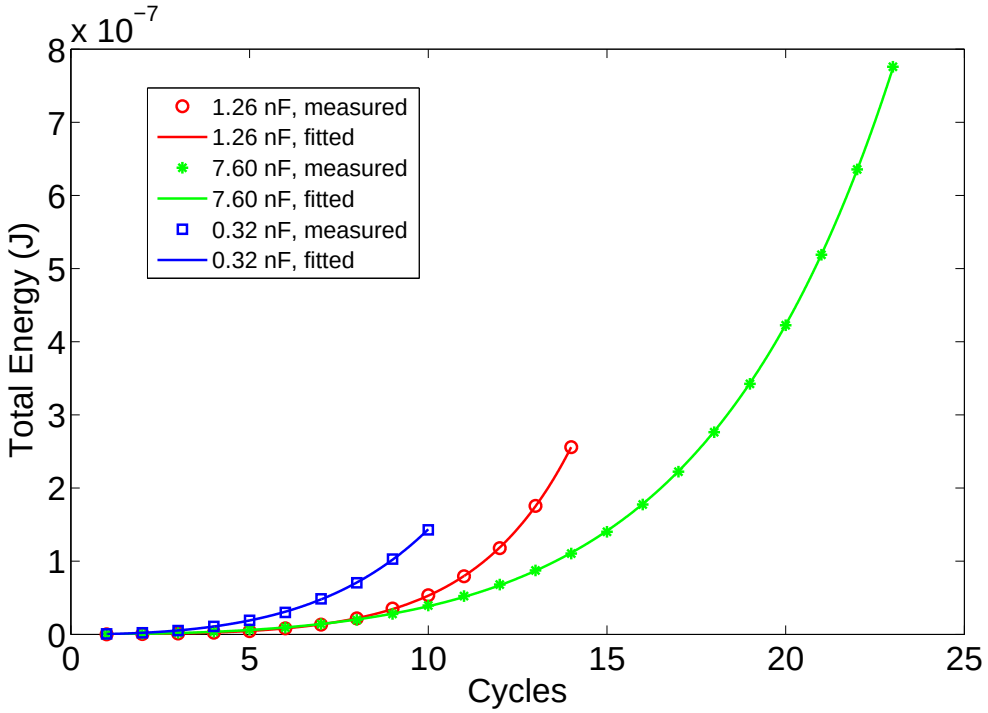

Figure 3.68: The total energy of the system with different values of source capacitance versus cycles by using three 300 μL water-droplet variable capacitors.

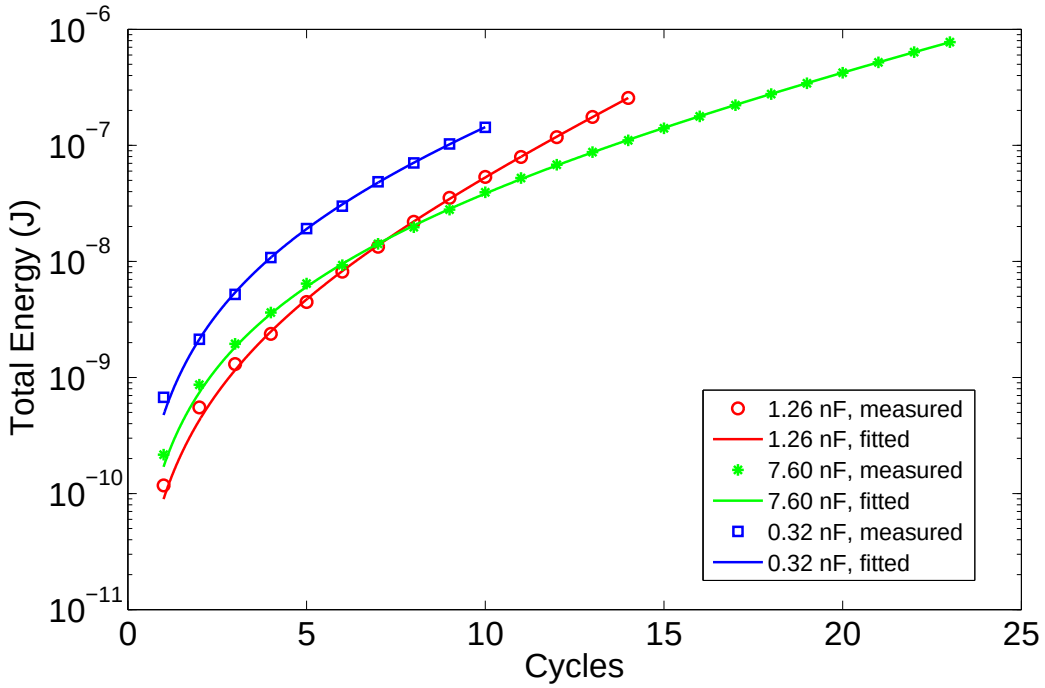

Figure 3.69: Logarithmic scale of the total energy of the system with different values of source capacitance versus cycles by using three 300 μL water-droplet variable capacitors.

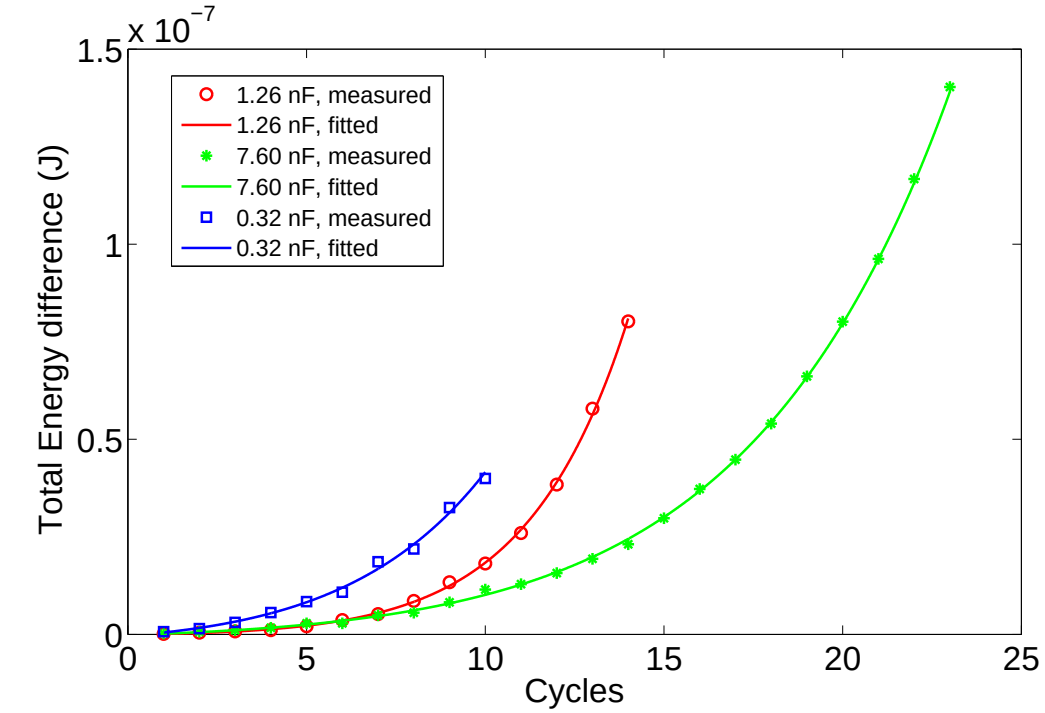

Figure 3.70: The total energy difference of the system with different values of source capacitance versus cycles by using three 300 μL water-droplet variable capacitors.

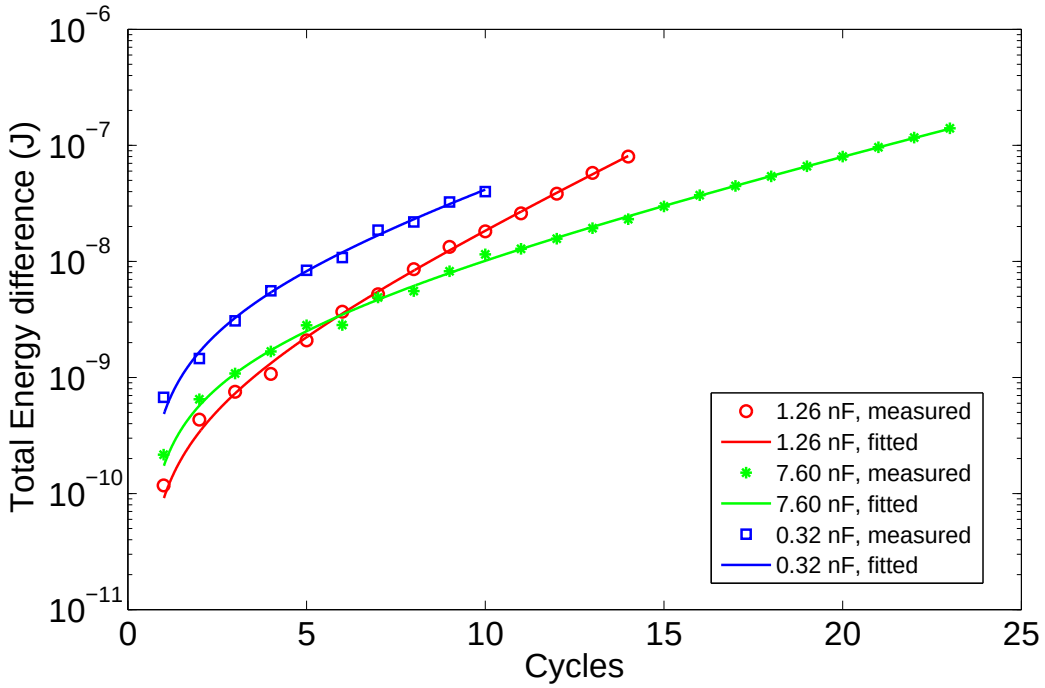

Figure 3.71: Logarithmic scale of the total energy of the system with different values of source capacitance versus cycles by using three 300 μL water-droplet variable capacitors.

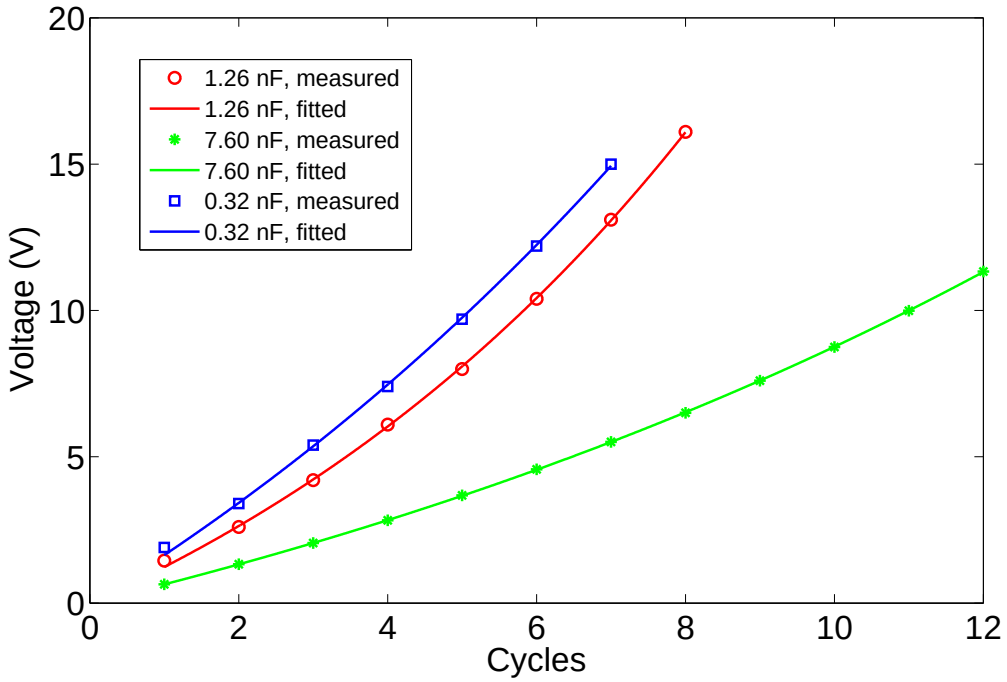

Figure 3.72: The voltages of different values of source capacitance versus cycles by using four 300 μL water-droplet variable capacitors.

increase fastest. The effective growth rate γ_{rf}, the equivalent voltage V_{eq2} and the theoretical effective growth rates γ_{rt} are shown in Table 3.5. The results show the fitted effective growth rates agree well with the theoretical effective growth rates. Compared to the results of Table 3.4, the electric outputs of the systems with three water droplets grow faster than these with two water droplets.

Figures 3.72-3.79 illustrate the electric outputs of the system using four 300 μL water-droplet variable capacitors as sink capacitors. In those figures, the electric outputs of all the systems, i.e. voltage, charge, energy, and energy difference, grow exponentially. Among three values of source capacitance, the electric outputs of the systems with 1.26 nF source capacitance increase fastest. The effective growth rate γ_{rf}, the equivalent voltage V_{eq2} and the theoretical effective growth rates γ_{rt} are shown in Table 3.6. The results show the fitted effective growth rates have good fit with the theoretical effective growth rates. Compared to the results of Table 3.4 and 3.4, the electric outputs of the systems with $n = 4$ grow slowest while those with $n = 3$ grow

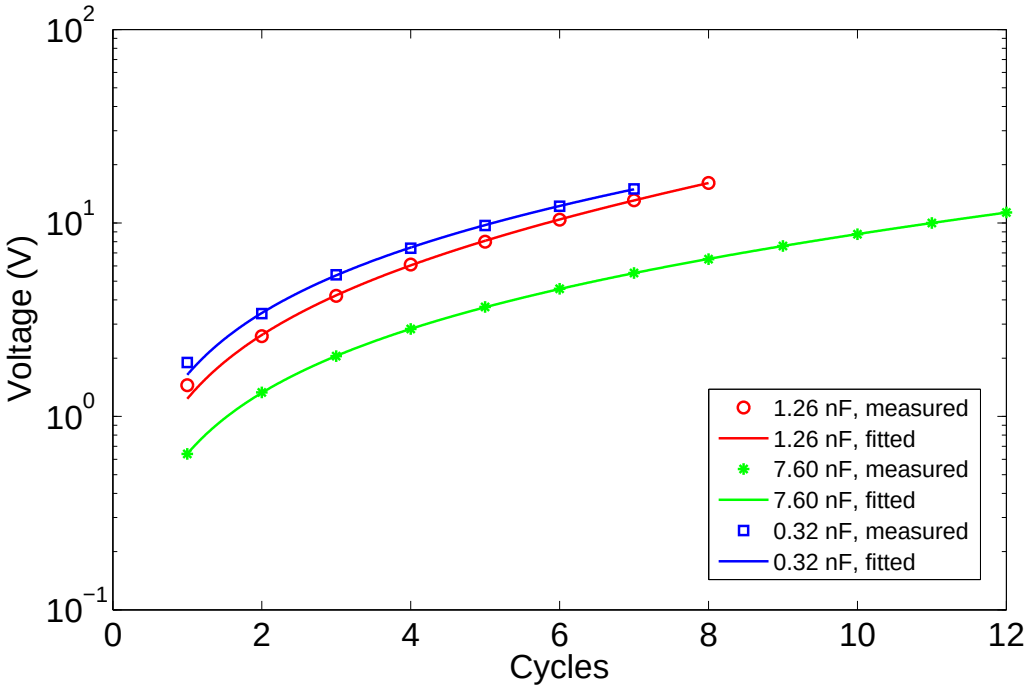

Figure 3.73: Logarithmic scale of the voltages of different values of source capacitance versus cycles by using four 300 μL water-droplet variable capacitors.

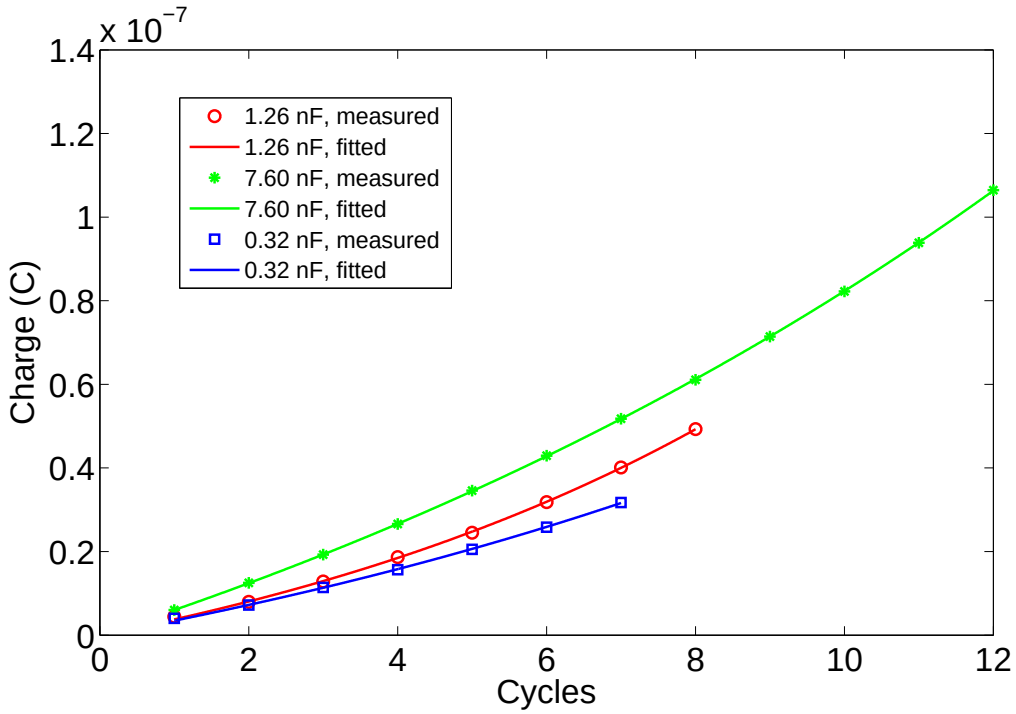

Figure 3.74: The charges of different values of source capacitance versus cycles by using four 300 μL water-droplet variable capacitors.

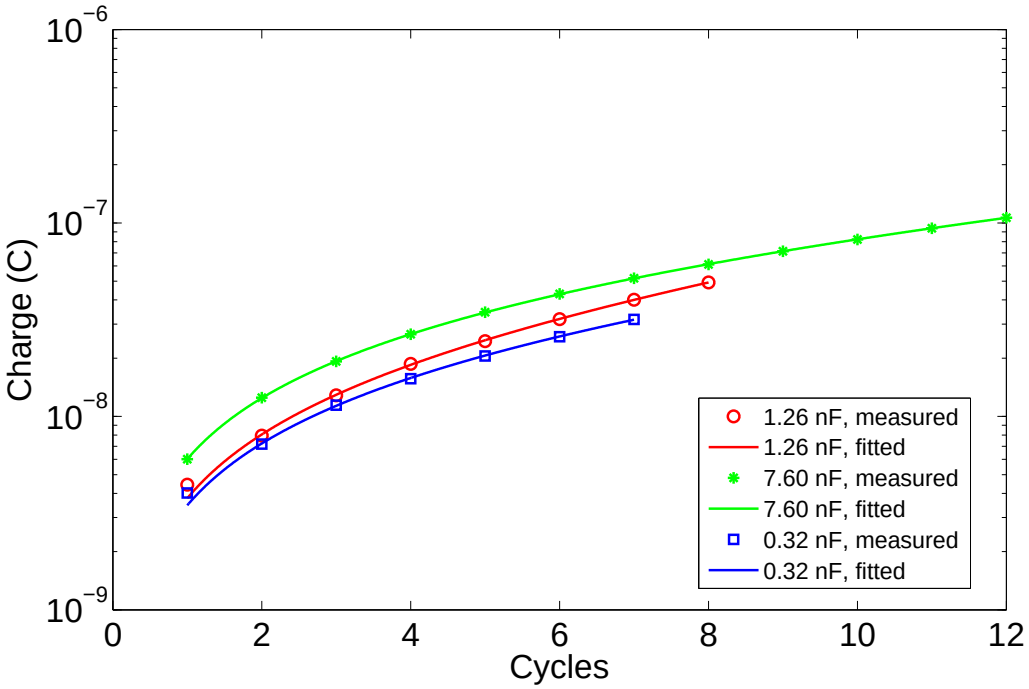

Figure 3.75: Logarithmic scale of the charges of different values of source capacitance versus cycles by using four 300 μL water-droplet variable capacitors.

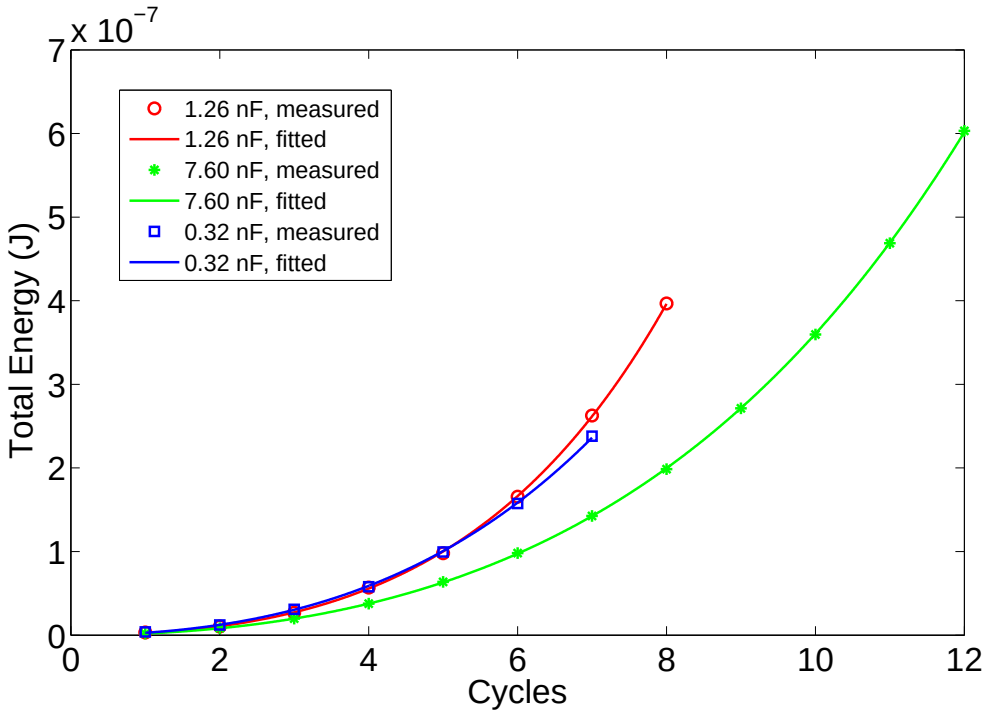

Figure 3.76: The total energy of the system with different values of source capacitance versus cycles by using four 300 μL water-droplet variable capacitors.

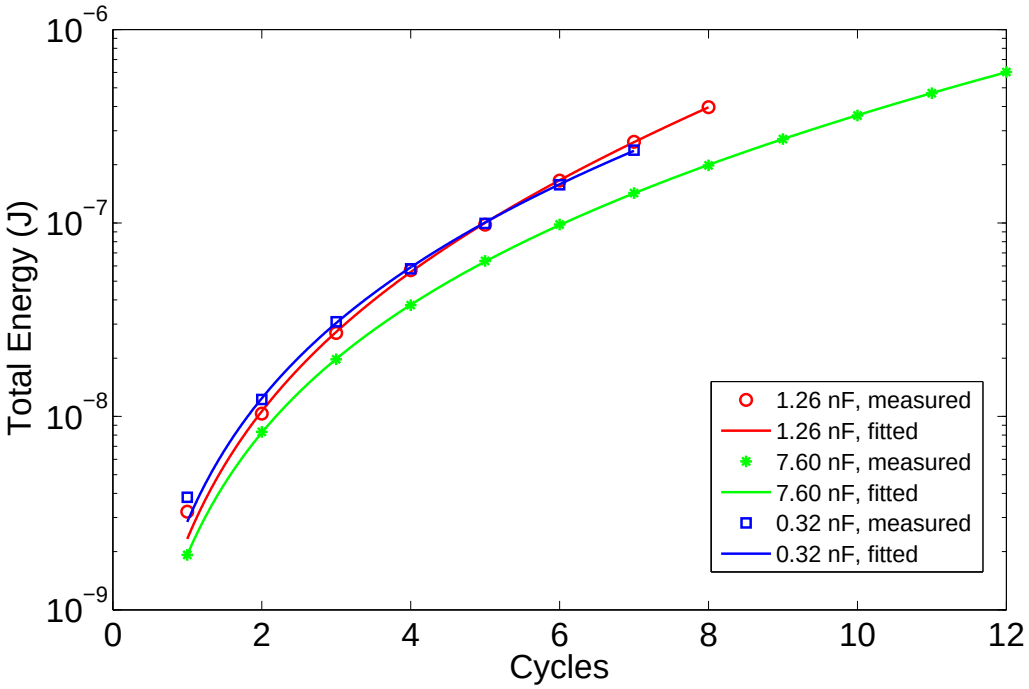

Figure 3.77: Logarithmic scale of the total energy of the system with different values of source capacitance versus cycles by using four 300 μL water-droplet variable capacitors.

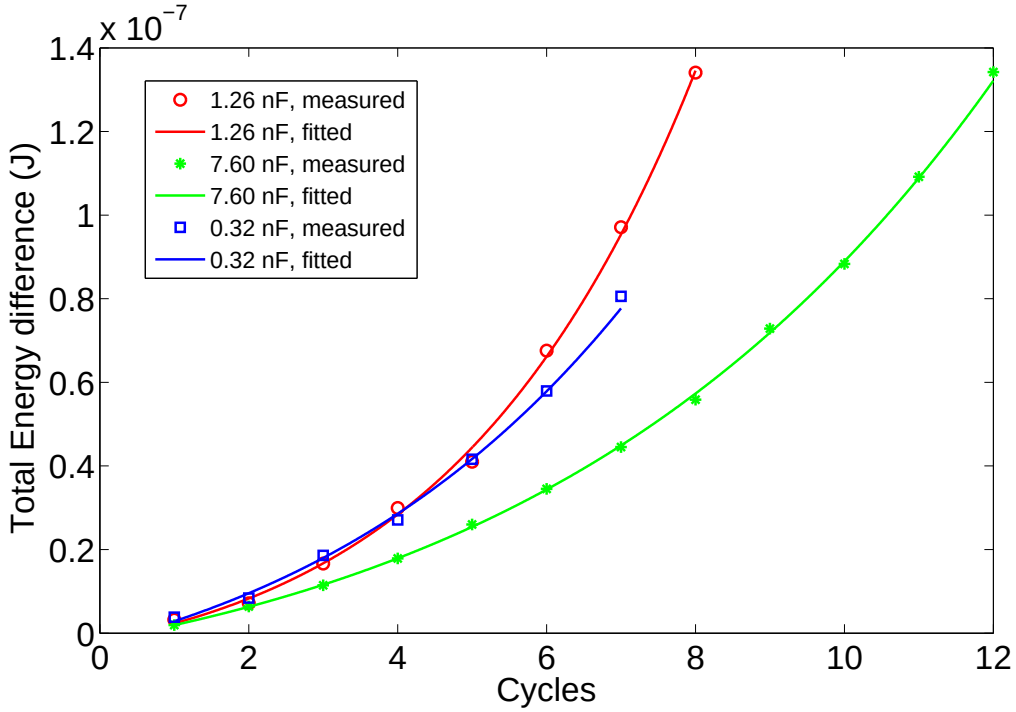

Figure 3.78: The total energy difference of the system with different values of source capacitance versus cycles by using four 300 μL water-droplet variable capacitors.

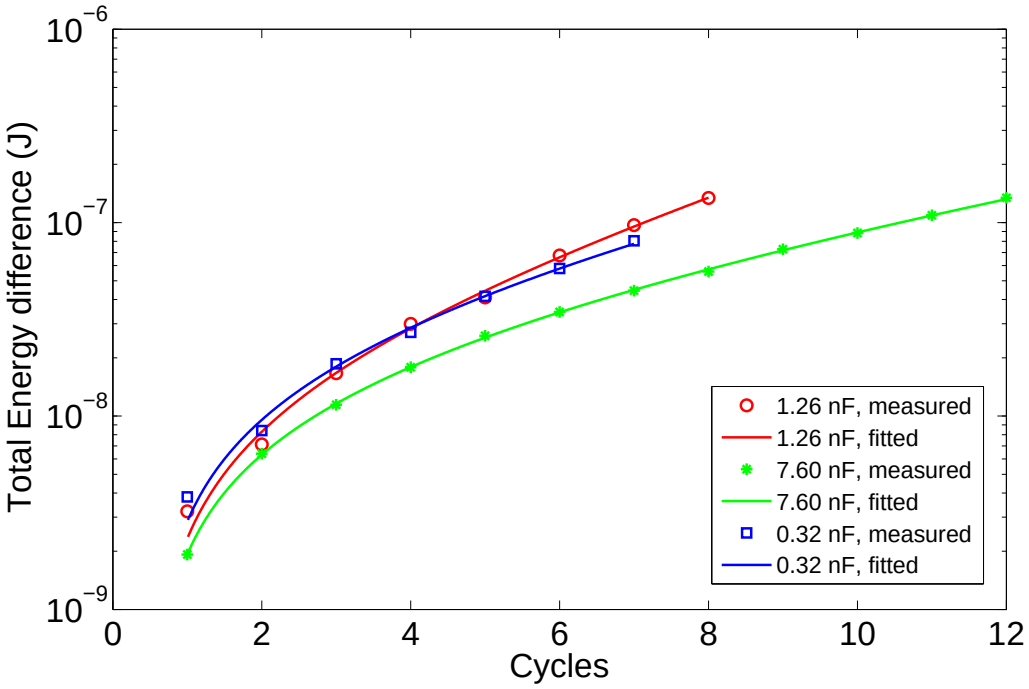

Figure 3.79: Logarithmic scale of the total energy of the system with different values of source capacitance versus cycles by using four 300 μL water-droplet variable capacitors.

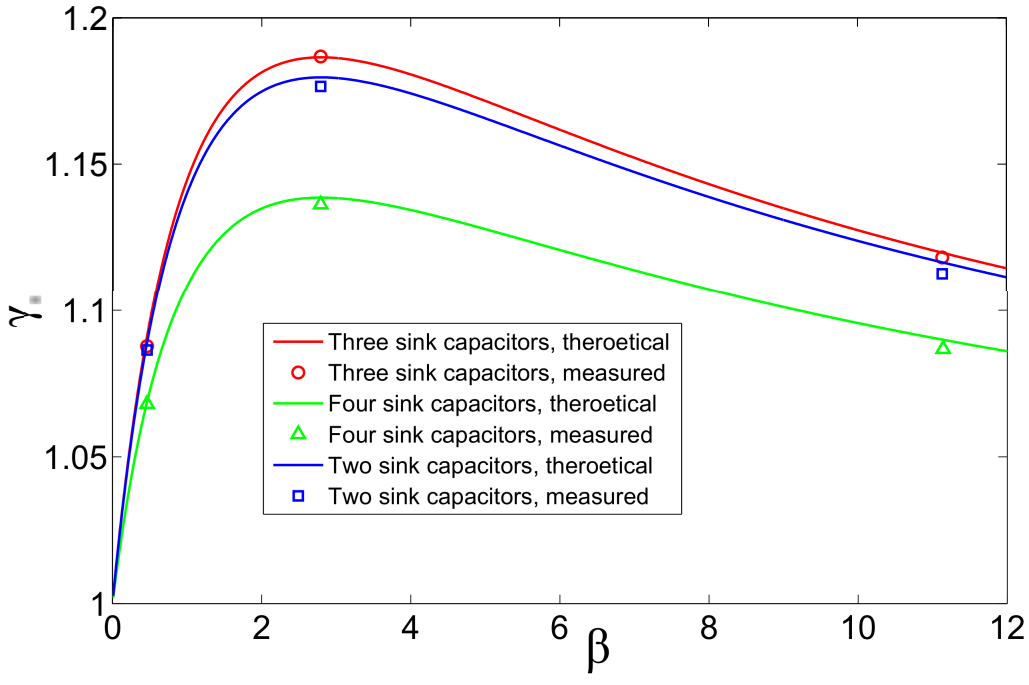

Figure 3.80: γ_r versus β using water-droplet variable capacitors as sink capacitors.

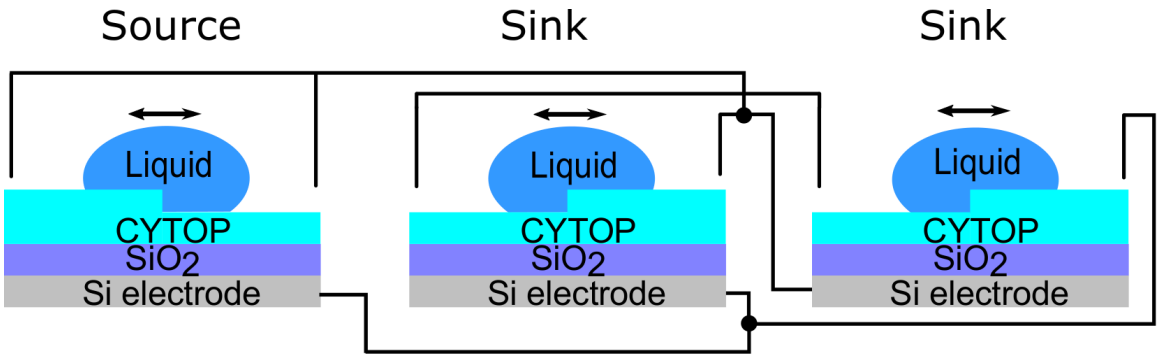

Figure 3.81: Schematic diagram of an energy-harvesting device using contact variable capacitors as source and sink capacitors.

fastest. Figure 3.80 shows all the effective growth rates versus β. Equation 3.37 is used to calculate the theoretical data. According to equations 3.44, 3.46, and 3.47, based on the measured capacitance, the effective growth rate has the theoretical maximum value 1.187 when $\alpha = \beta = 2.797$, $n = 3$, and $C_0 = 1.259\ nF$. The fitted data agree very well with the theoretical data. The dielectric film can be injected into charge when a high voltage is applied. Such change can lead to different surface charge densities. In order to maintain the surface properties during the experiments, the maximum voltages generated by the systems are controlled down to ~ 16 volts. Compared to mercury drops, the extra charge using water droplets is less than that using mercury droplets because of the lower surface tension of water. Furthermore, more surface charge trapping effects take place when water contact variable capacitors are used.

$C_0\ (nF)$	**Fitted** $V_{eq2}\ (V)$	**Fitted** γ_{rf}	**Theoretical** γ_{rt}	**Difference between** γ_{rf} **and** γ_{rt}
0.32	18.902	1.087	1.091	-0.37%
1.26	9.051	1.136	1.138	-0.18%
7.60	9.411	1.068	1.069	-0.09%

Table 3.6: The fitted equivalent voltage V_{eq2}, effective growth rates γ_{rf} and theoretical effective growth rates γ_{rt} using four 300 μL water-droplet variable capacitors.

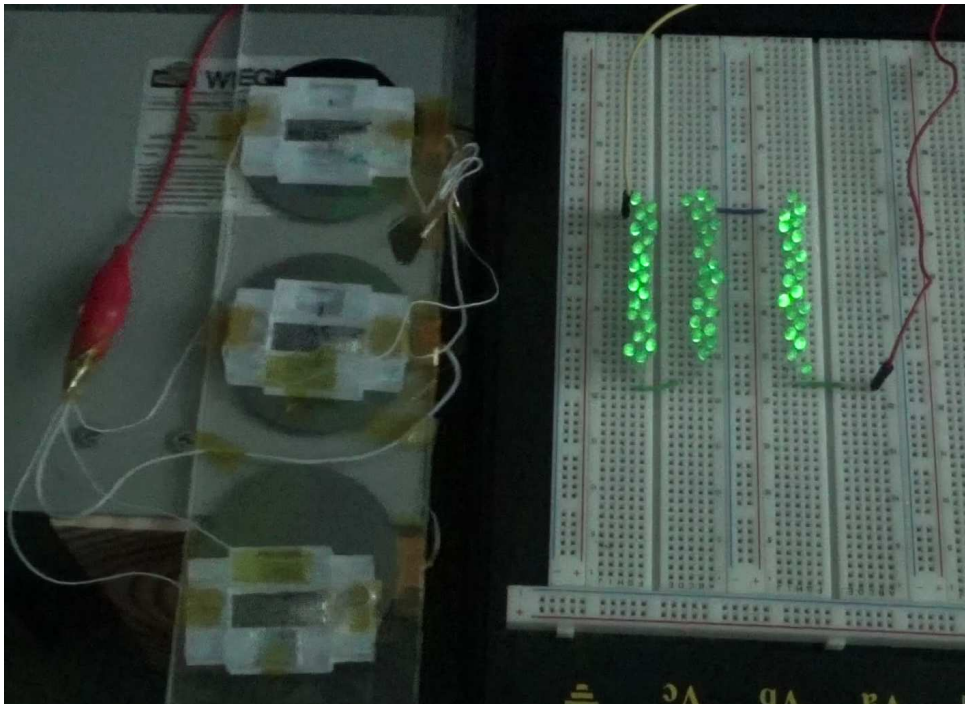

(a)

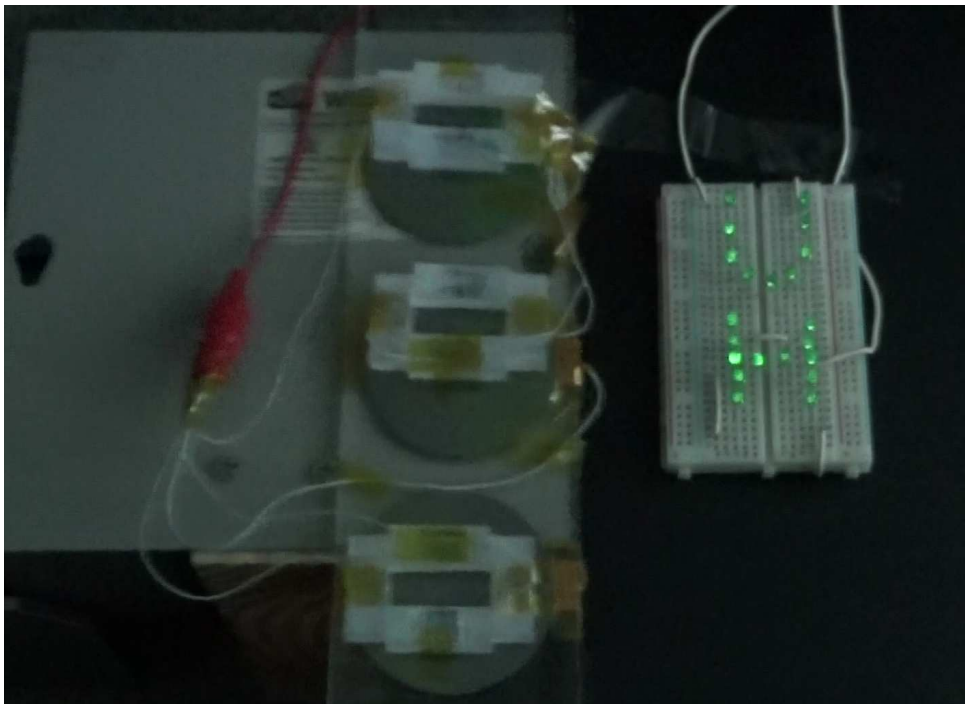

(b)

Figure 3.82: energy-harvesting devices illuminating light-emitting diodes (LEDs) connected in series under 2.5 Hz vibrations. **(a)** A device with three 300 μL mercury droplets illuminating 60 LEDs in series. **(b)** A device with three 300 μL water droplets illuminating 20 LEDs in series.

3.5 Contact variable capacitor as the source capacitor

In the previous sections, a fixed-capacitance capacitor was used as the source capacitor. According to equation 3.37, the effective growth rate would be much higher if a variable capacitor is used as the source capacitor. In this section, the energy harvesting devices made from three contact droplet-based variable capacitors are used to illuminate commercial LEDs under low-frequency mechanical vibrations. Here, one contact variable capacitor is used as the source capacitor while two other contact variable capacitors are used as sink capacitors. The thicknesses of thinner and thicker CYTOP sides are 200 nm and 3 μm, respectively. Vibrations of 2.5 Hz were used as the external energy source to stimulate vibrations induced by human walking, is chosen as the energy source. In the experiment, 300 μL Plain water droplets and mercury droplets were used, respectively. Figure 3.81 shows the schematic diagram of the energy-harvesting devices. From the figure, when the droplets are on the left sides, the sink capacitors are reaching their maximum capacitance while the source capacitor is reaching its minimum capacitance. All the capacitors are discharged before the experiments and LEDs are connected in series and then to the source capacitor. At the first cycles, the voltage is not high enough so that the LEDs are not lit. Therefore, no electric load is connected to the system, which leads to exponential growth of the charge. After a few cycles of accumulation, the voltage output of the device with three 300 μL mercury droplets reached 168 volts in the distributive state, which is higher than the sum of 60 working voltage of LEDs. Therefore, LEDs are lit up until the voltage of the system drops back to 168 volts, which is considered the control voltage of the system. The LEDs are not connected to the energy harvesting system until the voltage of source capacitor is higher than the control voltage. Part of electrical energy is consumed by LEDs until the voltage of source capacitor is under the control voltage. The left electrical energy in the system provide sufficient charge bias so that 60 green LEDs can be lit up as shown in Figure 3.82**(a)** in each cycle afterwards. Under the same condition, the device with water droplets of the same size could generate 56 V, sufficient to illuminate 20 green LEDs connected in series as shown in Figure 3.82**(b)**. The maximum number

of LEDs that were lit depended on the breakdown voltage of the thinner side of the CYTOP film. Based on experimental results, the breakdown voltage was conservatively estimated to be around 12 V when water droplets were used, corresponding to a peak value of 56 V on the source capacitor in the distributive state. The values for generators using mercury drops were estimated to be 29 V and 168 V, respectively.

Because both the source and sink capacitors had the same position-dependent capacitance, the resulting effective growth rate is much higher than those of the cases using a fixed source capacitor. More specifically, in this case, γ_r is 1.674 for mercury drops and 1.669 for water droplets. It is noted that $\alpha\beta = 10.15^2$ in this case, which is an order of magnitude higher than those in the cases of a fixed source capacitor. The effects of charge trapping for mercury and water droplets were considerably reduced because of the dramatically decreased γ_p. The actual resulting values of γ_r for mercury and water droplets were thus very close. The voltages due to contact electrification are 4.69 and 2.72 V for mercury and water, respectively. Therefore, the voltage of the source capacitor with mercury droplets reached 168 V after 7 cycles and it took the device with water droplets 6 cycles to reach 56 V.

It has been shown that if energy storage elements are used as the primary energy harvesting components of a system, appropriate reconfigurations of the system can create a positive feedback of the potential energy in the elements, leading to an exponential growth of the energy that is harvested as the elemental potential energy. The efficacy of this method has been demonstrated with droplet generators. Consider the device with a fixed source capacitor of 0.94 nF and three 150 μL mercury drops and the device with a fixed source capacitor of 1.26 nF and three 300 μL water droplets. In the experiments conducted, the tilting angle of the wafer was within $\pm 5^o$. The total available energy was calculated to be 83.2 μJ for the mercury drops and 15.4 μJ for the water droplets by adding the two peak values of the potential energy of the drops in a cycle. It has been shown that devices with mercury drops and those with water droplets can sustain a continuous operation at 168 and 56 V, respectively. If operated at these voltages, the device with mercury drops can harvest energy at the rate of 10.2 μJ per cycle, corresponding to a harvesting

efficiency of 12.2% and the values for the device with three water droplets will be 1.2 μJ per cycle and 7.9%. Because energy is harvested as electric potential energy in this method, the harvesting efficiency is independent of the electrical load to which the energy can be delivered. The efficiencies of the prototype devices fabricated in this study far exceed those of the droplet generators reported in the literature, which are on the order of 0.01% under the optimal condition [89]. The devices can be operated at a higher energy level with a higher efficiency. However, since energy is harvested only in the distributive state in this study, the efficiency is limited to 50% per cycle when the total potential energy in both states is considered.

4 HARVESTING ENERGY USING ALTERNATE CONTACTS BETWEEN WATER AND TWO DIELECTRIC MATERIALS

The previous two chapters discussed the new concept of exponential energy harvesting through repetitive reconfigurations of the system and several applications. No charge bias is needed in the experiments and relatively high capacitance is achieved. In this section, another new mechanism is discussed for harvesting energy from low-frequency excitations through alternate contacts between water and two different dielectric materials.

Recent studies have demonstrated the benefits of water-dielectric interfaces in electrostatic energy harvesting. Most efforts have been focused on extracting the kinetic energy from the motions of water droplets on hydrophobic surfaces, and thus, the resulting schemes inherently prefer cases where the water droplets move at a high speed, or vibrate at a high frequency. The proposed method utilizes harvesting ambient mechanical energy as electric potential energy through water droplets to make alternate contacts with CYTOP and PTFE thin films [92]. Because CYTOP and PTFE acquire significantly different surface charge densities during contact with water, such a difference can be utilized to effectively generate electricity. The larger the difference in surface charge density, the more the harvested energy. Because CYTOP and PTFE respond to contact electrification very differently, a hydrophobic surface created with them will be electrified at different levels if brought into contact with water [93, 94]. As a result, when a water droplet moves across the CYTOP and PTFE surface, a fixed amount of charge is induced. More importantly, the proposed method utilizes the strong electrostatic induction in the water droplet

due to the electrical double layer formed at the interface. Therefore, it is more effective than the other methods that are based on the much weaker electrostatic induction in the substrate. Also, unlike in the other methods, in which the charge of the drop is not delivered to external circuits, in our method, the water droplet possesses a dual function as both an electrode and a passive switch, leading to the direct harvesting of the peak electric potential energy. This method not only results in simple device architecture but also allows for the use of schemes based on variable capacitors to improve its performance. Using prototype devices, we demonstrate the effectiveness of this approach in scavenging energy from low-level and low-frequency ambient vibrations. Each device was fabricated on a doped silicon substrate with one side coated by a thin, dielectric oxide layer. CYTOP and PTFE were used to create the two-region hydrophobic surface on which a 400 μL water droplet was free to move. Under a 0.25 Hz vibration, the device in which the CYTOP and PTFE regions were fabricated with similar thicknesses could generate a peak open-circuit voltage of 42 V. When the CYTOP and PTFE regions were fabricated with significantly different thicknesses, i.e. 8 μm and 0.5 μm for CYTOP and PTFE, respectively, the device could generate a peak open-circuit voltage of 115 V under an 8 V external bias when the device was driven under a 2.5 Hz vibration.

4.1 Working mechanism

The working principle of the proposed method is explained in Figure 4.1. A 3D rendered model of a prototype harvester fabricated is shown in Figure 4.1**(a)**. A schematic circuit model of the generator is shown in Figure 4.1**(b)**. The process of electricity generation is illustrated in Figure 4.1**(c)** – 4.1**(f)**. The energy harvester was fabricated on a doped silicon substrate, which functioned as a fixed electrode. One side of the substrate was grown with a 300 nm layer of tantalum pentoxide (Ta_2O_5). On the surface of Ta_2O_5, two types of amorphous fluoropolymer solutions, i.e. PTFE and CYTOP, are coated on half of the surface, respectively (Figure 4.1**(a)**). After proper curing, PTFE and CYTOP can create a hydrophobic surface. A free-standing water

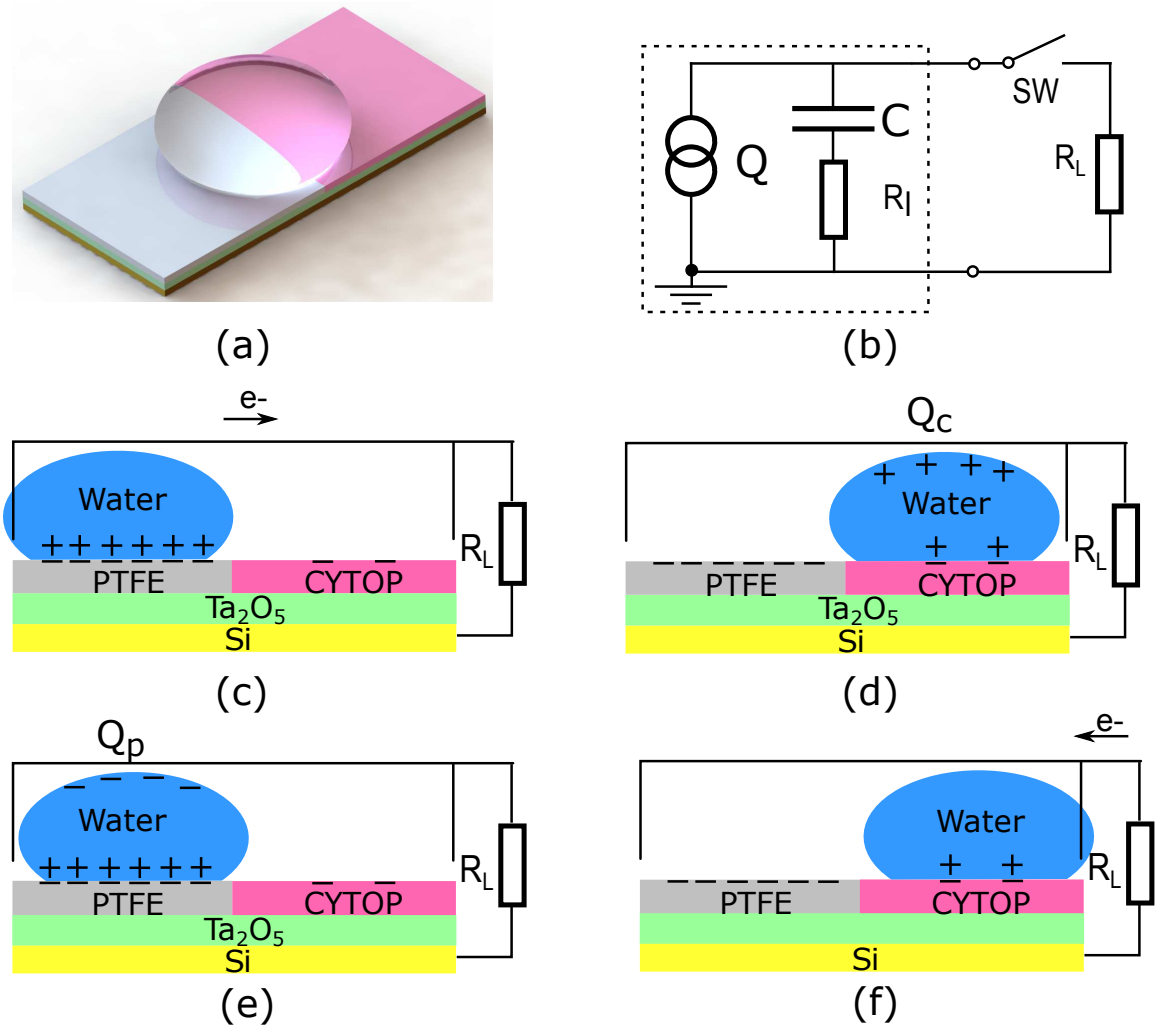

Figure 4.1: Working principle of the prototype harvester. **(a).** A 3D rendered model of the device. **(b).** The equivalent circuit model of the generator. Q, C, and R_I represent the induced charge, the equivalent capacitor, and the internal resistive loss, respectively, and $Q = Q_p = -Q_c$, where subscripts p and c represent values for cases of the water droplet being on PTFE and CYTOP, respectively. **(c) – (f).** Schematics of an energy harvesting cycle. **(c).** A water droplet on PTFE with the electric load connected to the device. **(d).** Positive charge induced in the water droplet when it was driven from PTFE to CYTOP. **(e).** Electrical power delivered to electric load connected to the device. **(f).** The drop driven to PTFE.

droplet on the hydrophobic surface functioned as a moving electrode. The oxide layer was necessary to prevent potential charge leaking due to pin-holes in the hydrophobic coatings. Due to contact electrification, the initial contacts between the water droplet and the electrically neutral surface will electrify the surface so that both PTFE and CYTOP are negatively charged. If multiple contacts are made, the charge will quickly saturate at very different values. The charge in PTFE and CYTOP will be quasi-permanent, making the two sections behave as electrets. Subsequent motions of the water droplet on the surface will not only help maintain the charge in the hydrophobic coatings but also invoke electrostatic induction. If an electrically neutral water droplet is placed on the charged PTFE surface, the positive charge in the drop will be attracted to the interface to form an electric double layer [95], and the negative charge is repelled away from the interface, creating a negative potential relative to the silicon substrate, which will create an electrical current through the metal contact as illustrated in Figure 4.1**(c)**. While CYTOP and PTFE generate similar water contact angles, and thus similar contact areas, the saturated surface charge density of CYTOP is significantly lower. If the drop subsequently moves to the CYTOP surface, the electric double layer will change accordingly. Therefore, the potential of the drop will become positive relative to the silicon substrate (Figure 4.1**(d)**). An opposite current can be generated if the drop is connected to the external load as shown in Figure 4.1**(e)**. The subsequent motion of the drop back to the PTFE surface will reestablish the original electric double layer and create a negative potential of the drop (Figure 4.1**(f)**). Therefore, an alternate current can be generated when the drop continuously moves across the surface. Note that electrostatic induction will also take place in the silicon substrate due to the quasi-permanent surface charge. Therefore, the generated current theoretically includes the induced charge in the substrate. However, because the thickness of the double layer formed at the water-polymer interface is on the order of 10 nanometers [96], much smaller compared to the distance between the substrate and the surface charge, which is on the order of micrometers, the electrostatic induction in the water droplet is the dominant mechanism in the process as confirmed experimentally. The potential energy of the induced charge on the water droplet can be modeled as the energy stored in an equivalent

capacitor, with the water droplet and the substrate as the electrodes. Therefore, the effect of electrostatic induction is equivalent to that of a charge source, which provides a fixed amount of charge to the equivalent capacitor. A schematic circuit model of the generator is shown in Figure 4.1**(b)**, where for simplicity, both the energy loss and the electrical load are assumed to be resistive with resistances of R_I and R_L, respectively. The charge transferred to the capacitor is equal to the electrostatically induced charge on the water drop, which can be estimated as

$$Q = -Q_p = Q_c = \sigma_c A_c - \sigma_p A_p \tag{4.1}$$

where Q, σ and A represent the induced charge, the surface charge density, and the contact area, respectively. Subscripts p and c indicate the values for PTFE and CYTOP, respectively. Due to the similar contact angles of PTFE and CYTOP [97, 98], the static contact areas were approximately the same, i.e. $A_p \approx A_c$. Because of the much higher relative permitivity of tantalum pentoxide, i.e. 25 as compared to 2.2 for CYTOP and 1.93 for PTFE, and its much lower thickness, the contribution of the Ta_2O_5 layer to the total capacitance between the water droplet and the substrate is negligible. Therefore, the capacitance can be calculated as $C_p = \varepsilon_0 \varepsilon_p A_p / d_p$ and $C_c = \varepsilon_0 \varepsilon_c A_c / d_c$, where ε_0 is vacuum permittivity, ε_p and ε_c are the relative permittivities of PTFE and CYTOP, respectively, d_p and d_c represent the thicknesses of the hydrophobic coatings. The total harvested energy in one cycle can be written as

$$E = \left(\frac{d_p}{2\varepsilon_0 \varepsilon_p A_p} + \frac{d_c}{2\varepsilon_0 \varepsilon_c A_c} \right) Q^2 \tag{4.2}$$

The performance of the harvesters can be enhanced if the scheme based on variable capacitors is used with an external bias. In this case, the hydrophobic coatings can be fabricated with significantly different thicknesses. The resulting device essentially behaves as a variable capacitor with the water droplet as the moving electrode. In this study, the PTFE and the CYTOP coatings were 0.5 μm and 8 μm, respectively, corresponding to measured capacitance of 3.99 nF and 0.26 nF, respectively. Figure 4.2 illustrates the working mechanism of this scenario. An

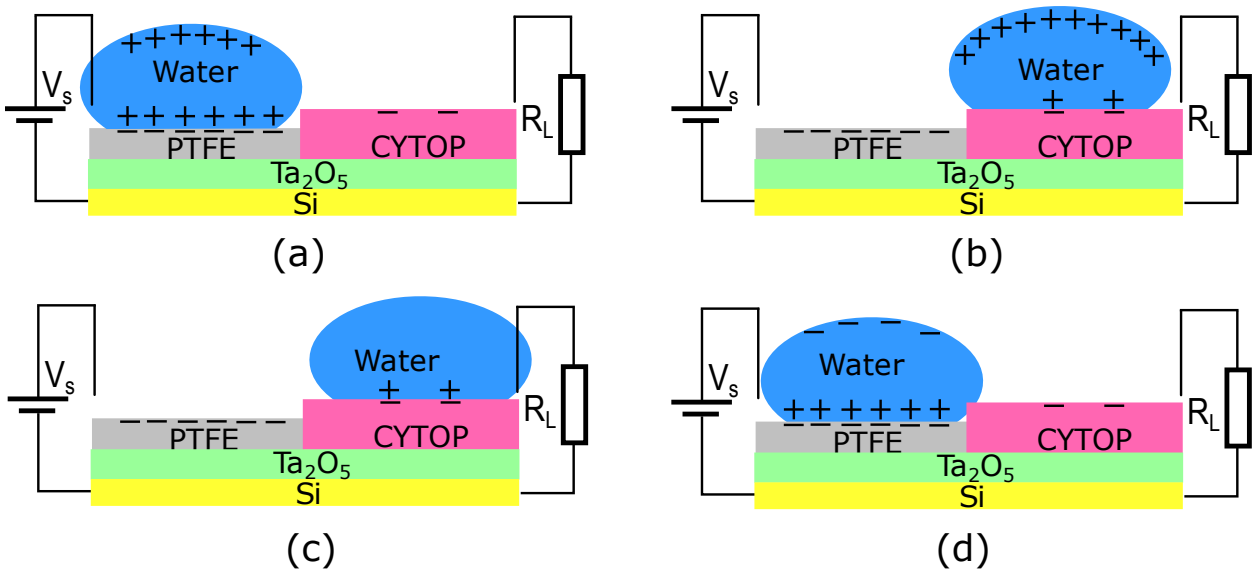

Figure 4.2: Harvesting energy using a variable capacitor-based scheme. **(a).** External bias applied to the water drop. **(b).** The drop moving to the thicker CYTOP coating. **(c).** Electricity delivered to the load. **(d).** Drop moving back to PTFE.

external, positive voltage bias is applied when the water droplet is on PTFE (Figure 4.2**(a)**). When the drop moves to the CYTOP side, the electric potential of the drop relative to the substrate increases due to the reduced capacitance and the additional, induced charge (Figure 4.2**(b)**). The electric potential energy increased accordingly, which is delivered to the resistor upon closing of the circuit (Figure 4.2**(c)**). When the drop moves back to the PTFE surface, the opposite charge is induced (Figure 4.2**(d)**) and will be neutralized when the bias is applied again (Figure 4.2**(a)**). Thus, the measured voltages will always be positive.

When the water droplet moves from Figure 4.2**(c)** to 4.2**(d)**, the total charge is $C_{pp}V_s - Q_p$. After the drop makes the connection with the metal contact on PTFE, the input energy can be expressed as below

$$E_I = \frac{1}{2}C_p V_s^2 - sgn(C_{pp}V_s - Q_p)\frac{(C_{pp}V_s - Q_p)^2}{2C_p} \tag{4.3}$$

Where $sgn(x)$ is the signum function. When the water droplet is on PTFE, the capacitor is charged to V_s. While the drop moves to the CYTOP surface, the energy delivered to the resistor

can be expressed as,

$$E_O = \frac{(C_{pr}V_s + Q_p)^2}{2C_c} \tag{4.4}$$

Therefore, the harvested energy per cycle is

$$E = E_O - E_I = \frac{(C_{pr}V_s + Q_p)^2}{2C_c} + sgn(C_{pp}V_s - Q_p)\frac{(C_{pp}V_s - Q_p)^2}{2C_p} - \frac{1}{2}C_pV_s^2 \tag{4.5}$$

4.2 Materials and fabrication

4.2.1 Device fabrication

Silicon wafers with a 300 nm-thick layer of tantalum pentoxide (Ta_2O_5) were used as substrates for the devices, one device per wafer. Two kinds of devices were fabricated. In the first kind, the thicknesses of the PTFE and CYTOP coatings were fabricated to be similar. The Teflon© AF 2400 solution was first uniformlly applied to one half of the tantalum pentoxide surface. The wafer with the coating was then oven dried at 200 °C for 1 hour. The process was repeated several times so that the desired thickness was obtained. The CYTOP © AF solution was then applied to the other half of the tantalum pentoxide surface in the same manner. The wafer was then cured at 250°C for one day. The thicknesses were 6.6 μm and 10 μm for the PTFE and CYTOP coatings, respectively. In the second kind of the devices, the PTFE coating was first spin coated onto tantalum pentoxide. The thickness of the coating was 0.5 μm. After the coated wafer was oven dried, a thick layer of CYTOP was applied to half of the PTFE coating to reach a total thickness of 8 μm. The wafer was then cured at 250°C for one day. Acrylic sheets (12 mm $\times$ 25 mm) coated with a commercial super-hydrophobic material (RUST-OLEUM NeverWet) were used as side walls to keep the water droplet within the desired area. Tungsten wire leads were used as the metal contacts to avoid chemical reactions with water.

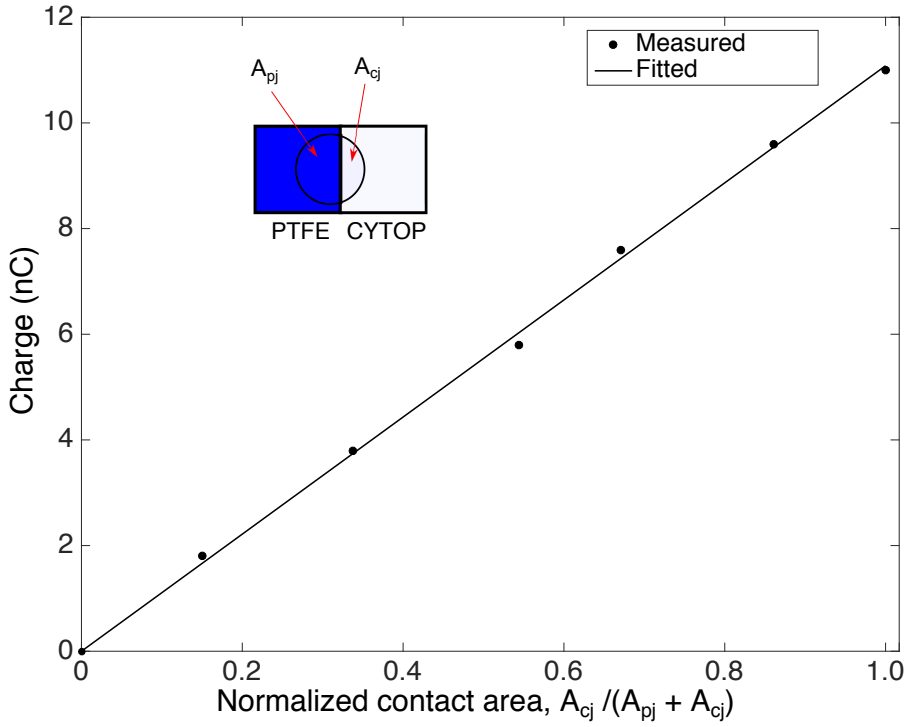

Figure 4.3: Relationship between the charge induced on a 400 μL water droplet and the normalized contact area. A_{pj} and A_{cj} represent the partial contact areas of the drop that belong to the PTFE and CYTOP sides, respectively.

4.2.2 Measurements

A shaker (Labworks ET-126-1) was used to excite the devices. Measurements were obtained with an electrometer (Keithley 6517B). The parasitic capacitance of the Triax cable provided by Keithley Inc. was approximately 300 pF. Cables that avoided such parasitic capacitance were fabricated and used to obtain the measurements. The communications between a computer and the electrometer were established with a KUSB-488B cable.

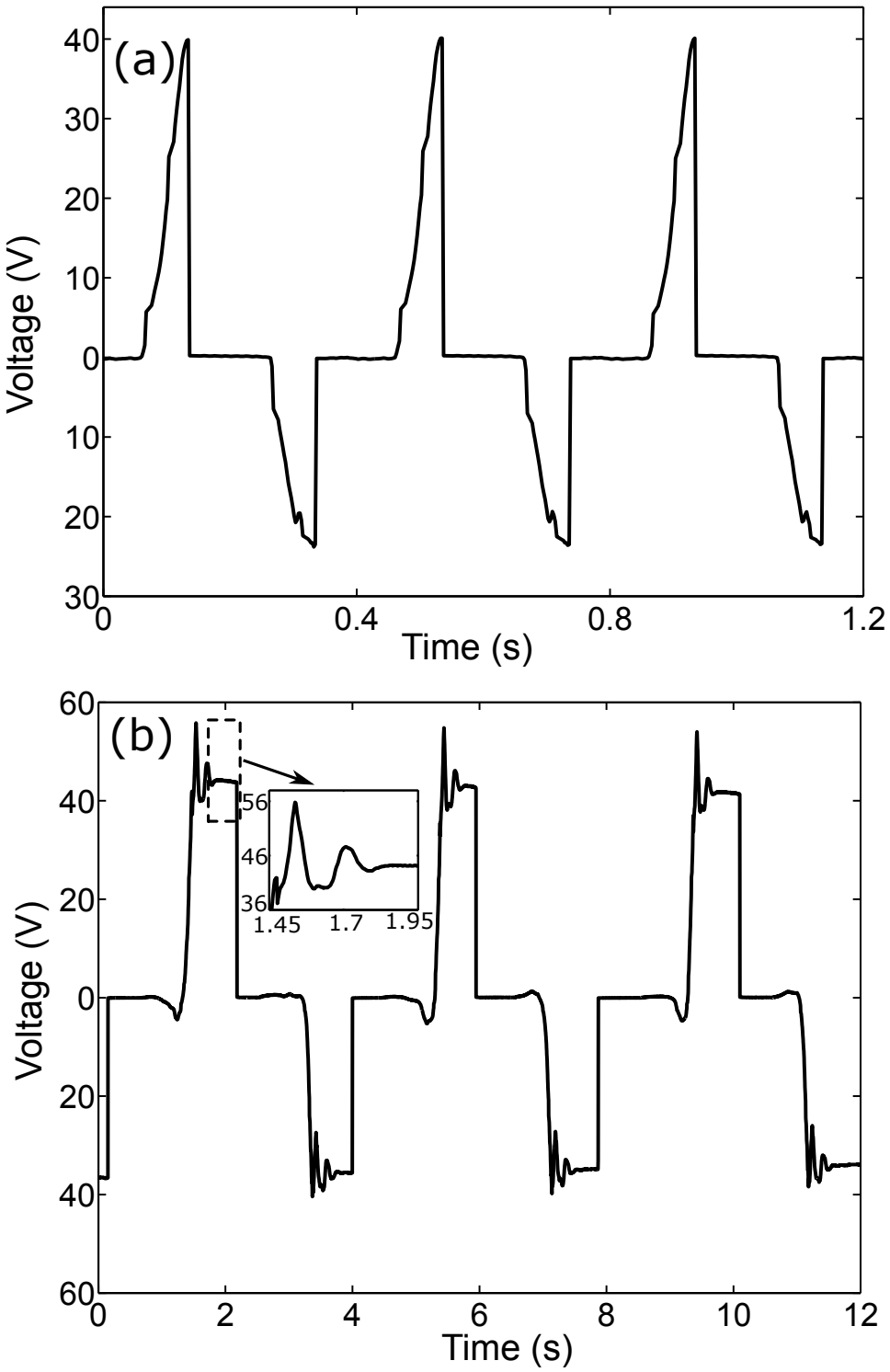

Figure 4.4: Voltages measured between the water droplet and the substrate. **(a).** The device driven by a 2.5 Hz excitation and the electric load connected via tungsten contacts. **(b).** The device driven manually at 0.25 Hz and the electric load connected via manual switches.

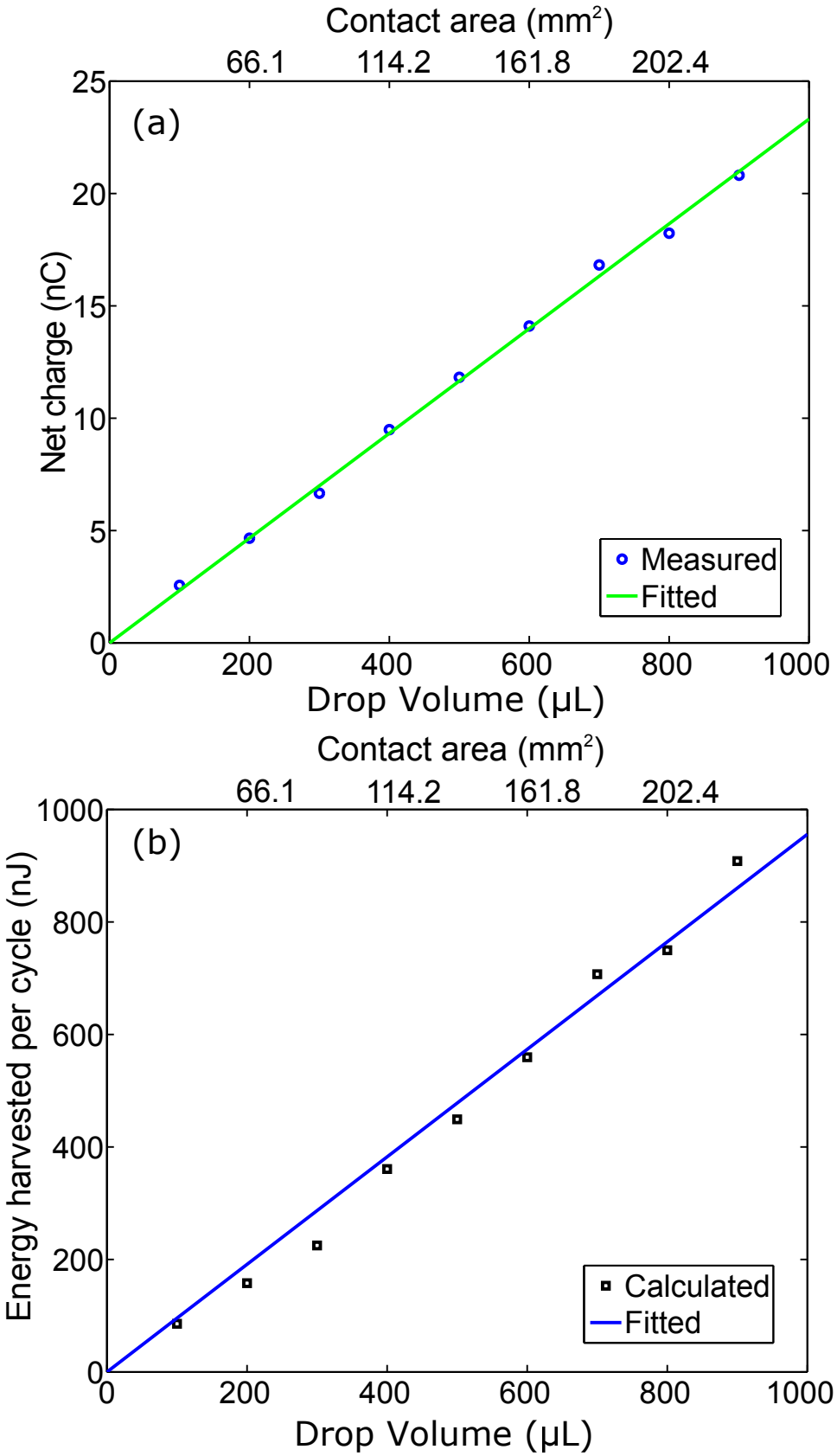

Figure 4.5: Effect of drop volume on device performance. **(a).** Net charge generated. **(b).** Energy harvested per cycle.

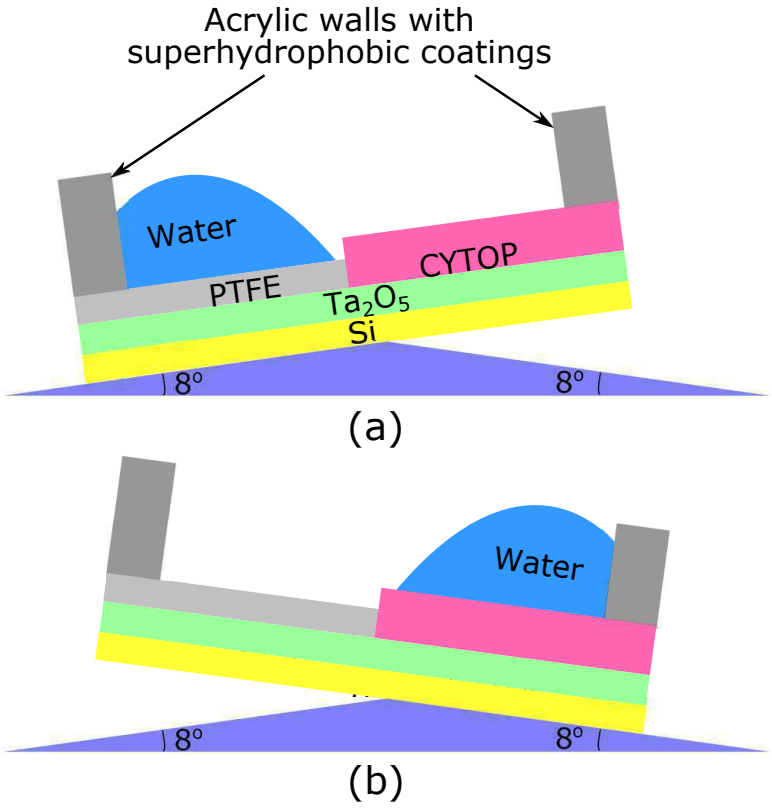

Figure 4.6: A prototype generator driven manually on inclined surfaces. **(a).** The water droplet located on PTFE. **(b).** The water droplet located on CYTOP.

4.3 Experimental data and results

4.3.1 Two hydrophobic regions with similar thicknesses

Here we present the results from a harvester, in which the thicknesses of the PTFE and CYTOP were 6.6 μm and 10 μm, respectively. A tungsten contact was used at each side for the connection to the external circuit. Multiple contacts were first made between water and the CYTOP and the PTFE surface to create a charged surface. A fresh water droplet was then deposited respectively onto the surfaces and the charge induced in the drop was measured with an electrometer using the silicon substrate as the reference. In this study, PTFE and CYTOP acquired -10.7 nC/cm^2 and -1.8 nC/cm^2, respectively. In order to study the induced charge when a water droplet moves across the junction, a 400 μL water droplet was first placed on the PTFE surface with the induced

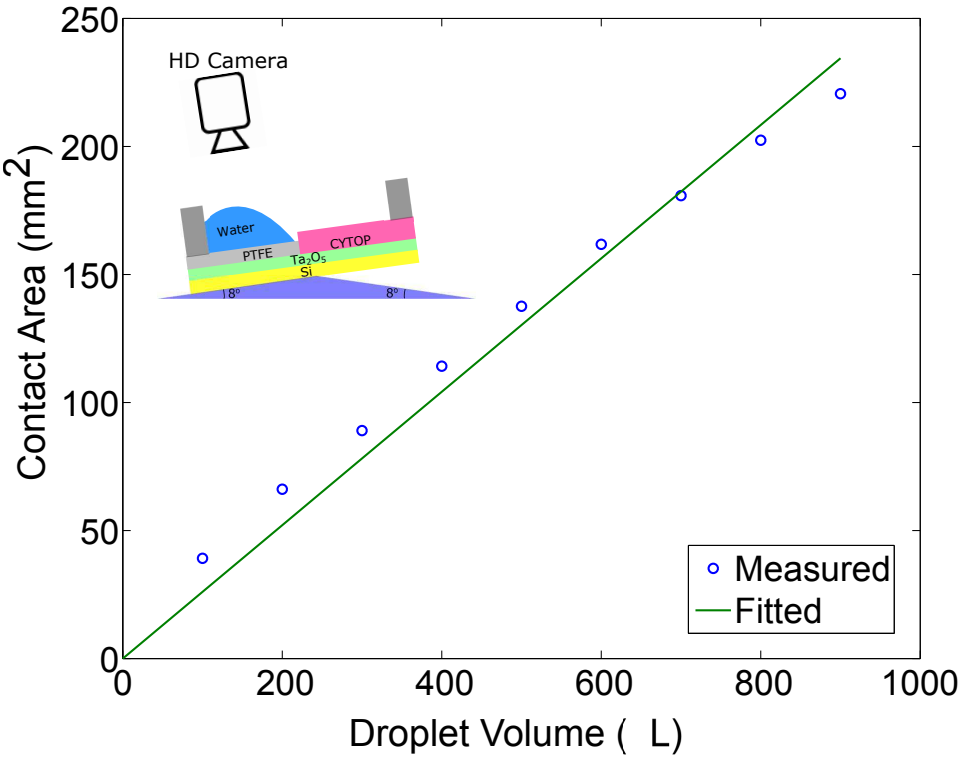

Figure 4.7: The relationship between the drop volume and the contact area.

charge zeroed by connecting a short circuit between the drop and the silicon substrate. The drop was then moved across the junction towards the CYTOP surface with the induced charge measured at different locations. The results are shown in Figure 4.3. The linear relationship is consistent with the model indicated by Eq. (4.1). The difference in surface charge densities of the two surfaces can be determined from Figure 4.3 to be 9.4 nC/cm^2, which is consistent with that (8.9 nC/cm^2) obtained from direct measurements of the two surface charge densities.

To evaluate its effectiveness in harvesting energy from low-frequency vibrations, the harvester was first driven by a 2.5 Hz excitation, a frequency close to those of vibrations induced by human walking. A 400 μL water droplet and a resistor of 1 MΩ were used in the experiments. The contact areas were calculated to be $A_p \approx A_c \approx 1.14$ cm^2. The capacitance when the water droplet was on CYTOP and PTFE was measured statically to be 0.23 nF and 0.28 nF, respectively. Figure 4.4**(a)** shows the voltages measured between the water droplet and the substrate. Power was delivered to the resistor whenever the water droplet moved across the

surface, i.e. twice in a cycle. When the water droplet was driven from the PTFE to the CYTOP surface, the voltage increased from 0 V to 40 V immediately before the resistor was connected. When the drop was driven back to the PTFE surface after releasing the positive potential to the resistor, the voltage changed from 0 V to -23.5 V. The asymmetry of the positive and negative peak values was due to the different capacitance associated with the two regions. Such difference in capacitance resulted from several factors associated with the two regions, including differences in thicknesses, dielectric constants, and dynamic contact areas, etc. In order to evaluate its performance under excitations of ultra-low driving frequencies, such as those of vibrations of large, flexible structures [99], the harvester was manually driven on inclined surfaces (Figure 4.6) at a very low frequency, about 0.25 Hz. Figure 4.4**(b)** shows the output voltages of the harvester. A manual switch was used to close the circuit so that the charge could be delivered to the load. When the water droplet moved from the PTFE to the CYTOP surface, the open-circuit voltage was about 42 V while the corresponding charge was measured to be 9.5 nC, which is consistent to the estimated value of 10.1 nC based on Eq. (4.1). The open-circuit voltage stayed at the same value when the water droplet was held in the same place. This confirms the capacitive behavior of the device. After the drop was discharged, the water droplet was moved back to the PTFE surface. An open-circuit voltage of -34 V was then obtained. The corresponding charge was measured to be -9.5 nC. The difference in the capacitance associated with the CYTOP and the PTFE surfaces accounted for the different positive and negative peak voltages. The ripples, shown in Figure 4.4**(b)**, were due to the damped vibrations of the water droplet when it collided with the acrylic walls at each end. Cases involving water droplets of different sizes were also studied. Figure 4.7 shows the relationship between the drop volume and contact area. The contact area was estimated using the image provided by a HD camera when the water droplet stayed on an 8^o inclined PTFE surface with acrylic walls. Because the contact area was found to be proportional to the volume of the water drop, a linear relationship between the amount of induced charge and the contact area was observed as expected (Figure 4.5**(a)**). Using Eq. (2), one can estimate the energy harvested

per cycle as shown in Figure 4.5**(b)**. The linear relationship indicates an energy density of 0.36 μJ/cm^2 per cycle.

4.3.2 Enhanced performance with a variable capacitor-based scheme

The open-circuit voltages obtained with this scheme under a 2.5 Hz vibration were measured continuously. They are presented in Figure 4.8**(a)** for the case of a zero bias and in Figure 4.8**(b)** for the case of an 8 V bias. In this scenario, because the external bias is applied when the drop is on PTFE, the measured voltage on the PTFE side is the same as the applied bias. Therefore, the voltages shown in Figure 4.8**(a)** and 4.8**(b)** are non-negative. For a 400 μL water drop, the peak voltage reached 44 V and 115 V for the two cases, respectively. Note that with a more than 10-fold decrease in the thickness of the CYTOP layer, i.e. from 6.6 μm to 0.5 μm, the increase in voltage was less than 5%, i.e. from 42 V shown in Figure 4.4 to 44 V. Because such thickness variation does not change the thickness of the double layer at the interface, the resulting slight change in the peak voltage indicates the electrostatic induction in the silicon substrate was negligible in this case.

The effects of the external bias were studied by using different values in experiments and measuring the open-circuit voltages as shown in Figure 4.9. The water droplet was driven from the PTFE to the CYTOP surface by introducing an 8° inclination. The open-circuit voltages were measured when the drop was on CYTOP. As shown in Figure 4.9**(a)**, the open-circuit voltage was proportional to the applied bias. It reached 33 V and 92 V for a zero and an 8 V bias, respectively. The peak values presented in Figure 4.8**(a)** and 4.8**(b)** are higher because of the overshoot resulting from the collisions of the drop and acrylic wall. Note that not all charge will move with the drop if it moves from one material to the other [90, 91, 29]. However, if the drop is always discharged before it moves to the other material, the leftover charge from the previous cycle will always be discharged, leaving no effect on the harvest energy as shown in Figure 4.4. In this scenario, the drop was discharged only on CYTOP; thus, the leftover charge on PTFE need to be included in the calculation of the energy harvested. Figure 4.10 illustrates the charge trapping

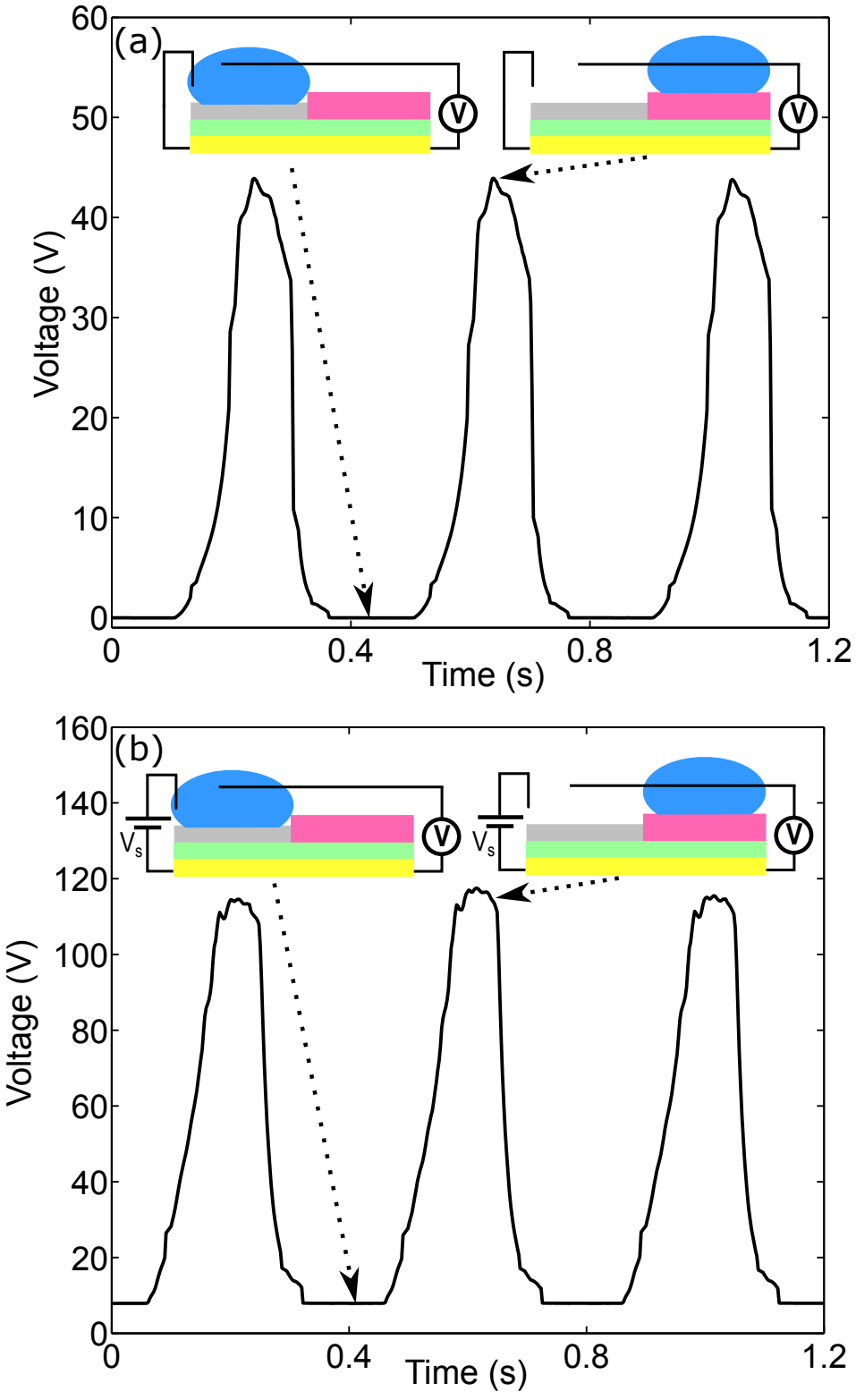

Figure 4.8: Results from devices using an external bias to enhance performance. **(a).** The open-circuit voltages with a zero external bias, i.e. $V_s = 0$. **(b).** The open-circuit voltages under an $V_s = 8V$ bias.

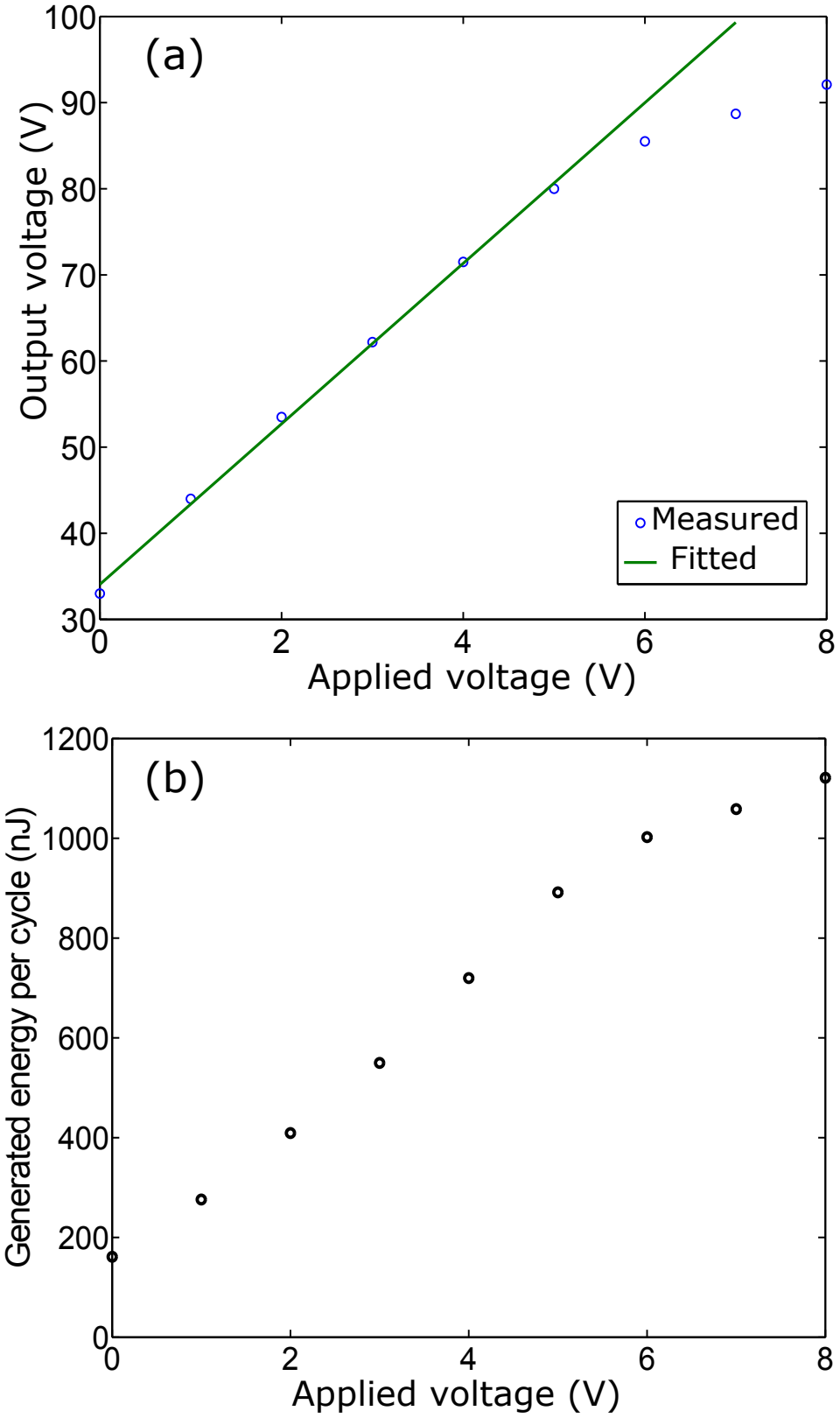

Figure 4.9: Performance of devices applied with various voltage. **(a).** Peak voltages versus external bias. **(b).** Energy generated per cycle versus external bias.

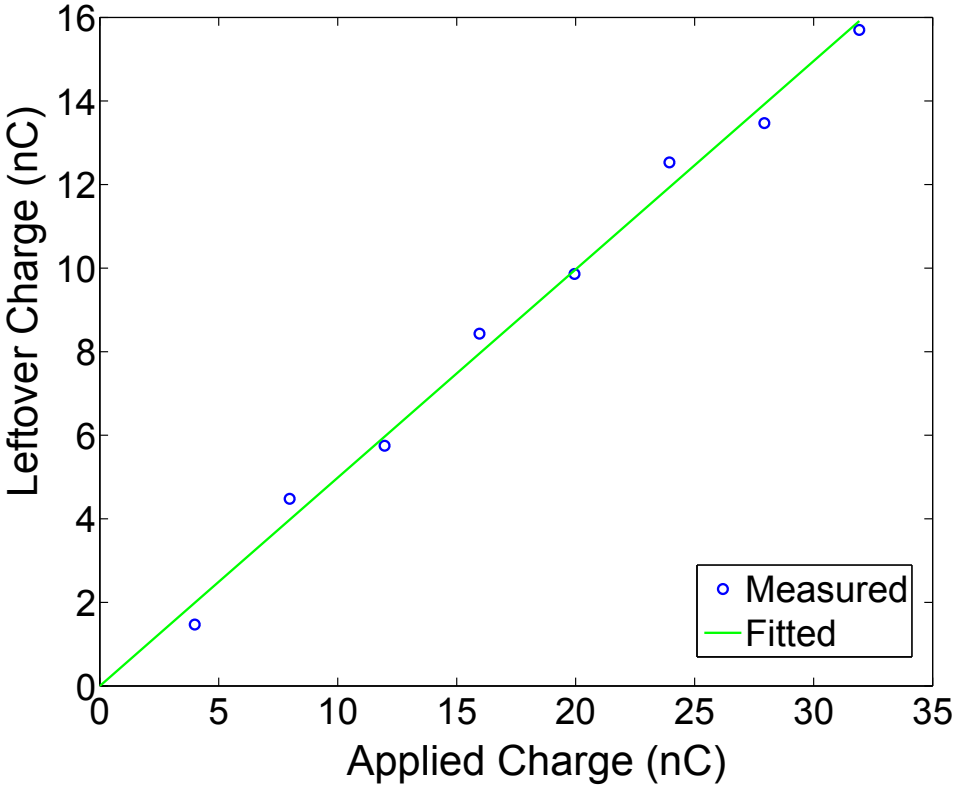

Figure 4.10: Charge remaining on PTFE after the water droplet moved away

.

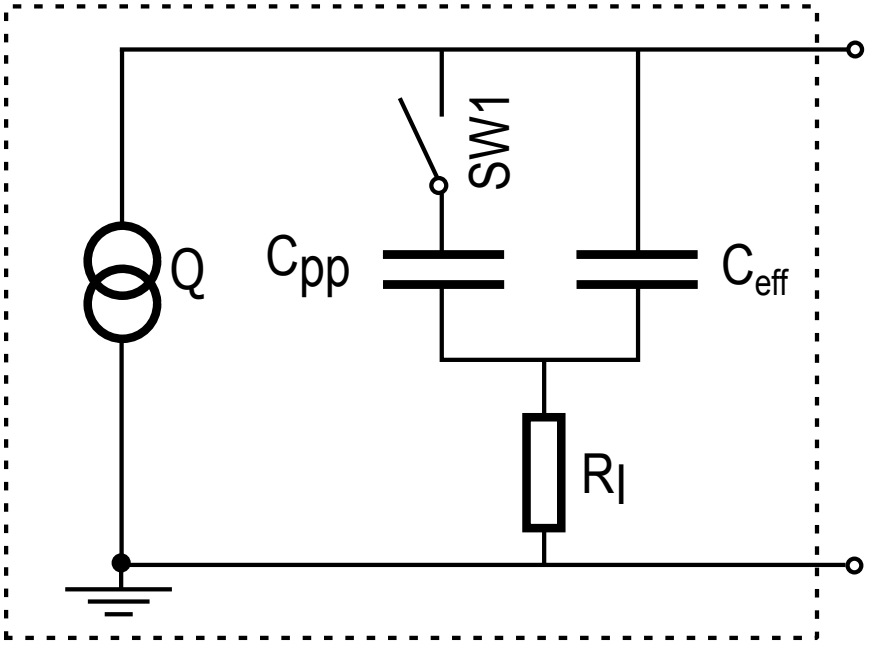

Figure 4.11: Circuit model incorporating a parasitic capacitor to account for charge left on PTFE

.

effect versus applied charge. The water droplet was first charged by an external voltage source when the drop was on PTFE. The drop was then driven to CYTOP, where it was discharged. Finally, the drop returned to PTFE and an electrometer Keithley 6517B was used to measure the charge in the drop. The remaining charge shown in the figure is the sum of the measurement of 6517B and Q_c. The experimental results suggest that the leftover charge is linearly proportional to the applied bias. A parasitic capacitor, therefore, can be used to model such a behavior as shown in Figure 4.11. When the water droplet is on PTFE, the total capacitance is $C_p = C_{pp} + C_{pr}$, where C_{pp} denotes the parasitic capacitance and C_{pr} the actual effective capacitance. When the drop is on PTFE, SW1 is closed to allow C_{pp} to be charged. When the water droplet moves away from the PTFE surface, SW1 is open so that the charge in C_{pp} remains on PTFE. The effective capacitance of the water droplet is denotd by C_{eff}, which is $C_{eff} = C_{pr}$ when the drop is on PTFE and $C_{eff} = C_c$ when it is on CYTOP. The net energy harvested per cycle, which is the difference between the total raised potential energy and the initial energy input from the bias, can thus be calculated. The results are shown in Figure 4.9**(b)**. According to the data collected, a higher bias increases the harvested energy. For example, the energy harvested per cycle increased from 0.16 μJ with a zero bias to 1.12 μJ with an 8 V bias. Figure 4.12 demonstrates that the energy harvested from a low-frequency vibration by a water droplet is sufficient to illuminate commercial LEDs. Under a 2.5 Hz vibration, a harvester illuminated 15 commercial LEDs that were connected in series (Figure 4.12**(a)**) with a zero bias. Under an 8 V bias, it illuminated 30 commercial LEDs connected in series (Figure 4.12**(b)**).

One of the unique features of the proposed approach is that the hydrophobic surface is created with two materials, i.e. PTFE and CYTOP, which acquire very different amount of saturated, negative charge from contact electrification. In particular, a -8.9 nC/cm^2 difference in surface charge density was obtained, which triggered strong electrostatic induction so that energy could be harvested efficiently as electric potential energy. Furthermore, the electrical energy can be delivered to external circuits at its peak value via a simple passive switching mechanism. Because potential energy depends only on the position and not the frequency of the motions of the

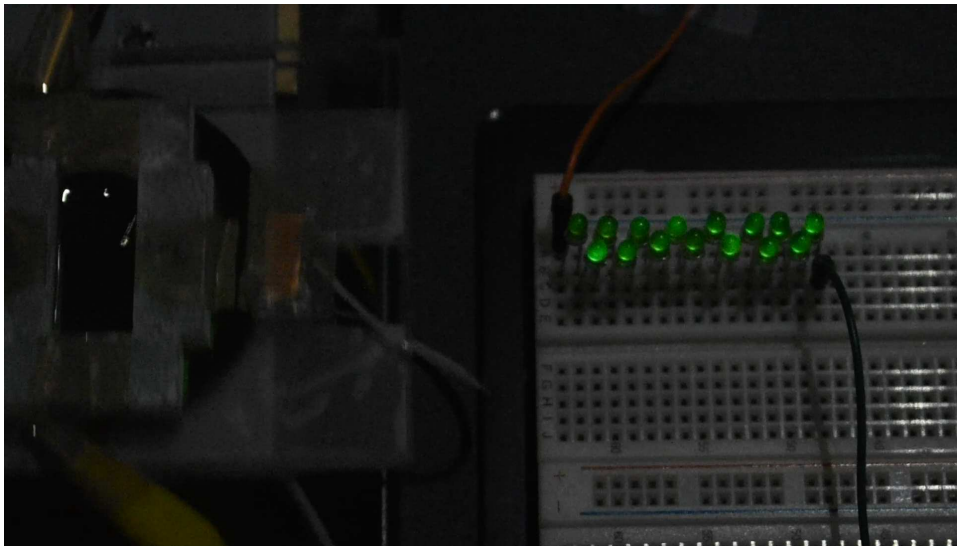

(a)

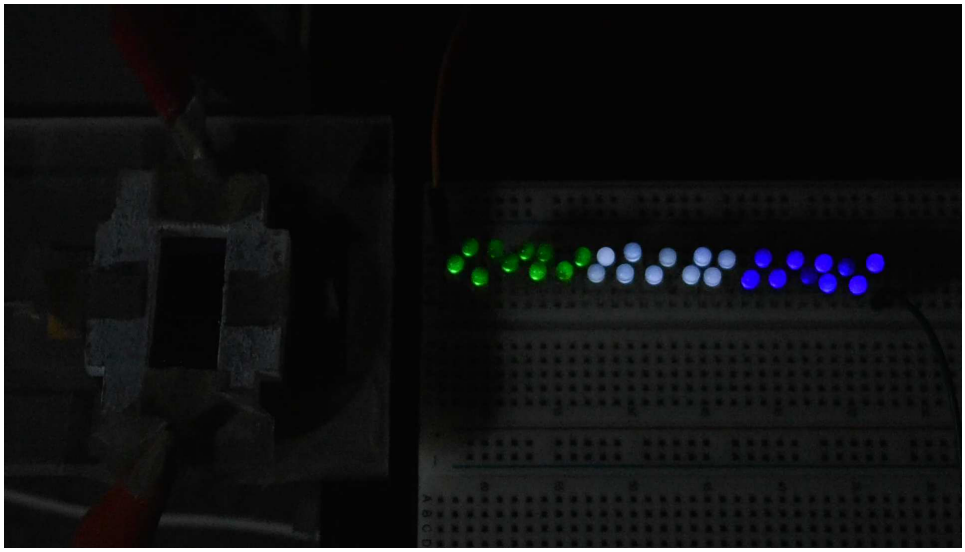

(b)

Figure 4.12: Devices using a 400 μL water droplet to illuminate commercial LEDs. **(a).** 15 green LEDs lit a zero external bias. **(b).** 30 LEDs (10 green LEDs, 10 white LEDs, and 10 blue LEDs) lit under an 8 V bias.

water drop, this approach is suitable for harvesting energy from low-level, low-frequency excitations. It is worth noting that an 8° inclination is sufficient to drive a 400 μL water droplet to move across the two-region surface with a distance of 1.3 cm. The total mechanical potential energy available for harvesting is thus 7.1 μJ. As demonstrated in Figure 4.5**(b)**, a harvesting efficiency of 2.5% has been achieved in this study. The efficiency is independent of the load

resistance and is two orders of magnitude higher than the optimal efficiency of 0.011% reported in a previous study for triboelectric generators [100], in which a 30 μL water droplet harvested 30 nJ from the released potential energy, 265 μJ, of the droplet falling from a height of 90 cm. When vibratory excitations are concerned, a 1.5 μW optimal power output has been reported with 1 mL of water (24 droplets, 42 μL each) based on existing methodology [53]. If driven under the same vibration, our device would produce 27 μW, an 18-fold increase. Although nanocomposite materials with improved properties, e.g. MoS_2/PDMS, can be used to improve the efficiency of existing triboelectrical energy harvesting schemes [101], such improvement is limited by the strength of the electrostatic induction in the substrate.

In summary, electrostatic energy harvesting relies on the work done by the external energy source against electrostatic forces between opposite charges. Therefore, an electrostatic harvester behaves capacitively in nature and prefers more charges to be involved and a wider range of capacitance change. The use of different materials in creating a hydrophobic surface allows for a continuous electrostatic induction process, leading to an alternate current when the water droplet is driven across the surface continuously. The performance can be further improved if materials with larger difference in surface charge densities are used. For example, if the hydrophobic surface can be created with PTFE and a material that acquires positive charge through contact electrification, the amount of induced charge in the water droplet will greatly increase, resulting in much increased electric potential energy.

As demonstrated, this method can effectively harvest energy from low-level, low-frequency energy sources. It may lead to methods for harvesting energy from motions of liquids ranging from ocean waves [102] to falling raindrops [103, 104]. While a silicon substrate was used as the back electrode in this study, flexible substrates such as graphene can be used instead. With enclosed designs and proper packaging strategies [29, 53], flexible, encapsulated devices can be fabricated. As the method works without an external electrical source, it holds potential in applications such as self-powered wearable electronics [105].

5 CONCLUSIONS AND FUTURE WORK

5.1 Conclusions

Electrostatic energy harvesting is one promising solution to generate electricity from ambient energy sources. Compared to other methods, electrostatic approach has various advantages. However, some challenges still exist, such as relatively small initial charge and capacitance, requirement of an external power supply, and complex power management control circuits to extract generated energy at the appropriate time. The aim of this dissertation is to find solutions to overcome the current challenges of electrostatic energy harvesting, thus making the method more practical in applications.

Two novel methods have been proposed in this dissertation. The first method utilizes an appropriate, repetitive reconfiguration process of the system to create a positive feedback mechanism, in which even a small disturbance on a system could significantly increase the amplitude of electric output. Because of the exponentially increasing rate of energy extraction, this method is particularly effective for distributed devices to scavenge energy from low-level ambient sources. Furthermore, the proposed method can be applied in various energy sources. The novel concept has been studied both theoretically and validated with results from the proposed systems. As a proof of concept, two commercial rotary variable capacitors in addition with one constant ceramic capacitor were chosen to build the positive-feedback system to harvest mechanical energy. In the rotary variable capacitor, air was used as the dielectric material. A rotating shaft was used to change the capacitance. Passive switches were fabricated so that two configurations of the system can be achieved by rotating the shafts of the capacitors. In the

experiments, a small amount of charge transfer was observed when two metal needles were manually brought into contact, which brought extra charge in each energy harvesting cycle. For the source capacitor, one commercial ceramic capacitor with constant capacitance was chosen for the system. In this system, if the maximum and minimum capacitance has been determined, the growth rate of the system reaches the maximum value under an optimal source capacitance. It has been theoretically proven and experimentally verified that the electric outputs of the system can grow exponentially if a certain condition is satisfied. The measured data agree well with the theoretical modeling. The capacitance of a rotary variable capacitor is only several hundred picofarads, which leads to a high voltage while only a few μJ is stored. In reality, an insulating material has finite dielectric strength, which limits the maximum working voltage for a capacitor. Therefore, a small capacitance limits the maximum coupled energy it can store, and thus limits the coupling efficiency. Compact variable capacitors with high capacitance are desired for the proposed method.

In this study, liquid-contact variable capacitors have been developed to achieve relatively high capacitance. Because of contact electrification and electrostatic induction, the contact variable capacitors can provide relatively high extra charge in each cycle. The basic components of a capacitor include two conductive plates separated by a dielectric material. In this capacitor, the droplet is movable and considered as one of the conductors for the capacitor. Non-polar material CYTOP is used as one of the dielectric materials. Compared to air variable capacitors, droplet-based contact variable capacitors use less space while achieving high capacitance. Also, when liquid is brought into contact with solid, it can minimize the gaps between them since liquid is shapeless and contact the solid very tightly, and thus lead to high contact area and capacitance. Such high contact area can cause high extra charge pumping into the system in each cycle because of contact electrification and electrostatic induction effects. In the model, this effect accelerates the charge accumulation in the first cycles. However, surface charge trapping effect only allows a portion of the charge in the droplet to be transferred, which reduces the growth rate. In the model, a parasite capacitor is used to represent this effect. Various distances between two

conductors are used as an example to establish a contact variable capacitor by fabricating various thicknesses of dielectric materials. Mercury and water are both used for the liquid-contact variable capacitors. It is shown by the experiments that the mercury-contact variable capacitors have less charge trapping effect and reach higher maximum voltage of the system than water-contact variable capacitors. Within a few cycles of a low-level, low-frequency mechanical excitation, a device with three 300 μL mercury drops generated an exponentially growing voltage that reaches 168 V, which was sufficient to illuminate 60 commercial green LEDs in each cycle. The same device with water droplets can generate a similarly growing voltage that reaches 56 V, which was sufficient to illuminate 20 commercial green LEDs in each cycle. The devices can be operated at a higher energy level with a higher efficiency. However, since energy is harvested only in the distributive state in this study, the efficiency is limited to 50% per cycle when the total potential energy in both states is considered.

The exponential method offers several advantages over the conventional electrostatic energy harvesting methods. First, the proposed method only needs two reconfigurations to achieve the positive-feedback mechanism. Therefore, the proposed method inherits all the advantages of the conventional electrostatic approaches: low-cost fabrication, high reachable energy harvesting efficiency, capability of large-scale integration and miniaturization, and enabling to harvest a variety of ambient energy sources (mechanical, thermal and chemical). Second, because of establishment of positive-feedback mechanism, the generated voltage can reach a high value without any voltage-boosting circuit, which leads to an optimal energy coupling efficiency. Third, unlike the conventional method, the generated energy can be temporarily stored in the system, without the need of a complex power management control circuit. Fourth, although we demonstrated its effectiveness in scavenging low-level environmental energy, this method can be applied at a much larger scale. If applied to high-capacitance devices [75, 106, 107] driven by abundant environmental sources [108, 102], this concept may lead to efficient, large-scale and possibly grid-level DC power supply systems. In this regard, it is envisioned the proposed method will stimulate the emergence of new research areas, supercapacitors for example, with a wide

range of adjustable capacitance. Because the concept of exponential energy harvesting is not domain specific, it may lead to new research in directional energy transfer systems in various energy domains.

The other proposed method utilizes water droplets alternate contacts with CYTOP and PTFE thin films to provide high initial charge for electrostatic approach. Unlike the first proposed method, this one is only applicable to harvest mechanical energy. Because CYTOP and PTFE acquire significantly different surface charge densities during contact with water, this difference can be utilized to effectively generate electricity. The larger the difference in surface charge density, the higher the amount of the harvested energy. The use of different materials in creating a hydrophobic surface allows for a continuous electrostatic induction process, leading to an alternate current when the water droplet is driven across the surface continuously. The proposed method utilizes the strong electrostatic induction in the water droplet due to the electrical double layer formed at the interface. Therefore, it is more effective than existing methods that are based on the much weaker electrostatic induction in the substrate. Also, unlike in other methods, in which the charge of the drop is not delivered to external circuits, the water droplet in our method possesses a dual function as both an electrode and a passive switch, leading to the direct harvesting of the peak electric potential energy. The prototype devices demonstrate the effectiveness of this approach in scavenging energy from low-level and low-frequency ambient vibrations. In the experiments conducted, a water droplet of 400 μL alone could generate a peak open-circuit voltage of 42 V under a 0.25 Hz vibration. Under a 2.5 Hz vibration, the peak open-circuit voltage reached 115 V under an external bias of 8 V. The demonstrated efficiency is orders of magnitude higher than those of existing devices of similar dimensions. The performance can be further improved if materials with larger difference in surface charge densities are used. For example, if the hydrophobic surface can be created with PTFE and a material that acquires positive charge through contact electrification, the amount of induced charge in the water droplet will greatly increase, resulting in much increased electric potential energy.

5.2 Future work

In this dissertation, two novel methods have been proposed to solve the current challenges of the conventional energy harvesting. The work presented in this thesis can be extended in many aspects. Future investigations for these two proposed methods are outlined here:

- In this method, part of the generated energy is lost during the process of capacitor-to-capacitor energy transfer. Methods need to be developed to reduce such energy loss. Also, the proposed method is not domain specific. In other words, it can be applied to harvest other types of ambient energy sources. This may lead to new research in directional energy transfer systems in various energy domains. For example, this method can be used to extract energy from mixing fresh water and ocean water.

- Liquid-contact variable capacitors have been developed in the mechanical energy harvesting applications to achieve high capacitance. New types of variable capacitors with high capacitance should also be developed. Furthermore, other methodologies may improve the variety of surface charge densities.

- In the applications, the input voltage for most electrical devices is several volts while the generated voltage in the proposed methods can be significantly high. Therefore, there is a need on an efficient voltage-controlled circuit.

- In the exponential method, switches are needed to achieve repeated configurations. Metal contacts have been used as passive switches in the applications to harvest mechanical energy, which may not be applied for other types of ambient energy sources. Investigations are needed for this methodology.

REFERENCES

[1] John Conti, Paul Holtberg, Jim Diefenderfer, Angelina LaRose, James T Turnure, and Lynn Westfall. International energy outlook 2016 with projections to 2040. Technical report, USDOE Energy Information Administration (EIA), Washington, DC (United States). Office of Energy Analysis, 2016.

[2] Samir Kouro, Jose I Leon, Dimitri Vinnikov, and Leopoldo G Franquelo. Grid-connected photovoltaic systems: An overview of recent research and emerging pv converter technology. *IEEE Industrial Electronics Magazine*, 9(1):47–61, 2015.

[3] Frede Blaabjerg and Dan M Ionel. Renewable energy devices and systems–state-of-the-art technology, research and development, challenges and future trends. *Electric Power Components and Systems*, 43(12):1319–1328, 2015.

[4] Stefan Weitemeyer, David Kleinhans, Thomas Vogt, and Carsten Agert. Integration of renewable energy sources in future power systems: The role of storage. *Renewable Energy*, 75:14–20, 2015.

[5] Caineng Zou, Qun Zhao, Guosheng Zhang, and Bo Xiong. Energy revolution: From a fossil energy era to a new energy era. *Natural Gas Industry B*, 3(1):1–11, 2016.

[6] Alicia Valero, Antonio Valero, Guiomar Calvo, and Abel Ortego. Material bottlenecks in the future development of green technologies. *Renewable and Sustainable Energy Reviews*, 93:178–200, 2018.

[7] Donghee Son, Jongha Lee, Shutao Qiao, Roozbeh Ghaffari, Jaemin Kim, Ji Eun Lee, Changyeong Song, Seok Joo Kim, Dong Jun Lee, Samuel Woojoo Jun, et al. Multifunctional wearable devices for diagnosis and therapy of movement disorders. *Nature nanotechnology*, 9(5):397, 2014.

[8] Mitesh S Patel, David A Asch, and Kevin G Volpp. Wearable devices as facilitators, not drivers, of health behavior change. *Jama*, 313(5):459–460, 2015.

[9] Geetha Manivasagam, Durgalakshmi Dhinasekaran, and Asokamani Rajamanickam. Biomedical implants: Corrosion and its prevention-a review. *Recent patents on corrosion science*, 2010.

[10] Analod Devices. Adxl362-micropower, 3-axis,$\pm$2 g/$\pm$4 g/$\pm$8 g, digital output mems accelerometer, rev, 2013.

[11] Christian Piguet. *Low-power electronics design*. CRC press, 2004.

[12] Kateryna Bazaka and Mohan V. Jacob. Implantable devices: Issues and challenges. *Electronics*, 2:1–34, 2012.

[13] Kateryna Bazaka and Mohan V Jacob. Implantable devices: issues and challenges. *Electronics*, 2(1):1–34, 2012.

[14] Dennis Fitzpatrick. *Implantable electronic medical devices*. Elsevier, 2014.

[15] S Boisseau, G Despesse, S Monfray, O Puscasu, and T Skotnicki. Semi-flexible bimetal-based thermal energy harvesters. *Smart Materials and Structures*, 22(2), 2013.

[16] Scott Meninger, Jose Oscar Mur-Miranda, Rajeevan Amirtharajah, Anantha Chandrakasan, and Jeffrey H Lang. Vibration-to-electric energy conversion. *IEEE Transactions on Very Large Scale Integration (VLSI) Systems*, 9(1):64–76, 2001.

[17] S Boisseau, G Despesse, and B Ahmed Seddik. Electrostatic conversion for vibration energy harvesting. *Small-scale Energy Harvesting*, 2012.

[18] S. Meninger, J. Mur-Miranda, R. Amirtharajah, A. Chandrakasan, and J. Lang. Vibration-to-electric energy conversion. *Very Large Scale Integration (VLSI) Systems, IEEE Transactions*, 9:64–76, 2001.

[19] K. Bult, A. Burstein, D. Chang, M. Dong, M. Fielding, E. Kruglick, and J. Ho. Low power systems for wireless microsensors. *In Low Power Electronics and Design*, pages 17–21, 1996.

[20] G. Asada, M. Dong, T. Lin, F. Newberg, G. Pottie, W. Kaiser, and H. Marcy. Wireless integrated network sensors: Low power systems on a chip. In *In Solid-State Circuits Conference*, 1998.

[21] R. Amirtharajah and A. Chandrakasan. Self-powered signal processing using vibration-based power generation. *Solid-State Circuits*, 33:687–695, 1998.

[22] CB Williams and Rob B Yates. Analysis of a micro-electric generator for microsystems. *sensors and actuators A: Physical*, 52(1-3):8–11, 1996.

[23] S. P. Beeby, M. J. Tudor, and N. M. White. Energy harvesting vibration sources for microsystems applications. *Measurement science and technology*, 17:R175, 2006.

[24] Adnan Harb. Energy harvesting: State-of-the-art. *Renewable Energy*, 36(10):2641–2654, 2011.

[25] R. Tashiro, N. Kabei, K. Katayama, E. Tsuboi, and K. Tsuchiya. Development of an electrostatic generator for a cardiac pacemaker that harnesses the ventricular wall motion. *Journal of Artificial Organs*, 5:0239–0245, 2002.

[26] Ghislain Despesse, Thomas Jager, Chaillout Jean-Jacques, Jean-Michel Léger, Andrea Vassilev, Skandar Basrour, and Benoit Charlot. Fabrication and characterization of high damping electrostatic micro devices for vibration energy scavenging. In *Proc. Design, Test, Integration and Packaging of MEMS and MOEMS*, pages 386–390, 2005.

[27] S. Roundy, P. Wright, and K. Pister. Micro-electrostatic vibration-to-electricity converters. In *In ASME 2002 International Mechanical Engineering Congress and Exposition*, 2002.

[28] Masayuki Miyazaki, Hidetoshi Tanaka, Goichi Ono, Tomohiro Nagano, Norio Ohkubo, Takayuki Kawahara, and Kazuo Yano. Electric-energy generation using variable-capacitive resonator for power-free lsi: efficiency analysis and fundamental experiment. In *Low Power Electronics and Design, 2003. ISLPED'03. Proceedings of the 2003 International Symposium on*, pages 193–198. IEEE, 2003.

[29] T. Krupenkin and J. Taylor. Reverse electrowetting as a new approach to high-power energy harvesting. *Nature Communications*, 2:448, 2011.

[30] Ron Pelrine, Roy D Kornbluh, Joseph Eckerle, Philip Jeuck, Seajin Oh, Qibing Pei, and Scott Stanford. Dielectric elastomers: Generator mode fundamentals and applications. In *Smart Structures and Materials 2001: Electroactive Polymer Actuators and Devices*, volume 4329, pages 148–157. International Society for Optics and Photonics, 2001.

[31] Claire Jean-Mistral, Skandar Basrour, and Jean-Jacques Chaillout. Dielectric polymer: scavenging energy from human motion. In *Electroactive Polymer Actuators and Devices (EAPAD) 2008*, volume 6927, page 692716. International Society for Optics and Photonics, 2008.

[32] Christian Graf and Jrgen Maas. Evaluation and optimization of energy harvesting cycles using dielectric elastomers. In *SPIE Smart Structures and Materials+ Nondestructive Evaluation and Health Monitoring*, 2011.

[33] Rainer Kaltseis, Christoph Keplinger, Richard Baumgartner, Martin Kaltenbrunner, Tiefeng Li, Philipp Mächler, Reinhard Schwödiauer, Zhigang Suo, and Siegfried Bauer. Method for measuring energy generation and efficiency of dielectric elastomer generators. *Applied Physics Letters*, 99(16):162904, 2011.

[34] P Gunther, H Ding, and R Gerhard-Multhaupt. Electret properties of spin-coated teflon-af films. In *Electrical Insulation and Dielectric Phenomena, 1993. Annual Report., Conference on*, pages 197–202. IEEE, 1993.

[35] R Kressmann, GM Sessler, and P Gunther. Space-charge electrets. *IEEE Transactions on Dielectrics and Electrical Insulation*, 3(5):607–623, 1996.

[36] P Kotrappa. Long term stability of electrets used in electret ion chambers. *Journal of Electrostatics*, 66(7-8):407–409, 2008.

[37] Reinhard Schwödiauer, Gerhard S Neugschwandtner, Simona Bauer-Gogonea, Siegfried Bauer, and Tom Rosenmayer. Dielectric and electret properties of nanoemulsion spin-on polytetrafluoroethylene films. *Applied Physics Letters*, 76(18):2612–2614, 2000.

[38] Yuji Suzuki, Daigo Miki, Masato Edamoto, and Makoto Honzumi. A MEMS electret generator with electrostatic levitation for vibration-driven energy-harvesting applications. *Journal of Micromechanics and Microengineering*, 20(10):104002, 2010.

[39] P Gunther. Charging, long-term stability, and TSD measurements of SiO_2 electrets. *IEEE Transactions on Electrical Insulation*, 24(3):439–442, 1989.

[40] T. Sterken, K. Baert, R. Puers, and G. Borghs. Power extraction from ambient vibration. In *In SeSens 2001. Dutch Technology Foundation STW*, 2001.

[41] Urlich Mescheder, P Urbanovic, B Muller, and Safi Baborie. Charging of SiO_2 electret film by ion implantation for mems based energy harvesting systems. In *Proceedings of PowerMEMS 2008+ microEMS2008*, pages 501–504, 2008.

[42] Gerhard Martin Sessler and Keshawa Shahi. Electrets, topics in applied physics. *Journal of The Electrochemical Society*, 127(12):530C–530C, 1980.

[43] Takumi Tsutsumino, Yuji Suzuki, Nobuhide Kasagi, and Yoshihiko Sakane. Seismic power generator using high-performance polymer electret. In *Micro Electro Mechanical Systems,*

2006. MEMS 2006 Istanbul. 19th IEEE International Conference on, pages 98–101. IEEE, 2006.

[44] Tom Sterken, P Fiorini, G Altena, Chris Van Hoof, and Robert Puers. Harvesting energy from vibrations by a micromachined electret generator. In *Solid-State Sensors, Actuators and Microsystems Conference, 2007. TRANSDUCERS 2007. International*, pages 129–132. IEEE, 2007.

[45] Yuji Suzuki, Masato Edamoto, Nobuhide Kasagi, K Kashwagi, and Yoshitomi Morizawa. Micro electret energy harvesting device with analogue impedance conversion circuit. *Proc. PowerMEMS*, 8:7–10, 2008.

[46] Y. Suzuki. Recent progress in mems electret generator for energy harvesting. *IEEJ Transactions on Electrical and Electronic Engineering*, 6:101–111, 2011.

[47] Wouter Olthuis and Piet Bergveld. On the charge storage and decay mechanism in silicon dioxide electrets. *IEEE Transactions on Electrical Insulation*, 27(4):691–697, 1992.

[48] Amarjit S Dhaliwal and KS Mann. Charge decay and relaxation times in electrets. 2001.

[49] Guang Zhu, Caofeng Pan, Wenxi Guo, Chih-Yen Chen, Yusheng Zhou, Ruomeng Yu, and Zhong Lin Wang. Triboelectric-generator-driven pulse electrodeposition for micropatterning. *Nano Letters*, 12(9):4960–4965, 2012.

[50] Guang Zhu, Zong-Hong Lin, Qingshen Jing, Peng Bai, Caofeng Pan, Ya Yang, Yusheng Zhou, and Zhong Lin Wang. Toward large-scale energy harvesting by a nanoparticle-enhanced triboelectric nanogenerator. *Nano letters*, 13(2):847–853, 2013.

[51] Zhong Lin Wang. Triboelectric nanogenerators as new energy technology for self-powered systems and as active mechanical and chemical sensors. *ACS Nano*, 7:9533–9557, 2013.

[52] Long Lin Sangmin Lee Zhong Lin Wang Zong-Hong Lin, Gang Cheng. Watersolid surface contact electrification and its use for harvesting liquid-wave energy. *Angewandte Chemie International Edition*, 52:12545–12549, 2013.

[53] Dongyun Lee Jong Kyun Moon, Jaeki Jeong and Hyuk Kyu Pak. Electrical power generation by mechanically modulating electrical double layers. *Nature Communications*, 4:1487, 2013.

[54] R. Kotz and M. Carlen. Principles and applications of electrochemical capacitors. *Electrochimica Acta*, 45:2483–2498, 2000.

[55] P. Simon and Y. Gogotsi. Materials for electrochemical capacitors. *Nature Materials*, 7:845–854, 2008.

[56] H. Becker. Low voltage electrolytic capacitor, 1957.

[57] A. K. Shukla, S. Sampath, and K. Vijayamohanan. Electrochemical supercapacitors: Energy storage beyond batteries. *Current Science*, 79(12):1656–1661, 2000.

[58] Atsushi Nishino, Akihiko Yoshida, and Ichiroh Tanahashi. Electric double layer capacitor, December 31 1985. US Patent 4,562,511.

[59] A. Yoshida I. Tanahashi and A. Nishino. Electrochemical characterization of activated carbon-fiber cloth polarizable electrodes for electric double-layer capacitors. *Journal of The Electrochemical Society*, 137:3052–3057, 1990.

[60] D. Grahame. The electrical double layer and the theory of electrocapillarity. *Chemical Reviews*, 41:441–501, 1947.

[61] Brian E Conway. *Electrochemical supercapacitors: scientific fundamentals and technological applications*. Springer Science & Business Media, 2013.

[62] Deyang Qu and Hang Shi. Studies of activated carbons used in double-layer capacitors. *Journal of Power Sources*, 74(1):99–107, 1998.

[63] Gregory Salitra, Abraham Soffer, Linoam Eliad, Yair Cohen, and Doron Aurbach. Carbon electrodes for double-layer capacitors i. relations between ion and pore dimensions. *Journal of the Electrochemical Society*, 147(7):2486–2493, 2000.

[64] M Endo, T Maeda, T Takeda, YJ Kim, K Koshiba, H Hara, and MS Dresselhaus. Capacitance and pore-size distribution in aqueous and nonaqueous electrolytes using various activated carbon electrodes. *Journal of the Electrochemical Society*, 148(8):A910–A914, 2001.

[65] E Raymundo-Pinero, K Kierzek, J Machnikowski, and F Béguin. Relationship between the nanoporous texture of activated carbons and their capacitance properties in different electrolytes. *Carbon*, 44(12):2498–2507, 2006.

[66] R. W. Pekala, J. C. Farmer, C. T. Alviso, T. D. Tran, S. T. Mayer, J. M. Miller, and B. Dunn. Carbon aerogels for electrochemical applications. *Journal of Non-Crystalline Solids*, 225:74–80, 1998.

[67] R Saliger, U Fischer, C Herta, and J Fricke. High surface area carbon aerogels for supercapacitors. *Journal of Non-Crystalline Solids*, 225:81–85, 1998.

[68] C Moreno-Castilla and FJ Maldonado-Hódar. Carbon aerogels for catalysis applications: An overview. *Carbon*, 43(3):455–465, 2005.

[69] Sander J Tans, Alwin RM Verschueren, and Cees Dekker. Room-temperature transistor based on a single carbon nanotube. *Nature*, 393(6680):49, 1998.

[70] Soshi Shiraishi, Hideyuki Kurihara, Keiji Okabe, Denisa Hulicova, and Asao Oya. Electric double layer capacitance of highly pure single-walled carbon nanotubes (hipco buckytubes) in propylene carbonate electrolytes. *Electrochemistry Communications*, 4(7):593–598, 2002.

[71] J. N. Barisci, G. G. Wallace, D. R. MacFarlane, and R. H. Baughman. Investigation of ionic liquids as electrolytes for carbon nanotube electrodes. *Electrochemistry Communications*, 6(1):22–27, 2004.

[72] Yan Wang, Zhiqiang Shi, Yi Huang, Yanfeng Ma, Chengyang Wang, Mingming Chen, and Yongsheng Chen. Supercapacitor devices based on graphene materials. *The Journal of Physical Chemistry C*, 113(30):13103–13107, 2009.

[73] Chenguang Liu, Zhenning Yu, David Neff, Aruna Zhamu, and Bor Z Jang. Graphene-based supercapacitor with an ultrahigh energy density. *Nano letters*, 10(12):4863–4868, 2010.

[74] Maher F El-Kady, Veronica Strong, Sergey Dubin, and Richard B Kaner. Laser scribing of high-performance and flexible graphene-based electrochemical capacitors. *Science*, 335(6074):1326–1330, 2012.

[75] D. Brogioli. Extracting renewable energy from a salinity difference using a capacitor. *Physical Review Letters*, 103:058501, 2009.

[76] Raul A. Rica, Roberto Ziano, Domenico Salerno, Francesco Mantegazza, Rene van Roij, and Doriano Brogioli. Capacitive mixing for harvesting the free energy of solutions at different concentrations. *Entropy*, 15(4):1388, 2013.

[77] D Brogioli, R Zhao, and PM Biesheuvel. A prototype cell for extracting energy from a water salinity difference by means of double layer expansion in nanoporous carbon electrodes. *Energy & Environmental Science*, 4(3):772–777, 2011.

[78] B. B. Sales, M. Saakes, J. W. Post, C. J. N. Buisman, P. M. Biesheuvel, and H. V. M. Hamelers. Direct power production from a water salinity difference in a membrane-modified supercapacitor flow cell. *Environmental Science & Technology*, 44(14):5661–5665, 2010.

[79] Andreas Härtel, Mathijs Janssen, Daniel Weingarth, Volker Presser, and René van Roij. Heat-to-current conversion of low-grade heat from a thermocapacitive cycle by supercapacitors. *Energy & Environmental Science*, 8(8):2396–2401, 2015.

[80] Fabio La Mantia, Mauro Pasta, Heather D Deshazer, Bruce E Logan, and Yi Cui. Batteries for efficient energy extraction from a water salinity difference. *Nano Letters*, 11(4):1810–1813, 2011.

[81] John T Stock and Mary Virginia Orna. *Electrochemistry, past and present*. ACS Publications, 1989.

[82] Seok Woo Lee, Yuan Yang, Hyun-Wook Lee, Hadi Ghasemi, Daniel Kraemer, Gang Chen, and Yi Cui. An electrochemical system for efficiently harvesting low-grade heat energy. *Nature Communications*, 5:3942, 2014.

[83] Jian Yu, Enze Ma, and Tianwei Ma. Exponential energy harvesting through repetitive reconfigurations of a system of capacitors. *Communications Physics*, 1(1):9, 2018.

[84] Philip Hofmann. *Solid state physics: an introduction*. John Wiley & Sons, 2015.

[85] J. Lowell and A. C. Rose-Innes. Contact electrification. *Advances in Physics*, 29(6):947–1023, 1980.

[86] Roger G Horn and Douglas T Smith. Contact electrification and adhesion between dissimilar materials. *Science*, 256(5055):362–364, 1992.

[87] Roger G Horn, DT Smith, and A Grabbe. Contact electrification induced by monolayer modification of a surface and relation to acid–base interactions. *Nature*, 366(6454):442, 1993.

[88] HT Baytekin, AZ Patashinski, M Branicki, Bilge Baytekin, S Soh, and Bartosz A Grzybowski. The mosaic of surface charge in contact electrification. *Science*, 333(6040):308–312, 2011.

[89] Zong-Hong Lin, Gang Cheng, Sangmin Lee, Ken C Pradel, and Zhong Lin Wang. Harvesting water drop energy by a sequential contact-electrification and electrostatic-induction process. *Advanced Materials*, 26(27):4690–4696, 2014.

[90] H. J. J. Verheijen and M. W. J. Prins. Reversible electrowetting and trapping of charge: model and experiments. *Langmuir*, 15(20):6616–6620, 1999.

[91] M. K. Kilaru, J. Heikenfeld, G. Lin, and J. E. Mark. Strong charge trapping and bistable electrowetting on nanocomposite fluoropolymer: $BaTiO_3$ dielectrics. *Applied Physics Letters*, 90:212906, 2007.

[92] Jian Yu, Enze Ma, and Tianwei Ma. Harvesting energy from low-frequency excitations through alternate contacts between water and two dielectric materials. *Scientific reports*, 7(1):17145, 2017.

[93] J Lowell and AC Rose-Innes. Contact electrification. *Advances in Physics*, 29(6):947–1023, 1980.

[94] Roger G Horn and Douglas T Smith. Contact electrification and adhesion between dissimilar materials. *Science*, 256(5055):362–364, 1992.

[95] R. J. Hunter and L. R. White. *Foundations of Colloid Science*. Clarendon Press, 1987.

[96] Dan Klarman, David Andelman, and Michael Urbakh. A model of electrowetting, reversed electrowetting, and contact angle saturation. *Langmuir*, 27(10):6031–6041, 2011.

[97] J. Zhang, J. Li, and Y. Han. Superhydrophobic ptfe surfaces by extension. *Macromolecular Rapid Communications*, 25(11):1105–1108, 2004.

[98] J. B. Chae, J. O. Kwon, J. S. Yang, D. Kim, K. Rhee, and S. K. Chung. Optimum thickness of hydrophobic layer for operating voltage reduction in ewod systems. *Sensors and Actuators A: Physical*, 215:8–16, 2014.

[99] J. M. W. Brownjohn, A. A. Dumanoglu, R. T. Severn, and A. Blakeborough. Ambient vibration survey of the bosporus suspension bridge. *Earthquake Engineering & Structural Dynamics*, 18(2):263–283, 1989.

[100] Zong-Hong Lin, Gang Cheng, Sangmin Lee, Ken C Pradel, and Zhong Lin Wang. Harvesting water drop energy by a sequential contact-electrification and electrostatic-induction process. *Advanced Materials*, 26(27):4690–4696, 2014.

[101] Jyun-Hao Lin, Yu-Hsiang Tsao, Mei-Hsuan Wu, Ting-Mao Chou, Zong-Hong Lin, and Jyh Ming Wu. Single- and few-layers MoS_2 nanocomposite as piezo-catalyst in dark and self-powered active sensor. *Nano Energy*, 31(Supplement C):575 – 581, 2017.

[102] Andreas Uihlein and Davide Magagna. Wave and tidal current energy–a review of the current state of research beyond technology. *Renewable and Sustainable Energy Reviews*, 58:1070–1081, 2016.

[103] R. Guigon, J. J. Chaillout, T. Jager, and G. Despesse. Harvesting raindrop energy: theory. *Smart Materials and Structures*, 17(1):015038, 2008.

[104] R. Guigon, J. J. Chaillout, and T. Jager. Harvesting raindrop energy: experimental study. *Smart Materials and Structures*, 17(1):015039, 2008.

[105] J. M. Donelan, Q. Li, V. Nating, J. A. Hoffer, D. J. Weber, and A. D. Kuo. Biomechanical energy harvesting: generating electricity during walking with minimal user effort. *Science*, 319:807–810, 2008.

[106] B. E. Conway. Transition from supercapacitor to battery behavior in electrochemical energy storage. *Journal of the Electrochemical Society*, 138(6):1539–1548, 1991.

[107] Dennis Sheberla, John C Bachman, Joseph S Elias, Cheng-Jun Sun, Yang Shao-Horn, and Mircea Dincă. Conductive MOF electrodes for stable supercapacitors with high areal capacitance. *Nature Materials*, 16(2):220, 2017.

[108] Richard S Norman. Water salination: a source of energy. *Science*, 186(4161):350–352, 1974.